U.S.NRC
United States Nuclear Regulatory Commission
Protecting People and the Environment

NUREG/CR-7216

Spent Fuel Pool Project Phase II:
Pre-Ignition and Ignition Testing of a 1x4 Commercial 17x17 Pressurized Water Reactor Spent Fuel Assemblies under Complete Loss of Coolant Accident Conditions

Office of Nuclear Regulatory Research

AVAILABILITY OF REFERENCE MATERIALS IN NRC PUBLICATIONS

NRC Reference Material

As of November 1999, you may electronically access NUREG-series publications and other NRC records at NRC's Library at www.nrc.gov/reading-rm.html. Publicly released records include, to name a few, NUREG-series publications; *Federal Register* notices; applicant, licensee, and vendor documents and correspondence; NRC correspondence and internal memoranda; bulletins and information notices; inspection and investigative reports; licensee event reports; and Commission papers and their attachments.

NRC publications in the NUREG series, NRC regulations, and Title 10, "Energy," in the *Code of Federal Regulations* may also be purchased from one of these two sources.

1. **The Superintendent of Documents**
   U.S. Government Publishing Office
   Mail Stop IDCC
   Washington, DC 20402-0001
   Internet: bookstore.gpo.gov
   Telephone: (202) 512-1800
   Fax: (202) 512-2104

2. **The National Technical Information Service**
   5301 Shawnee Rd., Alexandria, VA 22312-0002
   www.ntis.gov
   1-800-553-6847 or, locally, (703) 605-6000

A single copy of each NRC draft report for comment is available free, to the extent of supply, upon written request as follows:

Address: **U.S. Nuclear Regulatory Commission**
Office of Administration
Publications Branch
Washington, DC 20555-0001
E-mail: distribution.resource@nrc.gov
Facsimile: (301) 415-2289

Some publications in the NUREG series that are posted at NRC's Web site address www.nrc.gov/reading-rm/doc-collections/nuregs are updated periodically and may differ from the last printed version. Although references to material found on a Web site bear the date the material was accessed, the material available on the date cited may subsequently be removed from the site.

Non-NRC Reference Material

Documents available from public and special technical libraries include all open literature items, such as books, journal articles, transactions, *Federal Register* notices, Federal and State legislation, and congressional reports. Such documents as theses, dissertations, foreign reports and translations, and non-NRC conference proceedings may be purchased from their sponsoring organization.

Copies of industry codes and standards used in a substantive manner in the NRC regulatory process are maintained at—

The NRC Technical Library
Two White Flint North
11545 Rockville Pike
Rockville, MD 20852-2738

These standards are available in the library for reference use by the public. Codes and standards are usually copyrighted and may be purchased from the originating organization or, if they are American National Standards, from—

American National Standards Institute
11 West 42nd Street
New York, NY 10036-8002
www.ansi.org
(212) 642-4900

Legally binding regulatory requirements are stated only in laws; NRC regulations; licenses, including technical specifications; or orders, not in NUREG-series publications. The views expressed in contractorprepared publications in this series are not necessarily those of the NRC.

The NUREG series comprises (1) technical and administrative reports and books prepared by the staff (NUREG–XXXX) or agency contractors (NUREG/CR–XXXX), (2) proceedings of conferences (NUREG/CP–XXXX), (3) reports resulting from international agreements (NUREG/IA–XXXX), (4) brochures (NUREG/BR–XXXX), and (5) compilations of legal decisions and orders of the Commission and Atomic and Safety Licensing Boards and of Directors' decisions under Section 2.206 of NRC's regulations (NUREG–0750).

U.S.NRC
United States Nuclear Regulatory Commission
Protecting People and the Environment

NUREG/CR-7216

Spent Fuel Pool Project Phase II:
Pre-Ignition and Ignition Testing of a 1x4 Commercial 17x17 Pressurized Water Reactor Spent Fuel Assemblies under Complete Loss of Coolant Accident Conditions

Manuscript Completed: September 2013
Date Published: April 2016

Prepared by:
S.G. Durbin, E.R. Lindgren and L. Humphries
Sandia National Laboratories
Albuquerque, NM 87185

Z. Yuan, M. Zavisca and M. Khatib-Rahbar
Energy Research, Inc.
Rockville, MD 20847-2034

R. Beaton
U.S. Nuclear Regulatory Commission
Washington, DC 20555-0001

G. A. Zigh, NRC Technical Monitor
R. Beaton, NRC Project Manager
S. Gonzalez, NRC Project Manager

NRC Job Code N6777

Office of Nuclear Regulatory Research

ABSTRACT

The US Nuclear Regulatory Commission (NRC), in collaboration with the Organisation for Economic Co-operation and Development (OECD), and 12 international partners, conducted an experimental program to obtain experimental data for the characterization of hydraulic and ignition phenomena of prototypic light water reactor fuel assemblies in a spent fuel pool under complete loss of coolant accidents for validation of the MELCOR severe accident computer code. MELCOR is a fully integrated, engineering-level computer code whose primary purpose is to model the progression of postulated accidents in light water reactors as well as non-reactor systems (e.g., spent fuel pool and dry cask). The experimental program was conducted in two phases at Sandia National Laboratories. The first phase focused on axial heating and zirconium fire propagation in a single 17×17 PWR fuel assembly. The second phase consisted of pre-ignition and ignition tests of five prototypic PWR full-length 17×17 fuel assemblies to simulate a complete loss-of-coolant-accident in a spent fuel pool. The assemblies were placed in a 1×4 configuration where the center fuel assembly was electrically heated and the four surrounding assemblies were unheated. Two of the unheated assemblies contained pressurized rods to study ballooning effects.

TABLE OF CONTENTS

LIST OF FIGURES

LIST OF TABLES

EXECUTIVE SUMMARY

In 2001, an evaluation of the potential accident risk in a spent fuel pool (SFP) at a US nuclear plant was performed. NUREG-1738, "Technical Study of Spent Fuel Pool Accident Risk at Decommissioning Nuclear Power Plants," describes a modeling approach for a typical decommissioning plant with design assumptions and industry commitments, the thermal hydraulic analyses performed to evaluate spent fuel stored in the SFP, the risk assessment of SFP accidents, the consequence calculations, and the implications for decommissioning regulatory requirements. Some of the assumptions in the accident progression were known to be necessarily conservative, especially the estimation of the fuel damage. The SFP accident research continued by applying best-estimate computer codes to predict the severe accident progression following various postulated initiators. These studies identified various modeling and phenomenological uncertainties that prompted a need for experimental confirmation.

Previous analyses have shown that fuel assemblies can ignite and propagate in a SFP during a complete loss of coolant scenario. Hence, qualified data obtained in representative fuel configurations were needed to confirm these results. In 2003, the NRC undertook an experimental program to address thermal-hydraulic conditions and zirconium fire propagation during a complete loss of coolant event in a boiling water reactor spent fuel pool. These experiments are summarized in NUREG/CR-7143. The experiments showed that the measured form and friction loss coefficients of a prototypic BWR assembly were significantly different from generally accepted values and that the use of the measured coefficients was vital for accuracy when calculating (with MELCOR) the naturally induced air flow rate. The incorporation of "breakaway" Zircaloy oxidation kinetics into MELCOR was also necessary to accurately capture the Zircaloy heat-up to ignition and oxygen consumption.

In May 2009, the NRC, in collaboration with the Organisation for Economic Co-operation and Development/Nuclear Energy Agency (OECD/NEA) and 12 international partners signed an agreement called the "OECD/NEA SFP Project – An Experimental Programme and Related Analyses for the Characterization of Hydraulic and Ignition Phenomena of Prototypic Water Reactor Fuel Assemblies." This program defined an experimental test matrix, experimental conditions and parameters to be examined with the overall objective being to perform a highly detailed thermal-hydraulic characterization of a full-length commercial fuel assembly mockup to provide data for the direct validation of severe accident computer codes (i.e., MELCOR). This experimental work was valuable to the OECD/CSNI community to facilitate severe accident code validation (ATHLET-CD, ASTEC, Ansys Fluent, DRACCAR, and MELCOR) and reduce modeling uncertainties within the codes. Further, it provided a collaborative exchange of information on severe accident modeling which resulted in increased knowledge to participating members that can be used in their regulatory programs and future research.

The study was conducted in two phases; Phase I focused on axial heating and burn propagation in a single assembly and Phase II (documented in this report) focused on axial and radial heating, burn propagation and the effects of fuel rod ballooning. Phase II consisted of a single heated assembly surrounded by four unheated assemblies representing a 1×4 loading pattern. These experiments, completed in June 2012, were performed at Sandia National Laboratories.

In this second experimental phase, electrically resistive heaters with Zircaloy cladding were placed in the center cell of a 3×3 pool rack and surrounded by four unheated fuel assemblies. This arrangement imitated the situation of a recently offloaded assembly surrounded by much older and thus lower decay heat assemblies. Two of the peripheral fuel assemblies were constructed with pressurized rods that ballooned when sufficiently heated, and the other two

fuel assemblies were constructed with vented rods that did not balloon. Nine pre-ignition tests were conducted with powers ranging from 1 kW to 15 kW, representing assemblies from as young as 3 months after offload to as old as 8 years, assuming 45 GWd/MTHM burnup. The pre-ignition tests were conducted for 12 hours or until a peak cladding temperature of 900 K [1,160°F] was reached in the center assembly. Tests conducted at powers greater than 8 kW were terminated before 6 hours. Tests at 1 kW and 4 kW were conducted for 24 hours in attempts at achieving steady state. As a measure of repeatability, the 4 kW test was performed twice, once for 12 hours and again for 24 hours.

For the ignition test, the total applied power to the center assembly was 15 kW, which represented an assembly with a 45 GWd/MTHM burnup approximately 3 months after offload. All five fuel assemblies were completely consumed as a result of the Zircaloy cladding fire. The thermal-hydraulic behavior of the fuel assemblies was monitored during the ignition test as well as the timing of the ballooning of the pressurized rods. Finally, the depletion of oxygen and nitrogen in the exhaust stream were also directly measured.

Ignition of the Zircaloy was first observed in the center fuel assembly at the z = 3.302 m [130 in] level and at an elapsed test time of 6.31 hours based on a thermal criterion of 1,200 K [1,700°F]. The cladding fire also propagated transversely into the peripheral assemblies starting at 7.08 hours and at the z = 3.150 m [124 in] level. The ignition had progressed across the entire cross section of all of the peripheral assemblies by 8.74 hours. The ballooning events in the two assemblies occurred within approximately 3 minutes of each other at a given location despite the North and South assemblies being filled to pressures of 6.2 MPa [900 psi] and 5.2 MPa [750 psi], respectively. The thermal-hydraulic behavior of assemblies with ballooned rods did not appear to be discernible from the unpressurized assemblies.

The gases measured at the exhaust were nitrogen, oxygen, argon, water, carbon dioxide, and helium. The analysis shows two distinct stages of oxidation. The primary oxidation stage was very energetic and continued for 11 hours after ignition. The second stage continued for 88 hours after the first stage. During the first stage all oxygen entering the assembly was consumed by the zirconium oxidation and a substantial portion of the nitrogen was consumed by production of the nitride from much (if not most) of the remaining unoxidized zirconium. During the second stage, all of the oxygen entering the assembly was consumed by the oxidation of zirconium nitride as indicated by the release of nitrogen gas.

The additional release of energy from the production of zirconium nitride, along with the significant reduction in convective energy removal during the primary oxidation stage are phenomena to be considered when assessing the propagation of heat and fire to adjacent assemblies during a loss of water inventory accident in SFPs.

Several MELCOR models were developed to simulate the PWR spent fuel assembly experiment. These models include both 2-ring and 9-ring variants. The 9-ring model, where assemblies are subdivided by rows of fuel rods, provides a more detailed modeling of the experiment to be used in both assessing the MELCOR models as well as the limitations inherent in the 2-ring model. A 2-ring model is preferred as any reasonable full-scale modeling of a reactor plant spent fuel pool would be simulated with such a relatively coarse grid due to computer performance and model complexity issues. The MELCOR models were used to simulate both the pre-ignition and ignition tests.

The conditions of this experiment challenge the MELCOR approach to representing an assembly (or collection of assemblies) with a single MELCOR node (or ring) consisting of a single lumped parameter representing all fuel rods in that node. In particular, a single representative temperature for the fuel rods in the unheated assembly is insufficient to capture the large temperature gradients and the dependence of oxidation rates on the local clad temperature. Consequently, the MELCOR code was modified to allow improved temperature refinement within a single radial ring by providing a means for the user to specify multiple fuel rod types within that ring. Note that this work is a proof of concept and that the models are currently valid up until material begins to relocate. Further model development and refinement is necessary prior to these modifications becoming part of an official release version of MELCOR.

The resulting analysis shows that MELCOR is capable of predicting the conditions of the OECD/NEA SFP experiment with either a 9-ring or 2-ring multiple rod model. These models show good agreement to important parameters such as PCT, ignition time and ignition propagation. The new 2-ring multiple rod model has also been compared with the 9-ring model and comparisons show that the new modeling is able to predict a similar response but with fewer COR rings. As a result, code performance is improved and the input model is greatly simplified.

ABBREVIATIONS

ANL	Argonne National Laboratory
BWR	boiling water reactor
CFD	computational fluid dynamics
DAQ	data acquisition
D_H	hydraulic diameter
GWd	gigawatt-days
ID	inside diameter
IFM	intermediate fluid mixer
MELCOR	severe accident analysis code
MTHM	metric ton of heavy metal
NEA	Nuclear Energy Agency
NRC	Nuclear Regulatory Commission
OD	outside diameter
OECD	Organisation for Economic Co-operation and Development
PCT	peak cladding temperature
PWR	pressurized water reactor
PID	proportional-integral-derivative
RGA	residual gas analyzer
SCR	silicon controlled rectifier
SEM	secondary electron multiplier
SFP	spent fuel pool
slpm	standard liters per minute (standard defined at 0ºC and 1 atm)
SNL	Sandia National Laboratories
TC	thermocouple

1 INTRODUCTION

1.1 Objective

The objective of the Phase II testing was to perform a highly detailed thermal-hydraulic characterization of five full-length, commercial 17×17 pressurized water reactor (PWR) fuel assembly mock-ups to provide data for the direct validation of MELCOR or other appropriate severe accident codes. Phase I testing concluded with ignition of a single PWR assembly in 12.7 hours using 5 kW power. The present PWR characterization is similar to that conducted for the previous boiling water reactor (BWR) study and will lead to a full-scale multi-PWR fire test where the zirconium alloy cladding is heated in air to ignition and the fire propagates to adjacent assemblies (Ref. 1). This report details the findings from the Phase II testing of the Spent Fuel Pool (SFP) Project.

1.2 Testing Outline

The SFP project was conducted in two phases. The Phase I test series was conducted using a single PWR assembly and has been concluded (Ref. 1). Phase II focused on transverse heating and burn propagation in five full-length assemblies. The fuel assemblies were arranged in a pool rack with the heated assembly in the center cell. The four unheated peripheral fuel assemblies shared a cell wall with the center assembly, representing older spent fuel. All mock fuel assemblies were constructed with zirconium alloy cladding and prototypic structural components. The center assembly was constructed with electrically resistive heaters. The thermal mass of the compacted MgO powder, used to make the electric heater, is an excellent match to spent fuel as demonstrated in the previous BWR study. The peripheral assemblies were loaded with MgO pellets in order to closely match the thermal mass of spent fuel. Two of the four peripheral assemblies were pressurized with argon to simulate ballooning of the fuel clad during the ignition test.

A series of pre-ignition tests were conducted to build a database of the thermal-hydraulic response of fuel below ignition temperatures. Figure 1.1 shows the decay power of a PWR fuel bundle as a function of time from discharge. These values were calculated using the normalized decay heats provided in Ade and Gauld (Ref. 2). Several burnups are shown in the graph to orient the reader, but a value of 45 GWd/MTHM was chosen as the reference burnup because it approximates the current industry average (Ref. 3). The range of the pre-ignition tests represents fuel aged between 2.8 months to 8 years after discharge for the reference burnup of 45 GWd/MTHM, or 15.0 to 1.0 kW decay heats, respectively. The ignition test was conducted at a decay heat of 15.0 kW.

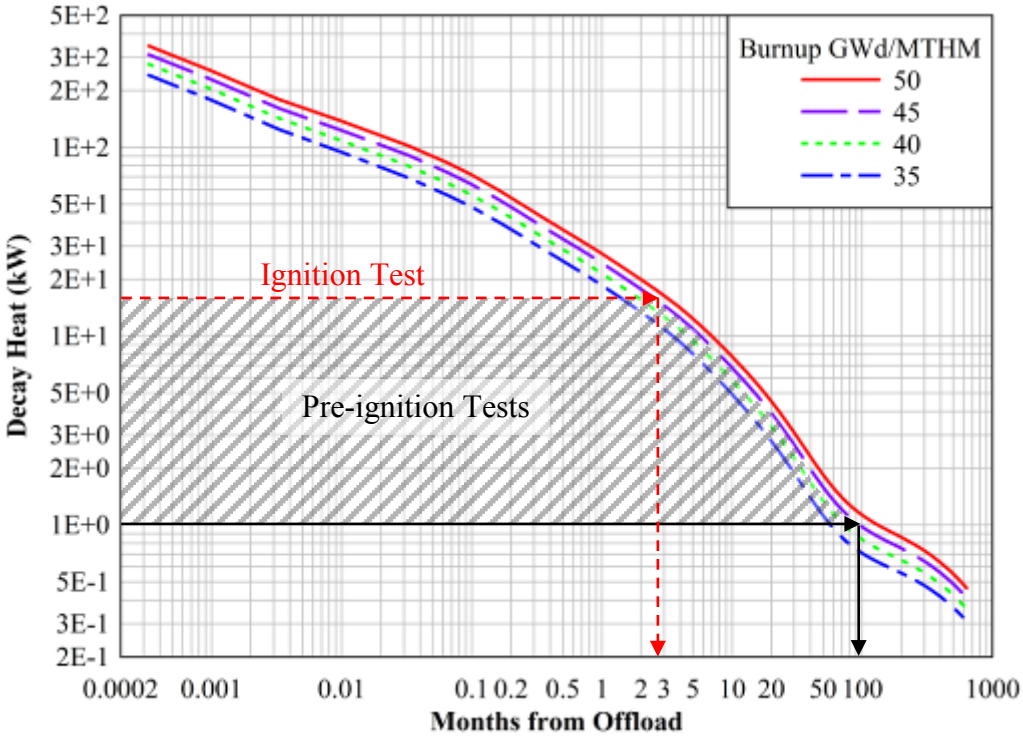

Figure 1.1 Decay heat of a PWR 17×17 assembly as a function of time from discharge

The baseline, testing parameters for Phase II are summarized below.

- Characteristic pool cell size – 224.2 and 222.7 mm [8.83 and 8.77 in] average, as-built inner dimensions of the center and peripheral assemblies, respectively
- Pre-ignition test powers – 1 to 15 kW (Simulated 96 to 2.8 months from offload for 45 GWd/MTHM, respectively)
- Ignition test power – 15 kW electrical input (Simulated 2.8 months from offload for 45 GWd/MTHM)

The ignition test determined the location in the center assembly where ignition first occurred and the nature of the burn propagation throughout the neighboring fuel assemblies. As shown in Figure 1.2, the unpowered peripheral assemblies experimentally represented a “cold neighbor” situation and demonstrated the potential of zirconium fires initiated in the higher decay power assemblies to spread through the remainder of a fully populated pool. The remainder of this report outlines the details of the Phase II pre-ignition and ignition test results.

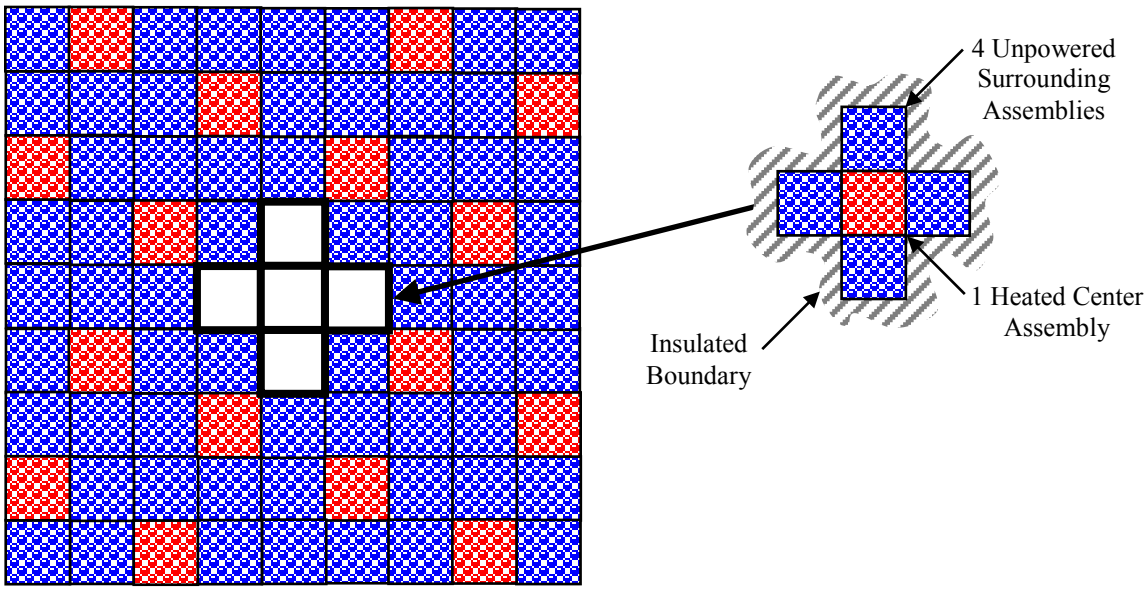

Figure 1.2 Approximate pool loading scheme for a 1×4 test layout with an insulated boundary condition

2 APPARATUS AND PROCEDURES

2.1 General Construction

The testing in the Spent Fuel Pool (SFP) Project Phase II focused on the nature of the zirconium fire in the five full-length fuel bundles and specifically the propagation of the fire from the center to the peripheral bundles. The test assembly prototypically represented five commercial 17×17 PWR fuel bundles. The various components comprising a typical 17×17 PWR assembly are illustrated in Figure 2.1. The main structural component of the assembly is the core skeleton, which consists of eleven spacers permanently attached to twenty-five guide tubes. The 264 fuel rods pass through the spacers and are held captive in the assembly by the top and bottom nozzles.

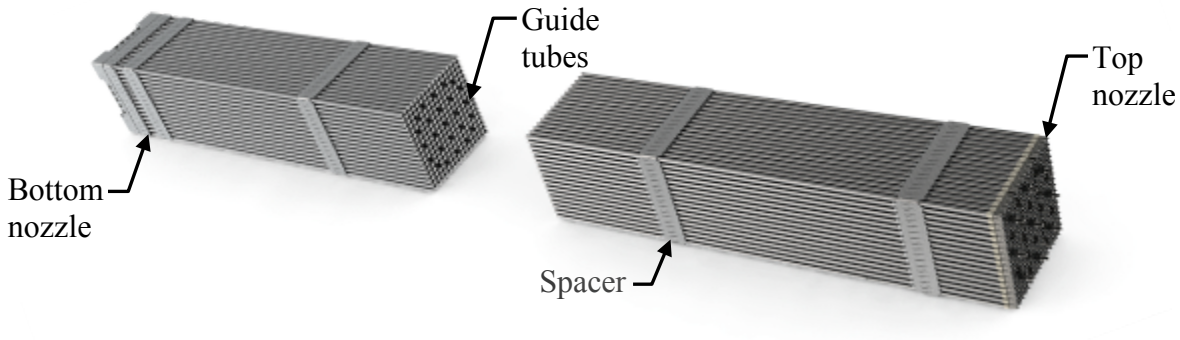

Figure 2.1 Various components in a typical 17×17 PWR fuel assembly

The four peripheral PWR assemblies were fabricated using prototypic, commercial 17×17 PWR components including a skeleton, top and bottom nozzles, 9.50 mm [0.374 in] OD by 0.57 mm [0.0225 in] wall tubing, top and bottom end plugs, and plenum springs. The center heated PWR assembly was fabricated using prototypic, commercial 17×17 PWR components and 9.53 mm [0.375 in] OD heater rods made from 11.18 mm [0.44 in] zirconium alloy tubing supplied by an industrial vendor. The wall thickness of the Zircaloy-2 cladding was approximately 0.71 mm [0.028 in] and was relatively unchanged by the heater fabrication process. The spent fuel rod simulators for Phase II had a linear power profile and a maximum output of 31.1 W/m [9.5 W/ft], which was twice that expected to produce ignition.

An important attribute of the mock fuel designs was the fact that the thermal mass of the magnesium oxide (MgO) powder used to simulate the spent fuel was virtually the same as spent fuel over the entire temperature range of interest (as shown in Figure 2.2). The thermal mass was estimated from the measured solid fraction of the MgO used in the heater rods and peripheral rods and the specific heat data for MgO compiled in Touloukian Vol. 5, 1970 (Ref. 4). These spent fuel simulators therefore heated at approximately the same rate and stored the same amount of thermal energy as prototypic spent fuel rods. The magnesium oxide in the heated rods was constructed by compacting MgO powder around a coil of electrically resistive Nichrome wire. This compacted ceramic powder also forms the electrical insulation between the central heating element and the Zircaloy-2 cladding. The peripheral assemblies were constructed using sintered MgO pellets, which were inserted into Zircaloy-4 cladding. The distinction between the two types of mock spent fuel were due to differences in the as-built densities of the MgO inside the rods. The symbols in the plot for the Phase II heater and peripheral rods represent the measured, average value for each design.

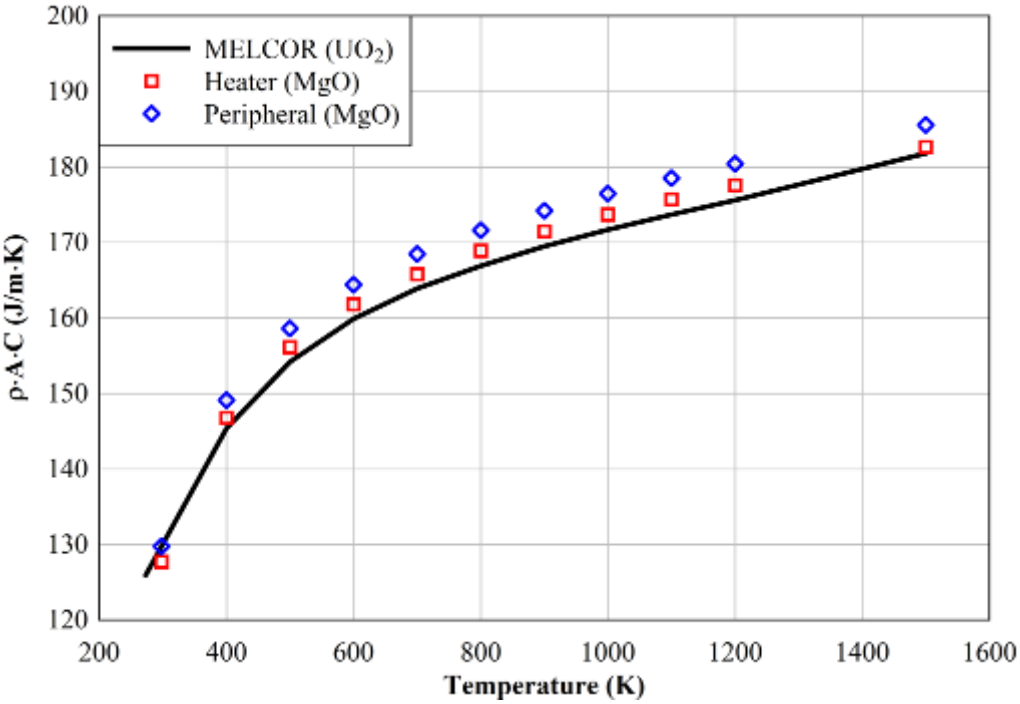

Figure 2.2 Thermal mass per unit length comparison of spent fuel and MgO fuel rod simulators

Next, the thermal conductivity of the compacted MgO powder was compared to the thermal conductivity of spent fuel and fresh UO_2 fuel. The thermal conductivity is of lesser importance due to the short conduction path between the heater element and the outer cladding and the slow heat rate of the simulated accident. Figure 2.3 compares the estimated thermal conductivity as a function of temperature for the compacted MgO used in the heater rods, the UO_2 used by MELCOR, and spent fuel from FRAPCON-3. The spent fuel estimate was based on corrections applied to the MELCOR UO_2 data as described in NUREG/CR-6534 Vol. 2. The thermal conductivity of compacted MgO powder is a function of the degree of compaction. The thermal conductivity of the compacted MgO used in the heater rods was estimated based on the measured solid fraction of MgO and extrapolation of data compiled in Touloukian Vol. 2, 1970. At low temperatures the thermal conductivity of the compacted MgO is about a third of the estimated thermal conductivity of spent fuel but as the temperature increases the comparison converges. At high temperatures the thermal conductivity of the compacted MgO is only 15 percent lower than spent fuel or fresh UO_2 fuel.

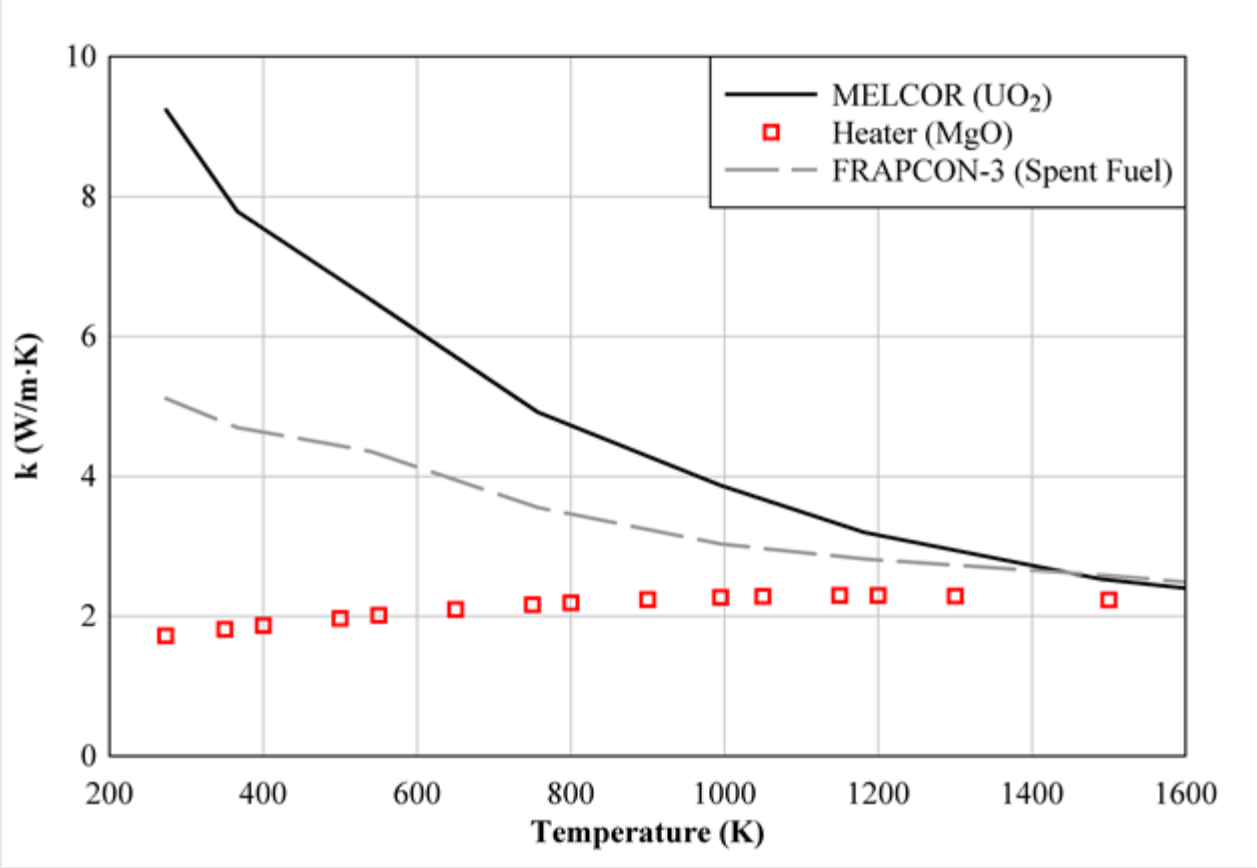

Figure 2.3 Comparison of thermal conductivity for UO_2, spent fuel, and MgO fuel rod simulators

Table 2.1 gives the individual and cumulative masses of all components within the SFP Phase II test assembly. Major sub-assemblies include the pool rack, PWR fuel skeletons, peripheral rods, and heater rods. The mass of thermocouples within the assembly is neglected. Note that the mass of Zircaloy in the center and peripheral assembly differs due to the different wall thickness of the Zr-4 tubing used in the peripherals and the Zr-2 tubing used to make the heater rods in the center assembly.

Table 2.1 Masses of components in the SFP project Phase II test assembly

Part Name	Material	Quantity	Individual Part Weight (kg)	Total Part Weight (kg)
3×3 Pool Rack				
Tie bar	Stainless steel	32	0.041	1.31
Neutron absorber	Aluminum 1100	16	5.77	92.32
Internal sheathing	Stainless steel	16	6.70	107.19
Pool cell	Stainless steel	5	57.35	286.74
Shim stock	Stainless steel	8	0.866	6.93
Filler panel	Stainless steel	4	16.63	66.51
Subtotal				561.00
Skeleton				
Skeleton*	ZIRLO	1	32.67	32.67
Bottom nozzle	Stainless steel	1	5.26	5.26
Top nozzle	Stainless steel	1	5.71	5.71
Debris catcher	ZIRLO	1	1.43	1.43
Bottom bolts	Stainless steel	24	0.007	0.18
Guide tube inserts	Stainless steel	24	0.004	0.09
Subtotal				45.35
Peripheral Rods				
Cladding	Zr-4	1056	0.406	428.92
Top end plug	Zr-4	1056	0.003	3.33
Bottom end plug	Zr-4	1056	0.008	8.62
Plenum spring	Stainless steel	1056	0.006	6.29
MgO ceramic	MgO	1056	0.512	541.01
Subtotal				988.16
Heater Rods				
Cladding	Zr-2	264	0.539	142.20
MgO 142.25" heated + 2" unheated	MgO	264	0.504	133.18
MgO 10" upper unheated "plenum"	MgO	264	0.036	9.48
Subtotal				284.86
Phase II Assembly Total				1879.37

* Includes 24 guide tubes, 1 instrumentation tube, 7 full spacers, and 3 IFM spacers

2.1.1 Assembly Layout

Figure 2.4 shows the layout of the Phase II fuel bundles with and without the pool rack in place. The heated assembly was placed in the center pool cell and was surrounded by unheated assemblies. Two of these peripheral assemblies were constructed with pressurized fuel rods to simulate ballooning of the cladding during the ignition test.

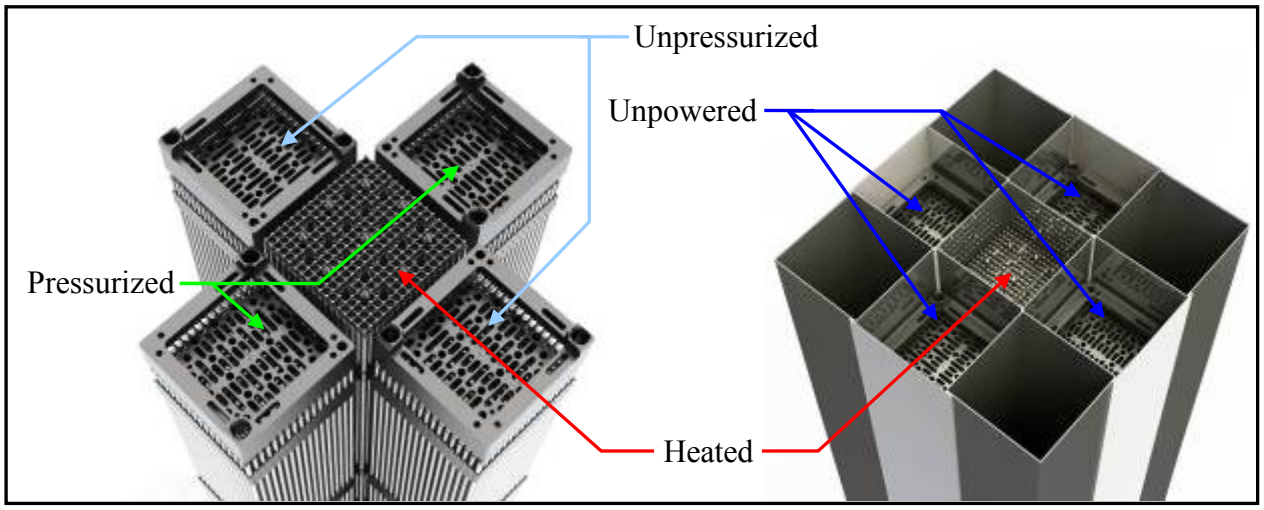

Figure 2.4 Layout of the Phase II test assembly

2.1.2 Dimensions of the Test Assembly

The Holtec pool rack for 17×17 PWR fuel assemblies incorporates pool cells with an inner dimension of 224.5 mm [8.84 in]. Therefore, a 224.5 mm [8.84 in] pool cell was the design basis for the Phase II ignition test. As with the Phase I pool cells, the Phase II pool rack was constructed of 1.91 mm [0.075 in] thick stainless steel material. The actual inner dimensions of each of the pool cells are shown in Figure 2.5. The inner dimension of the center cell, used in this experiment was 224.2 mm [8.83 in], which is nearly identical to the 224.5 mm [8.84 in] Holtec design. The as-built peripheral cells are slightly smaller than the design with an average inner dimension of 222.7 mm [8.77 in], or less than a one percent difference. The insulation scheme for Phase II is also illustrated in Figure 2.5. The corner cells were filled with high temperature insulation. The entire assembly was surrounded by approximately 152.4 mm [6 in] of the same high temperature insulation. A stainless steel thermal radiation barrier was installed around the external insulation.

-

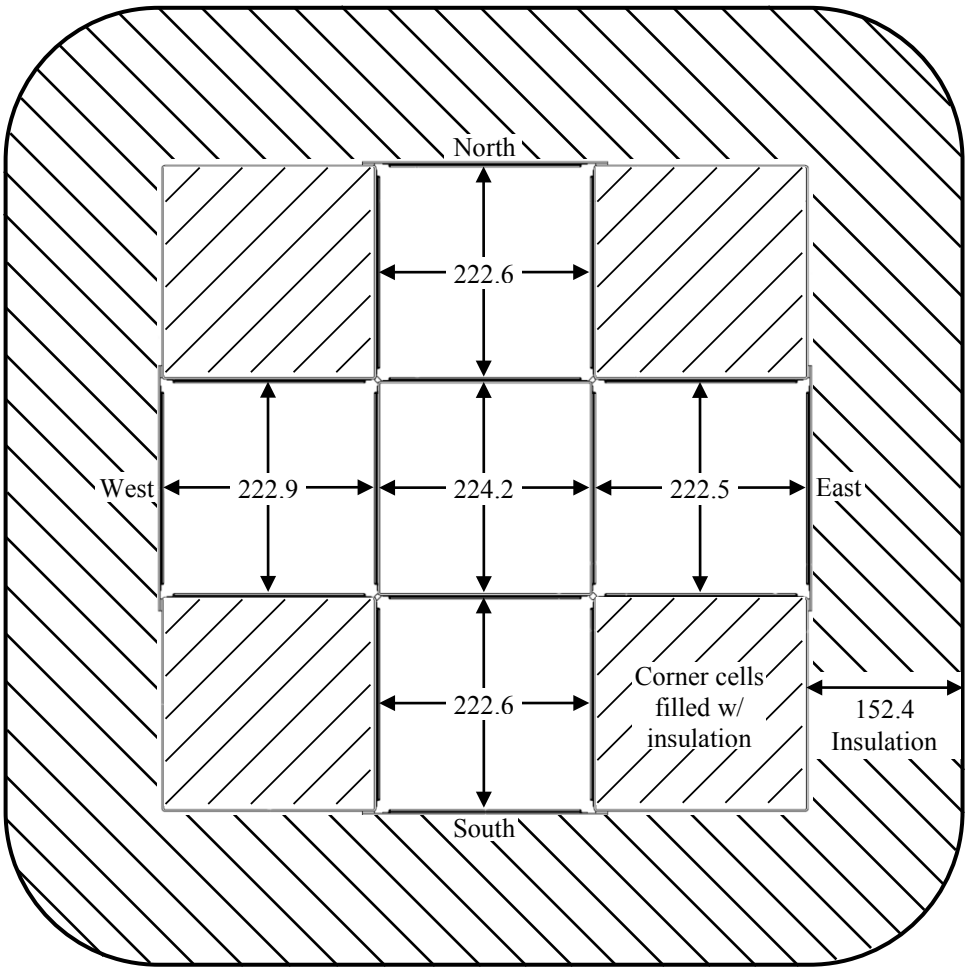

(All dimensions in mm)

Figure 2.5 Dimensions of the as-built pool rack and the design insulation thickness

2.2 Design of the Heated Fuel Bundle

2.2.1 Heater Design

The design for the Phase II heater rods is shown in Figure 2.6. This design is identical to those used in Phase I except that linear power density was doubled for Phase II. The heated and unheated lengths for the fuel rod simulator and a PWR fuel rod are compared for reference. As shown in Detail A, the lower, unheated length of the heater included a steatite standoff 15.9 mm [0.625 in] for electrical isolation and an internal power introduction length 50.8 mm [2 in]. The height of the axial heated zone with respect to the top of the bottom nozzle was preserved as closely as possible between the heater rod 3.680 m [144.875 in] and the reference PWR fuel rod 3.683 m [145 in]. Due to the necessary electrical connection at the top, the heater rod design was extended 0.066 m [2.60 in] above the prototypic length. Details of the top and bottom electrical connections are given in Section 2.2.2.

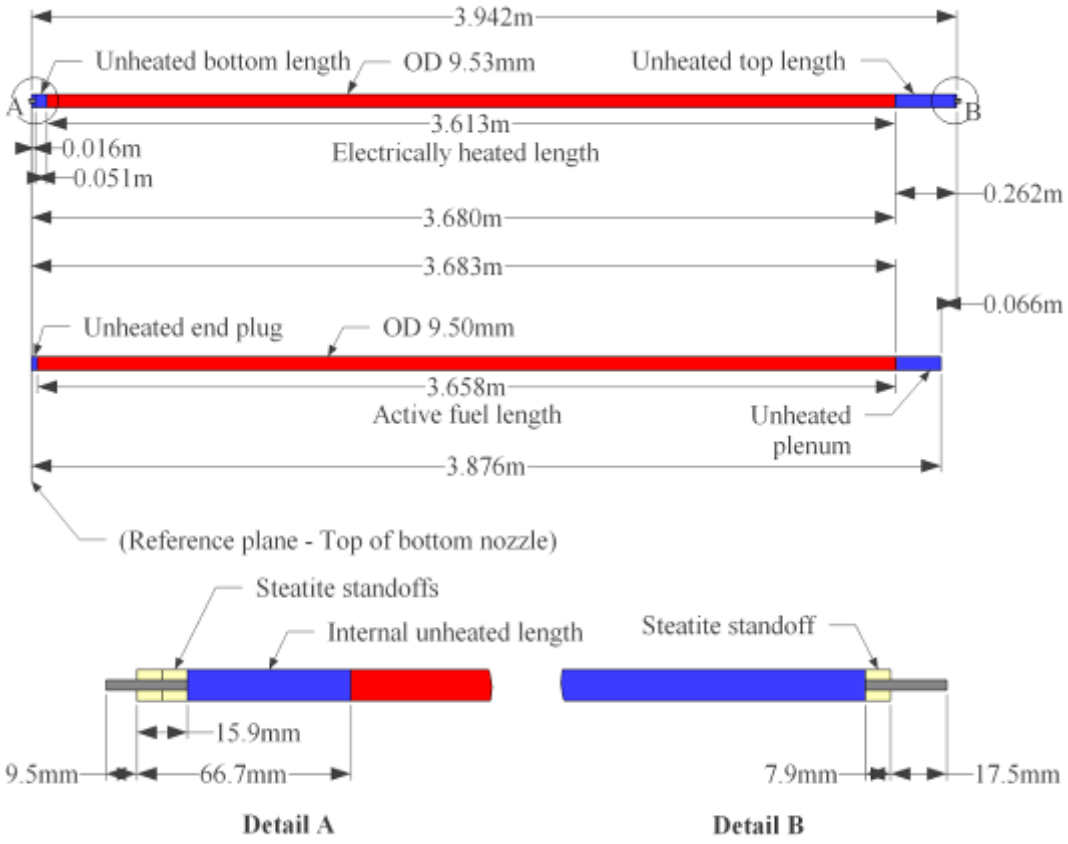

Figure 2.6 Design of the electrically heated fuel simulators

Note: The vertical dimension in the plan view has been scaled 6:1 to show the heated and unheated zones. PWR fuel layout shown for reference.

2.2.2 Heater Rod Electrical Connections

Introducing electrical power into the assembly presented several engineering challenges. An electrical current was fed into the assembly at the top of the assembly by applying voltage, up to 120 VAC, across the heater rods. The bottom electrical connections terminate in the bottom nozzle, which was tied to the circuit neutral leg. Electrically isolating the heater cladding, guide tubes, and pool cell was crucial to prevent a short circuit in the power loop.

The upper electrical bus plate and connections were specifically designed to survive at higher temperatures. Figure 2.7 shows a rendering of the design of the top electrical bus plates. The bus plates were cut from three pairs of nickel-copper alloy 400 (Monel) plates and replaced the top nozzle in the center fuel bundle. The bus plates were electrically divided into three zones of 88 heater rods each to accommodate the higher power requirements of the Phase II experiment and facilitated installation of the bus plates onto the heater rod power posts. To insure even distribution of power to the heater rods, the power was introduced into each zone via three 6.4 mm [0.25 in] Monel threaded rods as shown in Figure 2.7.

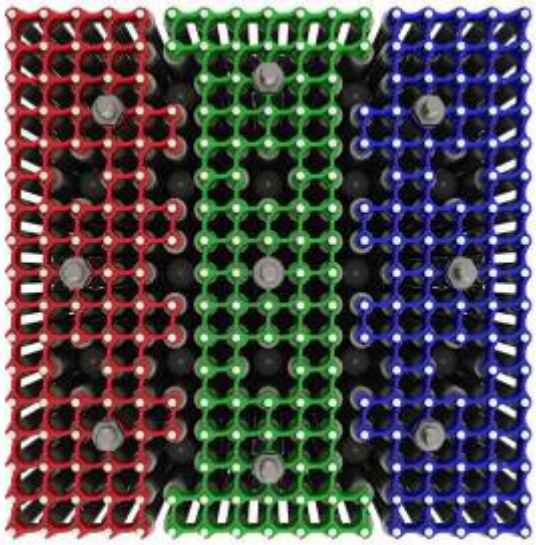

Figure 2.7 Design of the top electrical bus plate

Each bus plate zone was comprised of a pair of upper and lower plates. The heater rod connection collars for the 88 heater rods were open on the same quadrant corner on a given plate. The connection collars on the mating plate were open on the opposite quadrant. When installed, the 88 heater rod connection pins passed through the plate in the larger interstitial area between four pin connection collars. Then, the plate was slid diagonally until all of the heater rod pins were captured in the connection collars. The top and bottom plates were moved in opposite directions so once in position each heater rod pin has 360° contact with the connection collar as shown in Figure 2.8. The Monel threaded rods are truncated in this rendering. For the actual installation, the all-thread rods extended approximately 1 m above the bus plates before transitioning to a traditional copper power lead.

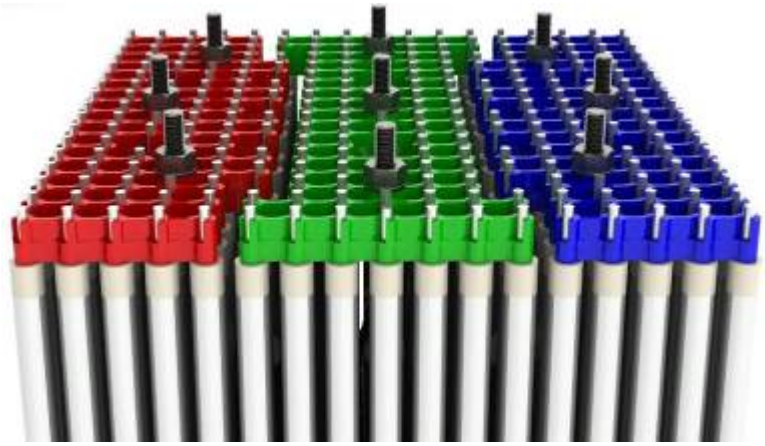

Figure 2.8 Assembly detail of the top electrical bus plate design

The top of the assembly is represented schematically in Figure 2.9. The top electrical bus plates were left out of the drawing to avoid confusion. Figure 2.9 shows the top of two heater rods and a guide tube in cross section. Steatite standoffs and an alumina sphere isolated the cladding and guide tubes from electrical contact with the top bus plates. The additional length of the heater rods over the prototypical value was required to place the electrical connection

above the top of the guide tubes. A detailed drawing of the power connection, including the top bus plates, is shown in Figure 2.10.

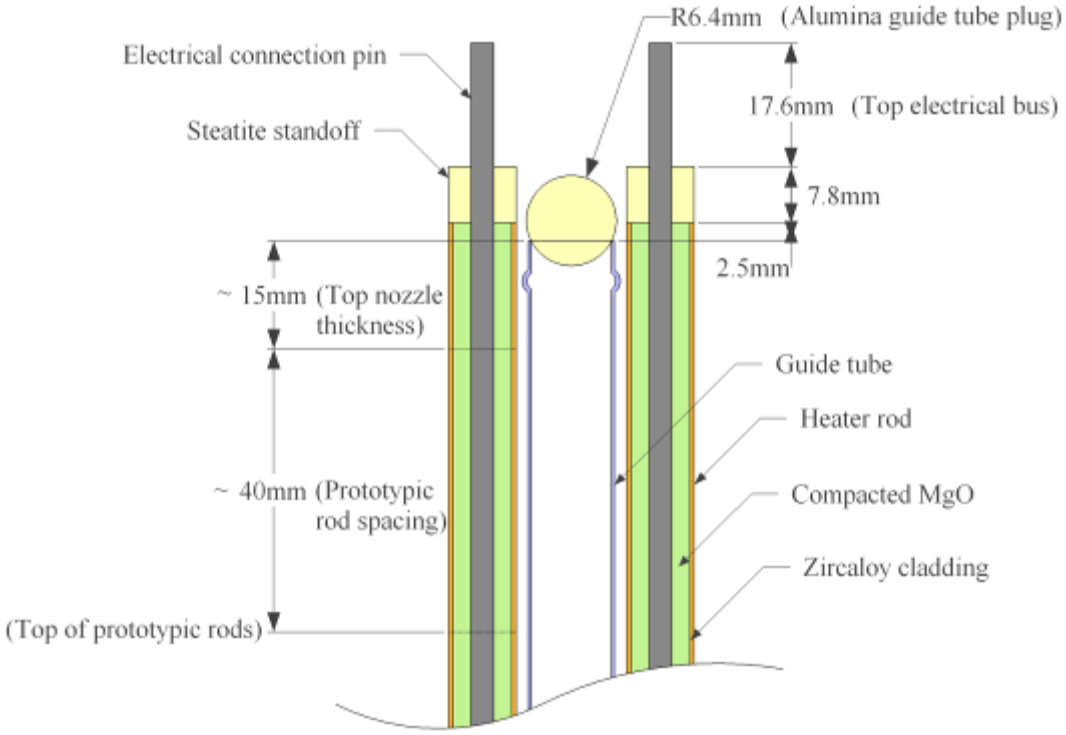

Figure 2.9 Detail drawing of the top of the assembly showing two heater rods and a single guide tube

The top and bottom plates were held in place by the threaded Monel power rods as shown in Figure 2.10. On the lower plates, the power connection locations were threaded to receive the power rod. The power connection locations on the top plate were slightly oversized, through holes. The power rod was passed through the upper plate and threaded into the lower plate. A Monel nut and washer was tightened down onto the top plate to lock the plate together.

The bottom PWR nozzle served as the electrical bus for the neutral connections. Blind holes machined into the bottom nozzle accepted the connection pin of each heater rod as shown in Figure 2.11. High temperature silver contact grease was placed in each hole to insure good connectivity.

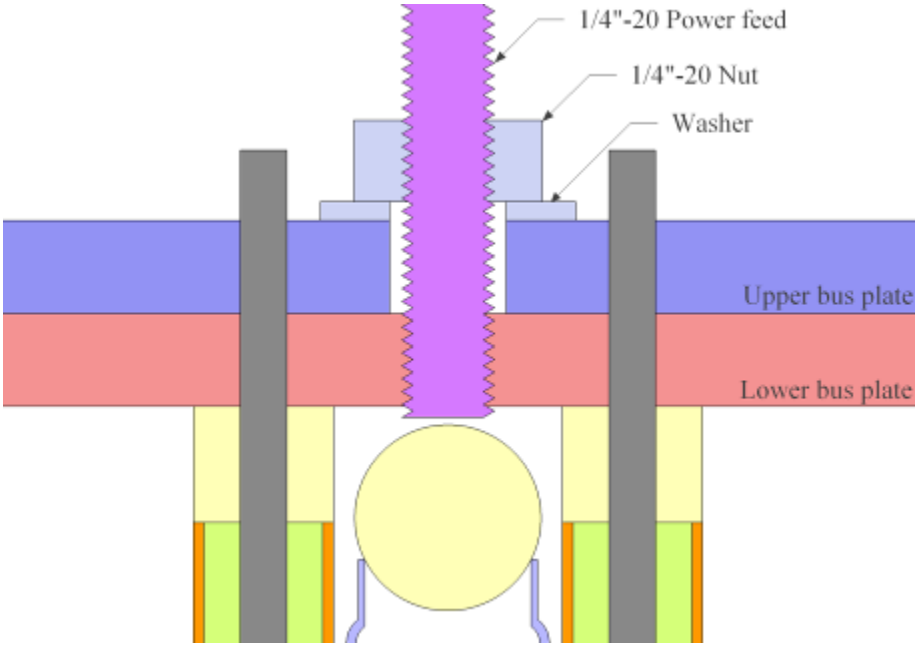

Figure 2.10 Cross-sectional detail drawing of the top electrical connection from the power feed into the heater electrical pins

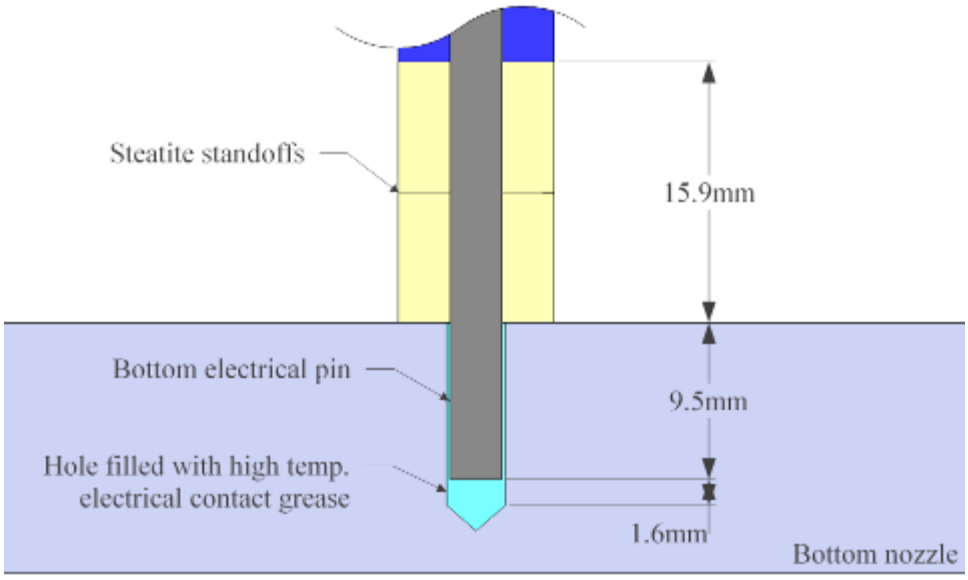

Figure 2.11 Detail drawing of the bottom of the assembly showing the electrical connection of a single heater rod to the bottom nozzle (neutral)

Figure 2.12 shows the configuration of the power control system for the SFP Phase II test series. The data acquisition (DAQ) system generated a power set point based on user input via a LabVIEW graphical user interface. This set point signal was relayed to a proportional-integral-derivative (PID) controller. The PID controller determined an appropriate power control signal by comparing the power set point to the feedback signal from the system Watt transducer. The silicon controlled rectifier (SCR) power controller received the control signal and allowed the prescribed electrical power into the resistive load of the test assembly.

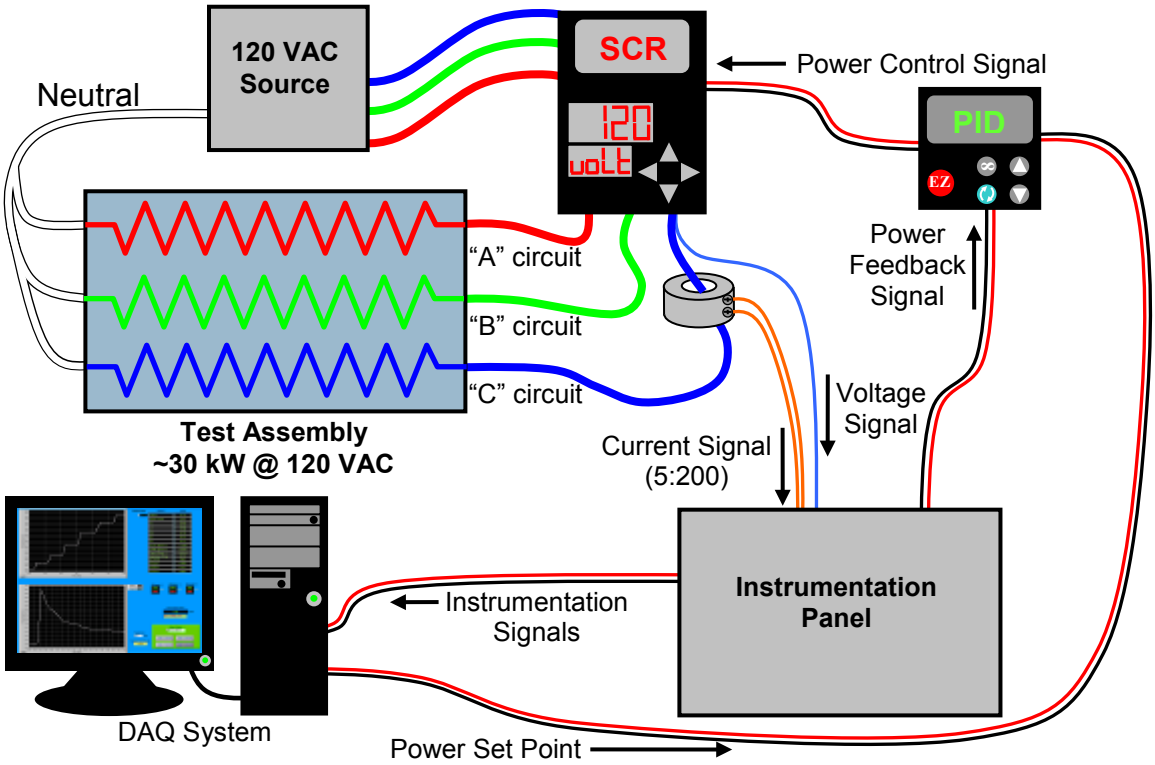

Figure 2.12 Power control system and test circuits

Note: Power instrumentation and control shown only for "C" circuit. Actual installation includes instrumentation and PID control for all three circuits.

The internal layout of the instrumentation panel is shown in Figure 2.13. The transducers measured Watts, voltage, and current applied to the assembly. The signal from the Watt transducer was output to the DAQ and the PID controller as a feedback signal. The components used in this testing are listed in Table 2.2.

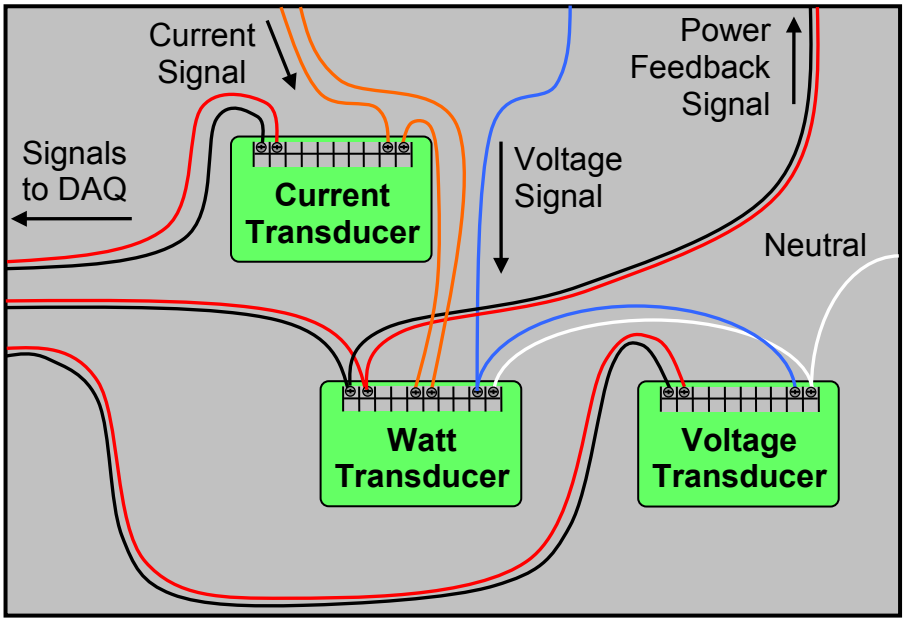

Figure 2.13 Schematic of the instrumentation panel for "C" circuit

Table 2.2 List of equipment used for power control

Description	Manufacturer	Model
AC Watt Transducer	Ohio Semitronics	PC5-001D
AC Voltage Transducer	Ohio Semitronics	3VTR-001D
AC Current Transducer	Ohio Semitronics	3CTR-010D
PID Controller	Watlow Electric Manufacturing	PM6C1FJ1RAAAAA
SCR Power Controller	Watlow Electric Manufacturing	PC91-F25A-1000

2.3 Design of the Pressurized Peripheral Bundles

A significant technical challenge in Phase II of the SFP Project was the manufacture and installation of pressurized fuel simulators in two of four peripheral assemblies. Welding techniques were developed for the attachment of the prototypic end plugs to the rod cladding. A total of 528 pressurized fuel rods were manufactured for installation in two peripheral assemblies for Phase II pre-ignition and ignition testing. These efforts used prototypic test articles with Zircaloy-4 (Zr-4) cladding and end plugs.

An initial series of small-scale rodlets were produced to evaluate the acceptability of welds between the fuel end plugs and the cladding and were documented in the Phase II test plan (Ref. 19). After the qualification of these welds during the pilot study, a production run of full-length rods was commissioned. These rods contained magnesium oxide (MgO) pellets and a stainless steel spring installed inside of the cladding to simulate the thermal mass of spent nuclear fuel. Figure 2.14 compares the design of the Phase II peripheral rods with spent fuel. Due to a higher gas volume fraction in the simulated fuel region, the fill pressure of the Phase II peripheral rods was compensated in order to mimic the pressure of spent fuel at the time of cladding rupture.

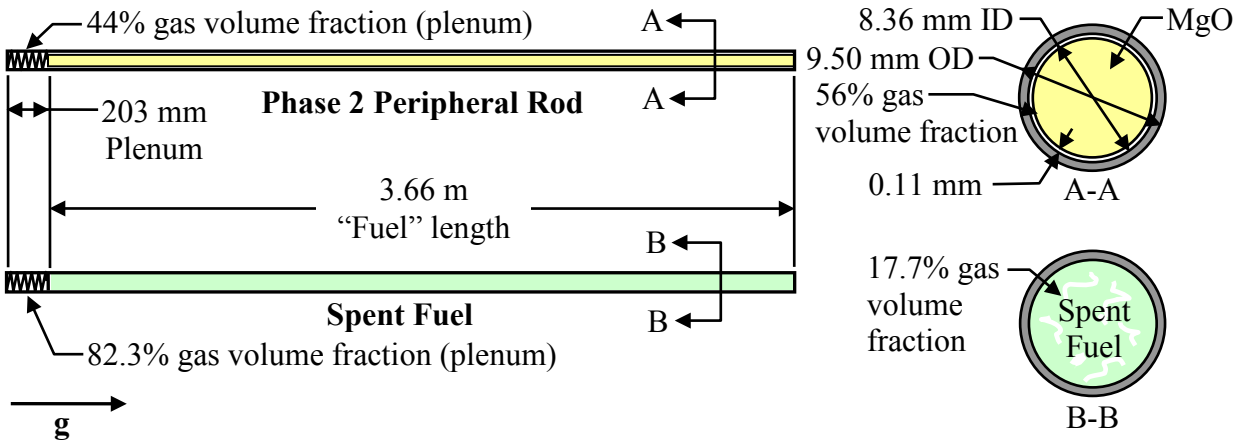

Figure 2.14 Schematic of the internal geometry of a Phase II peripheral rod and spent fuel

2.3.1 Welding Techniques

2.3.1.1 Orbital Welds

Two orbital welds were required between the Zr-4 cladding and fuel end plugs, one at the top and another at the bottom of the fuel rod. Figure 2.15 shows a cross-sectional view of the setup for welding the top end plug onto the Zr-4 fuel rod. Prior to the actual orbital welding procedure, both rod ends were reamed and all parts were thoroughly cleaned. External shield gas was provided by the orbital welding equipment.

Figure 2.15 Top end plug weld setup

With the top end plug welded, the argon purge setup was removed. The rod was then loaded with a stainless steel spring and MgO ceramic pellets as shown in Figure 2.16. Again, the design plenum spacing was 203.2 mm (8 in.).

Figure 2.16 Loading of fuel rod with MgO surrogate fuel and stainless steel plenum spring

Figure 2.17 shows the reversal of purging system in which the top portion of the fuel rod was inserted and secured into the purging apparatus. After purging the interior of the rod with argon,

the bottom end plug was then inserted and welded to the Zr-4 cladding. The Phase II peripheral fuel rod was then ready for final pressurization and closure welding.

Figure 2.17 Bottom end plug weld setup

2.3.1.2 Closure Weld

The 0.64 mm [0.025 in] through hole in the top end plug was used to pressurize the rods and was then welded closed. Figure 2.18 shows the closure weld fixture (CWF). A TIG electrode was inserted and secured at a predetermined depth such that when the fuel rod was inserted a small gap existed between the electrode tip and top end plug surface. The assembled fuel rod was inserted until the chamfered portion of the top end plug was seated firmly against the chamfered opening of the hex bushing as shown in Figure 2.19.

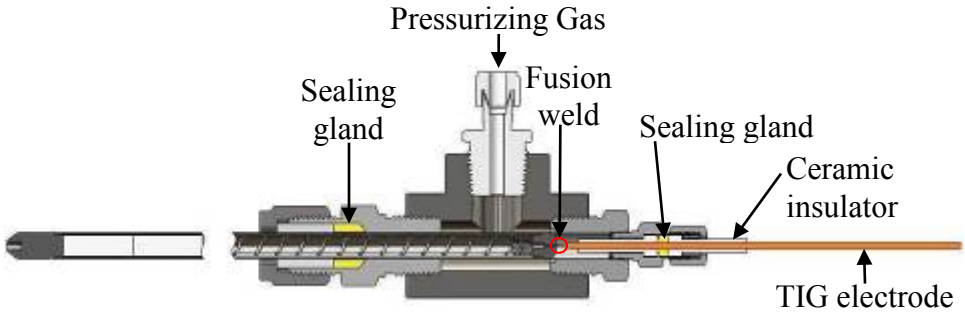

Figure 2.18 Schematic of the closure weld fixture

Figure 2.19 shows a close up of the flow path of the fill gas. The hex bushing had two machined slots on opposite sides to accommodate gas flow. The hole in the top end plug provided the final opening for the pressurizing gas to pass through allowing purging and pressurization.

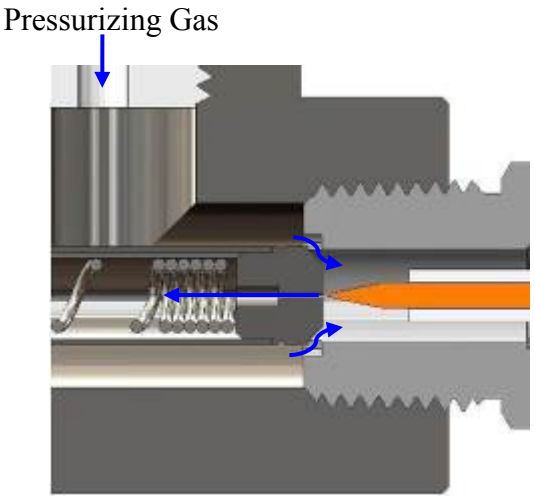

Figure 2.19 Close-up of gas fill process and top end plug weld location

After all electrical connections for the welder were configured, the final closure weld of the top end plug was made under pressure. Figure 2.20 shows a cross-sectional rendering and a photo of an actual welded top end plug. At this point the rod was fully pressurized and sealed.

Figure 2.20 Top end plug closure weld

2.3.2 Argon Fill Gas

Initial planning called for the use of helium to pressurize the Phase II rods. Initial attempts to implement a helium fill system for use with the SFP Phase II pressurized rods were unsuccessful in making the closure weld. Discussions with welding experts at Sandia National Laboratories (SNL) indicated that the high pressure helium gas was likely preventing sufficient ionization between the TIG welding tip and the top plug of the fuel element. For reference the first ionization energy of helium is approximately 1.6 times higher than argon. This ionization was crucial for forming and sustaining an electrical arc between the weld tip and the work piece. SNL was unable to determine from the fuel vendor their method of pressurization and closure. It is possible that the vendor utilizes some other technology such as laser or resistance welding that is not affected by the increased cover gas pressure.

As an alternative, argon was used as a substitute gas. The thermal mass of argon in a pressurized rod is theoretically identical to that of a helium-filled rod. Although helium is almost one order higher with regards to thermal conductivity, the effect on the thermal response of the Phase II pressurized rods, which is on the order of seconds, was negligible compared to the heat up times during testing of hours. Furthermore, a significant fraction of the gas inside spent fuel rods is comprised of the fission product gases Xe and Kr which would lower the effective thermal conductivity of the helium gas mixture.

The SFP Phase II South and North pressurized assemblies were filled to initial charging pressures of 5.2 MPa [750 psi] and 6.2 MPa [900 psi], respectively. These values represent a range of expected peak pressures typical of spent fuel in industry under similar accident conditions.

2.4 Instrumentation

The instrumentation of the SFP Phase II assembly was based on the designs proposed in the Phase II Test Plan (Ref. 19). The instrumentation included hot wire anemometers, oxygen sensors, residual gas analyzer (RGA), strain gauges, and thermocouples (TCs). The following sections give corrections for the as-built instrumentation and also document details not previously discussed.

2.4.1 Center Bundle Thermocouples

Approximately 160 TCs were located within the center bundle. The TCs were attached to the heaters and guide tubes by strapping the tip of the TCs with a small piece Nichrome shim stock to the rod. All TCs to be used in this testing were ungrounded, K-type with a 0.813 mm [0.032 in] Super Omegaclad XL sheath diameter. The majority of the TCs used were Omega Engineering part number TJ192-CAXL-032U-192-SMPW-M.

Thermocouples were installed using US customary units. The data file headers and TC identifiers give positioning in inches, e.g. C_J-9_124 was installed in the center bundle on the middle instrument tube at z = 3.150 m [124 in]. Ignition in the PWR occurred near the top of the assembly. Therefore, most of the bundle TCs were routed out the bottom of the assembly. TCs located at or above z = 3.30 m [130 in] were routed out the top of the assembly.

Figure 2.21 shows the TC layout of the center bundle. This updated schematic represents a 90° counterclockwise rotation compared to the Test Plan. A majority of the TCs were installed on the outside surface of the guide tubes before any of the heater rods were installed. TCs were also installed on some outer row heater rods. Red denotes the location of high density arrays where TCs were located at 15.25 cm [6 in] intervals. Yellow denotes the location of medium density arrays where TCs were located at 30.5 cm [12 in] intervals. Green denotes the location of low density arrays where TCs were located at 61 cm [24 in] intervals. The A-1 location in the center fuel bundle was oriented to the Northwest corner of the test apparatus.

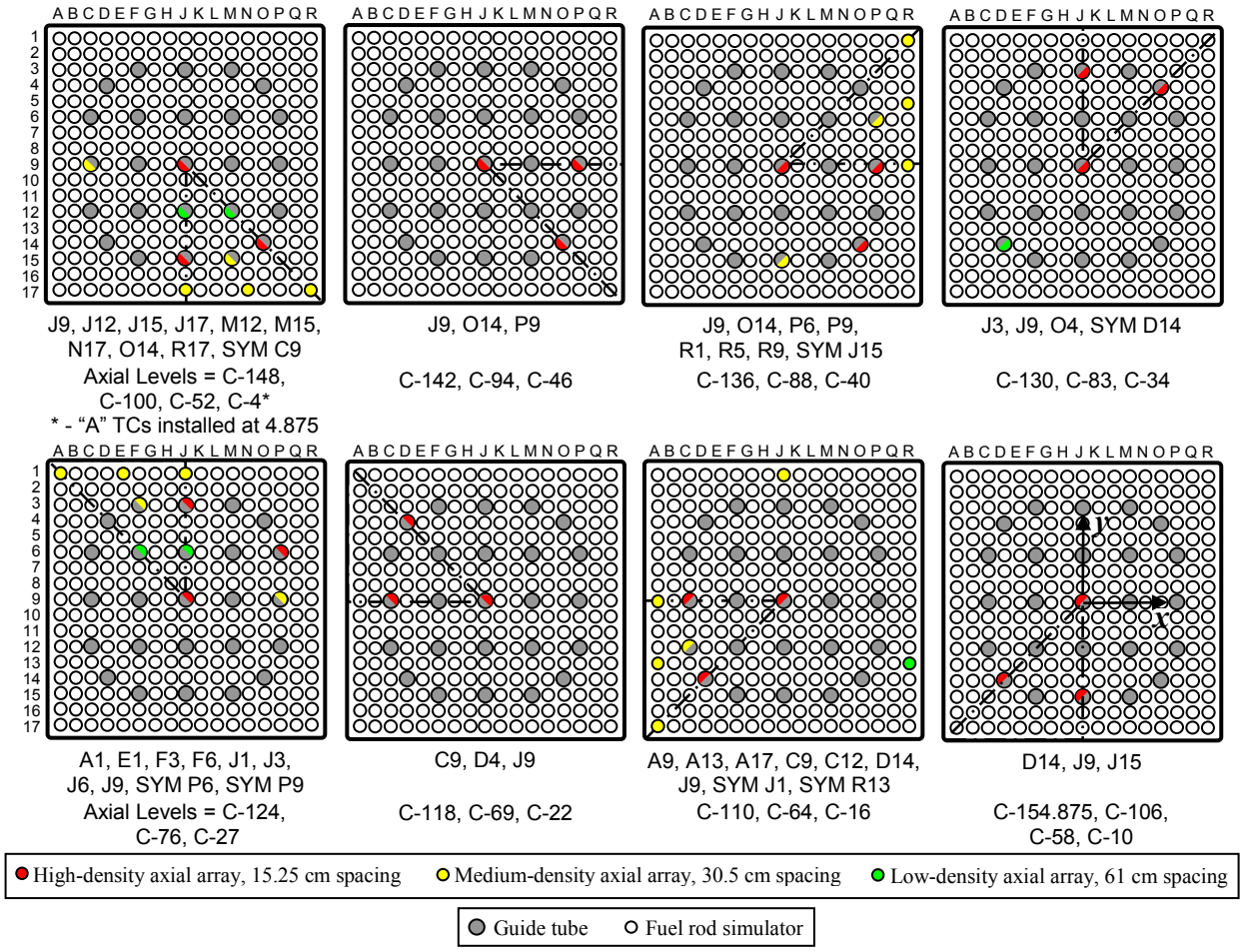

Figure 2.21 Thermocouple layout for the Phase II center, heated fuel bundle

Note: The center bundle was installed with rod A1 oriented nearest the Northwest corner of the center pool cell.

2.4.2 Peripheral Bundle Internal Instrumentation

The as-built installation for the TCs and strain gauges in the peripheral assemblies is the same as documented in the Test Plan but are repeated here for clarity. Similar to the center assembly, the peripheral assemblies were instrumented with TCs at 15.25 cm [6 in] spacing. Unlike the center assembly, which was ideally symmetric about both the local *x*- and *y*-axes, the peripheral assemblies are symmetric only along a single axis. Therefore, the TCs were placed throughout these assemblies to primarily measure the thermal gradient from the center-facing cell wall to the outer rack wall. As in the center bundle, most of the TCs were routed through the bottom of the fuel bundles. However, TCs located at or above z = 3.30 m [130 in] were routed out the tops of the bundles.

Figure 2.22 shows the layout of the thermocouples in the unpressurized, peripheral assemblies. An extra designator was added to distinguish the global orientation of each bundle, e.g. "E" for East. An example TC designator is E_U_J-9_124 for a TC installed in the center of the East, unpressurized bundle at z = 3.150 m [124 in].

Similarly, Figure 2.23 gives the layout of the internal instrumentation in the two pressurized, peripheral bundles. No TCs were attached to the mock fuel pins because welding to the pressurized rods was prohibited. In addition to TCs, twenty-four strain gauges (Vishay Micro-Measurements Model CEA-03-062UQ-350) were attached to the pressurized fuel pins as shown in the left diagram of Figure 2.23 in a 3-wire, quarter-bridge configuration. Twenty-three of the gauges were actively monitoring the strain in the cladding due to the internal pressure of the rods. These strain gauges were attached directly to the cladding in between the debris catcher elements between the z = 0.105 to 0.111 m [4.125 to 4.375 in] levels. The remaining strain gauge was attached to the nearby debris catcher as a control to quantify the apparent strain due to temperature changes experienced by the gauges.

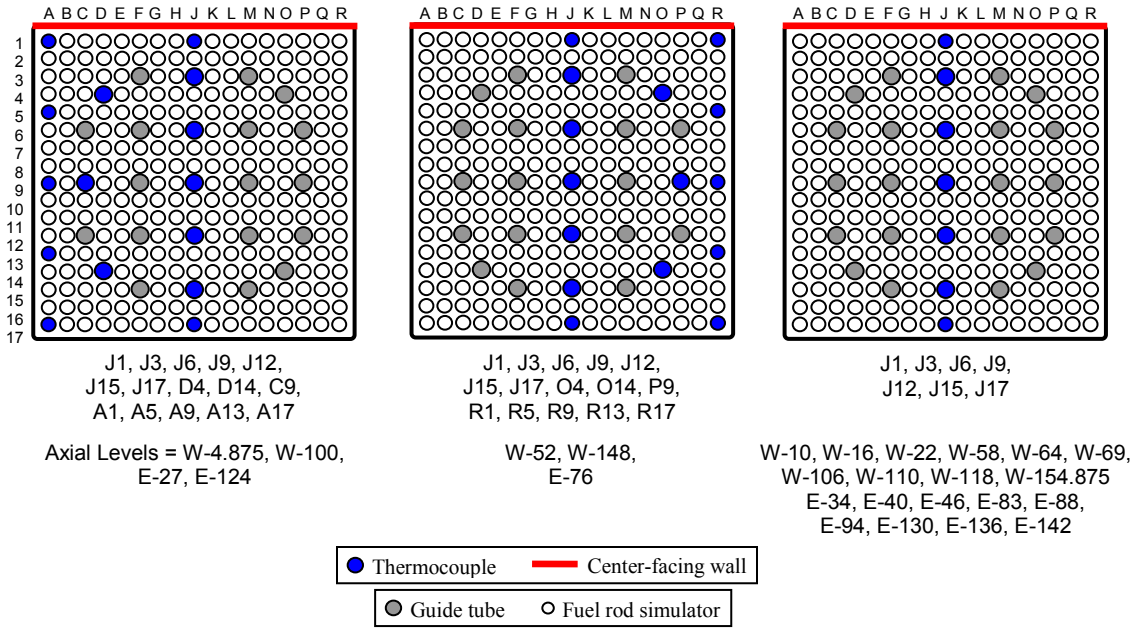

Figure 2.22 Layout of internal instrumentation for the unpressurized, peripheral fuel bundles

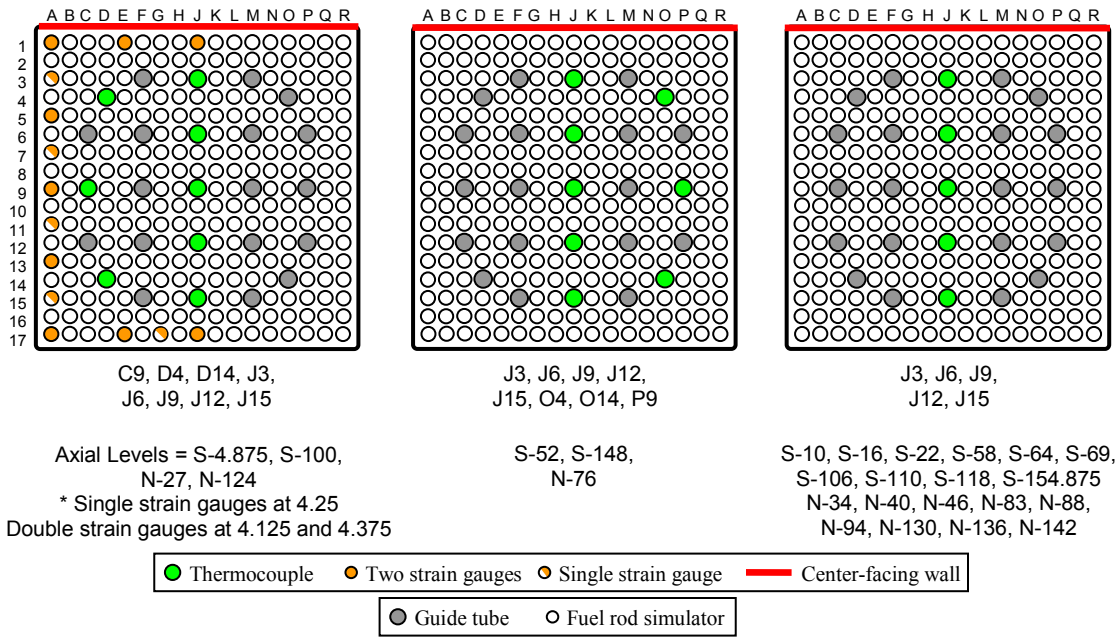

Figure 2.23 Layout of internal instrumentation for the pressurized, peripheral fuel bundles

2.4.3 Inlet Instrumentation

The inlet of the fuel assemblies were instrumented with hot wire anemometers, TCs, and pressure ports. Figure 2.24 shows an isometric view of the lower test stand and two side views of a center and peripheral pipe. The top of each inlet pipe was located at z = -38 mm [1.5 in], where z = 0 mm [0 in] at the bottom of the fuel assemblies by definition.

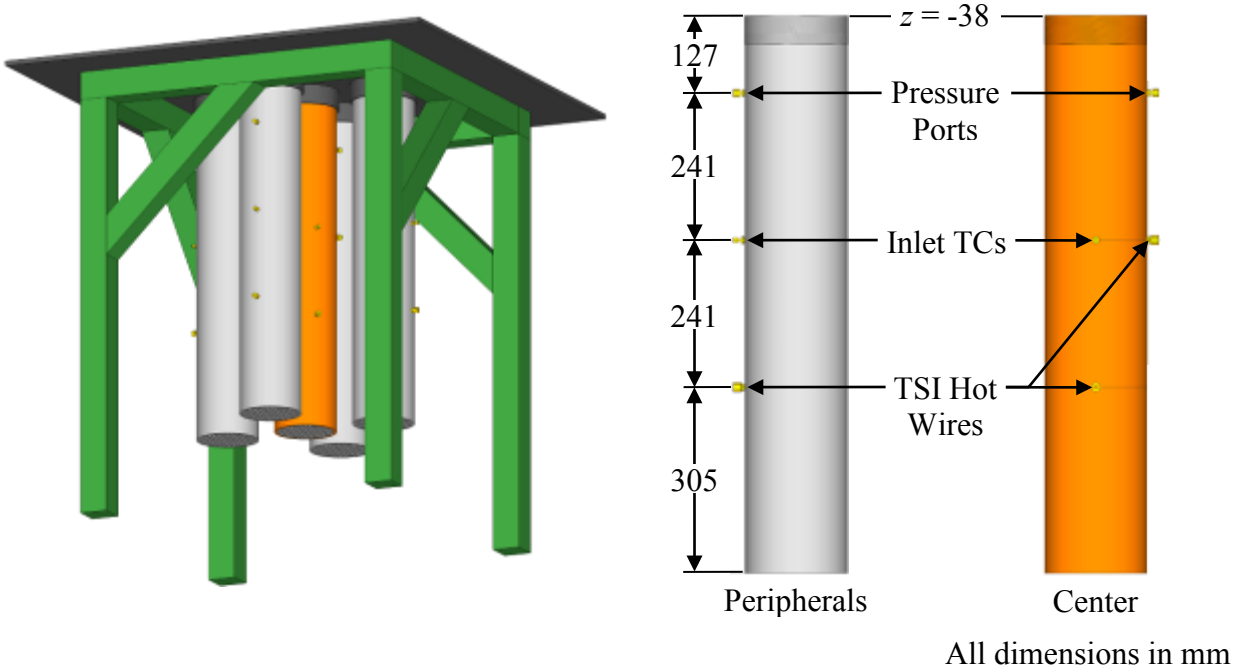

Figure 2.24 Layout of instrumentation in the inlets of the assemblies

A total of six hot wire anemometers were placed in each of the 154 mm [6.065 in] ID pipe that defines the inlet to the five test assemblies. One was located in the inlet pipe of each of the peripheral assemblies and two were located in the inlet pipe of the center assembly. Hot wire anemometers were chosen to measure the inlet flow rate because this type of instrument is sensitive and robust while introducing almost no unrecoverable pressure loss. A typical placement of the hot wire is shown in Figure 2.25. TSI Model 8455 hot wire anemometers were used for these tests. A honeycomb element was added to the inlet entrance to reduce the influence of any air flow disturbances within the experimental enclosure on the hot wire measurements. Also, the flow encountered a slight contraction of 127 mm [5 in] as it passed from the inlet pipe through the base plate. This diameter of 127 mm [5 in] was chosen based on the designs of commercial pool racks.

Figure 2.25 also shows the placement of the four pressure ports on the outside perimeter of the pool rack to the peripheral fuel assemblies. These pressure ports were centered in the middle of the fuel assemblies at z = 11 mm [0.43 in]. The center assembly was not accessible and therefore did not have a pressure port on the pool wall. All pressure drop measurements for the center fuel assembly were collected using the pressure port located in the inlet pipe as shown in Figure 2.24.

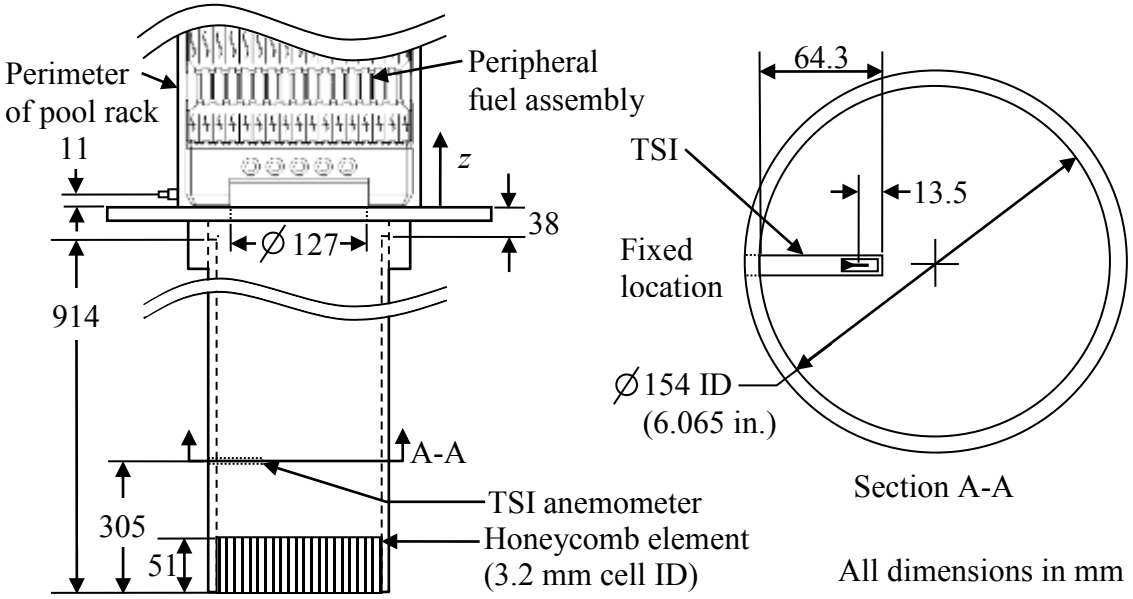

Figure 2.25 Details of the positioning of the hot wire anemometers and pool rack pressure ports

2.4.4 External Instrumentation

A number of thermocouples (TCs) were attached to the outside of the pool rack. Figure 2.26 shows the placement of these TCs on each face of the pool rack. The installation was staggered around the pool rack in 0.305 m [12 in] increments. The TCs were placed primarily in the center of the face of the peripheral cell, which was recorded as Pool_Face_Axial-Height_0. Arrays of TCs at the same axial level were placed to record the thermal gradient from the center of the peripheral cell to the corner of the pool rack. These TCs were recorded as Pool_Face_Axial-Height_Transverse-Location, where the three additional transverse locations of interest were the peripheral-corner cell interface 111.8 mm [4.4 in], the center of the corner cell 226.1 mm [8.9 in], and the corner of the pool rack 340.4 mm [13.4 in].

Thermocouples were also attached to the outside of the stainless steel thermal radiation barrier as shown in Figure 2.27. Similar to the pool rack, these TCs were installed in staggered fashion in 0.305 m [12 in] increments. All these TCs were placed either centered on a peripheral pool cell face or in the corner of the assembly. Quartz light pipes (3 mm [0.12 in] diameter) fully penetrated through the radiation barrier and insulation to the pool rack on both the North and East faces at 0.305 m [12 in] increments as a means to optically observe the location of the ignition front.

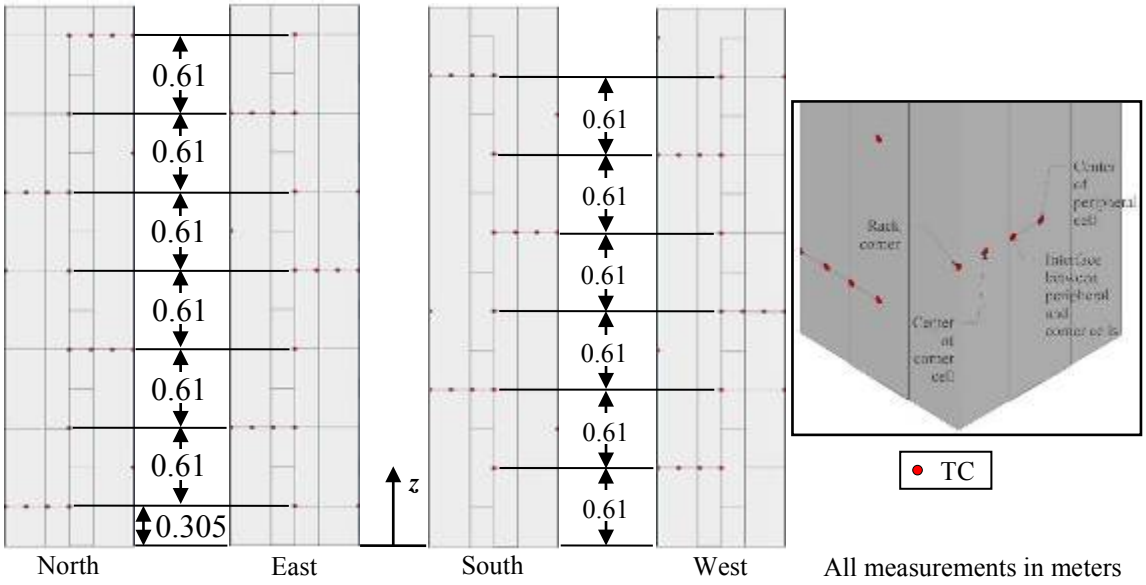

Figure 2.26 TC layout on the external faces of the pool rack

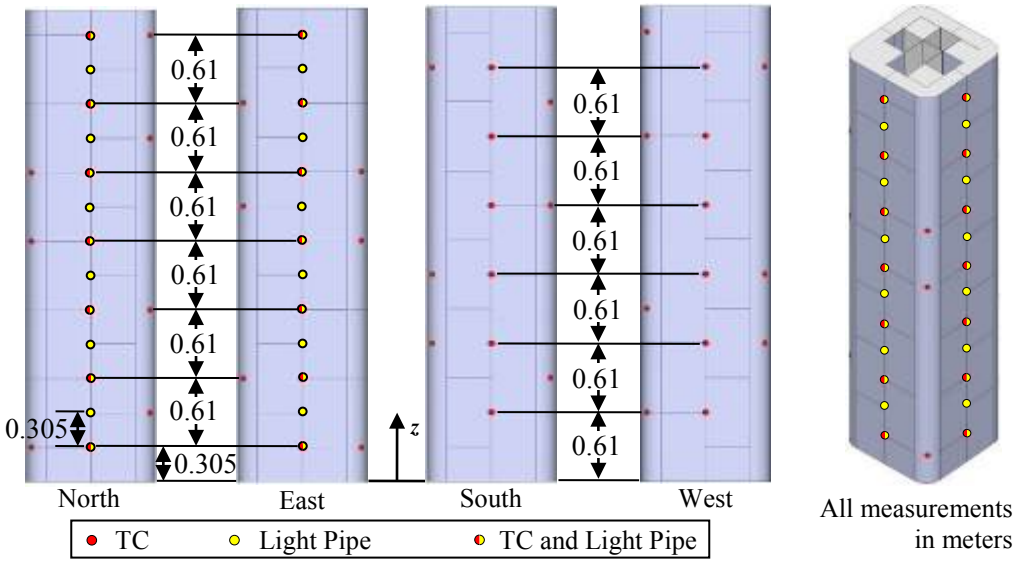

Figure 2.27 TC and light pipe layout on the exterior of the thermal radiation barrier

2.4.5 Pressure Loss Measurements

A series of isothermal, forced flow calibrations were conducted to characterize the hydraulics of the Phase II fuel assemblies. These results of these calibrations include the flow loss coefficients for the center and peripheral assemblies. As discussed in the previous section, all pressure measurements in the center assembly were collected via a pressure port installed on the inlet pipe. The pressure drop measurements in the peripheral assemblies were taken using pressure ports installed in the inlet pipe and in the pool rack wall at z = 0.011 m [0.43 in]. Cross-flow paths between the center and peripheral assemblies at the bottom of the pool rack were discovered as part of these analyses and are characterized for implementation in modeling efforts.

Figure 2.28 shows a cross section of the as-built test apparatus with the fuel bundles omitted. The cross-flow paths are interpreted for these analyses as four holes at the bottom of the pool rack. These flow paths were a result of an imperfect seal at the interface of the pool rack and the test stand.

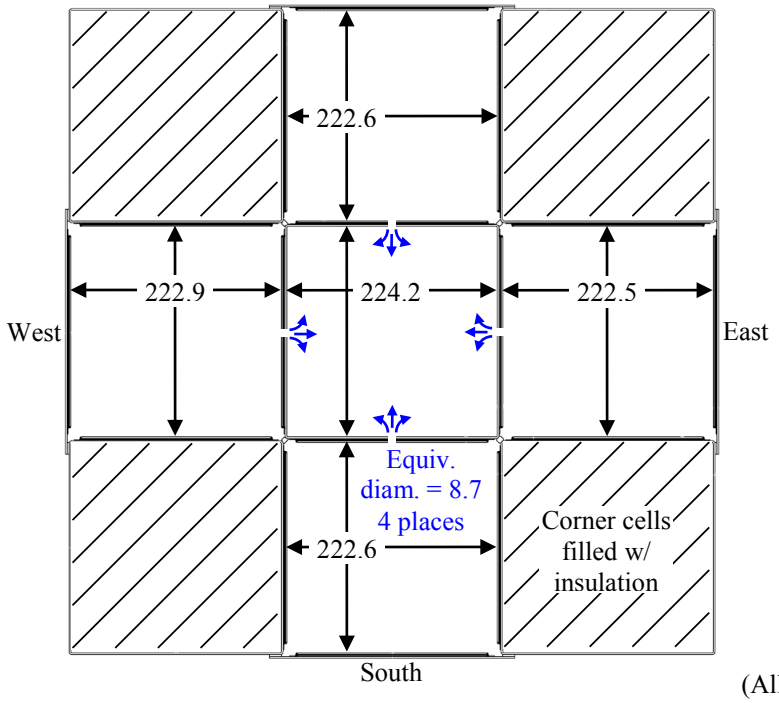

Figure 2.28 Definition of the equivalent cross-flow paths at the bottom of the pool rack

The hydraulics for the center and an average peripheral assembly are given in Table 2.3. The assumed hydraulics for the cross-flow paths are also defined. The cross-flow paths may alternatively be conceptualized as a small slit with dimensions of 1.2 × 51 mm [0.046 × 2 in]. These flow paths were not part of the original design but were instead an artifact of the apparatus construction.

Table 2.3 Hydraulic dimensions for the center assembly, average peripheral assembly, and the cross-flow path

Description	Center	Peripheral	Cross-Flow Path
Inner Dimension	224.2 mm [8.83 in]	222.65 mm [8.77 in]	8.7 mm [0.34 in]
Flow Area	0.0287 m^2 [44.49 in^2]	0.0283 m^2 [43.87 in^2]	5.89E-5 m^2 [0.0913 in^2]
Hydraulic diameter, D_H	11.7 mm [0.46 in]	11.6 mm [0.46 in]	8.7 mm [0.34 in]

Two pressure drops were recorded in the peripheral assemblies. The first pressure drop was between the bottom of the pool rack at z = 0.011 m [0.43 in] and atmosphere. The second pressure drop was between a pressure port located z = -0.165 m [6.5 in] from the bottom of the fuel assemblies in the 0.154 m [6.065 in] diameter inlet pipe and atmosphere. Between this lower pressure port and the one installed on the pool rack, the flow experiences a slight contraction followed immediately by an expansion as it passes through a 0.127 m [5 in] hole in the test stand plate with a thickness of 0.013 m [0.5 in].

Figure 2.29 shows the pressure drop in all four peripheral assemblies as a function of average assembly air velocity for the pressure port in the pool rack and inlet pipe. Because of the additional form losses from passing through the hole in the test stand plate, the pressure drop is slightly higher in the inlet pipe than just inside the assembly. These results account for the cross-flow leaving the peripheral assemblies into the center assembly.

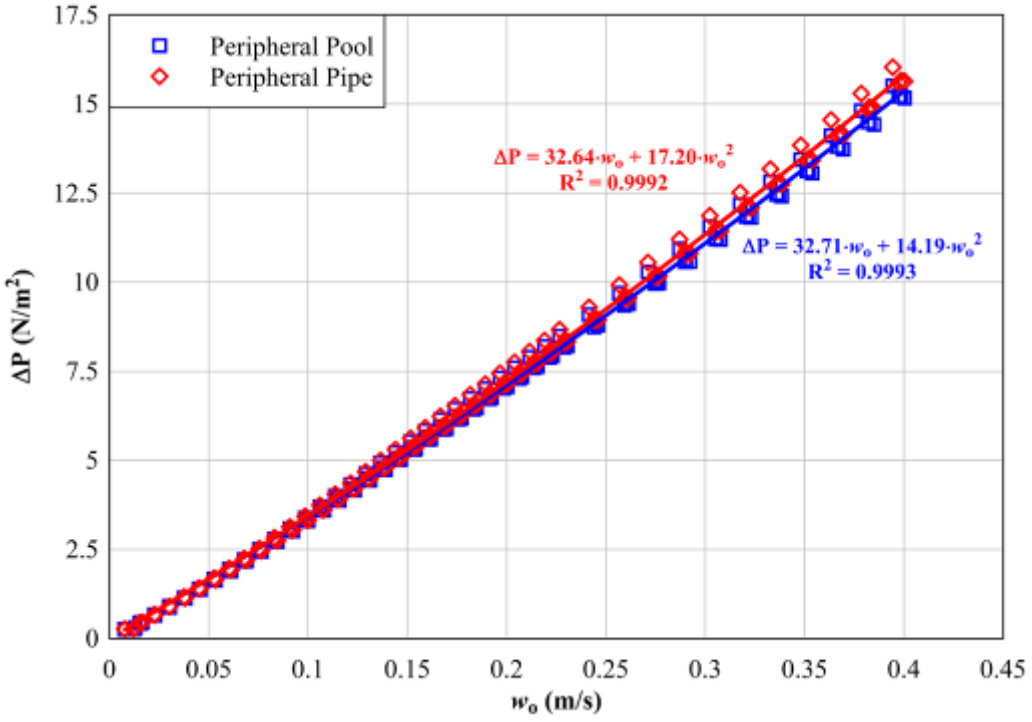

Figure 2.29 Overall pressure drop as a function of average air velocity in the assembly for all peripheral assemblies

Figure 2.30 shows the pressure drop for the center assembly as a function of air velocity. The pressure measurement for the center assembly was only possible for the inlet pipe because the pool rack wall of the center cell was not accessible. Again, the effects of the cross-flow were incorporated into these results.

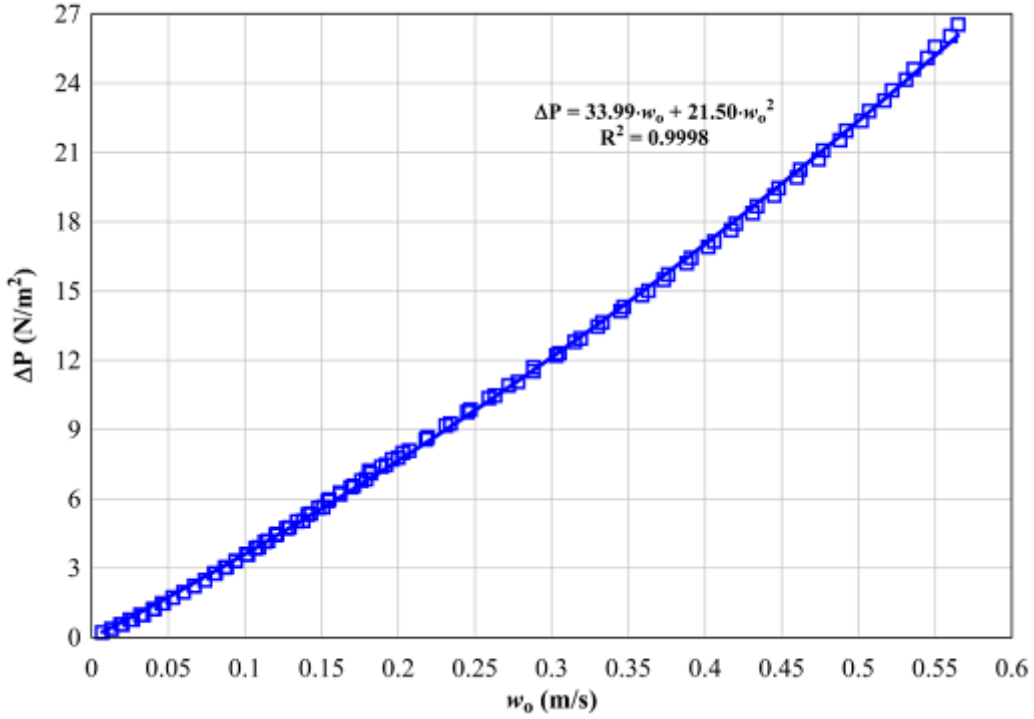

Figure 2.30 Overall pressure drop as a function of average air velocity in the assembly for the center assembly

The pressure drop across the center and peripheral assemblies is shown as a function of cross-flow velocity in Figure 2.31. This velocity was defined as the air velocity across a single cross-flow path. All four cross-flow paths were assumed to be equal for these analyses. The pressure drop across the center and peripheral pool cells was assumed to be completely from contraction and expansion.

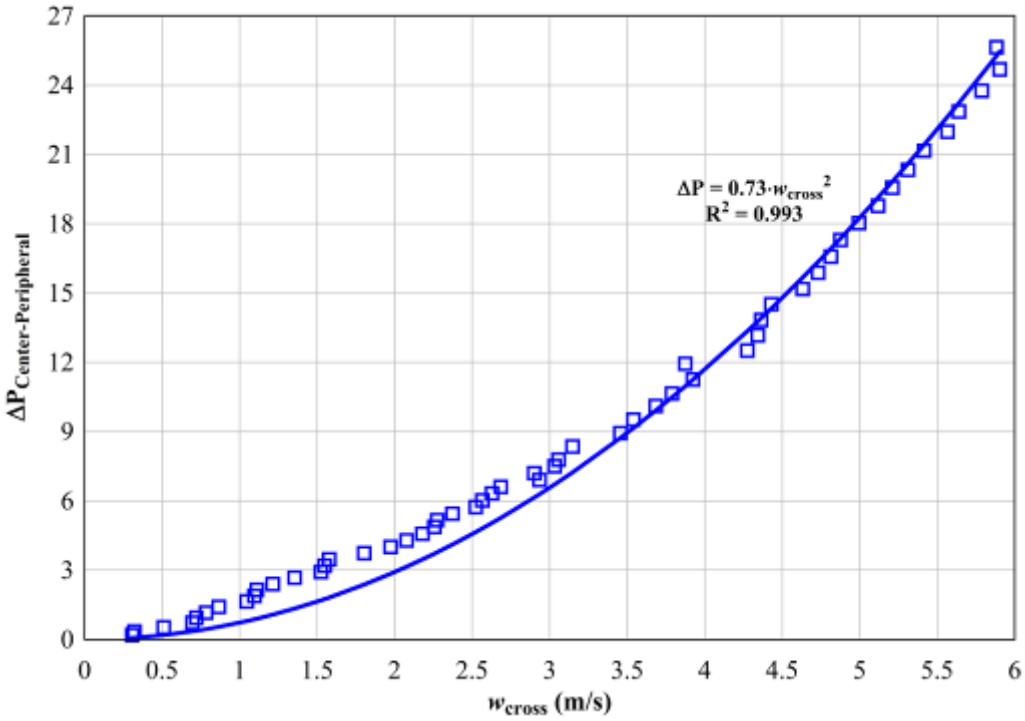

Figure 2.31 Pressure drop between the center and peripheral assemblies as a function of average cross-flow velocity

Table 2.4 summarizes the hydraulic loss coefficients for the Phase II apparatus. The friction and form losses appear slightly higher in the center assembly than in the peripheral assemblies. To compare with previous results, the appropriate difference in Σk from the peripheral measurements, pipe to pool, should be subtracted from the corresponding center Σk. Therefore, the form losses in the center assembly for the overall fuel bundle pressure drop are 68 and 31.7 for upper flow ranges of 300 and 600 slpm, respectively.

Table 2.4 Hydraulic loss coefficients of the SFP Phase II apparatus

	Center			Peripheral				Cross-Flow
	Pipe			Pool		Pipe		Center-Peripheral
Upper Flow Rate (slpm)	300	600	738	300	508	300	508	16
Upper velocity (m/s)	0.238	0.476	0.560	0.238	0.400	0.238	0.400	5.904
S_{LAM}	119	129	126	113	118	113	118	--
Σk	73.0	37.9	43.6	47.5	29.1	52.5	35.3	1.5

2.4.6 Exhaust Gas Analysis

2.4.6.1 Oxygen Sensors

Oxygen concentrations were continuously monitored (Advanced Micro Instruments, Model 65, Part 6ANA0056) at six locations at the top of the assemblies as shown in Figure 2.32. All sample lines consisted of stainless steel tubing and were placed below the top bus plates (or top nozzles in the peripherals), which was located 0.173 m [6.82 in] below the top of the pool rack. The center assembly was sampled at two locations, one near the center of the bundle (avoiding power leads) and the other from the annulus region between the power bus plate and

the storage cell wall. Each of the four peripheral assembles were sampled from the center of the bundle just below the top nozzle. In addition to the oxygen sensor, the exhaust gas in the center bundle was also monitored by a residual gas analyzer, which is detailed in the next section.

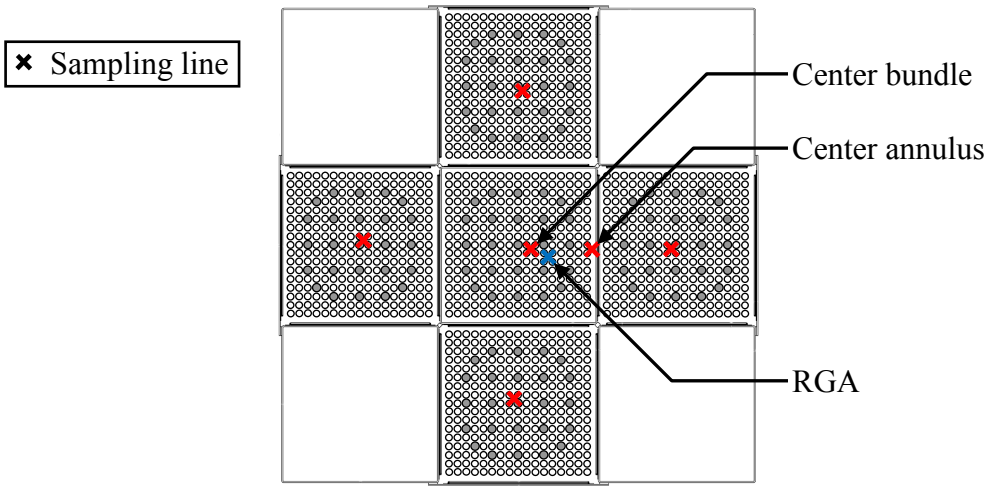

Figure 2.32 Schematic showing planned locations of gas sampling lines

2.4.6.2 Residual Gas Analyzer

Under the appropriate conditions, nitrogen will react with zirconium to form zirconium nitride (ZrN). Steinbrück (2009) has shown that the zirconium-nitrogen reaction occurs readily when oxygen is absent in the gas phase and simultaneously oxygen is present in the zirconium metal phase. In particular it was determined that oxygen-stabilized α-Zr(O) was the form of zirconium most reactive to nitrogen. After ignition in the present experiment, the conditions required for rapid nitriding were ideally present above the burn front as the burn front moved downward.

Nitrogen reactions within the burning center assembly were monitored in order to determine the degree and timing of zirconium nitride formation. Tracking nitrogen reactions required simultaneous measurement of nitrogen and ambient noble gas concentrations. The noble gases behaved as inert tracers. If nitrogen was consumed to form zirconium nitride, the ratio of nitrogen to the noble gases decreased. When zirconium nitride was oxidized, nitrogen was released and the ratio of nitrogen to the noble gases increased. The primary noble gas considered was argon, but helium was also monitored as a backup. The ballooning peripheral rods were pressurized with ultra-high purity argon so when the rods ruptured the background concentration of argon in the CYBL vessel was altered. As a mitigation, fresh air was introduced at the bottom of the CYBL vessel and the top floor of the CYBL building was actively ventilated. The total inventory of argon in the 528 pressurized rods was about half the amount of argon initially present in the air contained inside the CYBL vessel.

The sampling and analysis of the gas stream exiting the center assembly was performed with an in-house built sample conditioning system coupled to a mass spectrometer (Pfieffer Model GSD 300T). With the Pfeiffer GSD 300T RGA, gases were ionized by a tungsten filament. These ions were filtered by the quadrapole mass spectrometer and then detected and amplified by the secondary electron multiplier (SEM). The SEM produced an electric current for each unique ion species, which was converted into gas concentrations and gas concentration ratios.

The gases of interest and the ion masses monitored were helium (4.0), water (18.0), nitrogen (28.0 and 14.0), oxygen (32.0 and 16.0), argon (40.0) and carbon dioxide (44.0). The analysis of these eight ions was recorded every 10 seconds. At two hour intervals, ambient air was sampled for a few minutes for calibration purposes.

The sample was collected through a stainless steel tube near the center of the center assembly just below the bundle bus plate as depicted in Figure 2.32. Again, the bus plate was located 0.173 m [6.82 in] below the top of the storage cell. The sample conditioning system shown in Figure 2.33 was designed to continuously pull the gas sample at ambient pressure (84.1 kPa [12.2 psia]) from the top section of the center test assembly with a small vacuum pump (GAST model DOA-107-AA). The sample was passed through one of two parallel in-line filters (Swagelok model SS-4TF-05) housing a 0.5 micron filter cup (Swagelok model SS-4F-K4-05) and then into a capillary line for analysis by mass spectrometry. The pressure drop across the filters was monitored with a 13.8 kPa [2 psi] differential pressure gauge. The gas pressure at the capillary tip was kept constant at 76.19 kPa [11.05 psia] with an electronic backpressure controller (Proportion Air model DQPV1TFEE020BXL). As long as the pressure drop across the filter was less than 6.8 kPa [1.0 psi] the back pressure controller was able to maintain a constant sample pressure. Block valves permitted isolation of a filter for replacement without compromising the sample gas analysis. A 3-way solenoid valve (ASCO model EF8320G202), which was controlled through the RGA software, was used to periodically switch from the gas sample stream to an ambient air stream . The ambient air stream was also regulated to 76.19 kPa [11.05 psia] to serve as a calibration gas. It was drawn from inside the CYBL building, but outside the CYBL vessel.

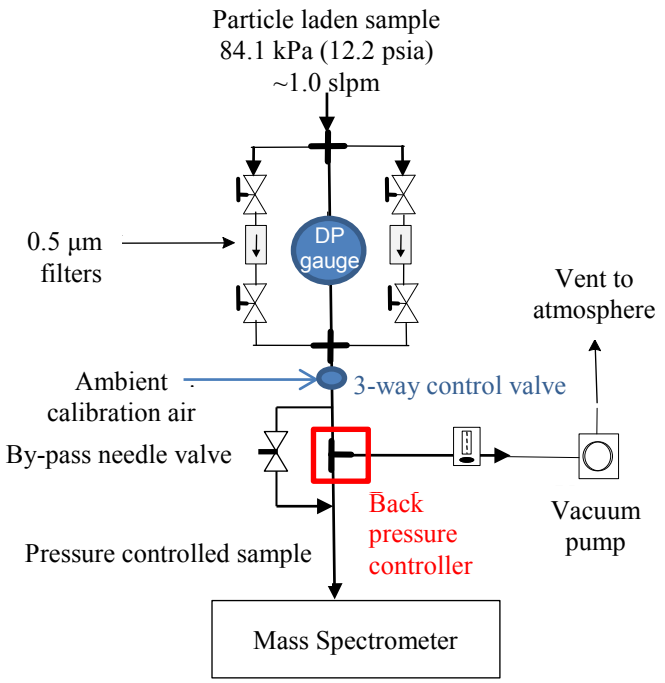

Figure 2.33 Schematic of gas sample conditioning system

When significant oxygen was present in the sample before ignition and after all oxidation reactions were complete, the detector current was converted to a mole or volume fraction based on the analysis of ambient air. When oxygen was absent after ignition the detector output was converted to mole or volume fraction based on the analysis of the five calibration gases

described in Table 2.5. The calibration gases were designed to span nitrogen to argon ratios of 27 to 140 which, when divided by the nitrogen to argon ratio found in ambient air correspond to normalized N_2/Ar of 0.33 to 1.67. Normalized N_2/Ar less than unity signifies nitrogen removal; normalized N_2/Ar greater than unity signifies nitrogen release. During the Phase I ignition test, the normalized nitrogen to argon ratio was found to range from 0.7 to 0.4.

Table 2.5 List of RGA calibration gases

Calibration Gas	Ar (%)	Balance N_2 (%)	N_2/Ar	Normalized N_2/Ar
1	3.54	96.46	27	0.33
2	1.76	98.24	55	0.67
3	1.18	98.82	84	1.00
4	0.89	99.11	112	1.33
5	0.71	99.29	140	1.67

3 PRE-IGNITION TEST RESULTS

A summary of Phase II pre-ignition testing is presented in Table 3.1. Only tests that extended to 12 hours are shown in the table. Three additional pre-ignition tests were conducted at powers of 10.0, 12.0, and 15.0 kW but did not exceed 6 hours duration. This table gives the average temperatures and flow rates at 3, 6, 9, and 12 hours for the center and peripheral bundles at z = 3.150 m [124 in]. The minimum and maximum temperatures of the center and peripheral bundles at each time are also shown. Figure 3.1 shows the maximum temperature in the center and peripheral assemblies at the 3.150 m [124 in] level and a time of 12 hours as a function of applied power. As expected, the peak temperature monotonically increased in all assemblies with higher applied power. Figure 3.2 shows the induced flow at 12 hours in the center and peripheral assemblies as a function of applied power. The value shown for the peripherals in this plot and in Table 3.1 represent an average across all the peripheral assemblies. The flow in the center assembly increased with power at low powers, peaked at 4.0 kW then decreased at higher powers. The flow in the peripheral assemblies increased with power until 8.0 kW, which may be the peak flow. The flows in the center and peripheral assemblies appear to converge at higher powers.

The 4.0 kW test was repeated to examine repeatability as shown in the third and fourth columns of test entries in Table 3.1, as well as in Figure 3.1 and Figure 3.2. The maximum and average temperatures in the center bundle were within 3 K [5.4°F] at all positions and times, which is slightly greater than the experimental uncertainty of ±2.2 K [±3.96°F]. The minimum temperature in the center bundle was as much as 8 K [14.4°F] higher in the second test. In addition, the temperatures in the peripheral assemblies were as much as 14 K [25.2°F] higher in the repeat test. These thermal differences are likely due to the accumulation of oxide on both the Zircaloy-2 cladding in the center bundle and on the center stainless steel pool cell, which continued to accrue between the initial 4.0 kW test on 5/9/12 and the second test on 5/21/12. The thermal record in the peripheral fuel bundles did not show temperatures high enough to indicate significant oxide layer growth during the entirety of pre-ignition testing. However, increases in the oxide layers on the center bundle and center pool cell surfaces would effectively increase the emissivity of the heated surfaces and therefore increase the radiative heat transfer between the center and peripheral fuel bundles. With the exception of the peripheral measurements at 3 hours, the air flow rates were within 10 slpm for the two measurements, which is better than the experimental uncertainty of ±12 slpm. The measurements in the peripherals at 3 hours are considered outliers because the hot wires were effectively unresponsive below flow rates of approximately 50 slpm.

Table 3.1 Summary of pre-ignition testing results for Phase II at z = 3.150 m (124 in.)

		True RMS Power (kW)	1.0	2.0	4.0	4.0	6.0	8.0
		Test Date	5/14/2012	5/7/2012	5/9/2012	5/21/2012	5/4/2012	5/18/2012
3 h	Center	Flow Rate (slpm)	109	162	193	185	191	193
	Peripheral	Flow Rate (slpm)	0	25	37	2	62	73
	Center	Max. Temp. (K)	361	414	515	515	618	684
		Avg. Temp. (K)	350	392	474	475	556	620
		Min. Temp. (K)	335	364	429	434	490	556
	Peripheral	Max. Temp. (K)	306	311	325	326	350	358
		Avg. Temp. (K)	300	297	298	300	312	312
		Min. Temp. (K)	298	294	291	294	301	298
	Pool Cell	Avg. Temp. (K)	299	295	294	296	305	302
	Rad. Barrier	Avg. Temp. (K)	298	293	294	299	300	294
	Ambient	Avg. Temp. (K)	297	292	294	299	300	294
6 h	Center	Flow Rate (slpm)	140	182	198	191	185	185
	Peripheral	Flow Rate (slpm)	28	54	79	71	102	117
	Center	Max. Temp. (K)	404	487	621	618	741	812
		Avg. Temp. (K)	382	450	567	567	672	745
		Min. Temp. (K)	359	410	507	516	600	674
	Peripheral	Max. Temp. (K)	317	334	362	371	406	462
		Avg. Temp. (K)	304	305	314	318	340	356
		Min. Temp. (K)	299	296	296	299	310	311
	Pool Cell	Avg. Temp. (K)	301	299	303	305	321	322
	Rad. Barrier	Avg. Temp. (K)	298	294	296	300	302	297
	Ambient	Avg. Temp. (K)	298	294	296	300	301	296
9 h	Center	Flow Rate (slpm)	154	187	197	191	191	180
	Peripheral	Flow Rate (slpm)	49	70	103	97	132	141
	Center	Max. Temp. (K)	431	526	668	665	784	859
		Avg. Temp. (K)	404	485	614	614	720	794
		Min. Temp. (K)	377	440	553	560	652	727
	Peripheral	Max. Temp. (K)	328	353	398	411	468	546
		Avg. Temp. (K)	309	316	334	343	376	416
		Min. Temp. (K)	302	302	309	313	333	345
	Pool Cell	Avg. Temp. (K)	304	306	317	321	344	359
	Rad. Barrier	Avg. Temp. (K)	299	295	298	301	302	300
	Ambient	Avg. Temp. (K)	298	295	298	300	300	299
12 h	Center	Flow Rate (slpm)	159	187	194	191	189	175
	Peripheral	Flow Rate (slpm)	56	83	118	115	148	150
	Center	Max. Temp. (K)	449	547	690	687	802	883
		Avg. Temp. (K)	419	504	637	637	742	822
		Min. Temp. (K)	390	456	579	583	676	758
	Peripheral	Max. Temp. (K)	336	368	427	440	503	595
		Avg. Temp. (K)	316	328	355	369	410	472
		Min. Temp. (K)	306	310	326	332	362	395
	Pool Cell	Avg. Temp. (K)	309	314	332	340	371	403
	Rad. Barrier	Avg. Temp. (K)	299	297	301	303	304	305
	Ambient	Avg. Temp. (K)	298	296	299	301	301	300

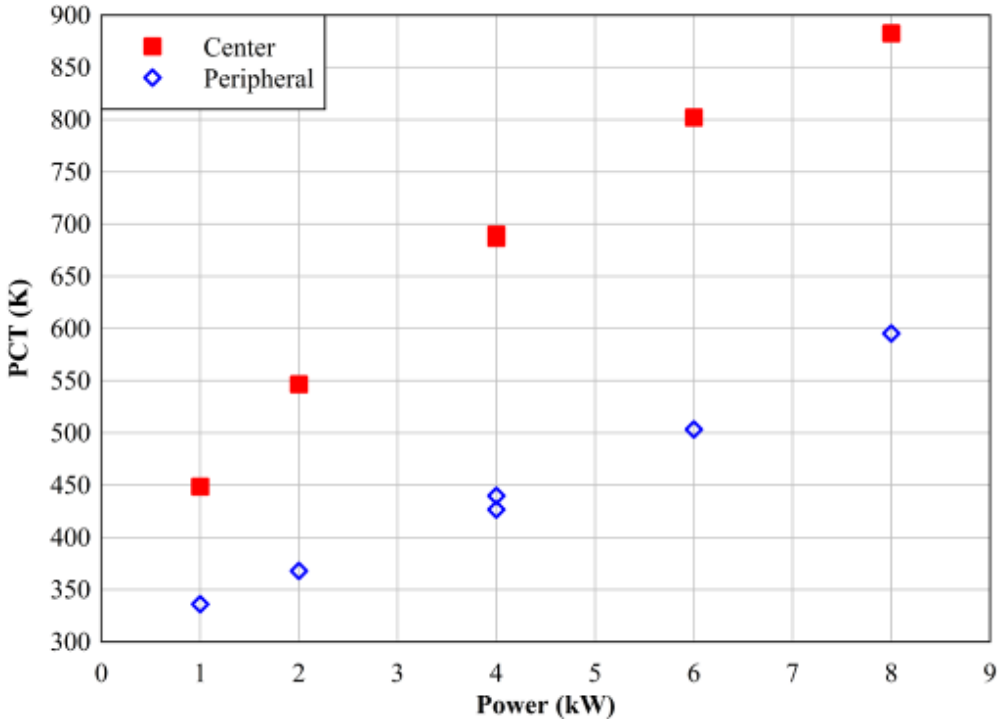

Figure 3.1 **Peak cladding temperatures in the center and peripheral bundles during Phase II pre-ignition testing at *z* = 3.150 m [124 in] and *t* = 12 h**

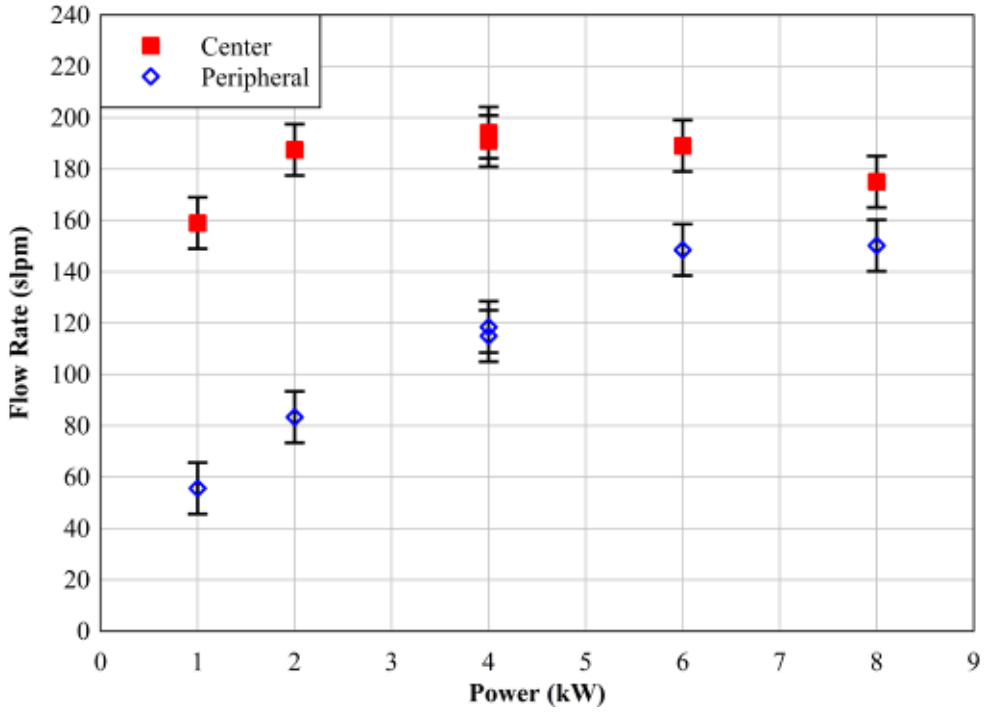

Figure 3.2 **Flow rates in the center and peripheral bundles during Phase II pre-ignition testing at *t* = 12 h**

The peak cladding temperature (PCT) and induced flow rate are respectively shown as a function of time in Figure 3.3 and Figure 3.4 for the center and peripheral assemblies operated at 1.0 kW simulated decay power. After 24 hours the PCT and flow in the center assembly appeared to reach steady state. After 24 hours the PCT and flow in the peripheral assemblies was still rising slowly. The flow in the four peripheral assemblies was measured independently and tracked in a nearly identical fashion.

Figure 3.5 and Figure 3.6 show respectively the PCT and induced flow as a function of time in the center and peripheral assemblies when powered at 4.0 kW. After 24 hours, the PCT in both the center and peripheral assemblies was still rising slowly while the flow in both had reached steady state. The 4.0 kW case was tested twice, once for 12 hours and again for 24 hours. For the 12-hour test conducted 12 days earlier than the 24-hour test, the peak cladding temperature in the center assembly agreed closely with the 24-hour test and ended only slightly higher. However, the peak cladding temperature in the peripheral assembly was noticeably lower at all times for the 12-hour test. This is consistent with increased radiative coupling between the center assembly and the inner pool rack walls as a result of increased emissivity produced by repeated heating during testing. The induced flow in both the center and peripheral assemblies for all times was greater during the 12-hour test. For clarity in the graph, the induced flow for the peripheral assemblies in Figure 3.6 is shown as the average of the four peripheral assemblies.

The PCT and induced flow for 8.0 kW simulated decay power are shown in Figure 3.7 and Figure 3.8, respectively. After 12 hours the PCT in both the center and peripheral assemblies was still increasing. At the same time, the induced flow was dropping in the center assembly and rising in the peripheral assemblies in convergent fashion. The four peripheral flow measurements were within the experimental error.

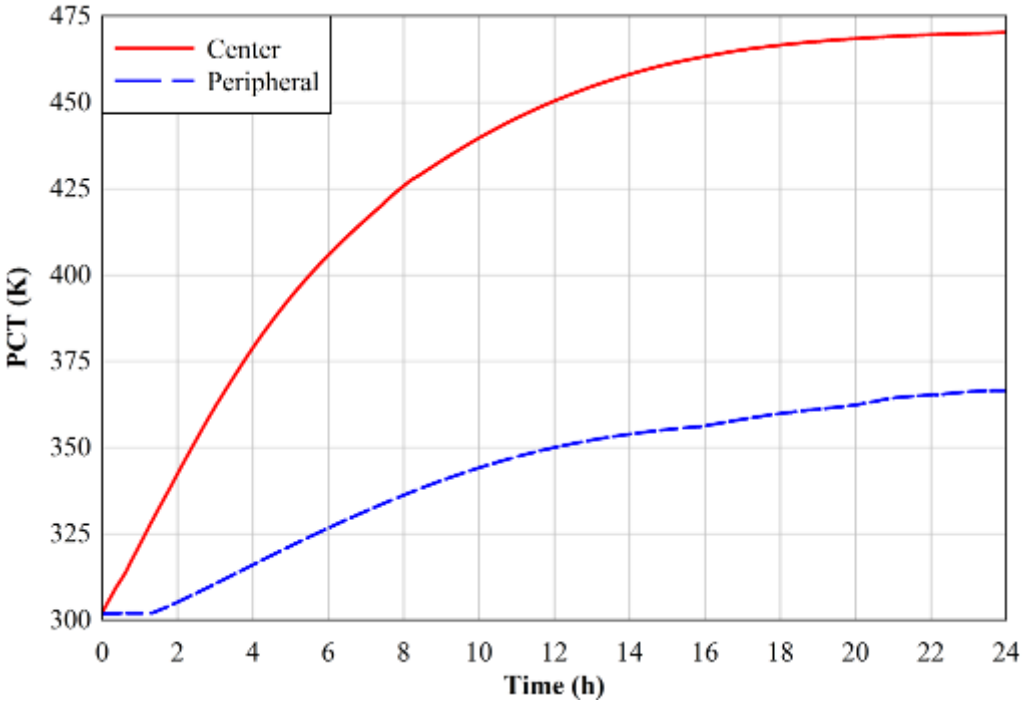

Figure 3.3 Peak cladding temperatures as a function of time at 1.0 kW simulated decay power for the center and peripheral bundles

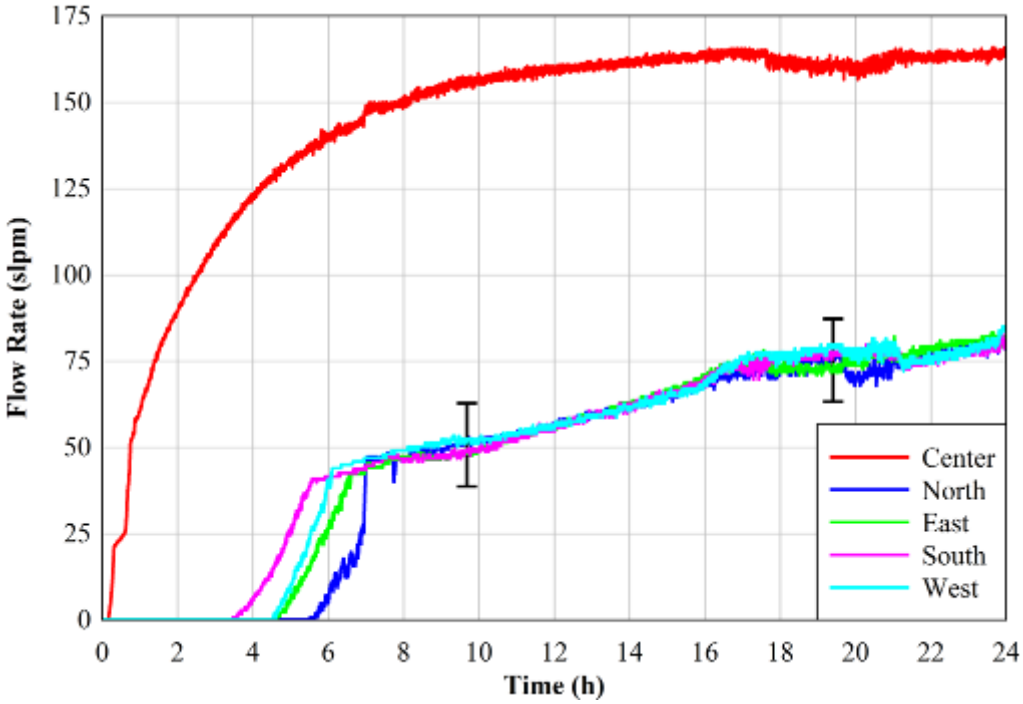

Figure 3.4 Induced flow rates as a function of time at 1.0 kW simulated decay power for the center and peripheral bundles

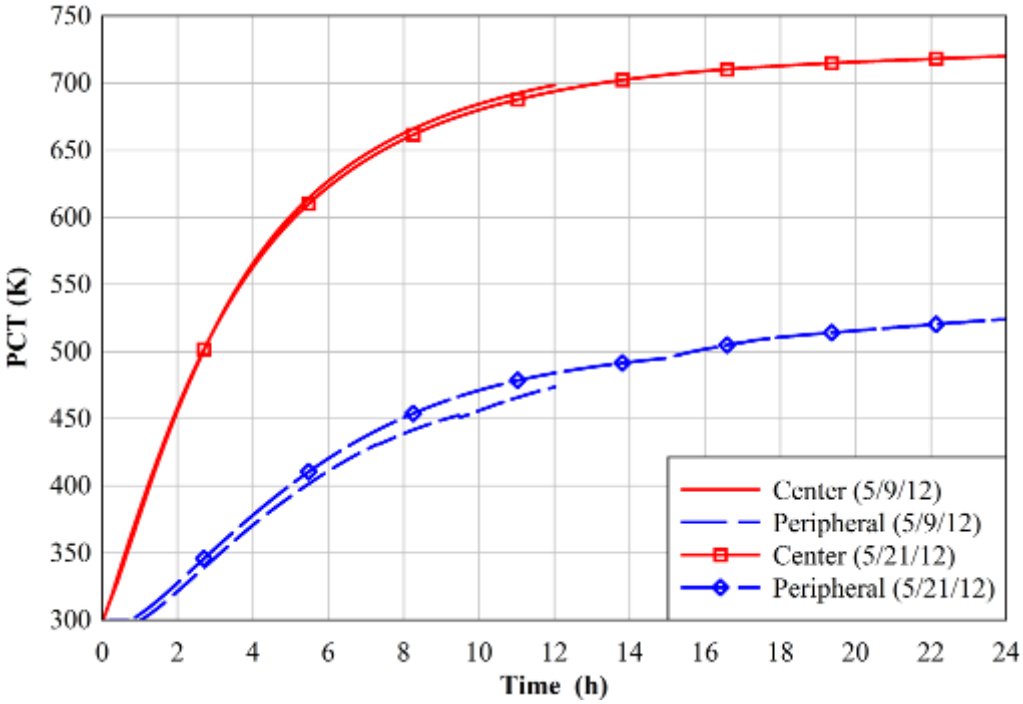

Figure 3.5 **Peak cladding temperatures as a function of time at 4.0 kW simulated decay power for the center and peripheral bundles**

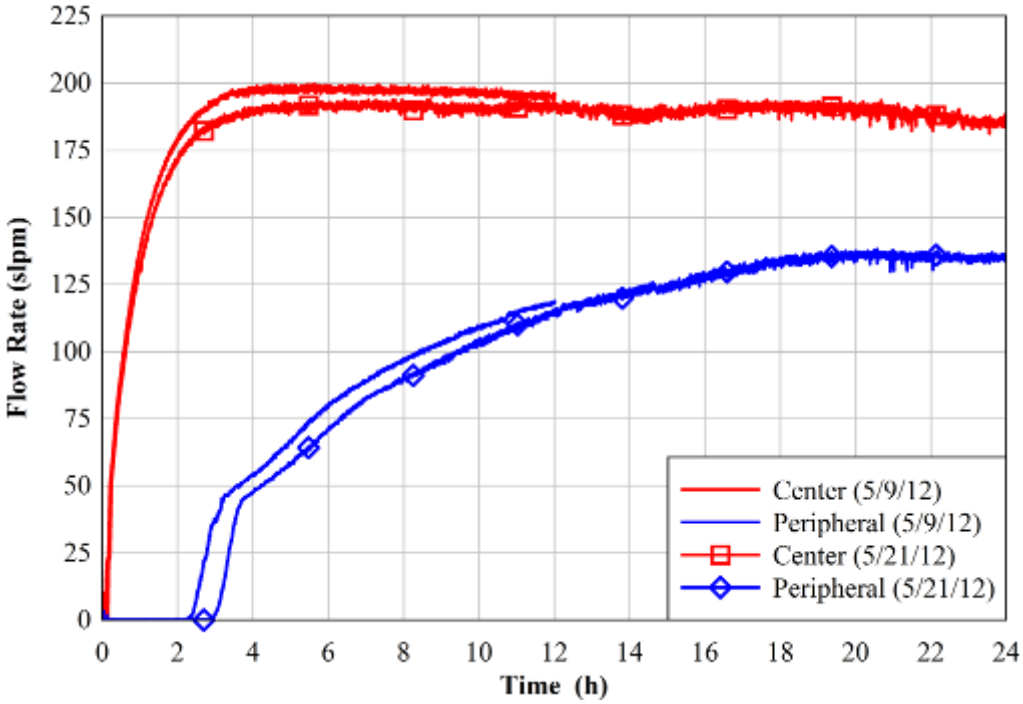

Figure 3.6 **Induced flow rates as a function of time at 4.0 kW simulated decay power for the center and peripheral bundles**

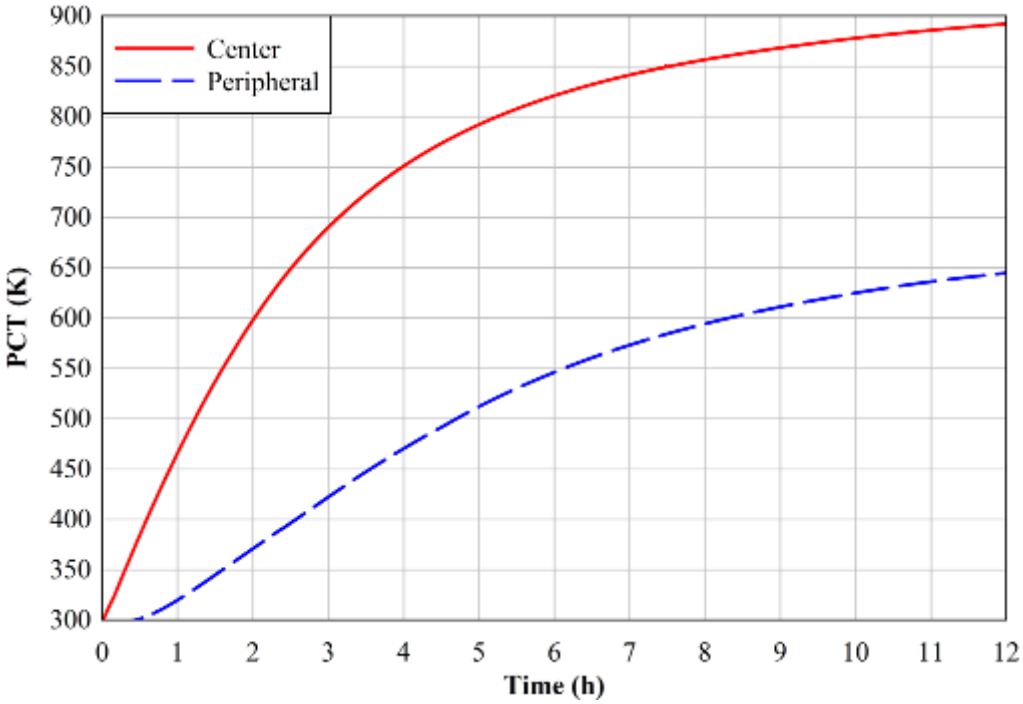

Figure 3.7 **Peak cladding temperatures as a function of time at 8.0 kW simulated decay power for the center and peripheral bundles**

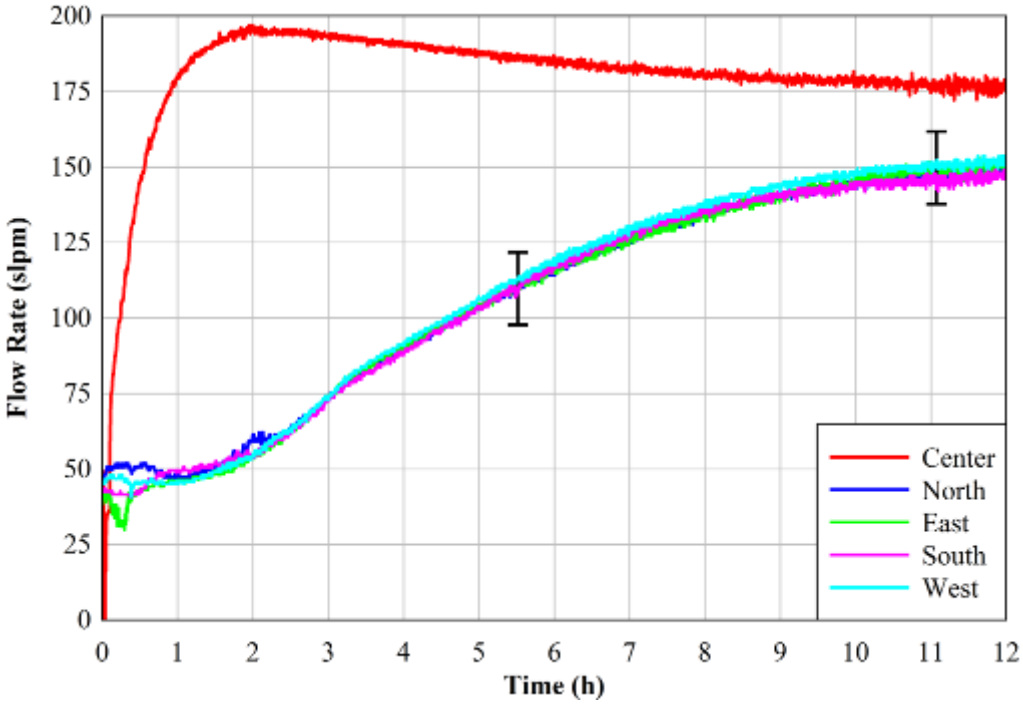

Figure 3.8 **Induced flow rates as a function of time at 8.0 kW simulated decay power for the center and peripheral bundles**

4 IGNITION TEST RESULTS

Phase II of the OECD/NEA SFP Project concluded with the ignition of the test assembly on June 6, 2012. The test was started at 00:01:42 Mountain Daylight Saving Time. The total applied power to the center fuel assembly was 15.0 kW, which represents an assembly with a 45 GWd burnup approximately 3 months after offload. The center assembly was surrounded on four sides by unpowered, peripheral assemblies. Ignition of the Zircaloy within the center assembly was first observed at the z = 3.302 m [130 in] level and at an elapsed test time of 6.31 hours based on a thermal criterion of 1,200 K [1,700°F]. The first ballooning event in the pressurized, peripheral assemblies occurred at 6.67 hours. Based on the same criterion of 1,200 K [1,700°F], the Zircaloy fire first propagated into the peripheral assemblies at an elapsed test time of 7.08 hours at the z = 3.150 m [124 in] level.

4.1 General Thermal-Hydraulic Response

Figure 4.1 gives the peak cladding temperature as a function of time for the center and peripheral assemblies. Both data series have been truncated due to the failure of the thermocouples at elevated temperatures. The center assembly first reached ignition based on a temperature of 1200 K [1,700°F] at 6.31 hours. The peripheral assemblies first registered ignition temperatures at 7.08 hours.

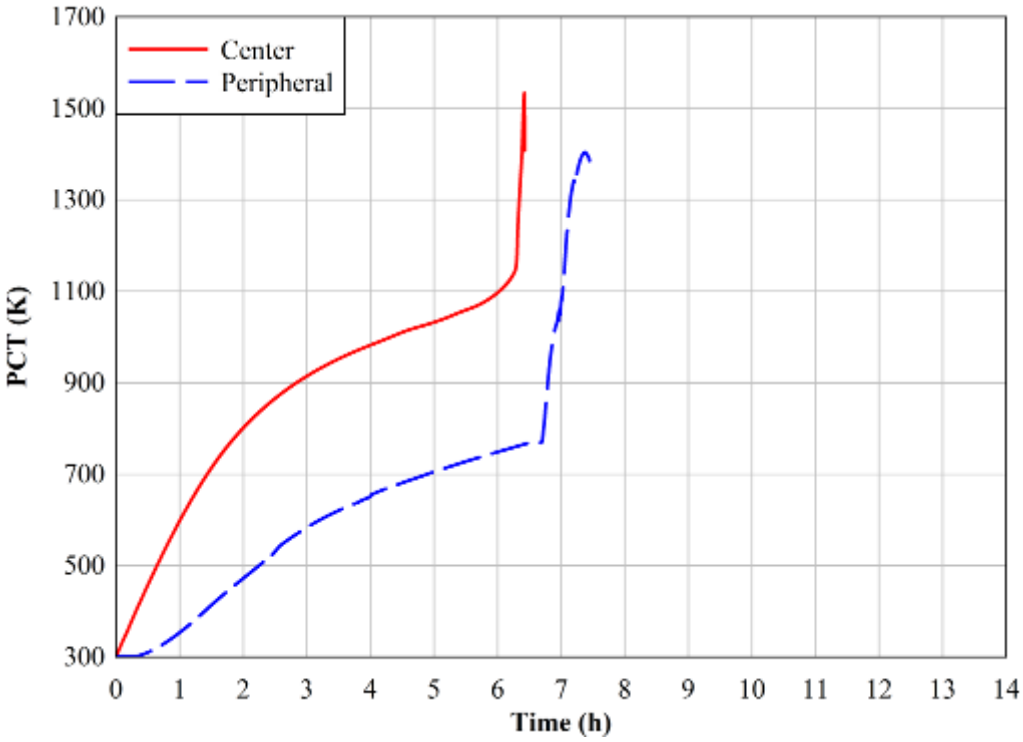

Figure 4.1 Peak cladding temperature in the center and peripheral assemblies during the ignition test

Figure 4.2 shows the measured flow rates in the center and peripheral assemblies as a function of time during the ignition test. The flow rates in the peripheral assemblies did not register accurately prior to about 1.4 hours due to the relative insensitivity of the hot wire anemometers at low flow rates. The first major disturbance in the flow occurs at approximately 6.7 hours and corresponds to the loss of electrical power in the center assembly. A sharp decrease in the

peripheral assembly flow rates was recorded after 8.7 hours, which coincides with the time at which the ignition front had progressed across the entire cross section of the peripheral assemblies. Debris was observed exiting the bottom of the inlet pipes and may be the cause of the erratic signals at times greater than t = 10 h.

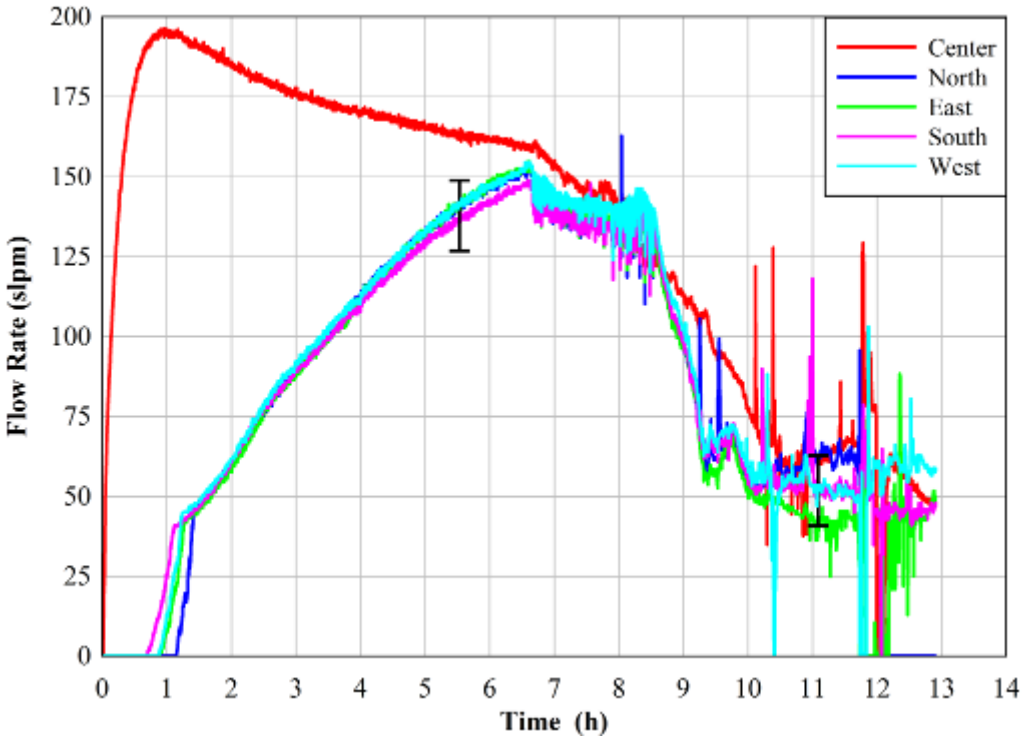

Figure 4.2 Measured flow rates in the center and peripheral assemblies during the ignition test

Figure 4.3 shows the oxygen concentration as measured in the center bundle, center annulus, and individual peripheral assemblies. The sampling pump was activated at 5.7 hours, after measurable oxygen depletion had already begun. The depletion of oxygen measured in the bundle of the center assembly corresponds with the ignition time of 6.31 hours. The peripherals began registering significant oxygen consumption at times greater than approximately 8 hours, which is when the burn front had neared the middle of the peripheral assemblies. None of the sensors registered complete depletion of oxygen, although the RGA does indicate near-complete consumption of oxygen immediately after ignition. Therefore, the O_2 concentrations as measured by the oxygen sensors are considered unreliable after the sample registers less than 8 percent. The non-zero response of the oxygen sensors after ignition is not understood, but air entrainment at the top of the fuel assemblies into the sample lines is the most likely explanation. Evidence of air entrainment was also observed in the RGA samples.

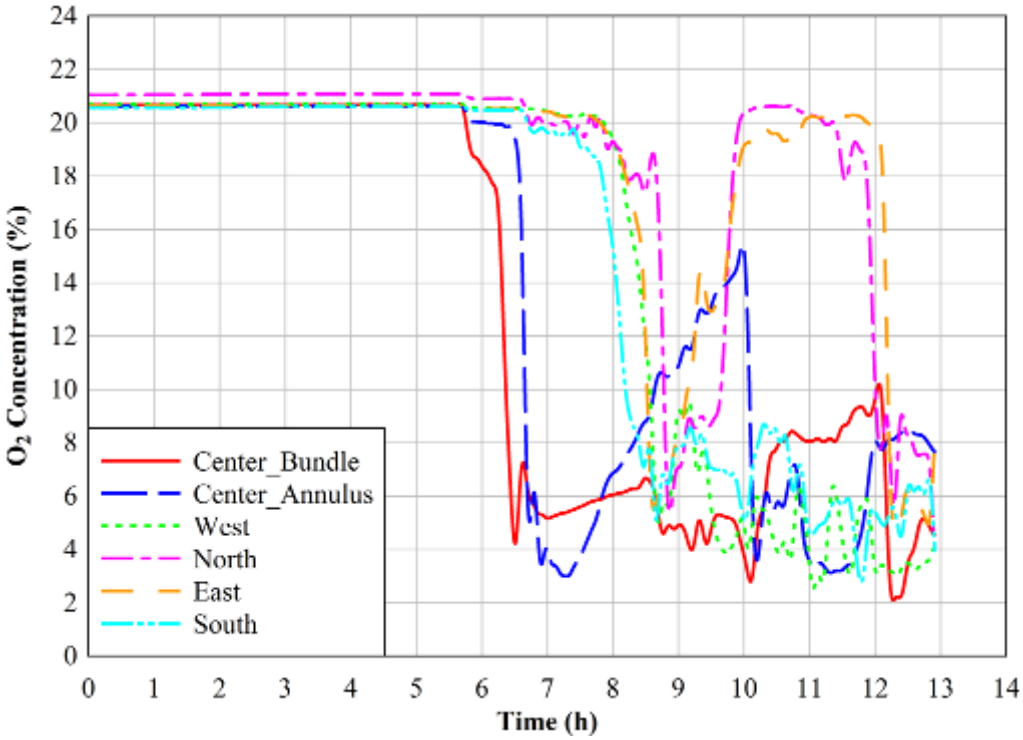

Figure 4.3 Oxygen concentrations of the center and peripheral assemblies during the ignition test

4.2 Burn Propagation

4.2.1 Axial Propagation

The Zircaloy ignition started in the middle of the center assembly at the z = 3.302 m [130 in] level. The burn front briefly propagated both upward and downward from this level but failed to reach the uppermost portion of the center assembly before becoming oxygen starved. The ignition front primarily swept down the assembly toward the source of oxygen at the assembly inlet. The burn progressed at an average rate of 0.457 m/h [18 in/h]. Figure 4.4 shows the temperature in the middle of the center assembly at different axial heights as a function of time.

Similarly, Figure 4.5 shows the axial propagation of the Zircaloy ignition in East and West assemblies. The cladding fire started at z = 3.150 m [124 in] level (not shown) and propagated almost exclusively downward. The fuel above this initial level in the peripheral assemblies exhibited heavy oxidation as evidenced during the post-test inspection but did not exhibit a thermal excursion typically associated with breakaway kinetics during the 13 hour test. As expected, the peripheral average burn rate of 0.466 m/h [18.35 in/h] nearly matches that of the center assembly.

Figure 4.6 depicts the manner in which the cladding fire spread through the fuel bundles. Initially, the burn front propagated preferentially downward in the center assembly. At late times in the test (t > 10 h), the burn fronts in the center and peripheral merged and appear as a planar front.

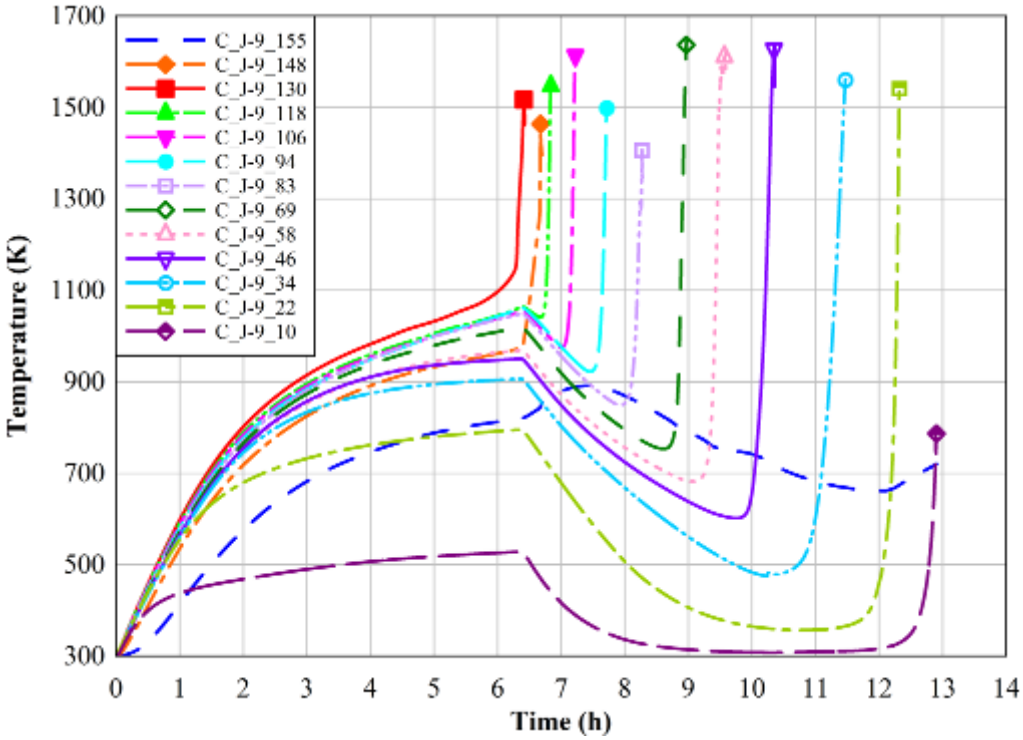

Figure 4.4 Temperature in the middle of the center assembly for different axial heights

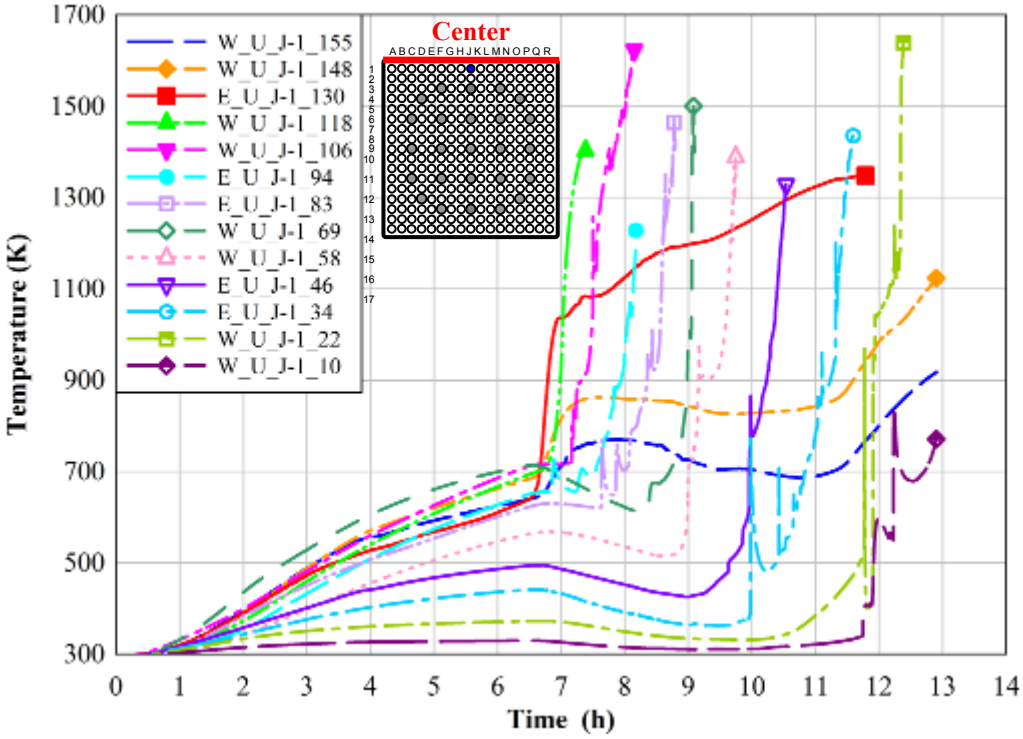

Figure 4.5 Maximum temperatures in the peripheral assemblies of the rods closest from the center assembly for different axial heights

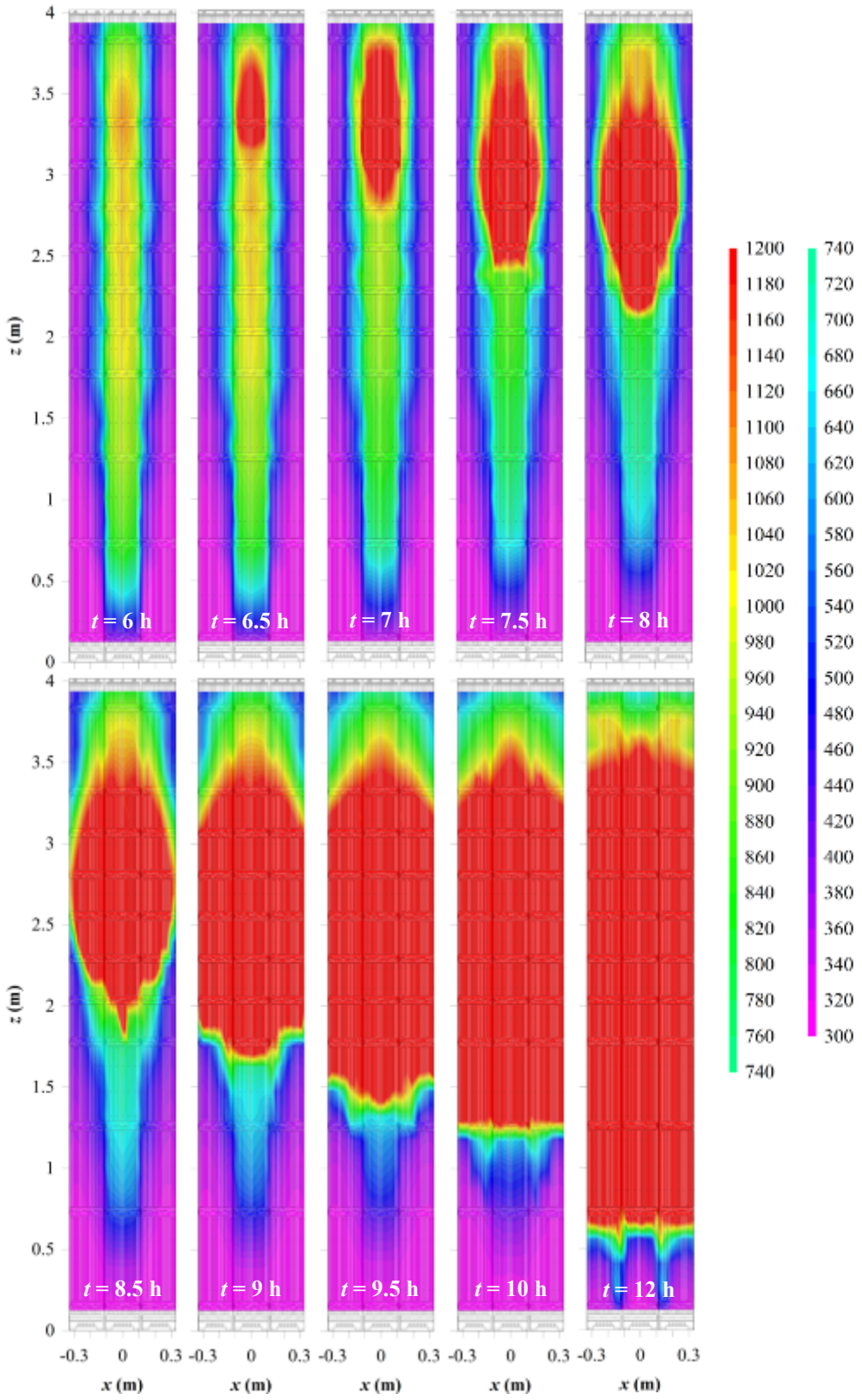

Figure 4.6 **Temperature contours at the midplane of the assembly and different times during the ignition test**

4.2.2 Transverse Propagation

The cladding fire also propagated transversely into the peripheral assemblies starting at t = 7.08 h. Figure 4.7 shows the maximum temperatures of the instrumented rods closest to the center assembly in the unpressurized (J-1) and pressurized assemblies (J-3) and the furthest from the center assembly in the unpressurized (J-17) and pressurized assemblies (J-15). The ignition had progressed across the entire cross section of all of the peripheral assemblies by t = 8.74 h. Examination of these results reveals a degree of asymmetry in the propagation into the peripheral assemblies. The East J-3 rod reached the ignition criterion 0.26 hours after the North J-3 rod. Similarly, the difference in time between the rods further from the center assembly show a 0.27 hours spread between the first to ignite (South J-15) and the last to reach 1,200 K [1,700°F] (North J-15).

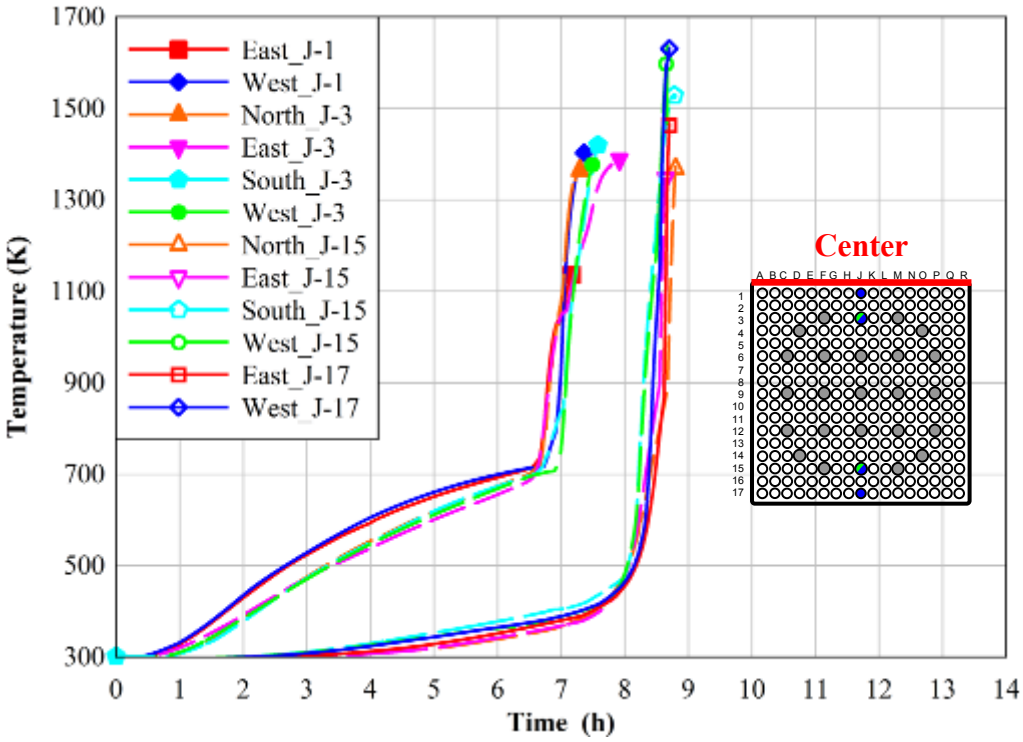

Figure 4.7 Maximum temperatures in the peripheral assemblies of the rods closest and furthest from the center assembly along the plane of symmetry

Figure 4.8 gives temperature contours across the center and peripheral fuel assemblies at the z = 2.540 m [100 in] level at different times of interest. This figure further demonstrates the nature of the burn propagation in the transverse direction. These contours were constructed with all available thermocouple data at this axial level with interpolation between measurement locations. These data were reflected across the diagonal plane of symmetry to represent one-fourth of the assembly geometry for visualization purposes and thus are artificially symmetric. As described earlier, the ignition front is known to have propagated asymmetrically into the peripheral assemblies by times of up to 0.27 hours but is ignored in these plots. Thermocouples that exceeded 1,480 K [2,204°F] were consumed but were assumed to remain at a temperature above this threshold for times after their destruction in the plots. The plots show that the cladding fire first propagated preferentially into the peripheral assemblies near the midplane and proceeded to burn from the center facing rod bank to the outermost rod bank in a nearly planar fashion.

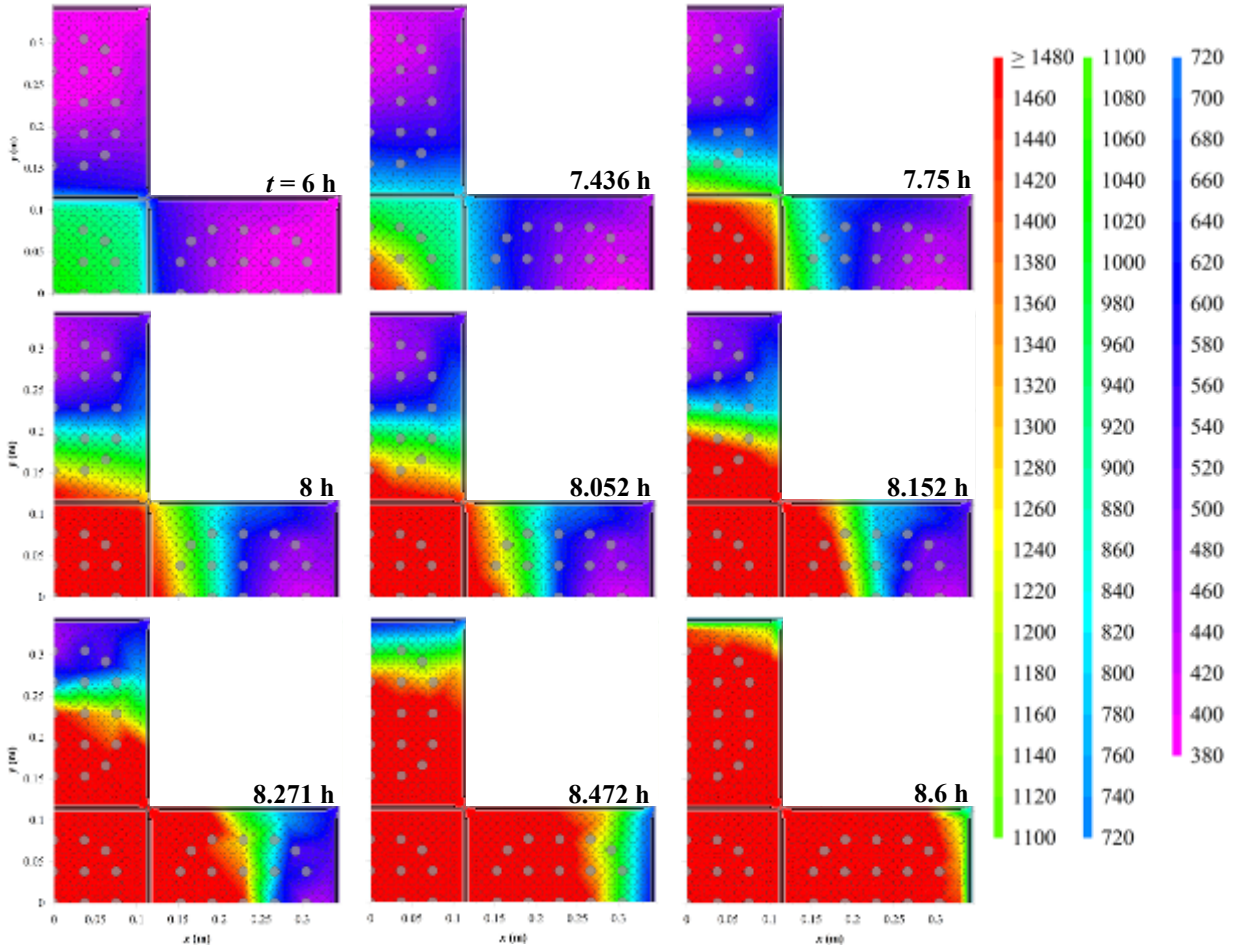

Figure 4.8 Temperature contours throughout the assembly at *z* = 2.540 m [100 in] and different times during the ignition test

4.3 Fuel Clad Ballooning

Figure 4.9 shows the indicated pressure in the rods closest (J-1) and furthest (J-17) from the center assembly. The North and South assemblies were initially filled to 6.2 MPa [900 psi] and 5.2 MPa [750 psi], respectively. The ballooning events in the two assemblies occurred within approximately 3 minutes of each other at a given location, regardless of the initial pressure. Ballooning did not likely occur at a single axial level but rather between *z* = 2.692 and 3.302 m [106 and 130 in] based on PCT data at the time each rod ballooned. The thermal-hydraulic behavior of assemblies with ballooned rods did not appear to be discernible from the unpressurized assemblies.

A photograph of post-test ballooned segments of fuel are shown in Figure 4.10. The stacked arrangement in the photo should not be perceived by the reader as a dual ballooning event on the same rod. Rather, each remnant represents the ballooning of a single rod. Due to the chaotic nature of the debris field, the originating location of these samples could not be determined. The variety of samples do show a spectrum of ballooning events ranging from extreme tears in the cladding to localized gashes. All the samples show the additional effects of slumping, oxidation, and spallation. The surrogate fuel is still visible in some samples such as in the lower-middle artifact.

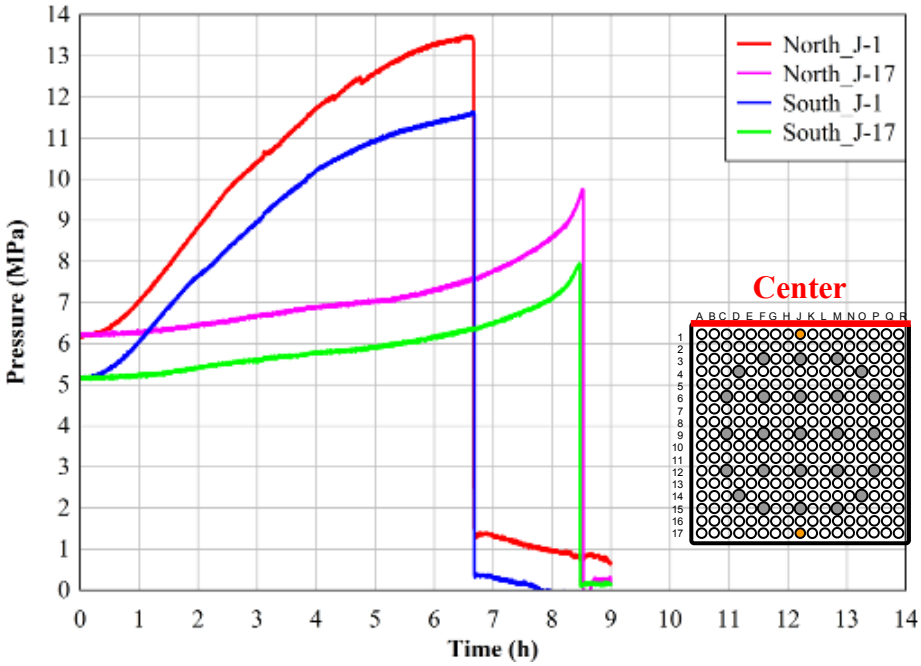

Figure 4.9 Indicated pressures in the peripheral assemblies of the rods closest (J-1) and furthest (J-17) from the center assembly along the plane of symmetry

Figure 4.10 Photograph of ballooned and oxidized sections of cladding from the SFP Phase II ignition test

4.4 Exhaust Gas Analysis

A residual gas mass spectrometer (RGA) was used to monitor the concentrations of the gas constituents exiting the center assembly over a 130 hour period. The gas constituents

monitored were nitrogen, oxygen, argon, water, carbon dioxide and helium. The gas sample stream was conditioned by filtering particulates and the sample pressure was held constant by an electronic back pressure controller. Ambient air was automatically sampled at two hour intervals to correct changes in the instrument sensitivity, which drifted downward by a factor of about four for all gases. Calibration gases containing certified levels of argon with the balance nitrogen were used to correct the argon and nitrogen concentrations for the periods when oxygen was absent from the gas sample.

Figure 4.11 shows the sample gas composition on a dry basis as a function of time over the entire 130 hour test period. Also shown on Figure 4.11 is the total of all mole fractions that should be unity. Any deviation from unity is a measure of the total error in the analytical scheme. From time zero until ignition at 6.3 hours the oxygen concentration was at ambient levels. At ignition the oxygen concentration dropped sharply to near zero. From about 10 hours until about 16 hours the oxygen concentration was unstable apparently due to air infiltration into the gas sample. Shortly after ignition occurred in the center assembly the pressurized rods in the North and South peripheral assemblies began to balloon. A series of ruptures occurred from about 6.6 hours until 8.5 hours. Since the pressurized rods were filled with argon, each rupture caused a spike in the argon concentration. At about 7.5 hours the CYBL vessel extraction fan was energized which began purging the vessel with fresh air. The excess argon was slowly removed and the argon concentration returned to ambient levels by about 30 hours. At about 64 hours the oxygen level began to rise. By 105 hours all gas concentrations had returned to ambient levels.

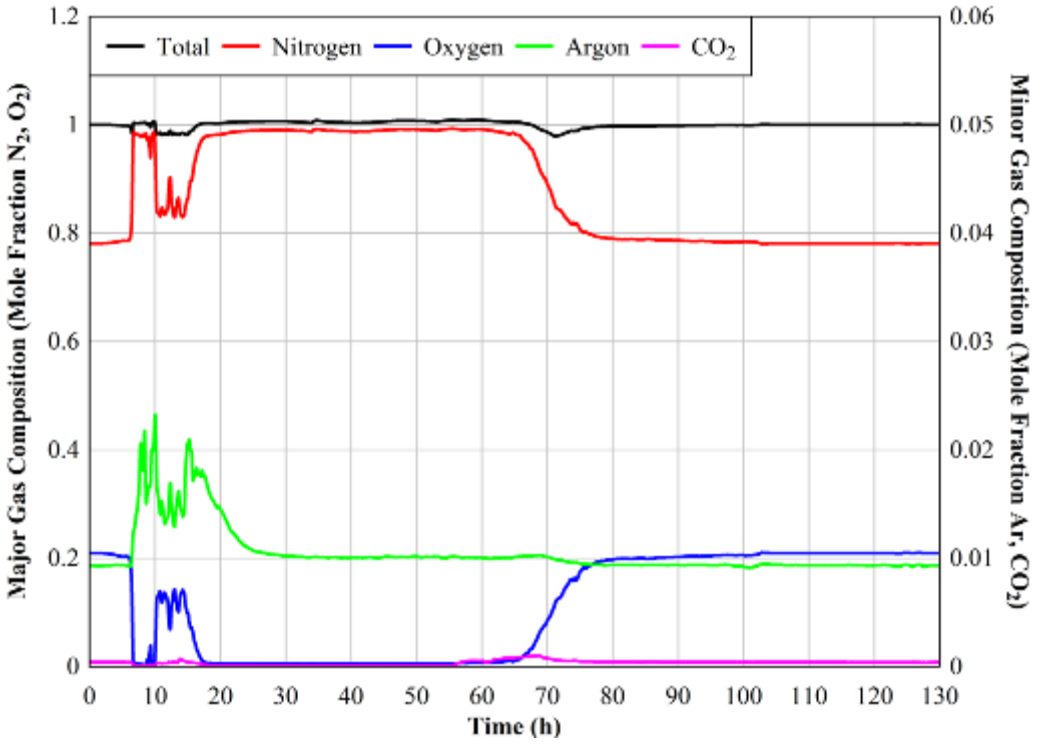

Figure 4.11 Mole fraction concentration of major and minor constituents of sample gas

Since argon and helium are inert noble gases and do not react with zirconium, the concentration of either of these gases relative to the reactive gas species provides a measure of a reactive gas removal and subsequent release. Figure 4.12 shows the ratio of nitrogen and oxygen to

argon (and helium for the case of nitrogen) normalized by the ratios found in ambient air. A normalized argon ratio of unity signifies no change from ambient air. Normalized ratios that are less than unity signify removal of a gas species. Normalized ratios greater than unity signify the release of a gas species. Due to the excess argon release during pressurized rod ballooning and the subsequent slow removal of this excess, the argon concentration between 6.5 and 30 hours is elevated above ambient. The increased argon concentration artificially reduces the argon ratios. During this period, the helium ratio is more relevant even though the very low concentration is near the detection limit of the instrument and results in a noisy signal.

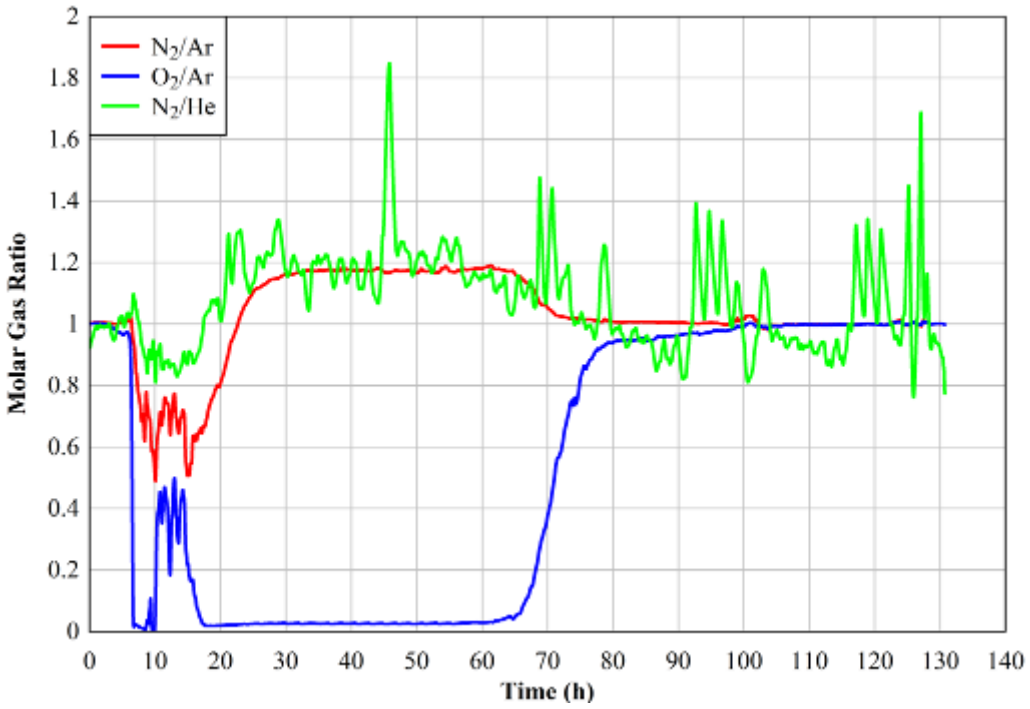

Figure 4.12 Normalized argon and helium ratios for nitrogen and oxygen

The O_2/Ar plot closely mirrors the oxygen concentration plot in the previous figure. At 6.31 hours when ignition occurs, the O_2/Ar ratio drops sharply to near zero where it remains until just after 60 hours. Air infiltration into the gas sample between 10 and 18 hours is evident. Between 60 and 80 hours, the O_2/Ar ratio rises rapidly to near ambient conditions. The return to ambient levels is complete at 105 hours signifying the end of all oxidation reactions.

Under the appropriate conditions, nitrogen will react with zirconium to form zirconium nitride (ZrN). Steinbrück (2009) has shown that the zirconium-nitrogen reaction occurs readily when oxygen is absent in the gas phase and simultaneously oxygen is present in the zirconium metal phase. In particular it was determined that oxygen-stabilized α-Zr(O) was the form of zirconium most reactive to nitrogen. The ratio of nitrogen to argon and helium was used to monitor the reaction of nitrogen with zirconium. The analysis shows two distinct stages of oxidation over the course of the test. The primary oxidation stage was very energetic and continued for over 11 hours after ignition as defined by the transition of the nitrogen to helium ratio from less-than unity to greater-than unity. During this stage, all of the oxygen entering the assembly was consumed by the oxidation of zirconium as described in Equation 4.1. Also, a substantial portion of the nitrogen was consumed by production of the nitride from much, if not most, of the unoxidized zirconium remaining above the burn front as given in Equation 4.2.

$$Zr + O_2 \rightarrow ZrO_2 \quad \Delta H_{rxn} = -1{,}094.8 \text{ kJ/mol Zr} \qquad 4.1$$

$$Zr + \tfrac{1}{2} N_2 \rightarrow ZrN \quad \Delta H_{rxn} = -365.4 \text{ kJ/mol Zr} \qquad 4.2$$

The nitride reaction releases about a third of the energy of complete oxidation; however, the mass of zirconium converted to nitride may be two to three times greater than the mass converted to oxide during the primary oxidation stage. The kinetics of Equation 4.2 has been studied by Steinbrück and Jung (2011). A strong reaction rate dependence on the oxygen content of the oxygen-stabilized □-Zr(O) metal phase was found such that an oxygen content increase from 2 wt. percent to 6.5 wt. percent increased the reaction rate at 1,100°C [2,012°F] by nearly two orders of magnitude. The reaction rate for 6.5 wt percent O metal was found to exhibit a complex temperature dependence where the rate increased for temperatures up to 1,200°C [2,192°F] but then decreased for higher temperatures.

All reactions consumed gaseous reactants so the flow exiting the assembly was substantially reduced, which may have allowed air infiltration into the exhaust gas sample. The additional release of energy from the wholesale production of the nitride coupled with the significant reduction in convective energy removal are important phenomena to consider when assessing the propensity of an ignited assembly to propagate the fire to adjacent assemblies.

During the second oxidation stage, all of the oxygen entering the assembly was consumed by the oxidation of zirconium nitride as indicated by the release of nitrogen gas in Equation 4.3.

$$ZrN + O_2 \rightarrow ZrO_2 + \tfrac{1}{2} N_2 \quad \Delta H_{rxn} = -729.4 \text{ kJ/mol Zr} \qquad 4.3$$

This stage continued for 88 hours with the end defined by the return of all gas normalized ratios to unity. The lower energy release of zirconium nitride oxidation (two thirds of complete zirconium oxidation) coupled with increased convective energy removal resulted in a less energetic burn during the second stage. The oxidation kinetics given in Equation 4.3 have been studied by Krusin-Elbaum and Wittmer (1983), where a parabolic dependence of oxide growth on time was observed which indicates a diffusion limited reaction.

4.5 Post-Test Examination

Figure 4.13 shows photographs of the test assembly from different perspectives during the deconstruction activities. Image (*a*) shows the top ~0.61 m [24 in] of the assembly with the insulation removed from the assembly. The North peripheral cell shows loss of structural integrity of the pool cell towards the bottom of the photo. Image (*b*) is a top-down perspective of the assembly after the top ~0.61 m [24 in] of the assembly was removed. The Zircaloy components were nearly all transformed to ceramic by the fire and were highly brittle. No evidence of the center pool rack walls remained. The East assembly is shown with the outer pool cell wall removed in image (*c*). The stainless steel plenum spring is seen protruding through the fuel to the right of the image. The top nozzles of the East and North assemblies are shown in images (*d* and *e*), respectively. Accumulation of MgO at the top of the assemblies was more pronounced in the North and West (not shown) than in the East and South (not shown). Finally, a piece of vitrified insulation from a corner cell is pictured in image (*f*). The high-temperature insulation in the corner cells relocated to the bottom of the assembly and fused into large solid blocks.

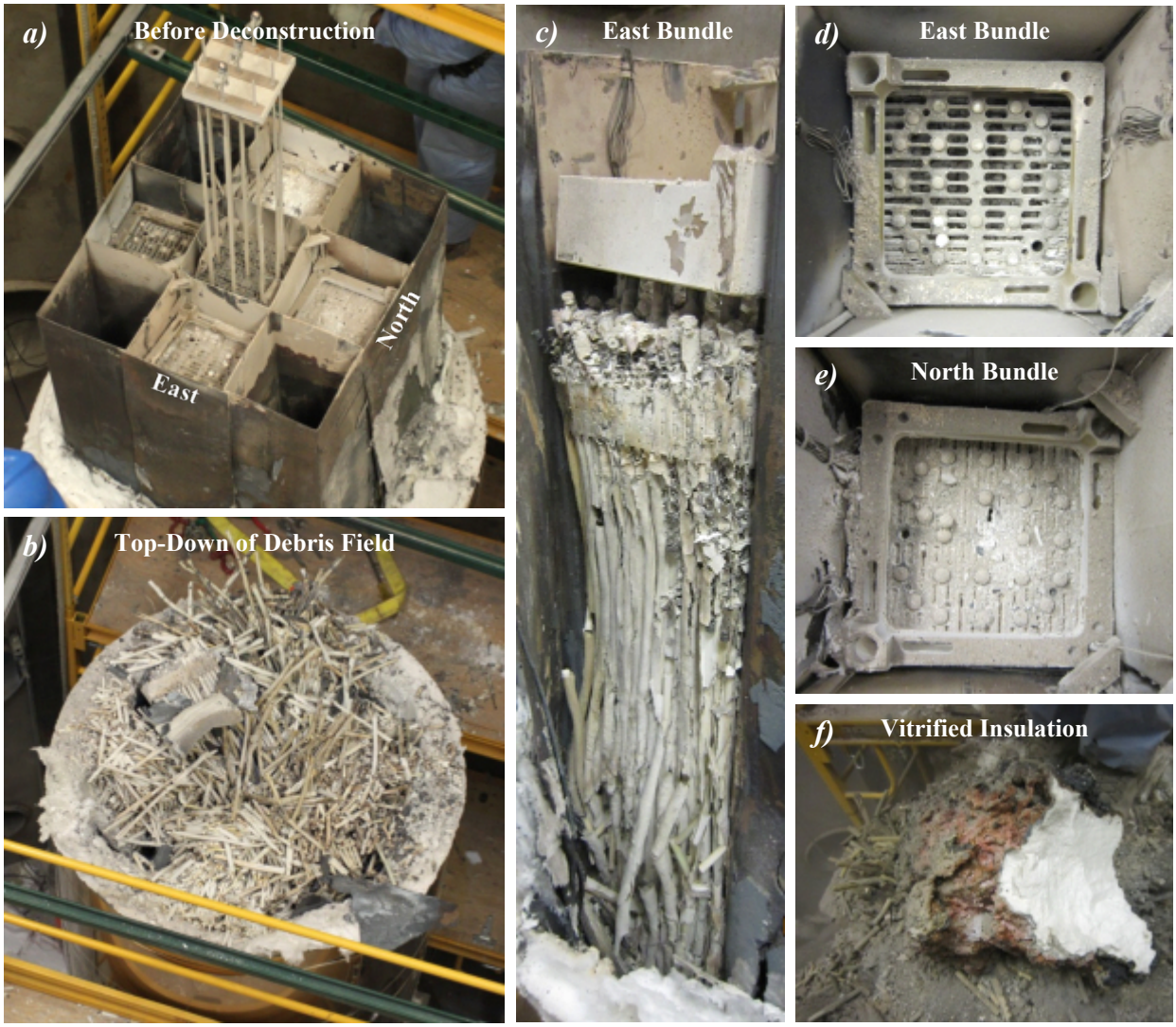

Figure 4.13 Photographs of the test assembly during various stages of deconstruction

5 MELCOR MODELING RESULTS

The OECD/NEA SFP Project Phase II experiments present a challenging modeling scenario where the central heated assembly can ignite, leading to an intense heat flux to the surrounding unheated assemblies, resulting in a large temperature gradient across the peripheral assemblies. These experiments are used to validate the spent fuel pool models that are part of the MELCOR code capabilities, including an assessment of the air oxidation models. The MELCOR input models used are described in Section 5.2. A developmental version of MELCOR based on version 2.1.5287 was used for these simulations. Code modifications are described in Section 5.3. Simulation results for the pre-ignition and ignition tests are described in Sections 5.4 and 5.5 respectively. Sensitivity studies are described in Section 5.6.

5.1 Introduction

For this analysis, 2-ring and 9-ring MELCOR models were developed to simulate the PWR spent fuel assembly experiments performed at Sandia National Laboratories. A 2-ring model is the preferred approach for a reasonable model of an actual spent fuel pool. The 2-ring model simulation using a relatively coarse nodalization improves code run time and decreases model complexities in comparison to the 9-ring model. In the 9-ring model, assemblies are subdivided by rows of fuel rods which provide a more detailed modeling of the experiment to be used in assessing the MELCOR models. The 9-ring model was developed by Energy Research Inc. and the 2-ring model was developed at SNL based on the 9-ring model. It is important to compare the detailed 9-ring calculation with a 2-ring calculation that utilizes identical radiation coupling between the spent fuel rack and the fuel rods in both the central and peripheral assemblies. The input models used are described in more detail in Section 5.2.

In order to more accurately predict the temperature response with the 2-ring model, code improvements were made to more adequately represent the intense thermal gradient between the central heated assembly and the unheated (peripheral) assemblies, as well as the temperature gradient between rods in the peripheral assemblies. The improvements involve the addition of multiple rods within a single core ring. These code changes, described in Section 5.3, are still developmental and have not been fully implemented into the code but were made as a proof of concept. In particular, the current implementation of these models does not account for core degradation properly and consequently, the calculations performed are only sufficient in calculating up to the point of ignition in the test. For the purpose of this analysis, this is acceptable given the test data is generally no longer available after ignition due to failures of the thermocouples at elevated temperatures. Additional work and refinement of these models is anticipated prior to these new features being incorporated in a release version of MELCOR. Comparisons of results predicted by the 2-ring and 9-ring models are discussed in Sections 5.4 and 5.5.

5.2 MELCOR Models

Three MELCOR models were developed to simulate Phase II of the OECD/NEA SFP experiments. These included a 2-ring model, a 2-ring multiple rod model and a 9-ring model. Table 5.1 presents a summary of the main design parameters for the five assemblies in the 1 by 4 configuration in Phase II of the tests.

Table 5.1 Summary of main facility design parameters for the Phase II tests

Parameter Group	Description	Units	Value
Overall	Five full-length assemblies in 3×3 pool rack with heated assembly in the center cell	-	-
	Power and time duration for nine pre-ignition tests	kW (h)	1 (24), 2 (24), 4 (12), 4 (24), 6 (12), 8 (12), 10 (4), 12 (4) and 15 (3)
	Power for ignition test	kW	15
Fuel Assembly	"Fuel" (MgO) outer diameter	mm	8.19
	Heater rod cladding outer diameter	mm	9.53
	Control rod guide tube outer diameter	mm	12.19
	Number of heater rods per assembly	-	264
	Number of control rod guide tubes per assembly	-	24
	Number of instrument tubes per assembly	-	1
	Number of spacers in assembly	-	11
	Heater rod filler material	-	MgO
	Heated rod axial length	m	3.613
	Fuel rod & tube axial length	m	3.918
	Total mass of steel cladding per assembly	kg	5.748
	Total mass of MgO in center assembly	kg	142.66
	Total mass of Zry in center assembly	kg	142.2
	Total mass of MgO in four peripheral assemblies	kg	541.01
	Total mass of cladding in four peripheral assemblies	kg	440.87
3×3 Pool Rack	Storage cell inside width (center cell/peripheral cells)	mm	224.2/222.7
	Flow area (center/peripheral)	m^2	0.0286/0.0279
	Equivalent hydraulic diameter (center/peripheral)	mm	11.74/11.46
	Storage cell rack thickness	mm	1.91
	Insulation thickness	mm	152.4
	Number of pool cells	-	5
	Total mass of 3×3 pool rack	kg	561
Others	Major loss coefficient (S_{LAM}) in the central assembly for 300 slpm upper flow range	-	119*
	Total form loss coefficient (Σk) in the central assembly for 300 slpm upper flow range	-	68*
	Major loss coefficient (S_{LAM}) in the peripheral assemblies for 300 slpm upper flow range	-	113*
	Total form loss coefficient (Σk) in the peripheral assemblies for 300 slpm upper flow range	-	47.5*

* Derived S_{LAM} and Σk values based on the low flow range pressure drop parameters (see Table 2.4.) Note that Σk = 68 for the center assembly eliminates the form losses incurred from passing through the inlet and test stand.

5.2.1 9-Ring Model

The 9-ring model has spatial representation of the five assemblies in a 1 by 4 configuration and is fundamentally limited by the MELCOR core (COR) package's restriction to two-dimensional geometry (i.e., axial and radial nodalization with no azimuthal component). In the model, 17 axial COR package levels were present in each of 9 radial rings, as shown in Figures 5.1 and 5.2. In COR axial levels 3 through 15, four COR cells (rings) were assigned to each axial level of the heated center assembly, whereas five COR rings describe the peripheral assemblies as a whole. Since in MELCOR version 1.8.6 (which was used early in the project) the total number of control volumes in the core and the lower plenum regions is limited to 99, each control volume (CV) was assigned to two axial levels in the lower region of the assemblies while each CV corresponded one-to-one to each axial level in the upper region of the assemblies. In MELCOR 2.1, which was used for this project, the limit of 99 CVs is no longer applied which allows development of larger more complex models, however, the model noding was not changed to take advantage of this as it was not expected to improve the results. COR axial levels 16 and 17 (above the top of the heated portion of the rods) shared a single level of nine control volumes, and axial levels 1 and 2 occupied the assembly inlet (a single level of two control volumes, one for the center and one for the peripheral assemblies).

Note that the nine COR rings describe cross-sectional regions of the test assemblies in increasing distance from the middle of the center assembly; the four peripheral assemblies were lumped together, with no distinction possible, for example, between the North and South assemblies. The steel-sheathed Kaowool insulation layer surrounding the peripheral assemblies was modeled as a series of MELCOR heat structures.

A total of 94 control volumes (CV) were used to represent the five assemblies in the 1 by 4 configuration (i.e., a vertical stack of 10 CVs in each of the nine COR rings, in addition to two inlet, one outlet, and one downcomer volume), which are denoted by the numbers in black color at the center of each cell in Figure 5.1. A total of 173 flow paths, denoted by the numbers in blue along with arrows, interconnected these control volumes, with vertical flow paths, and cross flow paths between adjacent rings of each assembly. There was no cross-flow path through the rack walls between the central and the peripheral assemblies, except for a leakage flow path at the bottom of the rack, representing an imperfect seal at the interface of the rack and the test stand. There were in total 153 COR cells, which are denoted by the numbers in red at the top on the right side of each cell (note that in some cases, above the heated length of the rods or the lower region of the assemblies, one CV is denoted as containing two COR cells). Air enters the assemblies from the inlet pipes at the bottom and flows upwards through the assemblies as a result of natural buoyancy forces as the assemblies are heated. The exits of the assemblies were connected to a time-independent control volume representing atmospheric conditions (CV020). Hydraulic loss factor values derived from experimental measurements (see Section 2.4.5) for the Phase II tests were used in this study.

In the COR package nodalization, the flow area and number of heated fuel rods in the center assembly were divided into four rings, while five rings model the four peripheral assembly unheated rods in increasing distance from the center. The flow area and the number of fuel rods varied with each ring, such that the radial nodalization became finer where larger temperature gradients were expected. In particular, rings 4 and 5 (i.e., adjacent to the rack wall) consisted of a single column of fuel rods. In order to preserve the rectangular geometry of the peripheral assemblies, rings 5 to 9 were modeled such that the distance from ring 4 to ring 9 was the same as the inner width of the peripheral assemblies. In the vertical direction, the core region consisted of 12 axial levels in the heated region (i.e., from core axial level 4 to axial level 15, colored in pink for the center assembly as seen in Figure 5.1), corresponding to about 0.3 m

[1 ft] length of heater rod per axial level; two axial levels above the top of the heated region to model the unheated plenum region and outlet nozzles (COR levels 16 and 17); and three axial levels below the heated region to model the inlet nozzles (COR level 3), the base-plate (COR level 2), and the pipe under the base-plate (COR level 1), respectively.

Heater rod, pool cell, and other dimensions and masses were modeled based on data obtained from the Phase II test plan (Ref. 20). The experimental tests used compacted MgO as rod filler that was uniformly heated by a central Nichrome wire to simulate UO_2 fuel; therefore, the thermo-physical properties of UO_2 fuel were replaced in the input model by MgO properties. As a simplification in the model, the mass of Nichrome resistive heating wire was excluded from consideration (i.e., the "fuel" component in the COR package was represented purely as the mass of MgO); this approximation was found in the case of Reference 8 to result in negligible differences in model output. Zircaloy mass in the cladding was specified as cladding component mass. The mass from the 24 guide tubes, one instrumentation tube, and 11 assembly grid spacers per assembly was specified as Zircaloy non-supporting structure (NS) component mass, whereas the base-plate was specified as a supporting structure component (SS) made of stainless steel. The relatively small masses of the upper plate and nozzle were included in the input model, but represented as MELCOR heat structures. These heat structures were defined as constituting the upper axial boundary of the “core” as required by the MELCOR COR package.

The steel racks surrounding the pool cells were represented by mass allocated to the new rack (RK) component for core model of type SFP-PWR. The layer of steel-wrapped Kaowool insulation surrounding the peripheral assemblies and at the corners of the 1 by 4 cell configuration was represented as a vertical stack of COR radial boundary heat structures, which thermally interacted with the peripheral assemblies by means of radiative and conductive heat transfer.

In order to represent the actual rectangular geometry of the test assemblies, component surface areas and coolant flow areas were calculated from the real geometry (e.g., the boundary surface area for each ring of rings 5 to 9 was a product of the width of a test assembly multiplied by 4 peripheral assemblies) rather than by first deriving a fictitious and approximate cylindrical model geometry.

The default radial model of thermal radiation in MELCOR for PWR spent fuel pools consist of intra-cell radiation between cladding and rack components in each cell, in addition to inter-cell radiation between each rack component and the cladding in the adjacent ring. Such a model was not best suited to the nodalization used in the present study, since MELCOR would (for example) calculate no direct thermal communication between heater rod surfaces in different rings of one assembly. Therefore, in order to correctly reflect inter-cell radiation exchange, the conventional radial inter-cell radiation view factor defined by input parameter FCELR was set to zero; view factor-surface area pairs were directly input between specific pairs of components (e.g., ring 5 cladding to ring 6 cladding) using the optional CORHTR cards. Calculation of these inter-cell component-to-component view factors in the radial direction were performed with ANSYS FLUENT (Refs. 17 and 18) and are based upon the component geometry.

ANSYS FLUENT can compute the view factors for radiation problems and save them to a file when the surface-to-surface (S2S) radiation model is invoked. The surface-to-surface radiation model can be used to account for the radiation exchange in an enclosure of gray-diffuse surfaces. The energy exchange between two surfaces depends in part on their size, separation distance, and orientation. These parameters are accounted for by a geometric function called a

"view factor". When using the S2S radiation model, ANSYS FLUENT provides two methods for computing view factors: the ray tracing method (which is selected by default) and the hemicube method. The hemicube method is available only for 3D and axisymmetric cases and ray tracing method is only available when Face to Face is selected for basis. The hemicube method uses a differential area-to-area method and calculates the view factors on a row-by-row basis. The view factors calculated from the differential areas are summed to provide the view factor for the whole surface. While the hemicube method projects radiating surfaces onto a hemicube, the ray tracing method instead traces rays through the centers of every hemicube face to determine which surfaces are visible through that face. The ray tracing method does not subdivide the faces as can be done when using the hemicube method. In the current calculation, the ray tracing method was used to obtain the view factors between surfaces. The approximation was made that the radiative heat transfer cannot travel further than the next adjacent component. For example, the fuel rods in ring 1 can only radiate to the fuel rods in ring 2. In reality, some small fraction of the radiation (~0.3 percent) would go directly from ring 1 to ring 3, ring 4 and the rack.

The true projection of each visible face onto the hemicube can be accurately accounted for by using a finite-resolution hemicube. As described previously, the faces are projected onto a hemicube. Because of the finite resolution of the hemicube, the projected areas and resulting view factors may be overestimated or underestimated. This type of error is referred to as aliasing effects and can be reduced by increasing the value of the resolution. The value of the resolution can be adjusted by the user in order to reduce the impact of aliasing effects, as described previously. Different resolution values were used to eliminate any errors from aliasing effects. In addition to the default resolution value of 10, values of 100 and 1,000 were used. Minimal differences were noticed between the view factor values for these resolutions. As such, the final view factor values were free from aliasing effects error.

For the 9-ring model, the COR_HTR input table is used to specify radiative heat transfer paths between rods and from the racks to the rods. Note that the user manual defines the radiation constant supplied by the user, VFA, as the product of the view factor and the surface area used in calculating the radiant heat flow. However, an optional field following this factor can be supplied by the user to indicate that VFA is the view factor and the surface area is taken from the intact area of the 'from' radiating component. Therefore, VFA represents the view factor for the 'from' component. Furthermore, the outer surface area is determined from ASCELR. When radiation occurs to or from the RK component, the inner surface area is calculated as the total intact rack surface area (inside and outside) and subtracting the outer surface area (ASCELR). A summary of all radiation view factors defined in the 9-ring MELCOR models is provided in Table 5.2.

The outer edge of the peripheral assemblies in the Phase II tests (i.e., the regions farthest from the center assembly) were expected to experience relatively low temperatures. Therefore, unlike conditions pertaining in an actual reactor core, thermal conduction at the radial boundary may be significant in comparison to radiative heat losses. This factor was accounted for by using the optional COR_BCP card to add a thermal conduction path from the cladding of ring 9 to the Kaowool insulation heat structure. Note that MELCOR modeling of the rack component does not permit such a conductive path to be specified directly from the rack to the insulation, necessitating the use of cladding temperature as a surrogate (since the gradient at that location is expected to be small).

Although ballooning occurred during the Phase II experiment, MELCOR does not include the option to model ballooning of fuel cladding. Consequently, the current input model does not reflect the fact that two peripheral assemblies were pressurized with noble gas (argon) to simulate ballooning of fuel cladding.

In addition, because the fuel region is fundamentally restricted to a two-dimensional representation in MELCOR (i.e., variation of properties allowed in only the vertical and radial directions), influence of the heat loss through the rack walls of the lateral sides of the peripheral assemblies on the temperature (an azimuthal variation) cannot be properly modeled. Nevertheless, the heat losses through the side walls of the peripheral assemblies were expected to be small due to the presence of thick insulation at the corners of the 1 by 4 cell configuration. The four corners of the 3 by 3 array were packed with Kaowool insulation.

Blockage of flow paths by particulate debris was not explicitly modeled in this input, since the thermocouples were expected to be damaged prior to debris relocation, and therefore code predictions past that time were not useful for validation.

The derived values of S_{LAM} and Σk were based on the flow measurements for Phase II apparatus, which were used in the present calculations. The selected values of S_{LAM} and Σk in the center assembly are 119 and 68, respectively, and the values of S_{LAM} and Σk in the peripheral assemblies are 113 and 47.5, respectively. In order to correctly predict the heat transfer in the laminar free convection regime, the MELCOR correlations for forced convection and turbulent free convection were de-activated. Only the MELCOR correlation for laminar free convection was used for these calculations since the flows have very low Reynolds numbers.

Table 5.2 Radiation view factors used in the MELCOR model

From	To	Radiation View Factor
Rods in ring 1	Rods in ring 2	0.322
Rods in ring 2	Rods in ring 3	0.215
Rods in ring 3	Rods in ring 4	0.264
Rods in ring 4	Center Assembly Rack	0.392
Center Assembly Rack	Rods in ring 5	1.000
Rods in ring 5	Rods in ring 6	0.398
Rods in ring 6	Rods in ring 7	0.269
Rods in ring 7	Rods in ring 8	0.211
Rods in ring 8	Rods in ring 9	0.138
Rods in ring 9	Peripheral Assembly Rack	0.072

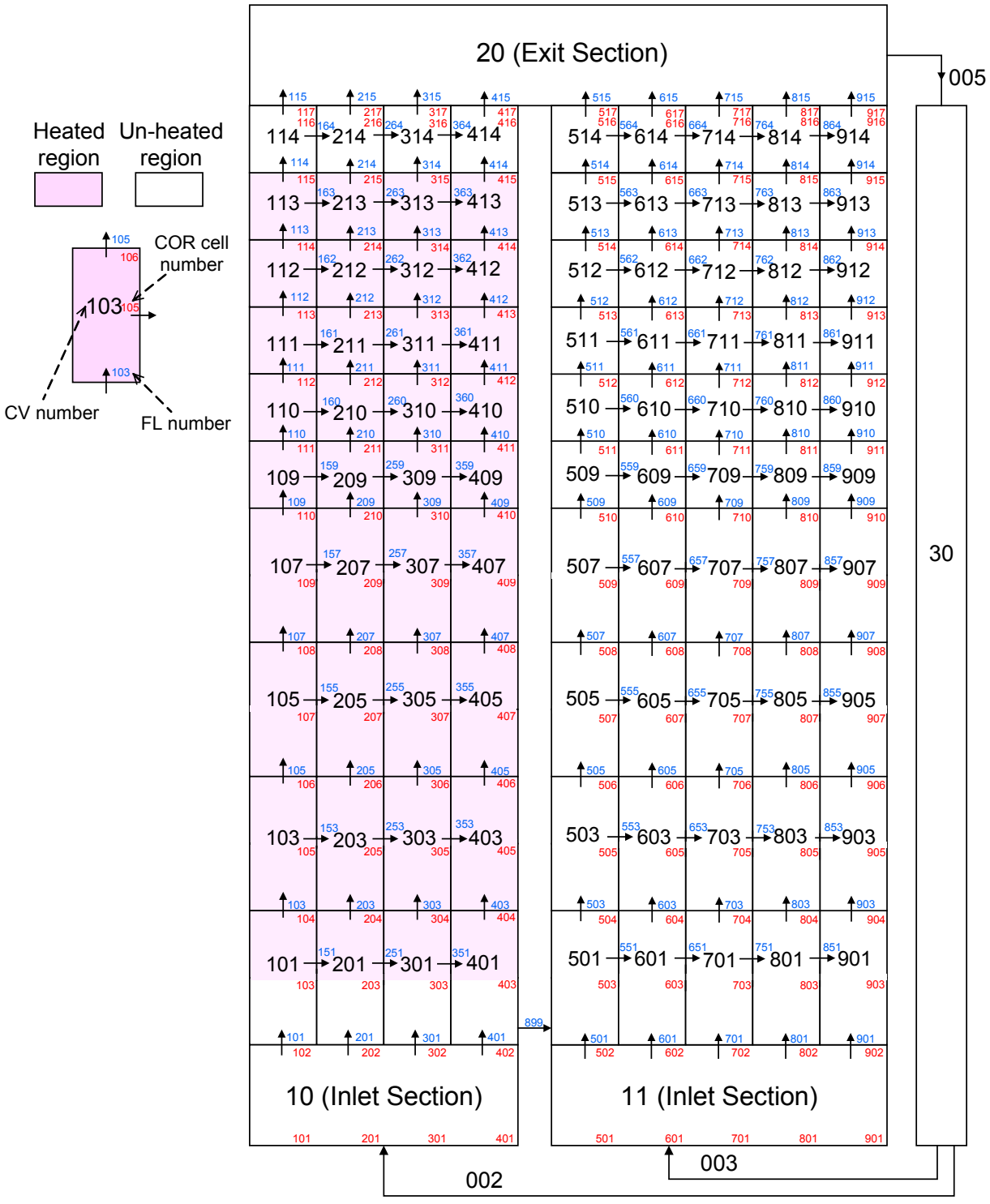

Figure 5.1 CVH and COR nodalization of PWR test assemblies in 1 by 4 configurations (side view).

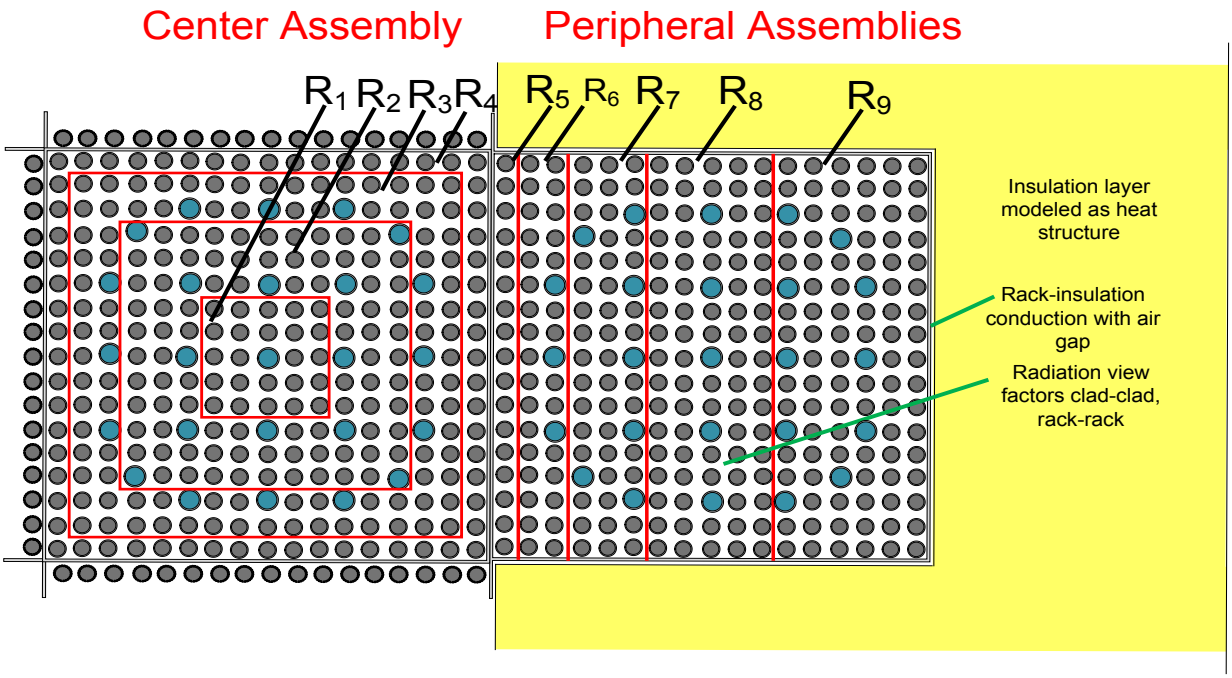

Figure 5.2 CVH and COR Nodalization of PWR test assemblies in 1 by 4 configuration (top view).

5.2.2 2-Ring Model

SNL converted the 9-ring model described above into a 2-ring model. Radially, there are two COR rings with the inner ring corresponding to the heated assemblies and the four peripheral assemblies modeled with a single outer ring (see Figure 5.3). The outer unheated assemblies are modeled in one ring having cross-sectional area equal to the sum of the cross-sectional area of all four unheated assemblies. Similarly, flow area, fuel mass, clad mass, control rod mass, and rack masses are conserved. The four inner rack walls that separate the heated assembly from the unheated assemblies is modeled as a rack component located in the inner ring and the remaining rack walls are located in the outer ring. The 2-ring model uses a total of 33 CVH control volumes and 34 flow paths as seen in Figure 5.4.

Two 2-ring input models were developed and assessed against the experimental data. The first model has only a single fuel rod type for each ring, resulting in a single temperature in that ring (at each axial node). This is the only modeling capability in the current released version of MELCOR. Consequently, MELCOR can calculate only an average fuel rod temperature for the heated assemblies and a single average for the four unheated assemblies. The second model, referred to as the 2-ring multiple rod model, utilizes new modeling features that were added to correct for current code limitations. This model allows multiple fuel rod types within each ring to better account for the temperature gradient that was observed in the experiment.

Multiple fuel rod components are modeled for both the inner assembly (4 groups) and the outer assemblies (5 groups) as seen in Figure 5.5. When the multiple rod/ring model is invoked, the nodalization is similar to the 9-ring model described above where now rod groups in the 2-ring multiple rod model correspond to rings in the 9-ring model.

While the intent is to have the 2-ring multiple rod model as similar as possible to the 9-ring model, it is recognized that there are still some modeling differences. One important difference between the two models is that each COR cell in the 9-ring model has a separate CVH control volume, while in the 2-ring multiple rod model, all fuel rod types for a given COR cell share the same CVH control volume. As an example, consider the four fuel rod types in the new 2-ring multiple rod model. While each fuel rod can have a unique temperature (at a given COR cell), all of these rods will see the same air temperature and velocity. In the 9-ring model, each of the associated four fuel rods can see a different air temperature and velocity. In the peripheral region, this can lead to natural circulation flow patterns that cannot be obtained in a 2-ring model where there is only a single flow path through the assemblies. As an example, one such flow pattern that has been observed in the MELCOR runs is in the peripheral region where air flow is upwards in ring 5 (closest to the center heated assembly) and downward in ring 9 (farthest from the center heated assembly). These natural circulation flow patterns affect the heat transfer early in the transient when convective heat transfer is still the dominate heat transfer mode and is responsible for some of the differences seen between the 2-ring multiple rod and 9-ring models.

The 9-ring and 2-ring multiple rod model use different approaches for specifying and calculating the radiant heat exchange between components. For the 9-ring model, view factors are specified on the COR_HTR records as user defined heat transfer paths and radiant heat transfer is calculated in subroutine COR_HTR. For the 2-ring multiple rod model, view factors are specified on the COR_ROD_VF records and radiant heat transfer is calculated from the COR_CORRAD subroutine. The same view factors that were applied in the 9-ring model were used in the 2-ring multiple rod model.

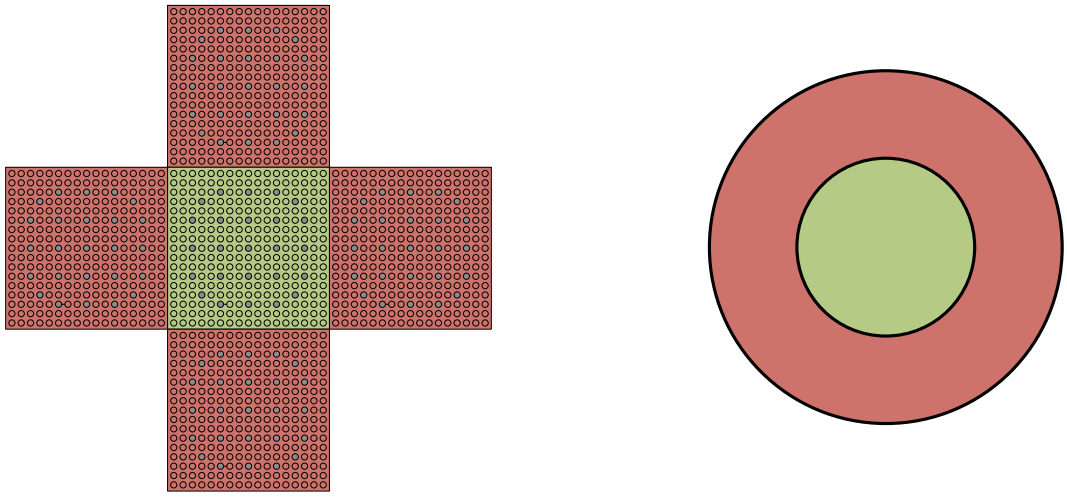

Experiment Geometry **MELCOR Geometry**

Figure 5.3 MELCOR radial layout of 2-ring model

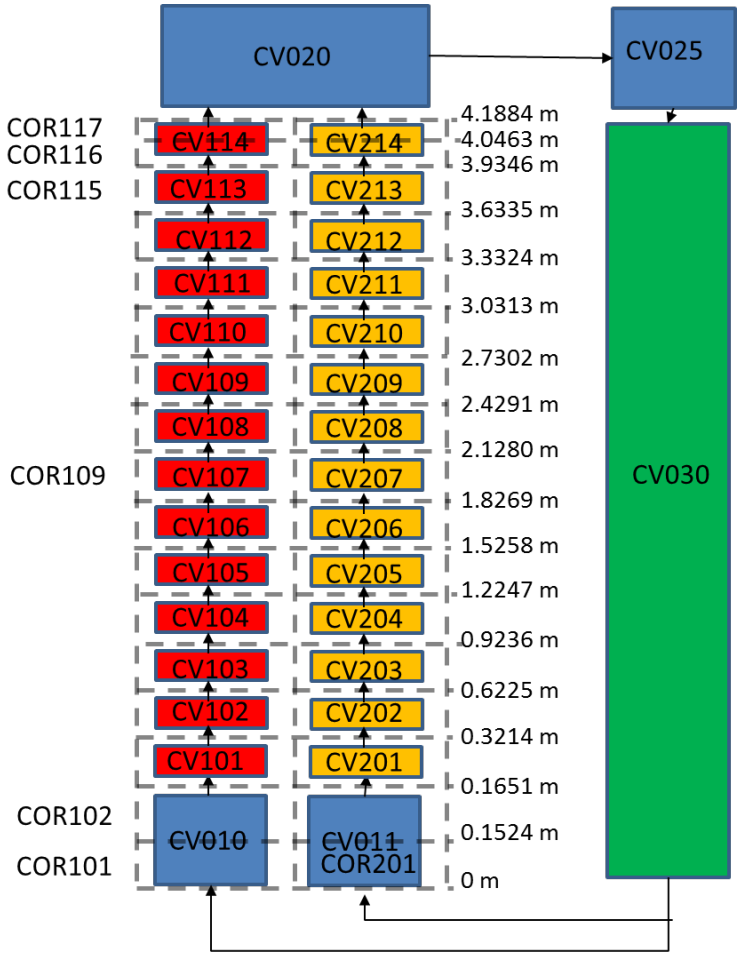

Figure 5.4 MELCOR 2-ring model nodalization

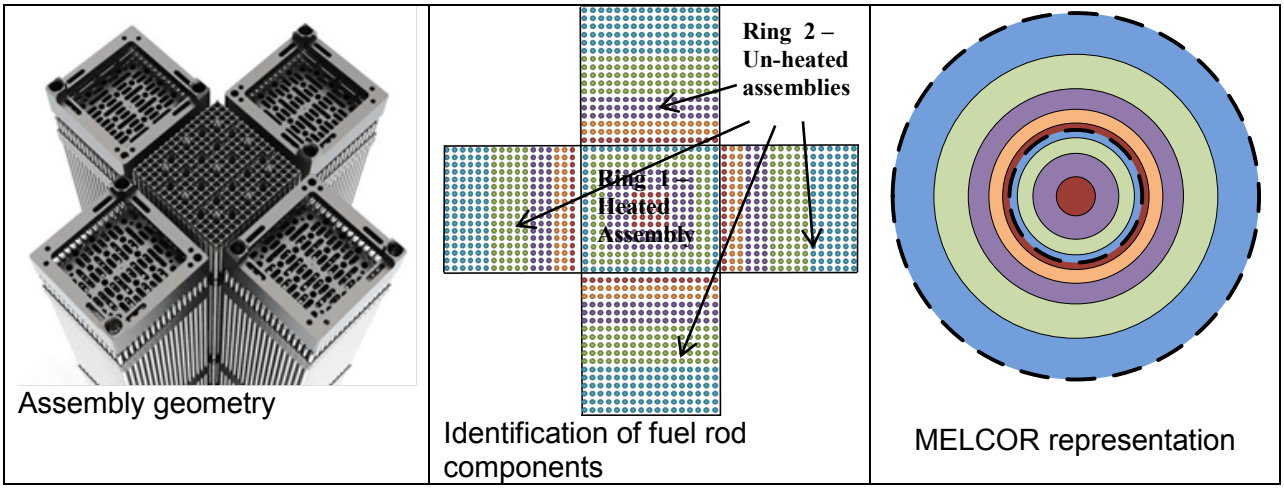

Figure 5.5 MELCOR 2-ring 9-rod Model of the PWR SFP Experiment

5.2.3 Oxidation Kinetics

The oxidation kinetics of zirconium in air is governed by the formation of high density zirconium nitride, resulting in the development of cracks that expose additional surface area for reaction with oxygen (i.e., breakaway). In addition, separate effect tests have shown the potential for strong breakup of the oxide crust under conditions of oxidation in pure air, resulting in enhanced oxidation rates, and therefore, to temperature excursions at the elevation of the breakup and following starvation of the oxidant. In the experiment, the crust breakup at different axial and radial nodes of the assembly was the starting point for the fuel heatup leading to ignition of the zirconium fire. Generally, ignition started in the upper region of the fuel assembly and subsequently, oxidation propagated downward into the assembly.

In MELCOR, metal oxidation is calculated using standard parabolic kinetics, with appropriate rate constant expressions for Zircaloy and steel, limited by gaseous diffusion considerations if necessary. The default treatment of breakaway is based on a simplified air oxidation model which is coupled with a breakaway model that has been based on an empirical fit to Argonne National Laboratory (ANL) experimental data (Ref. 13) as seen in Figure 5.6. The calculation of the breakaway oxidation reaction using a cumulative lifetime fraction (LF) function is defined in Equation 5.1.

$$LF(t) = \int_{o}^{t} \frac{dt}{\tau(T)} \qquad 5.1$$

The MELCOR breakaway oxidation model calculates the lifetime function at every node in the model with Zircaloy cladding. At a critical value of the lifetime fraction (LF=1.0), the transition to breakaway is assumed to begin. The transition to post-breakaway oxidation kinetics is completed when LF=1.2. The instantaneous breakaway lifetime τ(T) (in seconds) as a function of temperature T (in K) is given in Equation 5.2.

$$\tau(T) = 10^{-12.528 \log_{10} T + 42.038} \qquad 5.2$$

The coefficients in Equation 5.2 were obtained by log-linear regression on experimental data obtained in tests performed at ANL and are necessarily subject to some uncertainty due to measurement error and to scatter in the data. As seen in Figure 5.6, there is a rather large uncertainty in the breakaway time. Variations within the ANL experimental data were assumed to be ±0.626, i.e. the 95 percent confidence level as determined by the product of a two-sided t-student distribution (2.365) and the standard error of the curve fit (0.265). As a result, a lower and upper bound were obtained on the second term of the exponent in Equation 5.2 between 41.412 and 42.664, respectively.

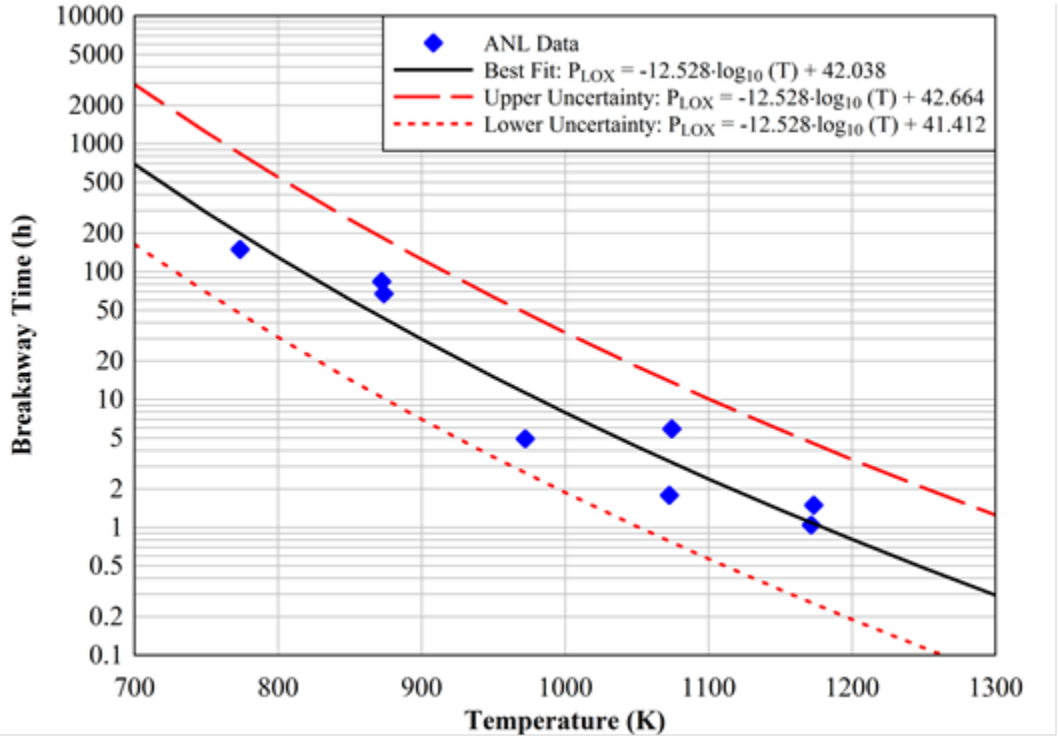

Figure 5.6 Comparison of the MELCOR breakaway timing fit to Zr-4 data.

5.3 Code Improvements

MELCOR Version 2.1.5287 was used as the starting point for the code modifications. This version includes the rack component in the COR package for modeling the spent fuel pool rack as well as the Sandia breakaway oxidation kinetics model allowing the code to predict the transition to breakaway oxidation in an air environment on a node-by-node basis. Furthermore, while it was not developed as part of this project, this code version contains the Paul Scherrer Institute (PSI) air oxidation models for breakaway (Ref. 15). It should be noted that the MELCOR COR package is the set of routines that models the components found in a reactor core. Because of similarities and flexibility in the code modeling, MELCOR can also be used for modeling the spent fuel pool assemblies and the user input distinguishes this configuration from an reactor core.

The conditions of this experiment challenge the MELCOR approach to representing an assembly (or collection of assemblies) with a single MELCOR node (or ring) consisting of a single lumped parameter representing all fuel rods in that node. In particular, a single representative temperature for the fuel rods in the unheated assembly is insufficient to capture the large temperature gradients and the dependence of oxidation rates on the local clad temperature. This is more readily understood when examining the temperatures measured in the unheated peripheral assemblies as shown in Figure 5.7 and the temperature contours as seen in Figure 4.8. Prior to ignition, the temperature of fuel rods near the interface with the heated assembly is almost 400 K [720°F] higher than it is for rods at the outer boundary of the assembly. The peak temperatures adjacent to the heated assembly are about 700 K [800°F] while the average temperature (which would be modeled by MELCOR using a 2-ring model) is only 450 K [350°F]. This large temperature gradient is particularly significant given that oxidation is highly temperature dependent and the oxidation reaction generates heat that then contributes further to the burn. For example, the oxidation rate at 700 K [800°F] is several orders of magnitude greater than it is at the average temperature of 550 K [530°F]. If MELCOR

were modeling the assembly with a single node (as is done in the 2-ring model), the average cell temperature would be used in calculating the oxidation rate in that ring. This would significantly underestimate the oxidation that occurs in the unheated assembly and would therefore also underestimate the associated heat generation.

Consequently, the MELCOR code was modified to allow improved temperature refinement within a single radial ring by providing a means for the user to specify multiple fuel rod types within that ring. As modified, the user can now specify up to five fuel rod types in each radial ring. For example, in the peripheral region, a single fuel rod type can be used to represent the row of rods closest to the rack that divides the center assembly from the peripheral assemblies. Additional rod types can be defined with coarser nodalization for rods as they move closer to the outer rack.

The input for these new fuel rod types (currently limited to five) is rather simple. The user specifies the total fuel rod masses, control rod masses, and areas for a ring, just as before. However, new inputs are used to specify mass fractions for each fuel type, mass fractions for each control rod type, and view factors connecting fuel rods.

The models are currently strictly valid up until material begins to relocate which is sufficient for the present experimental validation of the code. This is acceptable given the test data is generally unavailable after ignition due to failures of the thermocouples at elevated temperatures. Further model development and refinement are necessary to allow relocation of different fuel rod types for spent fuel pool accident progression analysis and before becoming part of an official release version of MELCOR.

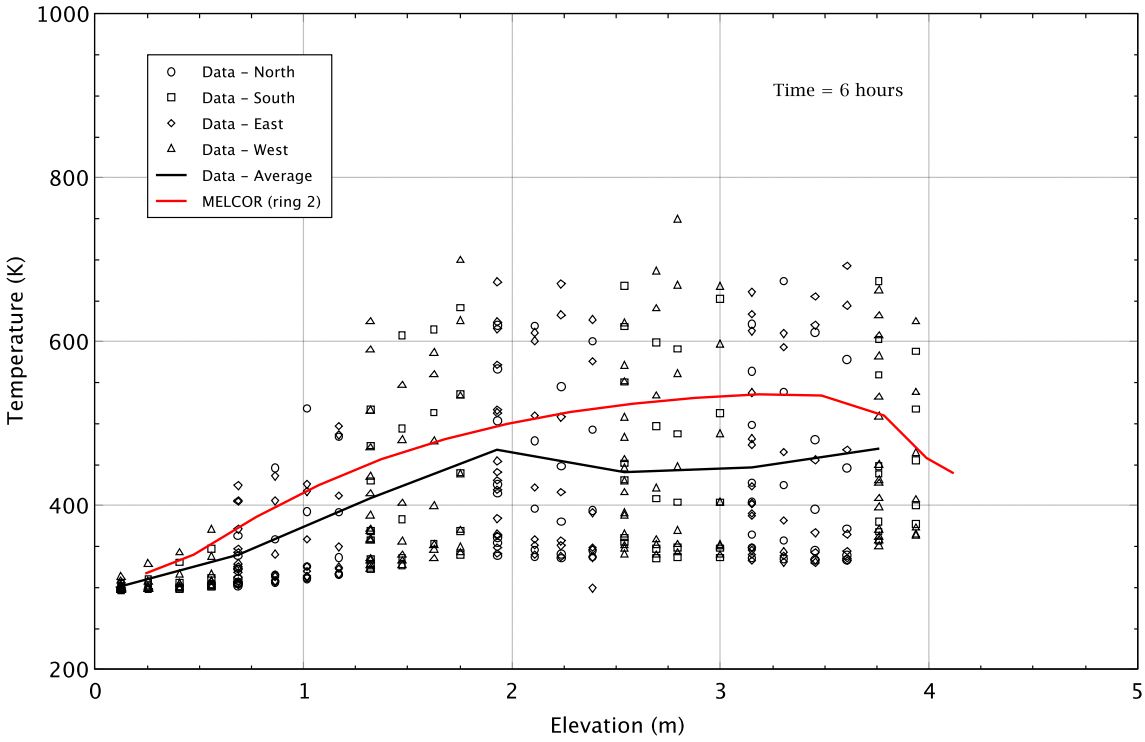

Figure 5.7 Cladding temperatures in peripheral assemblies for 15 kW ignition test at 6 hours

5.4 Pre-Ignition Tests

As described previously, there were nine pre-ignition tests performed at power levels ranging from 1 kW to 15 kW. MELCOR runs were made for all power levels using each of the three MELCOR models described in Section 5.2. The three MELCOR models include: 1) 2-ring, 2) 2-ring multiple rod/ring and 3) 9-ring. Modeling assumptions were as similar as possible for each calculation, though it is recognized that there may still be small modeling differences. Given the number of MELCOR simulations and the fact that most show the same phenomena, not all runs will be described and only selected results will be presented to demonstrate different topics of interest.

5.4.1 1 kW pre-ignition

The 1 kW pre-ignition test was run for 24 hours in an attempt to achieve steady state conditions. Figures 5.8 and 5.9 show the peak cladding temperature in the central and peripheral assemblies respectively for both 2-ring models and the 9-ring model. While close to steady state, the temperature is still increasing slightly at 24 hours in both the experiment and MELCOR simulations. For the experimental data, the PCT is computed as the maximum temperature observed at all locations in the assembly and may move from fuel rod to fuel rod as the transient progresses. For MELCOR, the PCT is a misnomer and is actually an average for a group of rods. For example, in the 9-ring model ring 1 contains 24 fuel rods (see Figure 5.2) that all must have the same temperature given they are all lumped together into a single rod component. By definition, the average temperature in a group of rods will be lower than the peak, so it is expected that the MELCOR PCT will generally be lower than the experimental data PCT.

In the center heated assembly, the MELCOR results show good agreement with the peak cladding temperature. In the peripheral assemblies, the 2-ring model shows poor agreement with the experimental data, while the other models show reasonable agreement. In all the MELCOR results, the heat from the center assembly rods is transferred to the rack by convection and radiation, then to the peripheral assembly rods by radiation only. The lack of convective heat transfer from the center assembly rack to the peripheral rods is a known limitation of the MELCOR code. Given the initial small temperature difference between the center assembly rods, rack and peripheral rods, the initial radiation heat transfer is close to zero. With little to no radiation and no convective heat transfer, the MELCOR prediction of PCT in the peripheral rods initially lags that of the test data. Once the center assembly rods and rack heat up, radiation heat transfer begins to dominate and the MELCOR calculations (2-ring multiple rod and 9-ring) show the PCT surpass that of the test data and generally show good agreement. However, the 2-ring model shows the PCT lagging significantly behind the test data. The peripheral temperature response in the 2-ring model lags that of the other two MELCOR models due to the fact that all of the peripheral rods must be heated up as opposed to only the first row of rods in the 2-ring multiple rod and 9-ring models.

Figures 5.10 and 5.11 show the central and peripheral temperature as a function of elevation for the 2-ring and 2-ring multiple rod models at 24 hours. While the MELCOR models show good agreement for the peak temperatures, both the 2-ring and 2-ring multiple rod model in general over predict the temperatures in the central heated assembly. The 2-ring multiple rod model shows a temperature difference of ~15 K [27°F] between the hottest and coldest rod in the center assembly, while the test data shows a difference of ~60 K [108°F]. In general, all the MELCOR results show that the temperatures in the center assembly are more tightly coupled together than observed in the test data. Examination of the test data show that the coldest rods in the center assembly are located in and around the corners. Given that the two-dimensional

MELCOR model does not allow for azimuthal variations, there are no rods in the MELCOR model which are in “corner” locations. Figures 5.12 and 5.13 show the central and peripheral temperatures as a function of elevation for the 9-ring model. These results are similar to the 2-ring multiple rod model.

The induced volumetric flow rate is shown in Figures 5.14 and 5.15 for the center and peripheral assemblies respectively. All three of the MELCOR calculations show the flow rate is over predicted in the center assembly. In the peripheral assemblies, the MELCOR calculations show the flow rate is under predicted. Note that while not shown in the Figures, the uncertainity in the experimental data is ±12 slpm for each assembly. Also note that the hot wire anemometers were generally unresponsive below 50 slpm/assembly. The differences in flow rate are mainly due to the use of constant loss coefficients S_{LAM} and Σk. Sensitivities on the use of constant versus variable loss coefficients are described in more detail in Section 5.6.1.

5.4.2 8 kW pre-ignition test

The 8 kW test was run for 12 hours and stopped prior to the center assembly PCT reaching 900 K [1,160°F]. Figures 5.16 and 5.17 show the peak cladding temperature in the central and peripheral assemblies respectively for both 2-ring models and the 9-ring model. In the center heated assembly, the MELCOR results for the 2-ring multiple rod and 9-ring model show excellent agreement with the peak cladding temperature. As expected, the 2-ring model somewhat underpredicts the peak cladding temperature. In the peripheral assemblies all MELCOR runs show a delayed increase in temperature similar to that in the 1 kW test.

Figures 5.18 and 5.19 show the central and peripheral temperature as a function of elevation for the 2-ring and 2-ring multiple rod models at 12 hours. In general, the 2-ring multiple rod model over predicts the temperatures in the center assembly similar to the 1 kW case. In the peripheral region, the 2-ring model temperature is in good agreement with the experimental average temperature. The 2-ring multiple rod model shows a good temperature distribution between the inner and outer most rods and somewhat overpredicts the temperatures relative to the data. Figures 5.20 and 5.21 show the central and peripheral temperature as a function of elevation for the 9-ring model. These results are similar to the 2-ring multiple rod model as expected.

The induced volumetric flow rate is shown in Figures 5.22 and 5.23 for the center and peripheral assemblies respectively. All of the MELCOR calculations show the flow rate is over predicted in the center assembly. However, the MELCOR flow rates in the center assembly for the 8 kW test show better agreement than the results from the 1 kW test. In general, the MELCOR center assembly calculated flow rates better match the experimental data as the power level increases. In the peripheral assemblies, the MELCOR calculations show the flow rate is initially under predicted, then over predicted. Note that the experimental data shows an initial flow rate just under 200 slpm which is believed to be in error as the flow was zero at the start of the experiment. The hot wire anemometers were generally unresponsive/errant below 50 slpm/assembly (200 slpm total for the four peripheral assemblies). In the peripheral assemblies, above 200 slpm (total for all four assemblies), the experimental data for this test shows the same overall trends and falls in line with the other pre-ignition tests measured flow rate, giving some confidence that the data is within the ±12 slpm/assembly instrument uncertainty. Similar to the 1 kW test described above, the differences in flow are mainly due to the use of constant loss coefficients S_{LAM} and Σk. Sensitivities on the use of constant versus variable loss coefficients are described in more detail in Section 5.6.1.

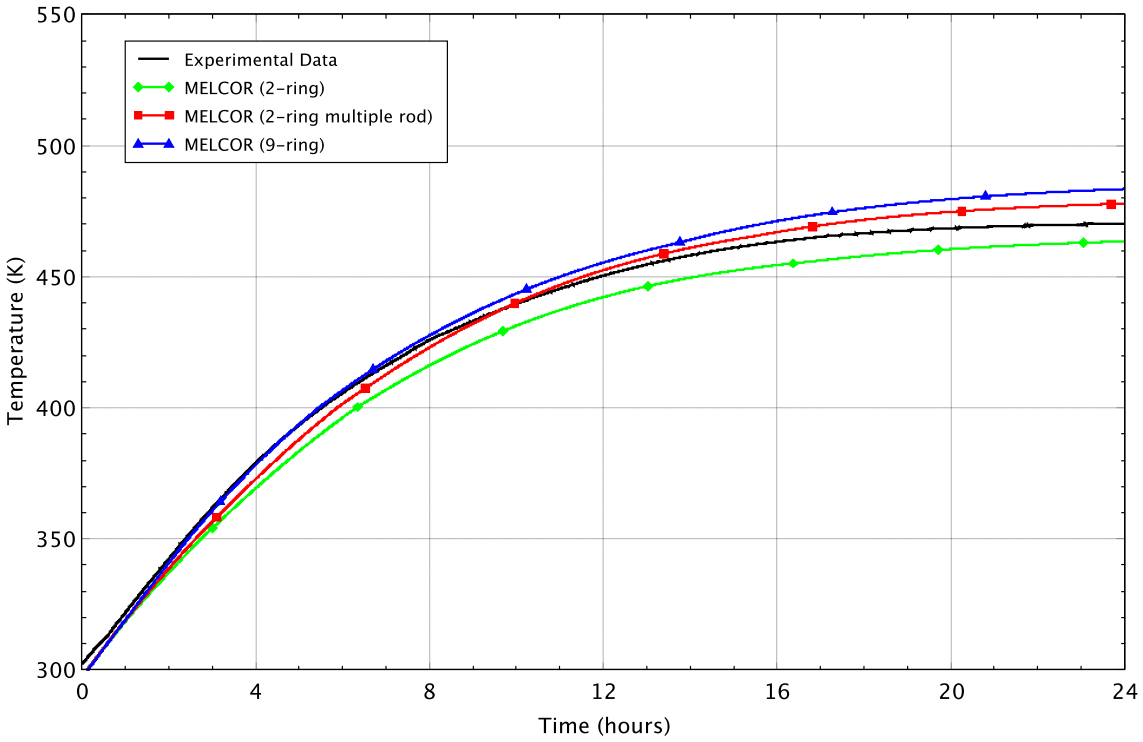

Figure 5.8 Center assembly peak cladding temperature for the 1 kW pre-ignition test

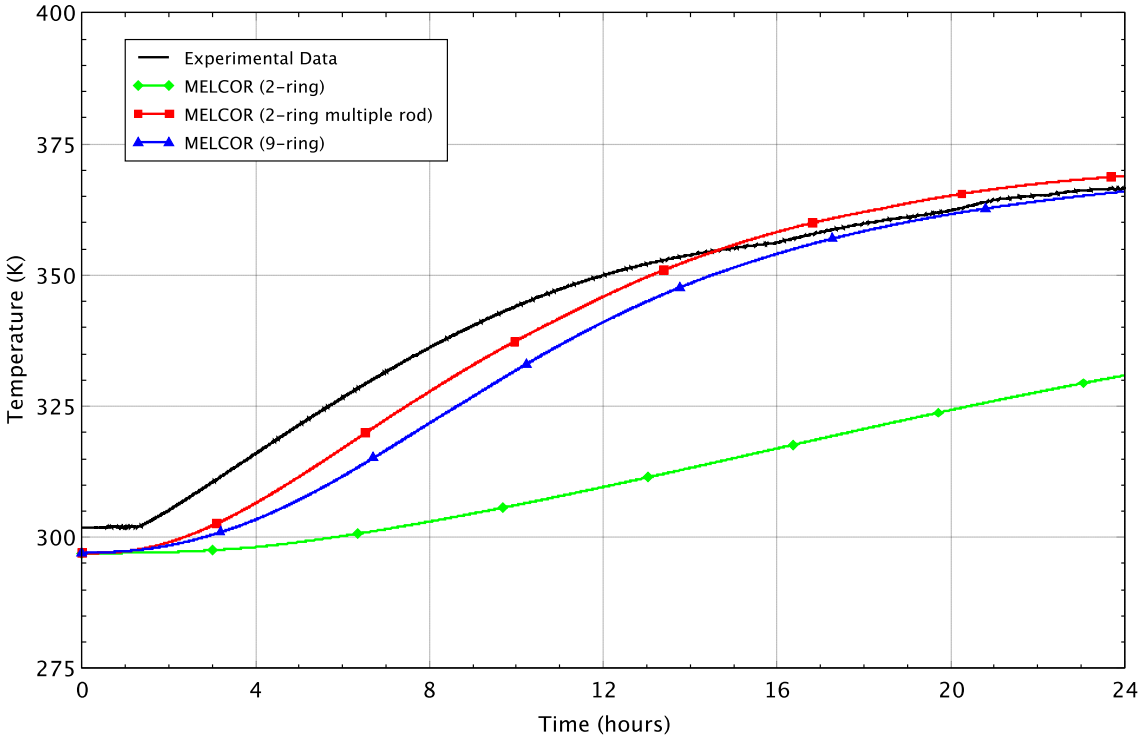

Figure 5.9 Peripheral assembly peak cladding temperature for the 1 kW pre-ignition test

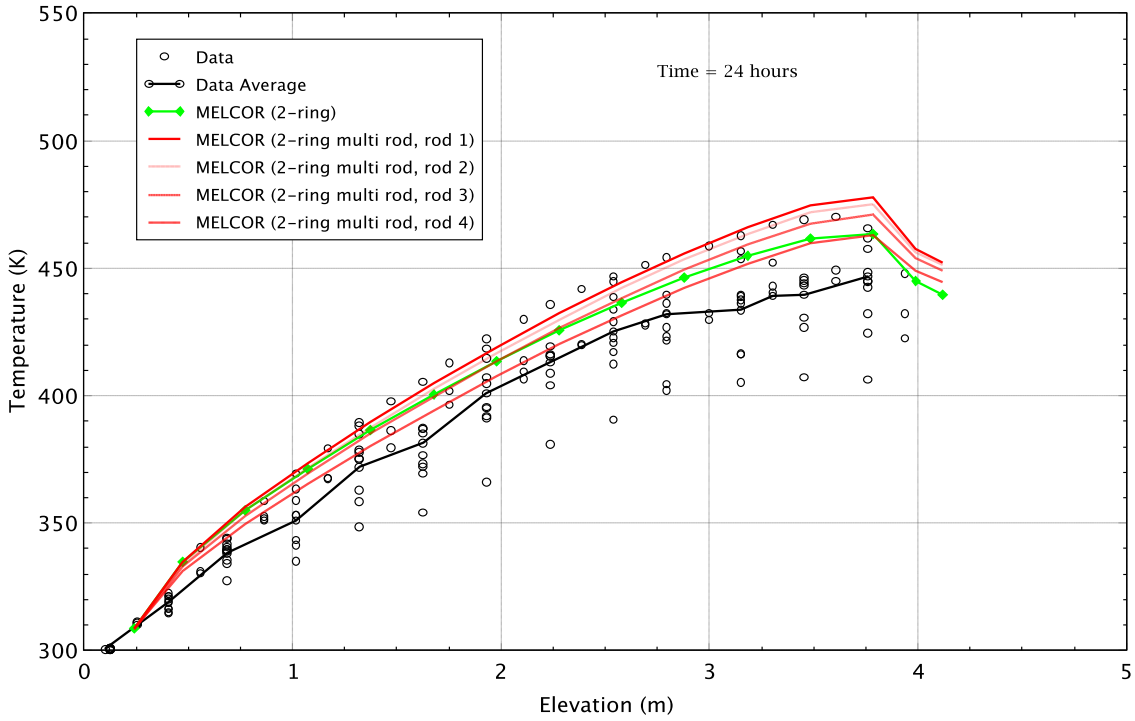

Figure 5.10 Central assembly temperature versus elevation for the 1 kW pre-ignition test at 24 hours

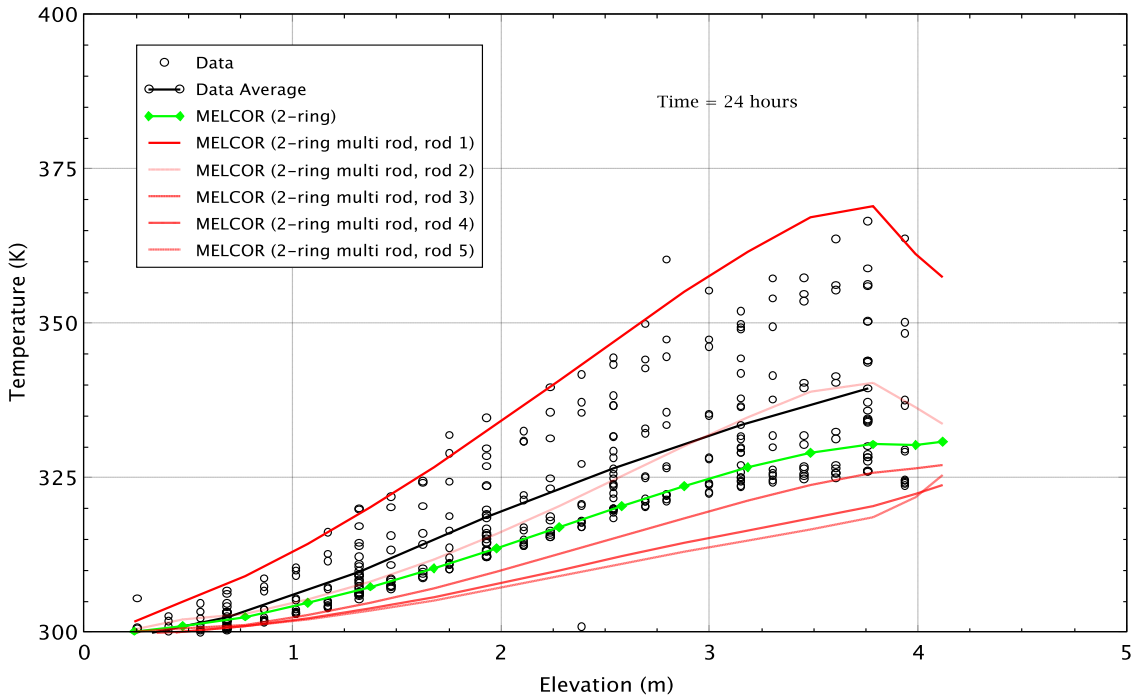

Figure 5.11 Peripheral assembly temperature versus elevation for the 1 kW pre-ignition test at 24 hours

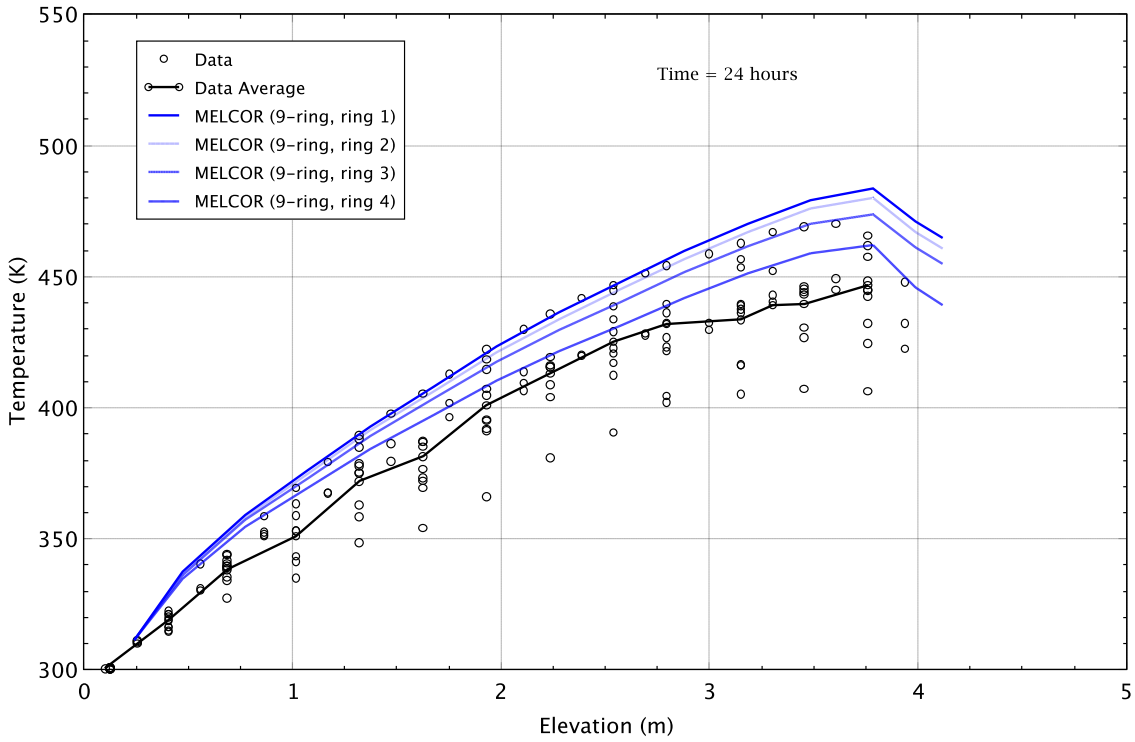

Figure 5.12 Central assembly temperature versus elevation for the 1 kW pre-ignition test at 24 hours

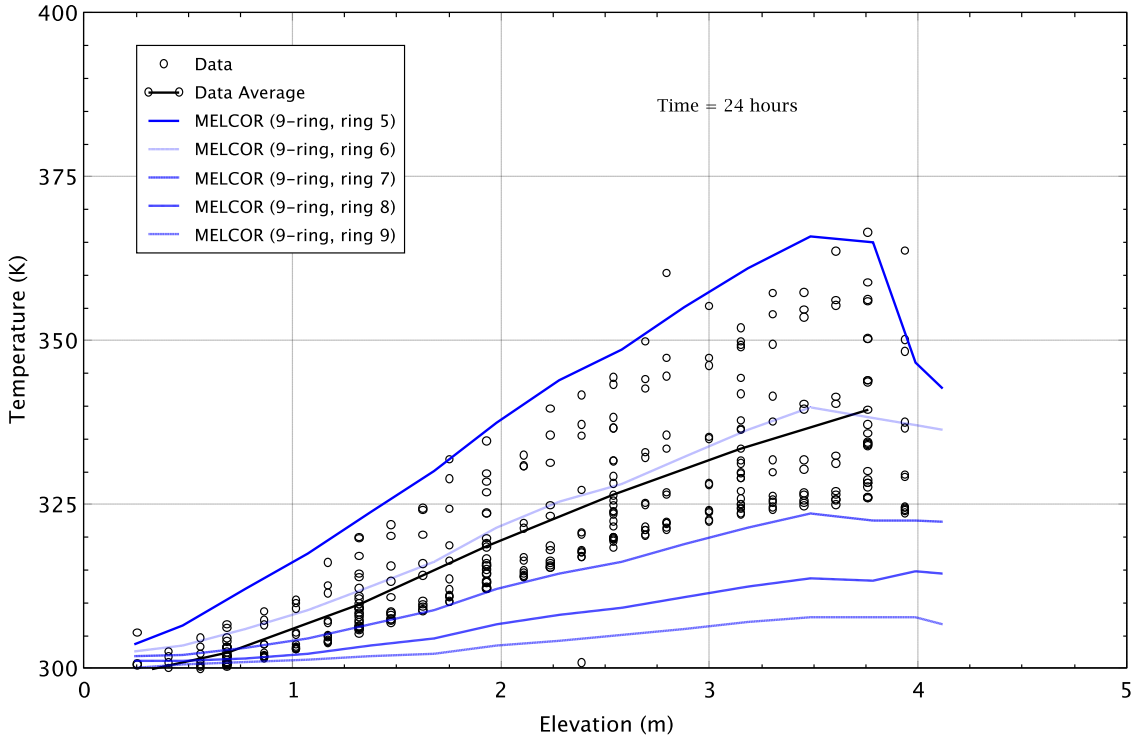

Figure 5.13 Peripheral assembly temperature versus elevation for the 1 kW pre-ignition test at 24 hours

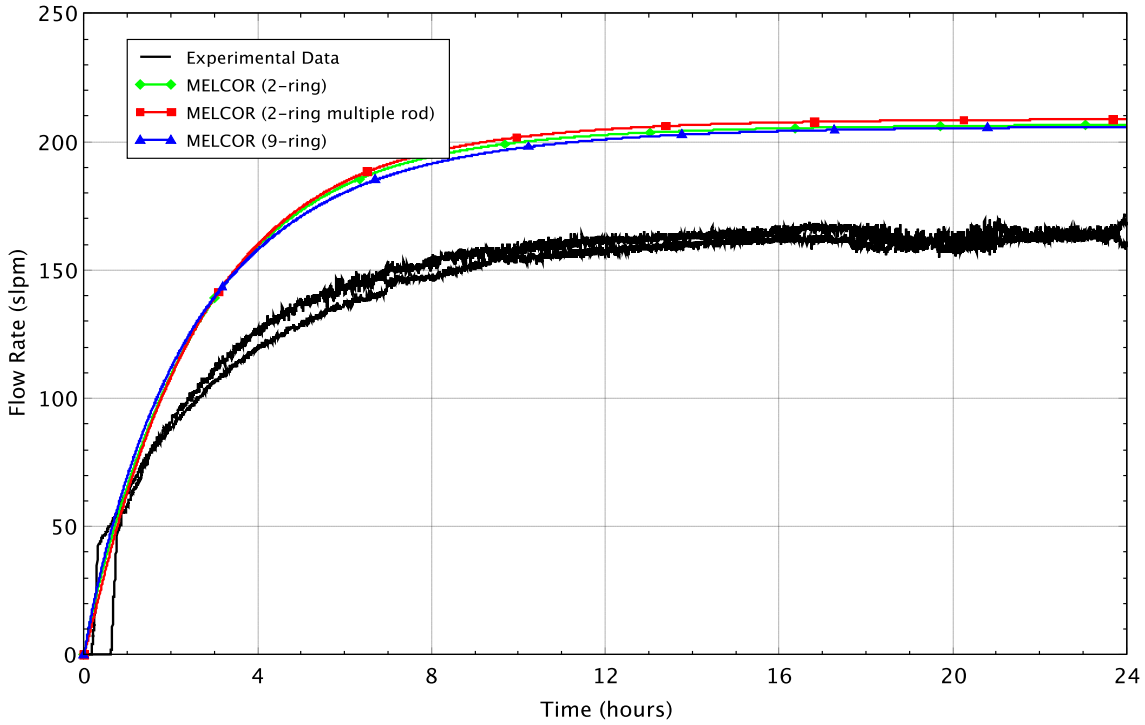

Figure 5.14 Central assembly volumetric flow rate for the 1 kW pre-ignition test

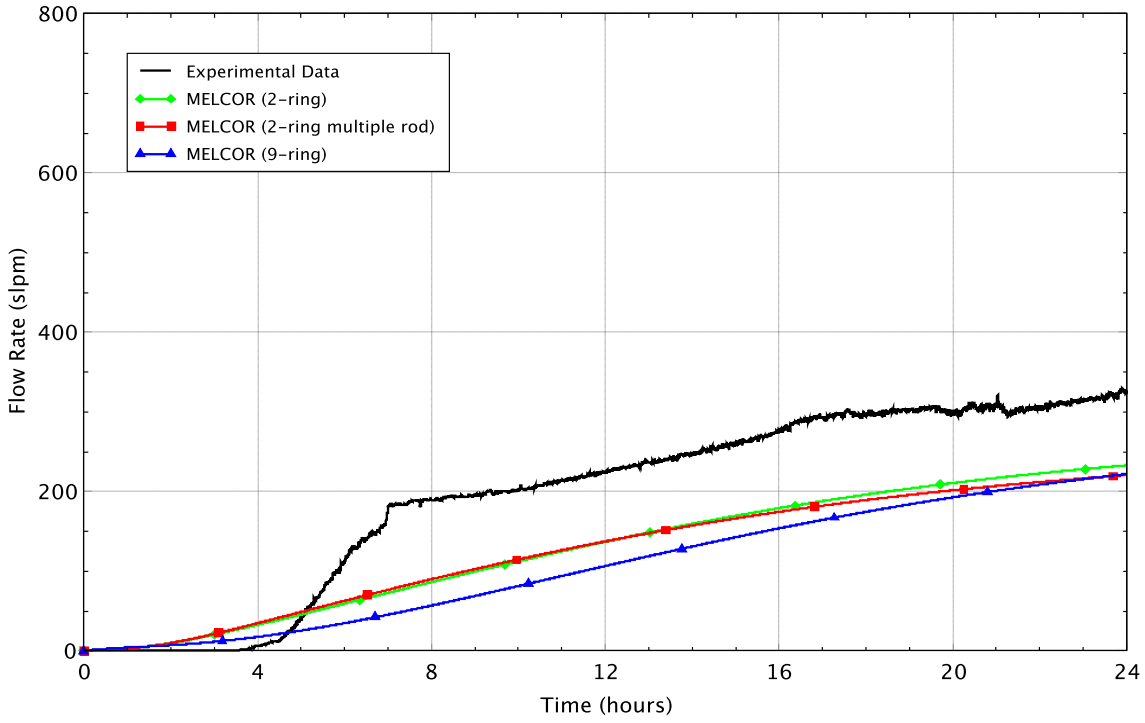

Figure 5.15 Total peripheral assembly volumetric flow rate for the 1 kW pre-ignition test

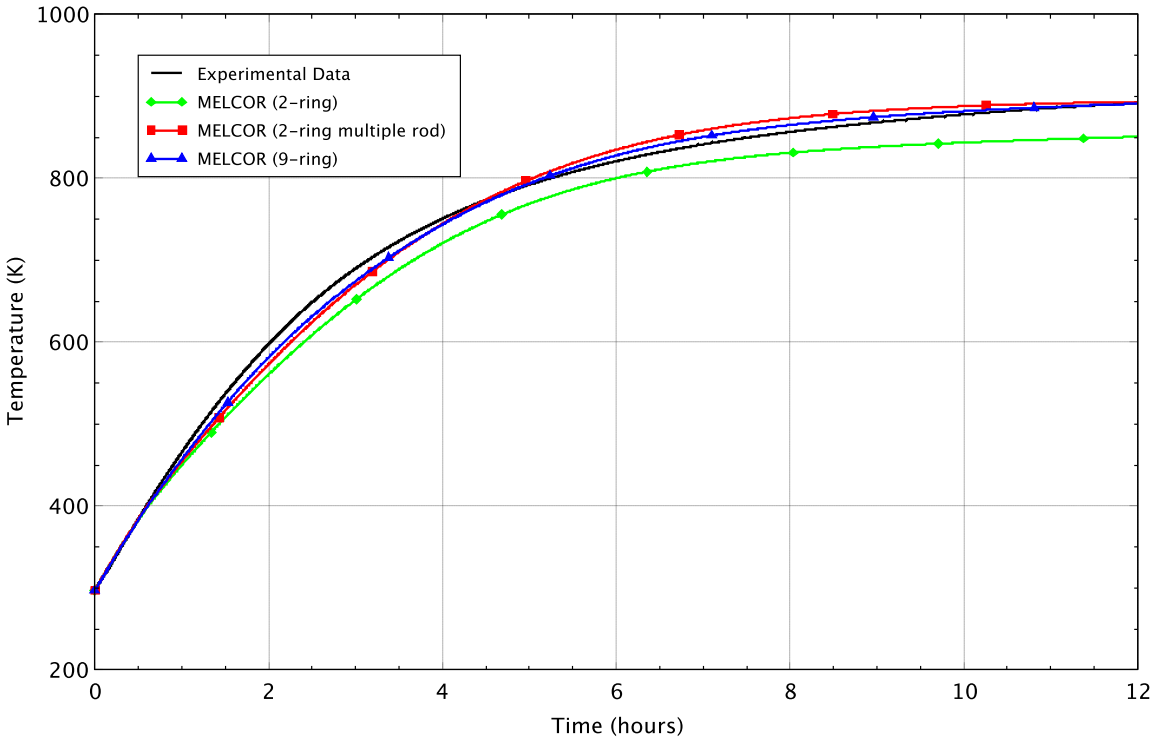

Figure 5.16 Center assembly peak cladding temperature for the 8 kW pre-ignition test

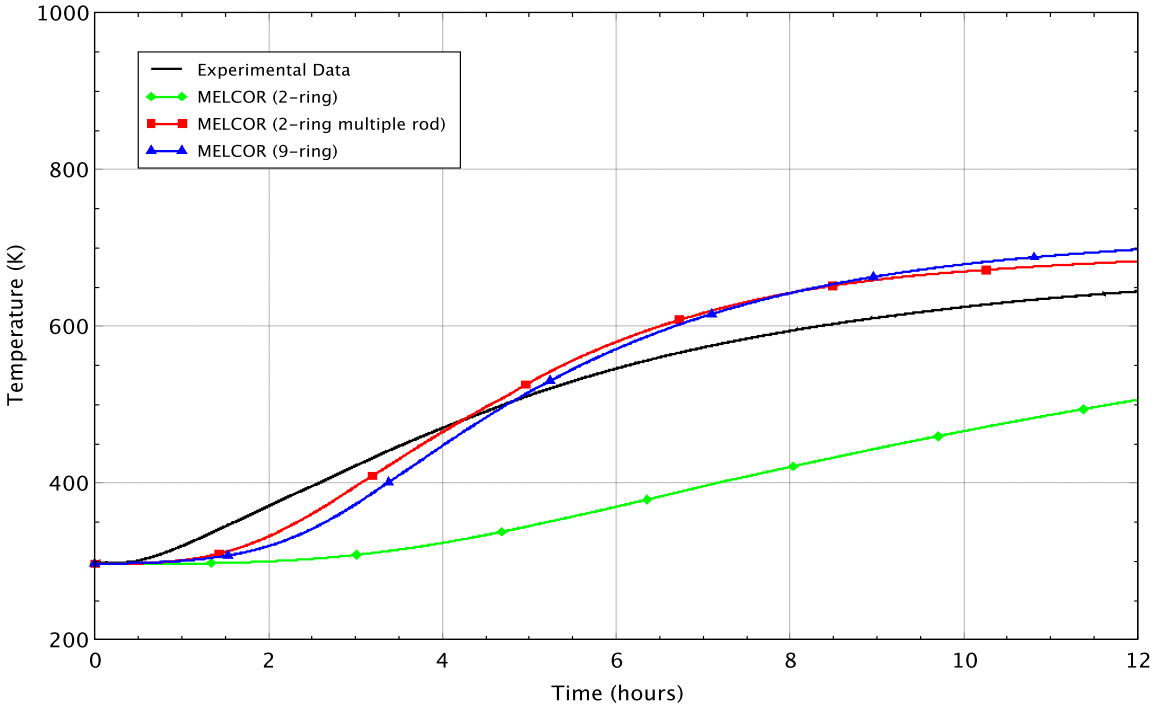

Figure 5.17 Peripheral assembly peak cladding temperature for the 8 kW pre-ignition test

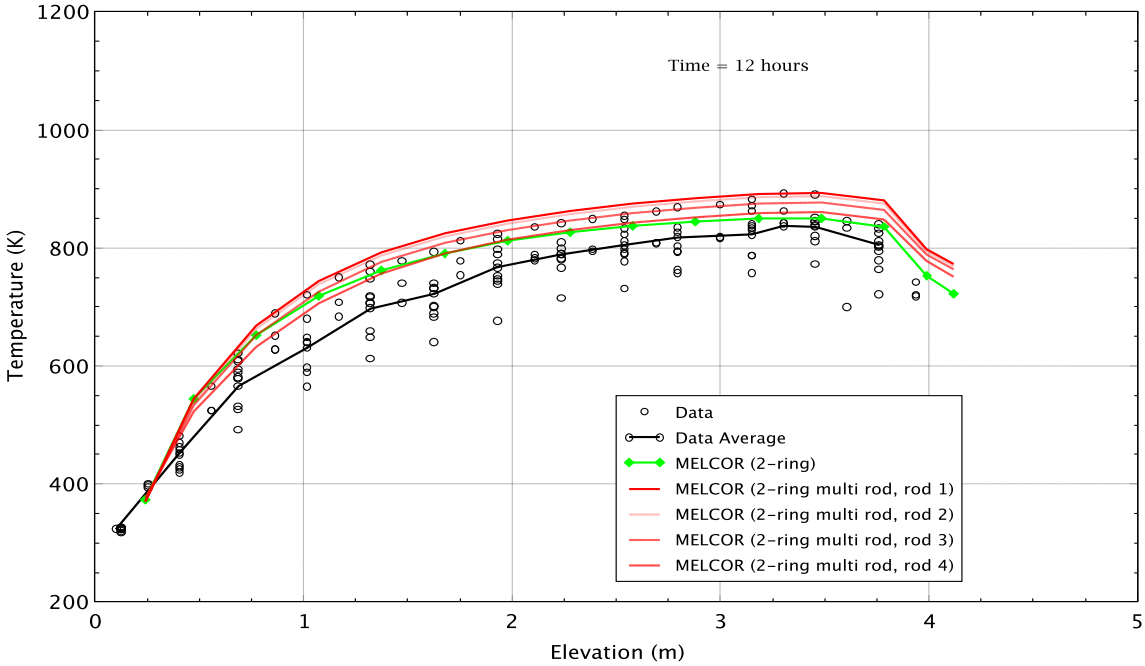

Figure 5.18 Central assembly temperature versus elevation for the 8 kW pre-ignition test at 12 hours

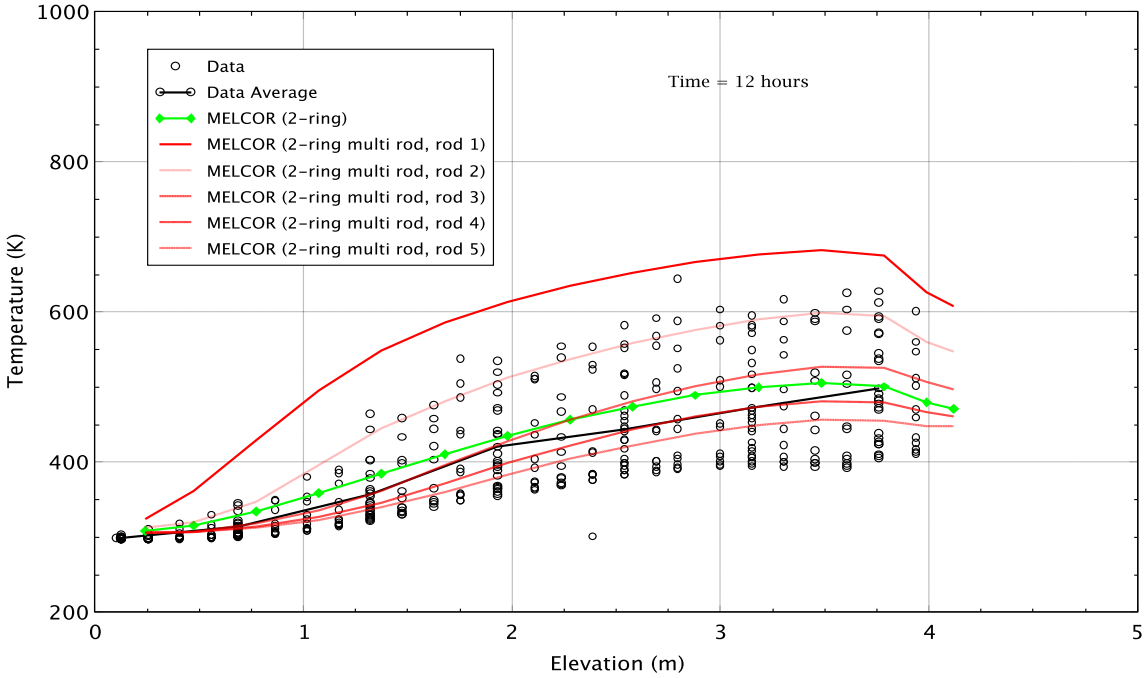

Figure 5.19 Peripheral assembly temperature versus elevation for the 8 kW pre-ignition test at 12 hours

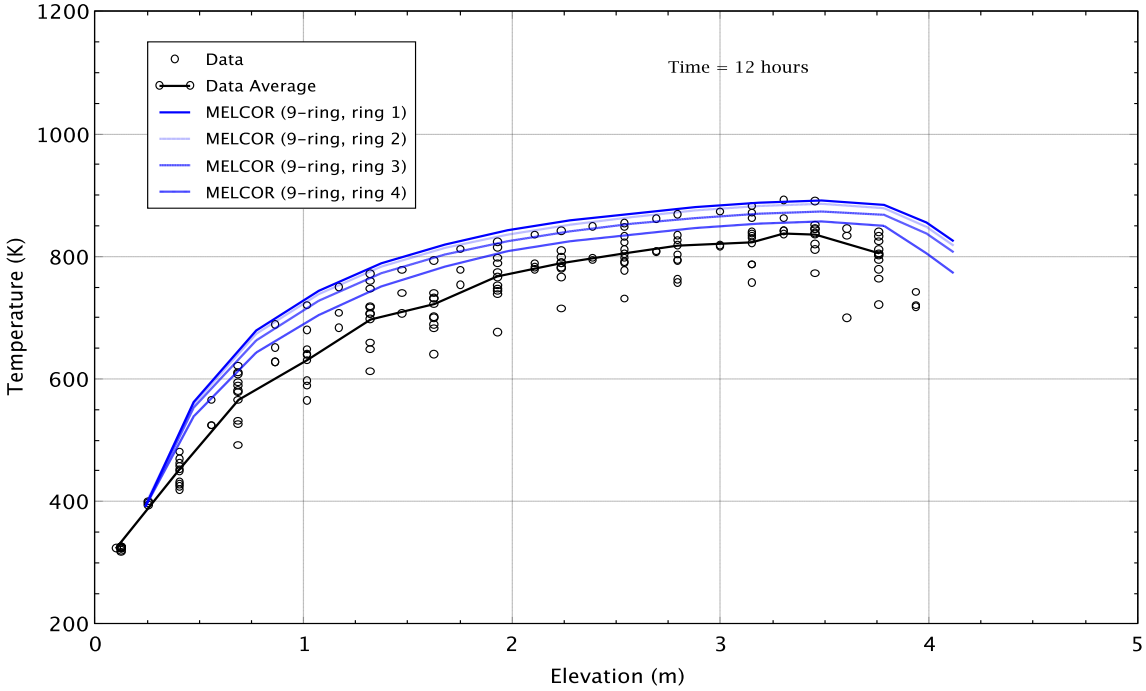

Figure 5.20 Central assembly temperature versus elevation for the 8 kW pre-ignition test at 12 hours

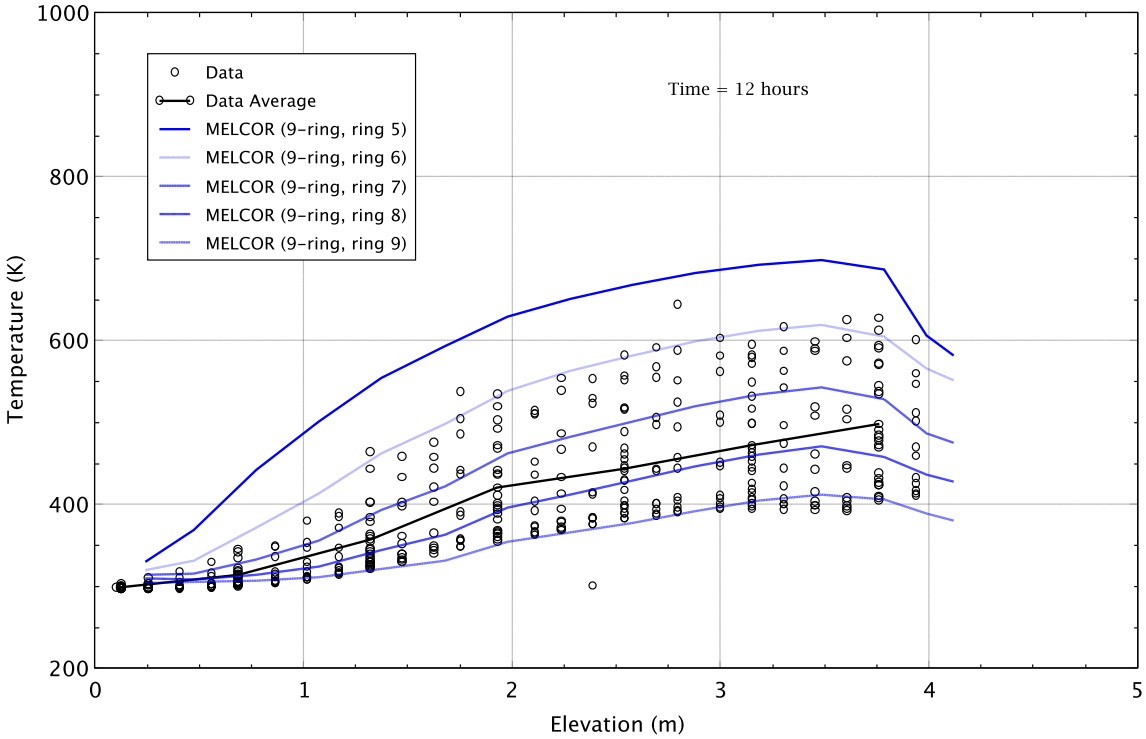

Figure 5.21 Peripheral assembly temperature versus elevation for the 8 kW pre-ignition test at 12 hours

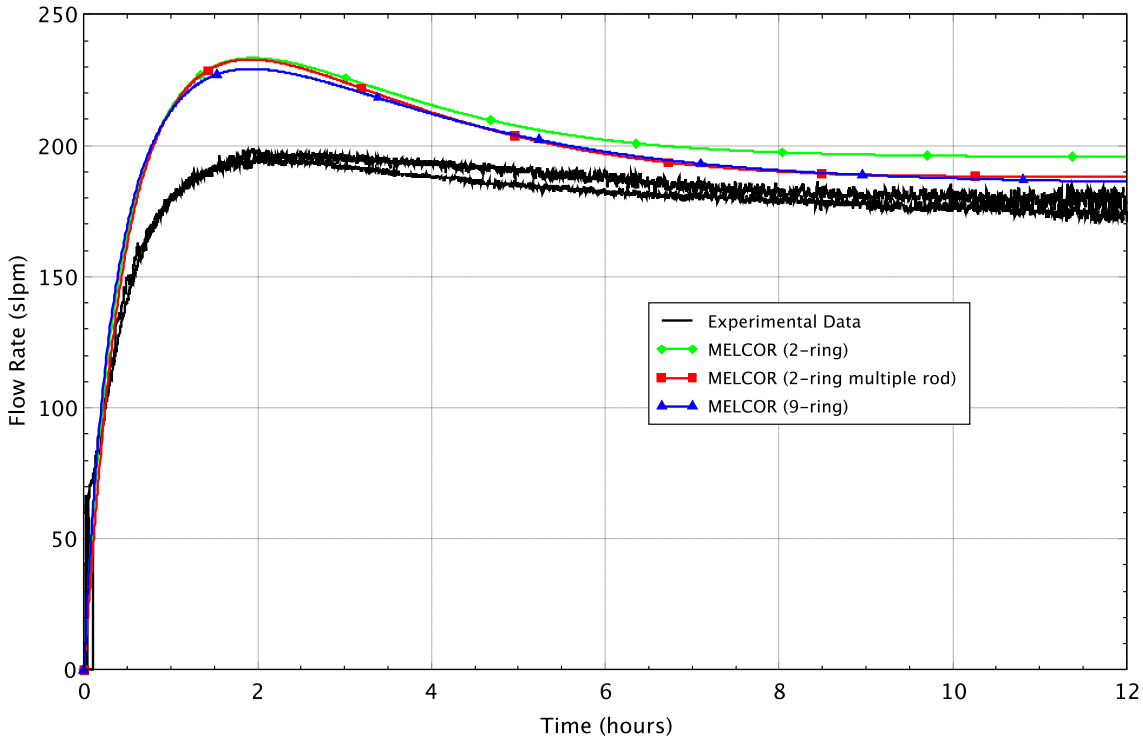

Figure 5.22 Central assembly volumetric flow rate for the 8 kW pre-ignition test

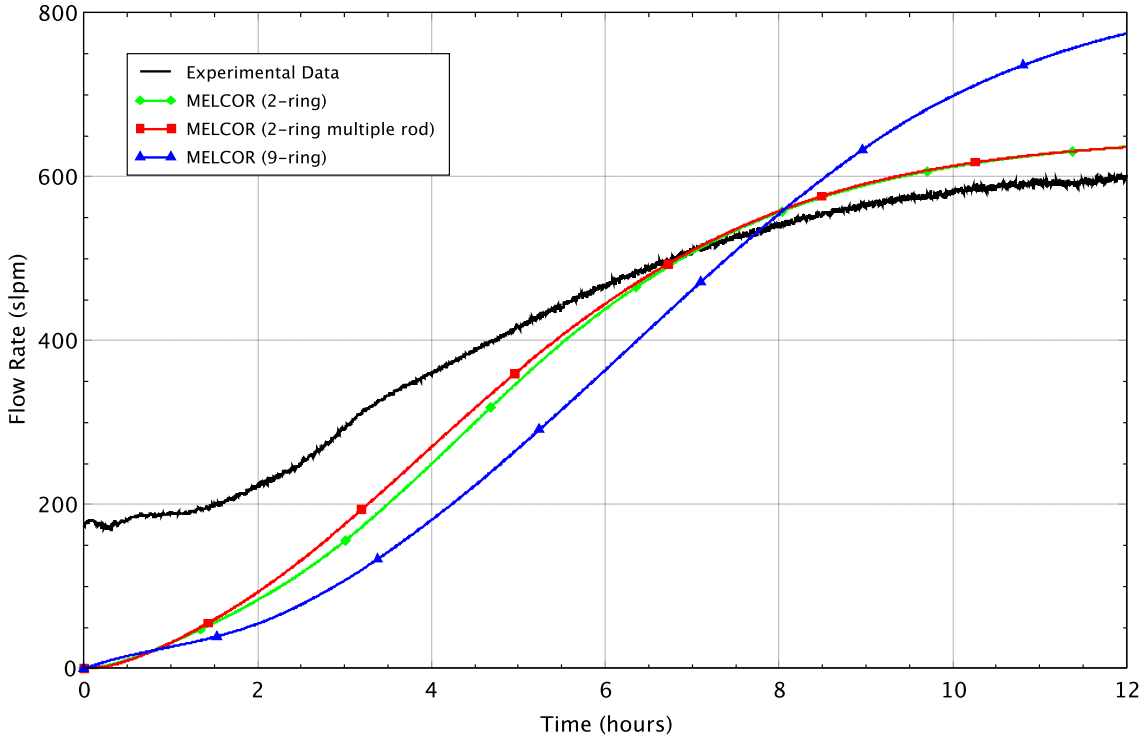

Figure 5.23 Total peripheral assembly volumetric flow rate for the 8 kW pre-ignition test

5.5 Ignition Test

The ignition test was conducted with a total applied power of 15 kW to the center fuel assembly. The first several hours of the ignition test, where the PCT is below 900 K [1,160°F], show results/trends similar to that of the pre-ignition tests described above. MELCOR calculations were performed for each of the three models described above which include: 1) 2-ring, 2) 2-ring multiple rod/ring and 3) 9-ring. Comparisons were made between the models and experimental data (when available) in Figures 5.24 through 5.38. Since the focus is on the new 2-ring multiple rod model, plots for the 2-ring and 9-ring models will only be shown in a few selected figures. In addition to the three models described above, a second calculation was performed with the 2-ring multiple rod model where the best fit curve to the ANL data was replaced with the lower uncertainty curve (as seen in Figure 5.6) to take into consideration the known uncertainty in this parameter. Further sensitivities on oxidation kinetics are described in Section 5.6.2.

Figures 5.24 and 5.25 show the peak cladding temperature response in the center and peripheral assemblies respectively. The 2-ring model, which uses a single rod/radial ring, shows the lowest temperatures and shows ignition is significantly delayed over the data and other models as expected. The 2-ring multiple rod and 9-ring models show good agreement with PCT until 1,025 K [1,385°F], at which point the experiment continues to heat up while the MELCOR results reach a quasi-steady condition. This quasi-steady condition remains until the time-at-temperature condition is met and the model switches from pre- to post-breakaway oxidation kinetics. Once this occurs, the additional heat supplied from the oxidation reaction increases the PCT leading to fuel rod ignition. It is understood that ignition does not occur at a specific temperature, however, for convenience and in order to make comparisons, it is defined in this report as when the temperature exceeds 1,200 K [1,700°F]. In the peripheral region, ignition for the 2-ring multiple rod and 9-ring models is delayed similar to that seen in the center assembly, however, the 2-ring model did not show ignition during the 12 hour time period shown in Figure 5.25 but does ignite prior to 14 hours.

While the intent is to have the 2-ring multiple rod model as similar as possible to the 9-ring model, it is recognized that there are still some modeling differences as described above in Section 5.2.2. These differences result in the 9-ring model retaining more heat in the center assembly thus an earlier ignition time. Similar to that seen in the pre-ignition tests, the 9-ring model temperature in the peripheral region lags that of the 2-ring multiple rod model.

Figures 5.26 and 5.27 show the PCT in the center and peripheral assemblies for the 2-ring multiple rod model with the uncertainty in the ANL data taken into consideration. As seen in these figures, when the lower uncertainty is used the MELCOR computed ignition occurs prior to the experiment. This implies the measured time to ignition is predicted by the ANL breakaway data within uncertainty. A summary of the ignition times and first location of igntion are shown in Table 5.3.

Ignition propagation for the center heated assembly and unheated peripheral assemblies is shown in Figures 5.28 and 5.29 respectively. In the center assembly the experimental data fall within the 2-ring multiple rod model with the ANL best fit and lower uncertainty curves. While ignition occurs earlier when using the lower uncertainty curve, the ignition propagates downward at a rate similar to the test data. In addition, the 2-ring multiple rod model shows good agreement for the elevation of the initial ignition in the center assembly. For about the first half hour after ignition, the burn front proceeded downward somewhat faster than in the test and results in the first occurrence of ignition in the peripheral assemblies at a much lower elevation than in the test data. There is more uncertainty in the peripheral region as ignition times vary from assembly to assembly (i.e., north, south, east and west) as seen in Figure 5.29.

Figures 5.30 and 5.31 show the temperature versus elevation at 5 hours. Note that at this time, cases with the ANL data best fit and lower uncertainty correlations are the same, so only the calculation using the best fit is shown. The MELCOR calculation shows the peak temperatures are in excellent agreement with the test data, however, the average MELCOR temperature is larger than the test data as the experiment still shows a wide range of temperatures at any given elevation. In the peripheral region, MELCOR is in excellent agreement with the test data, although the temperature of the rods closest to the center assembly rack are over predicted. Figures 5.32 and 5.33 show the temperature versus elevation at 6 hours, which is just prior to ignition in the experiment. Overall, the MELCOR calculation using the ANL data best fit shows good agreement to the peak temperature in the center assembly. However, as seen in Figure 5.32, at an elevation of 3.3 m [130 in], at least one rod has begun to increase in temperature and is near 1,100 K [1,520°F]. In the experiment, a single rod can heat up to the point of ignition and generate additional heat from the oxidation kinetics reaction, while in the MELCOR model, a minimum of 24 rods (smallest group of rods in this model) must undergo the same process. This is a known limitation of system level codes which use the lumped parameter approach.

Figures 5.34 and 5.35 show the radial temperature profile at 5 hours and two different elevations (1.93 m [76 in] and 3.45 m [136 in]). The experimental data presented here is that which is available in a straight line outward from the centerline of the center assembly towards each of the four peripheral assemblies (North, South, East and West). As such, it does not show temperatures that are from the corner rods in the assemblies. Prior to ignition, the MELCOR radial temperature profile is in excellent agreement with the test data. As previously described, the MELCOR temperatures in the center assembly are closely coupled together and show a relatively flat profile, while the data shows a somewhat larger decrease from assembly centerline outward. In the peripheral region, the MELCOR temperature closest to the center assembly rack is higher than the test data, otherwise is in excellent agreement. Overall, MELCOR is in good agreement predicting the radial temperature profile through the assemblies.

The volumetric flow rates for the center and peripheral assemblies are shown in Figures 5.36 and 5.37. In the central assembly, the flow is initially over predicted, however, by the time of ignition, the MELCOR model shows excellent agreement with the test data. In the peripheral region, the models initially under predict the flow, then over predict the flow after ~3 hours. As noted above for the pre-ignition tests, the differences in flow are mainly due to the use of constant loss coefficients S_{LAM} and $\sum k$. Sensitivities on the use of constant versus variable loss coefficients are described in more detail in Section 5.6.1.

The effect of nodalization (specifically the total number of cells used) on calculation performance can be significant. This calculation was run with the three models where the maximum time step was reduced to 0.2 seconds. This time step size was chosen because it meant that all calculations followed the same time history to eliminate the problem of excessive time step reduction in any particular model. Therefore meaningful comparisons can be made in the plots of total CPU time as seen in Figure 5.38. Initially, all calculations follow a linear trend, indicating that time-step reduction is not occurring in any of the models. Eventually, some of the models (particularly the 9-ring model) begin to show some time-step reduction and therefore the slope in the line increases. Note that the additional fuel rod types that are added to the 2-ring model has only a minor impact on the calculation time. This model offers an acceptable trade-off to the modeler in terms of improving the fidelity of the calculation to predict the burn propagation from the heated assembly into the unheated assemblies. However, when increasing the number of COR rings to nine, the calculation time is significantly larger. This would be a less acceptable trade-off for the modeler. It is also expected that with more control

volumes and flow paths, the CV package could have more numerical problems, leading to additional time-step reductions.

Another reason for using the 2-ring multiple rod model is the simplicity of the input model. The input model is nearly identical to the 2-ring model with a few new input records for defining mass fractions for fuel rod types, mass fractions for control rod types, and view factors. The inputs for the 9-ring model (COR_KFU, COR_KCL, COR_ KNS, COR_SS, COR_CIT, COR_EDR, CR_RDR, COR_BFA, COR_SA, and COR_RSA) are nine times larger than for the 2-ring model. This makes maintenance of an input model much more complex. For the 2-ring model, it is possible to renodalize within a ring by changing at most three input tables. For the 9-ring model, each of these input tables would need to be modified.

Table 5.3 Ignition times and locations for the 15 kW ignition test

Description	Time of ignition*		Location of Ignition**	
	Center	Peripheral	Center	Peripheral
Experiment	6.31 hours	7.08 hours	3.302 m [130.0 in]	3.150 m [124.0 in]
2-ring, ANL data best fit correlation	11.6 hours	13.8 hours	3.182 m [125.3 in]	2.279 m [89.7 in]
2-ring multiple rod, ANL data best fit correlation	10.1 hours	10.9 hours	3.182 m [125.3 in]	2.580 m [101.6 in]
2-ring multiple rod, ANL data lower uncertainty correlation	5.62 hours	6.67 hours	3.182 m [125.3 in]	1.978 m [77.9 in]
9-ring, ANL data best fit correlation	8.90 hours	10.7 hours	3.483 m [137.1 in]	2.279 m [89.7 in]

* Ignition defined when temperature exceeds 1,200 K [1,700°F].
** Location of MELCOR is at node center where ignition first occurred.

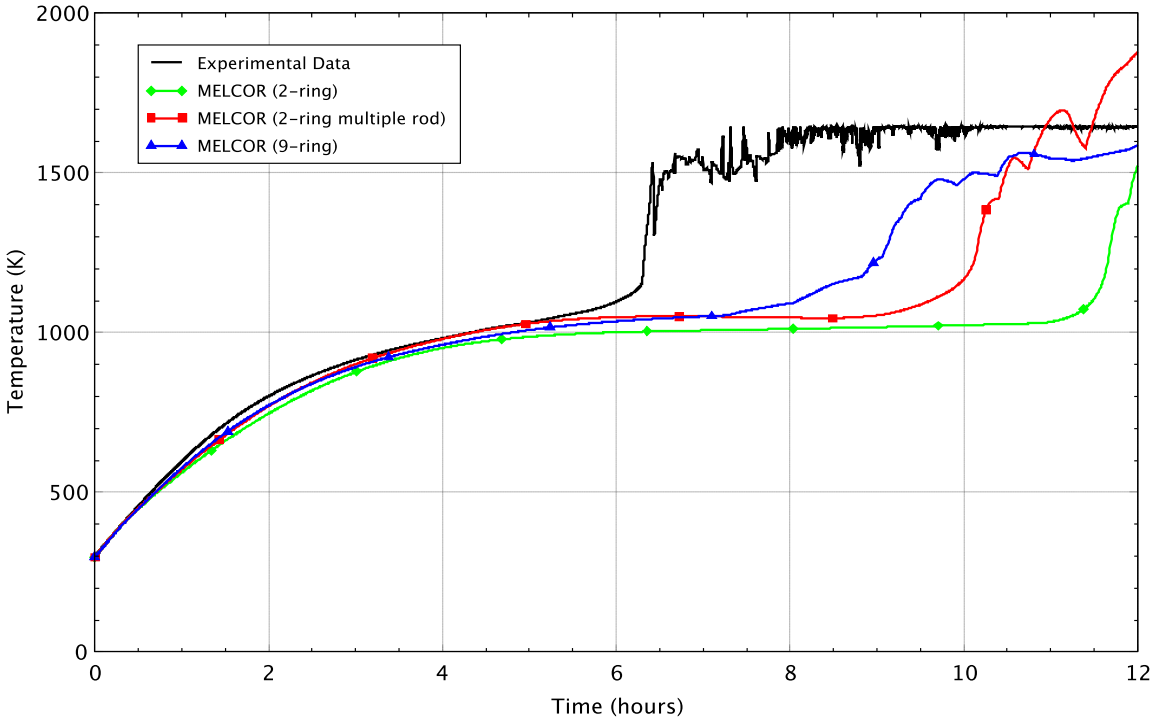

Figure 5.24 Peak cladding temperature in the center assembly for the 15 kW ignition test

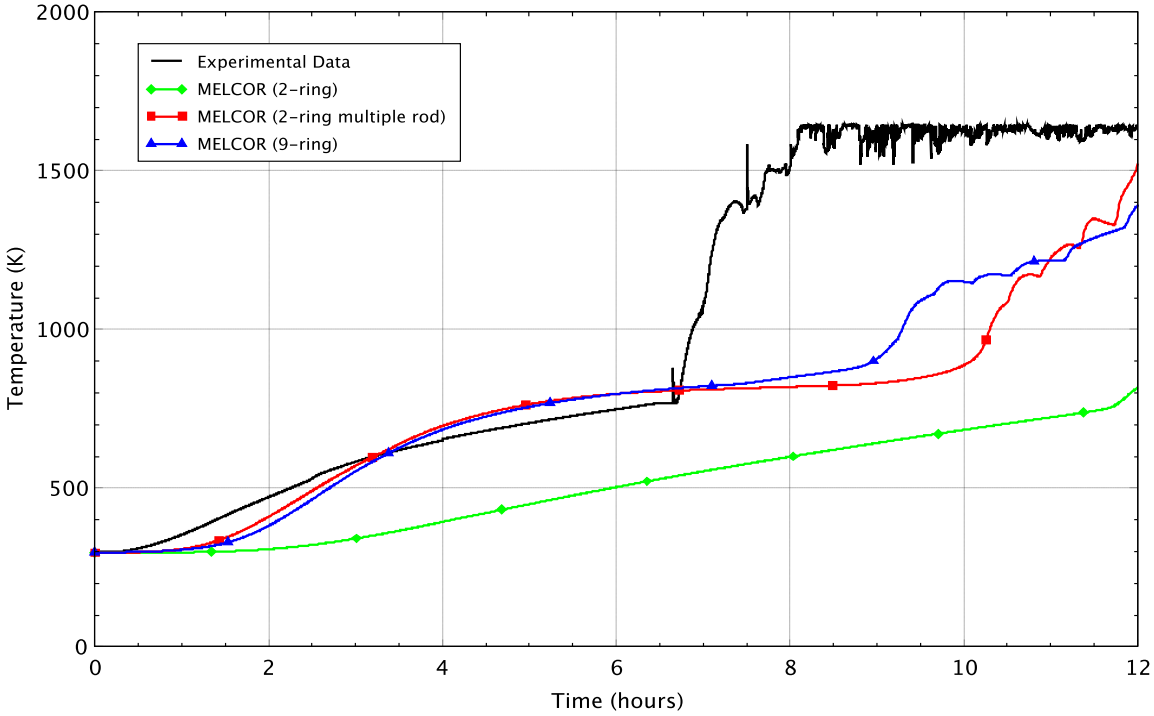

Figure 5.25 Peak cladding temperature in the peripheral assemblies for the 15 kW ignition test

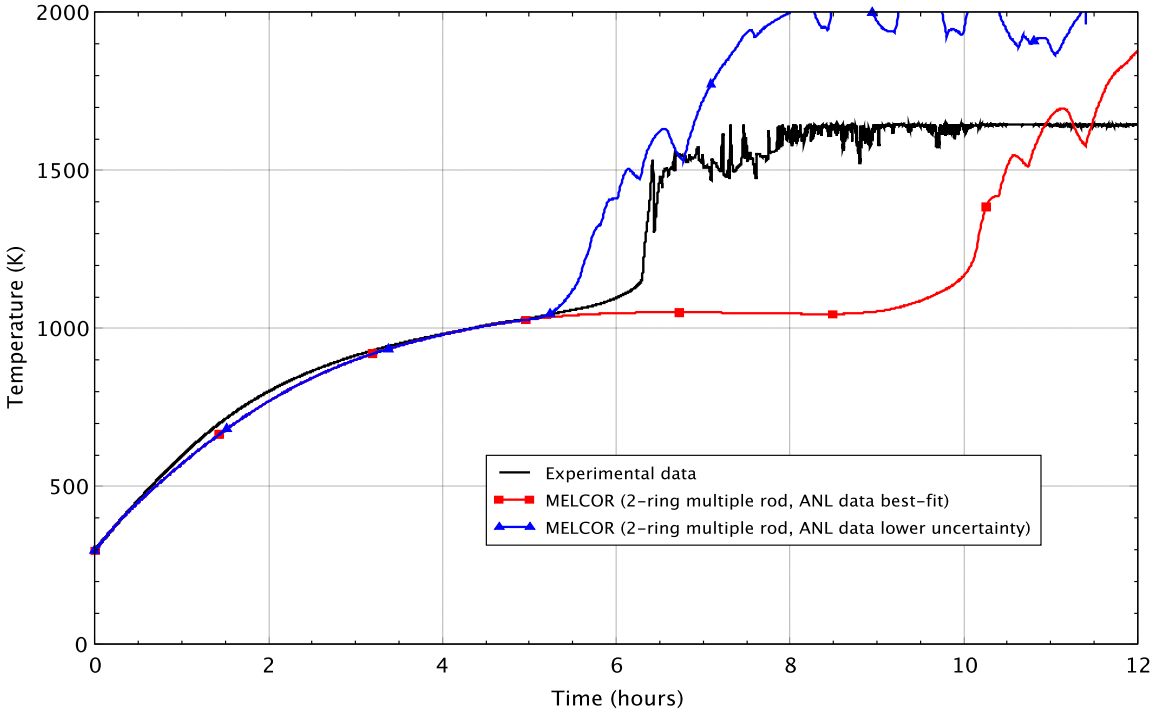

Figure 5.26 Peak cladding temperature in the center assembly for the 15 kW ignition test

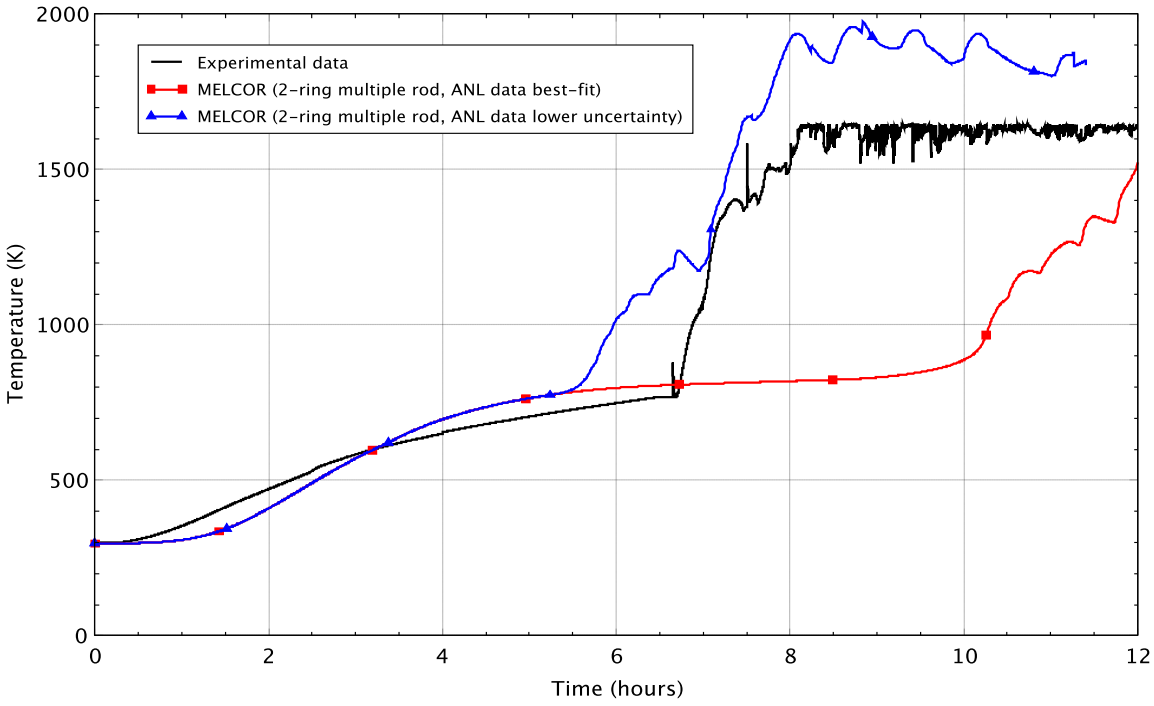

Figure 5.27 Peak cladding temperature in the peripheral assemblies for the 15 kW ignition test

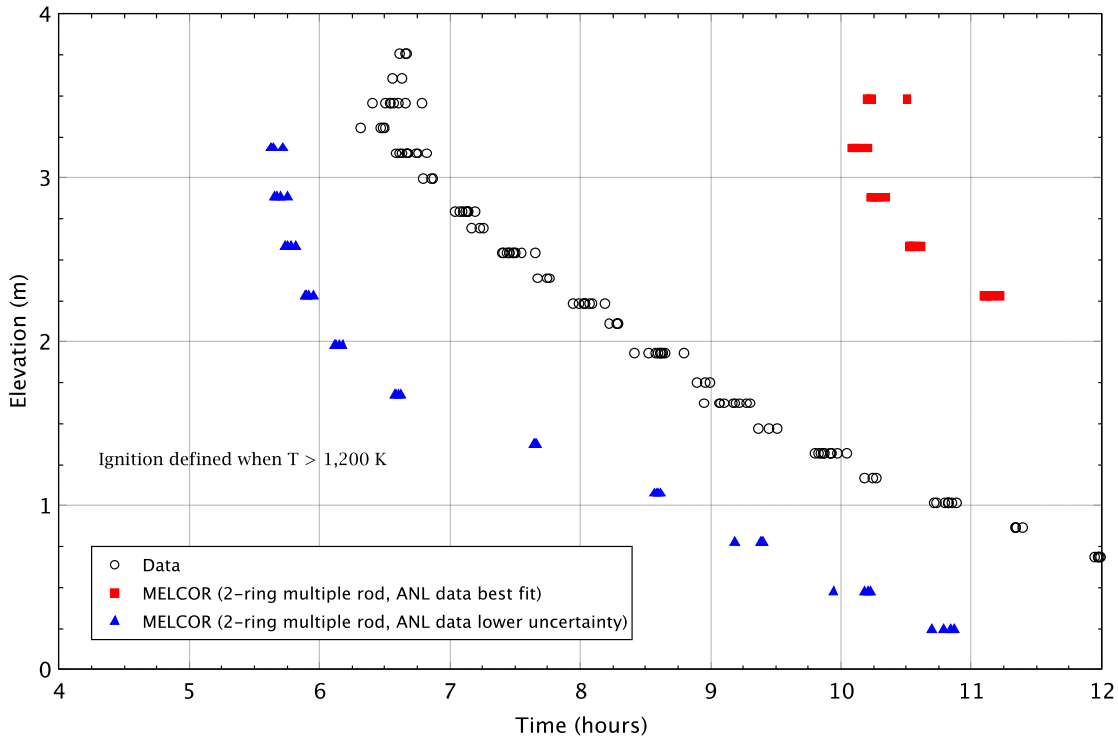

Figure 5.28 Central assembly ignition propagation for the 15 kW ignition test

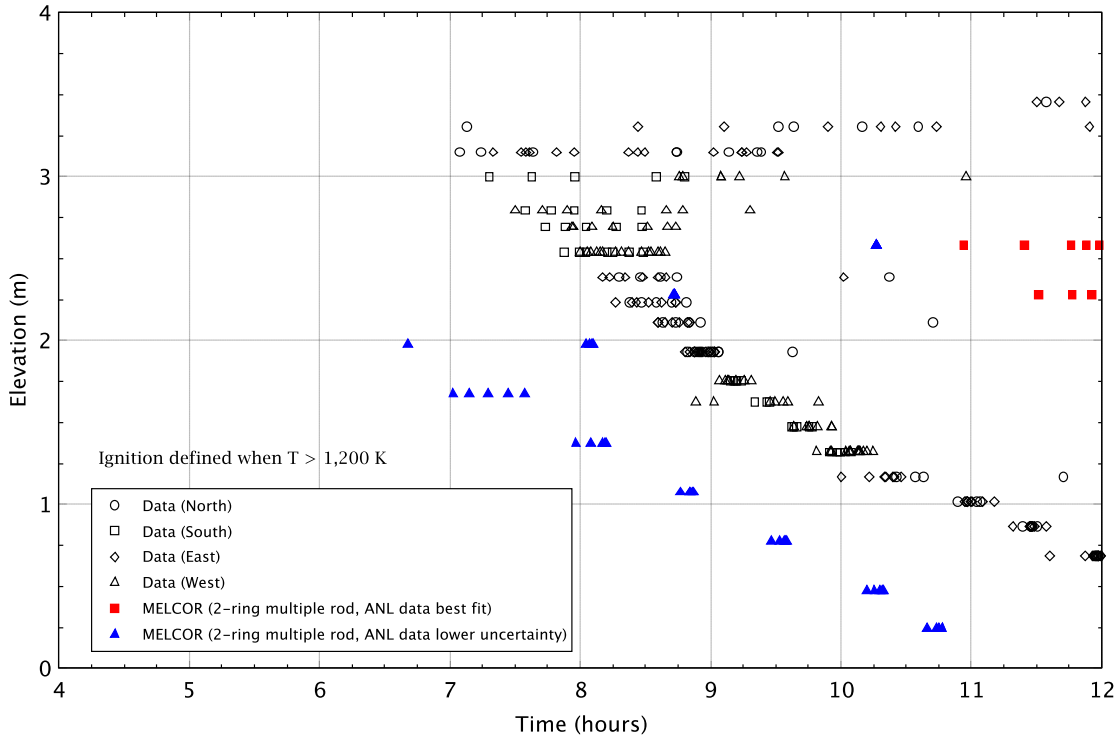

Figure 5.29 Peripheral assembly ignition propagation for the 15 kW ignition test

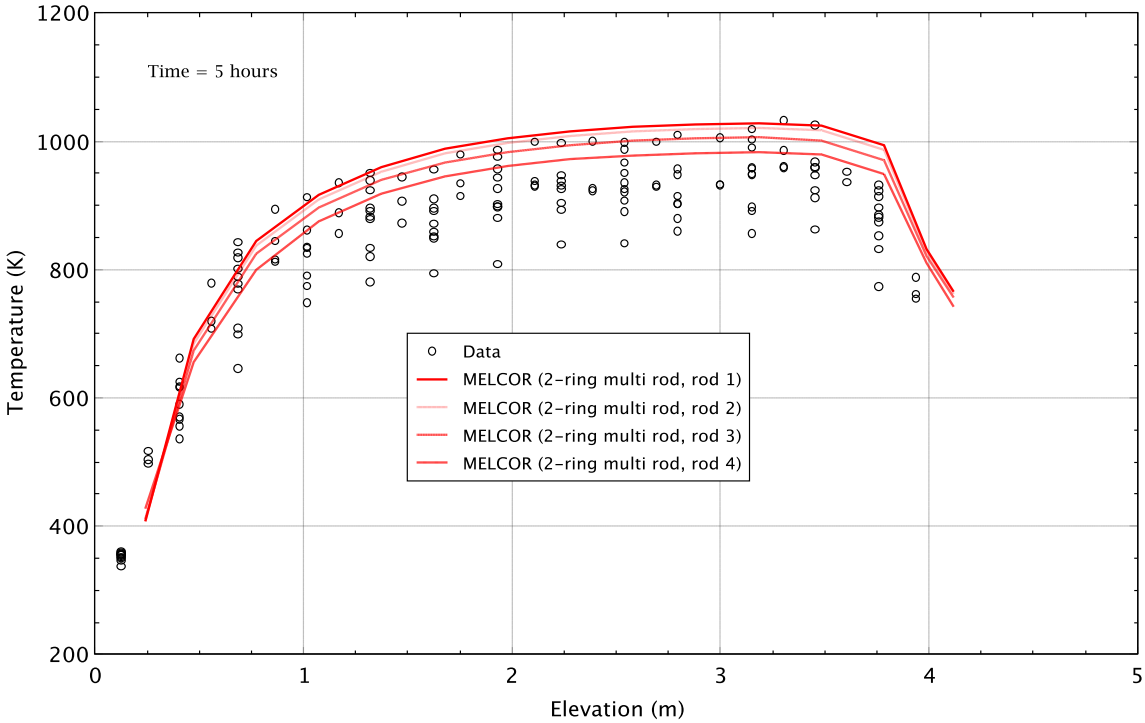

Figure 5.30 Central assembly temperature versus elevation for the 15 kW ignition test at 5 hours

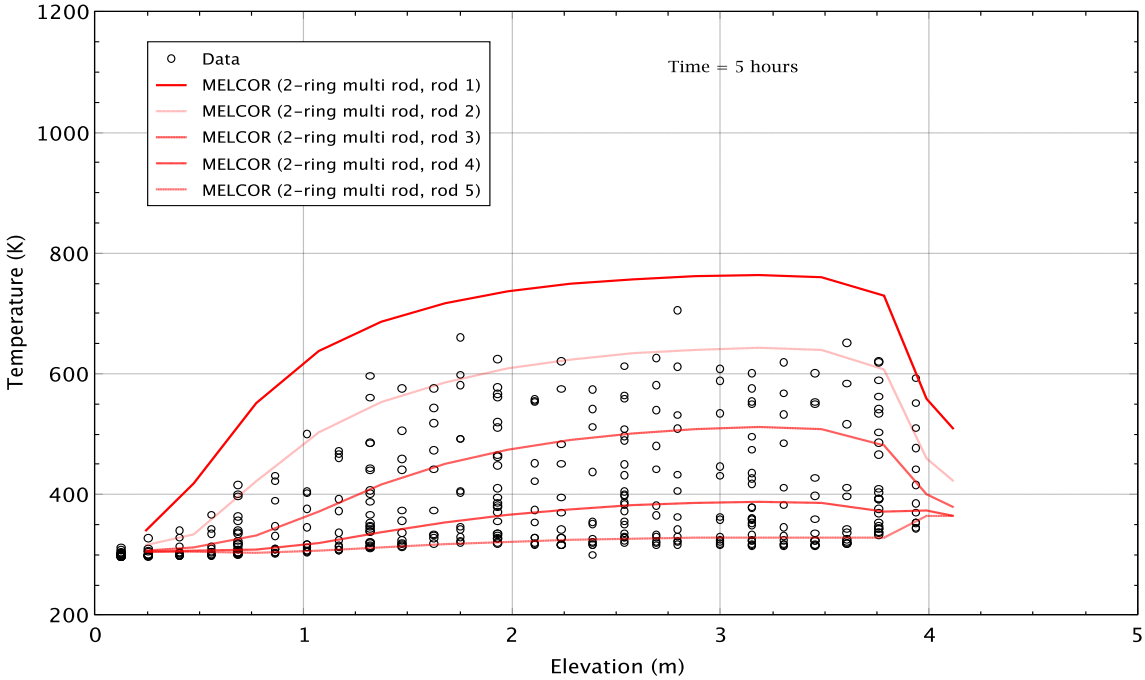

Figure 5.31 Peripheral assembly temperature versus elevation for the 15 kW ignition test at 5 hours

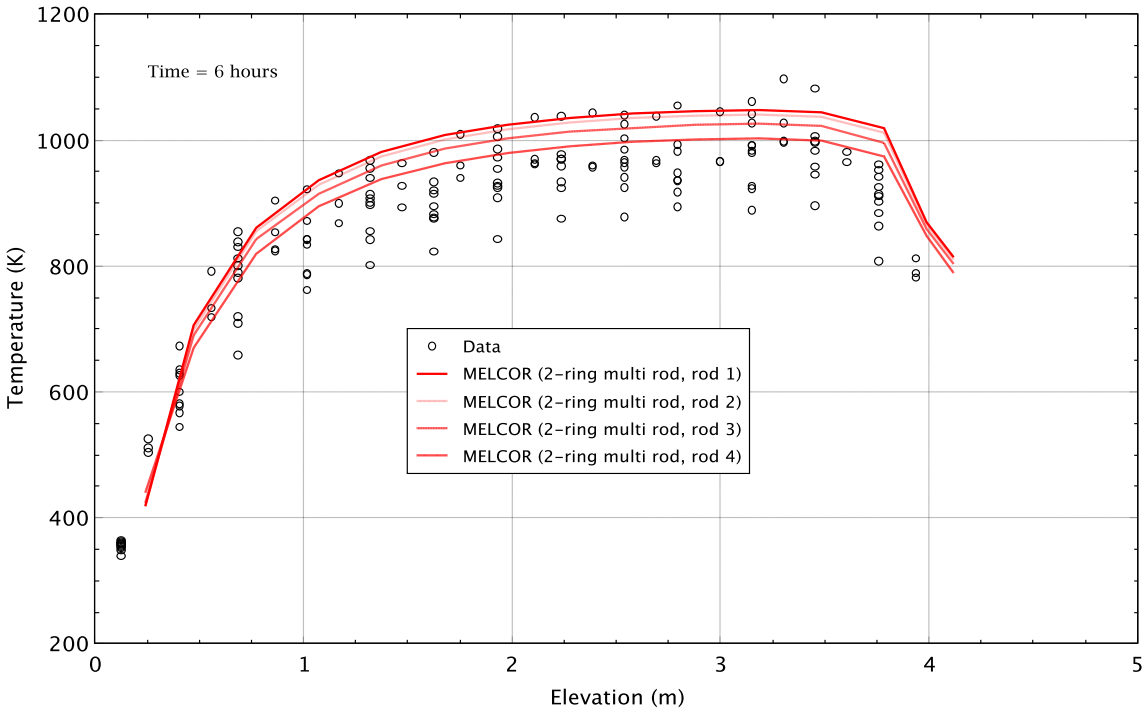

Figure 5.32 Central assembly temperature versus elevation for the 15 kW ignition test at 6 hours

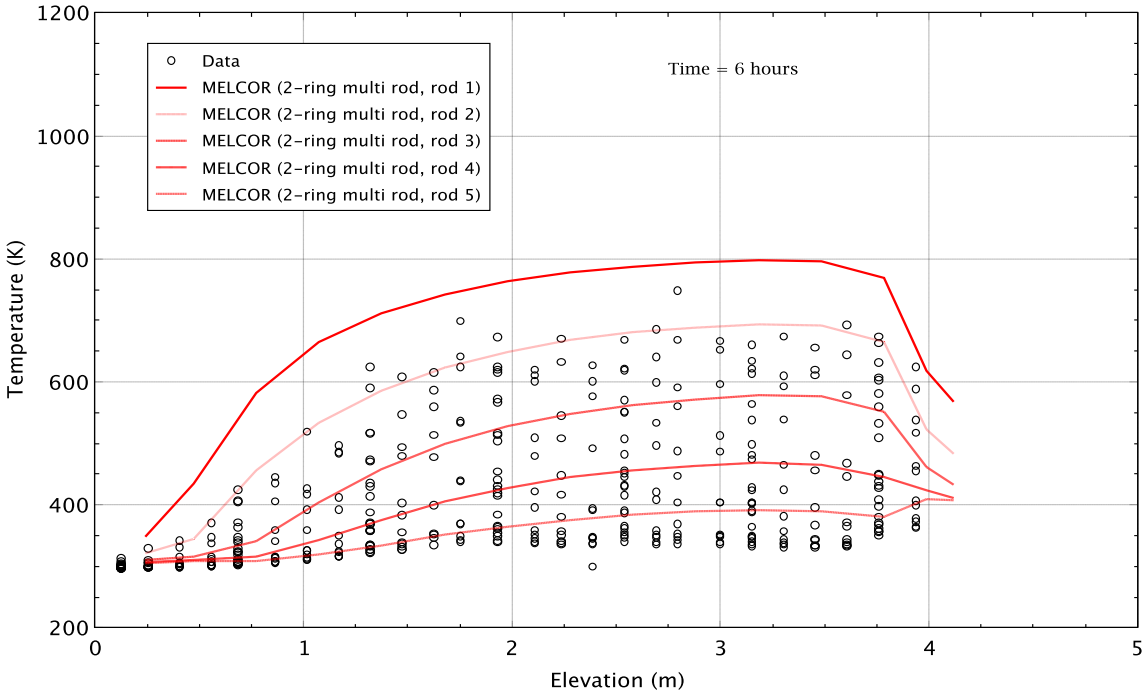

Figure 5.33 Peripheral assembly temperature versus elevation for the 15 kW ignition test at 6 hours

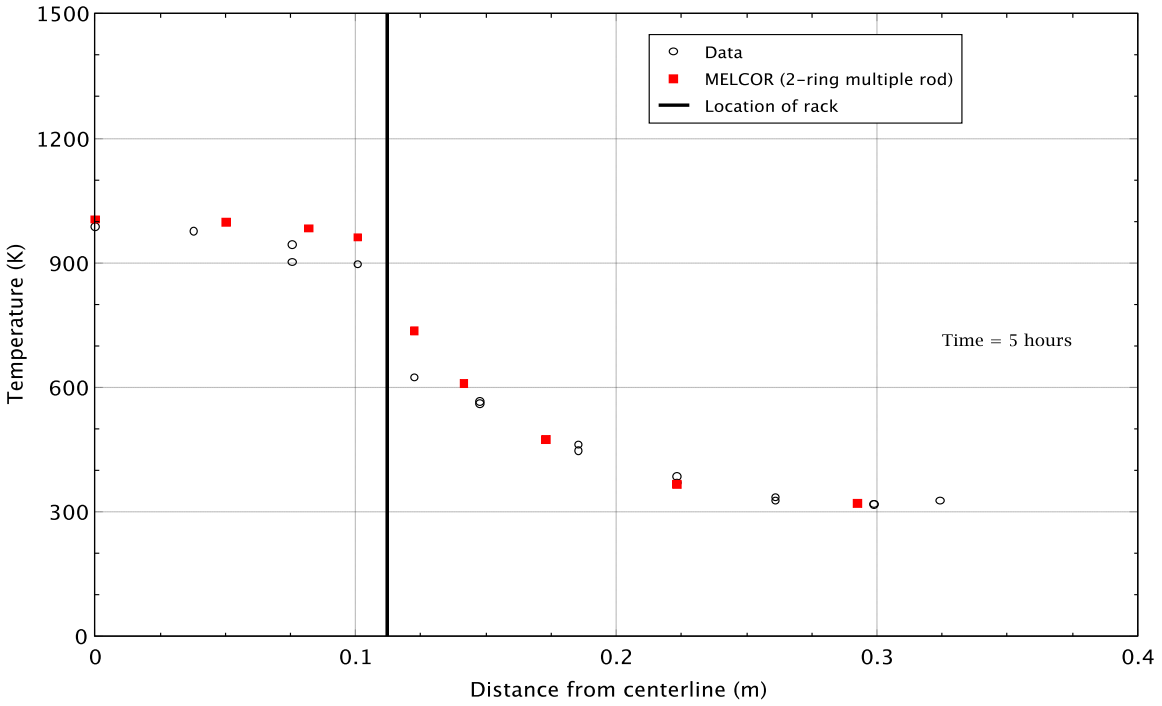

Figure 5.34 Radial temperature distribution at 1.93 m [76 in] for the 15 kW ignition test at 5 hours

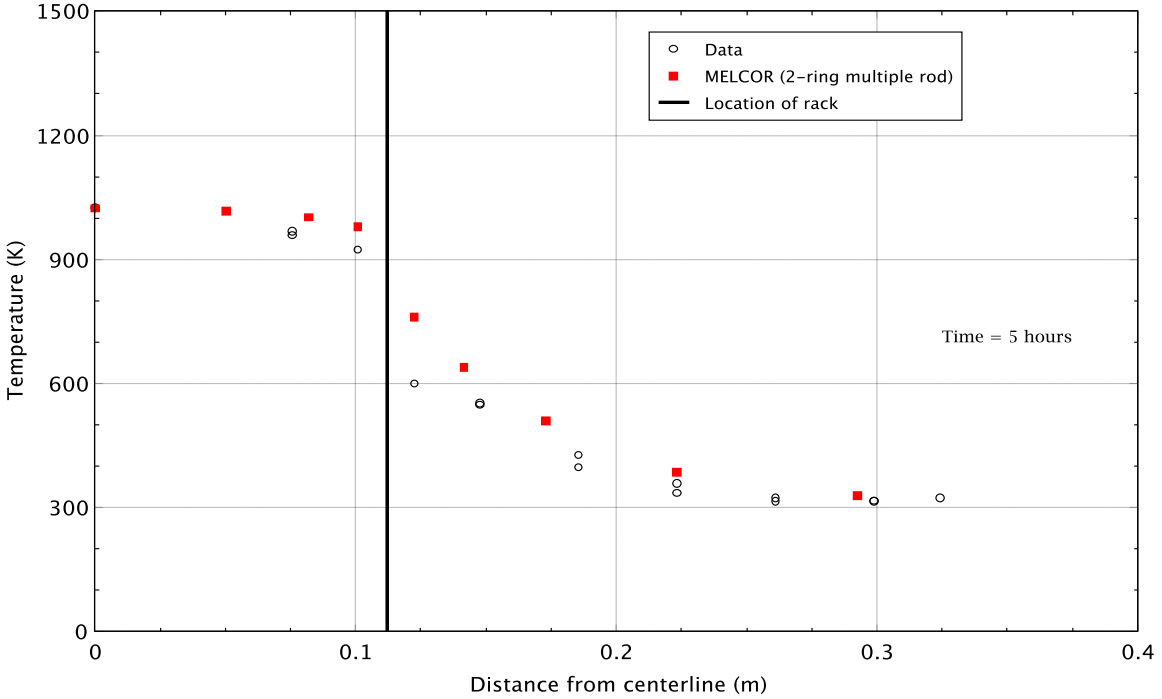

Figure 5.35 Radial temperature distribution at 3.45 m [136 in] for the 15 kW ignition test at 5 hours

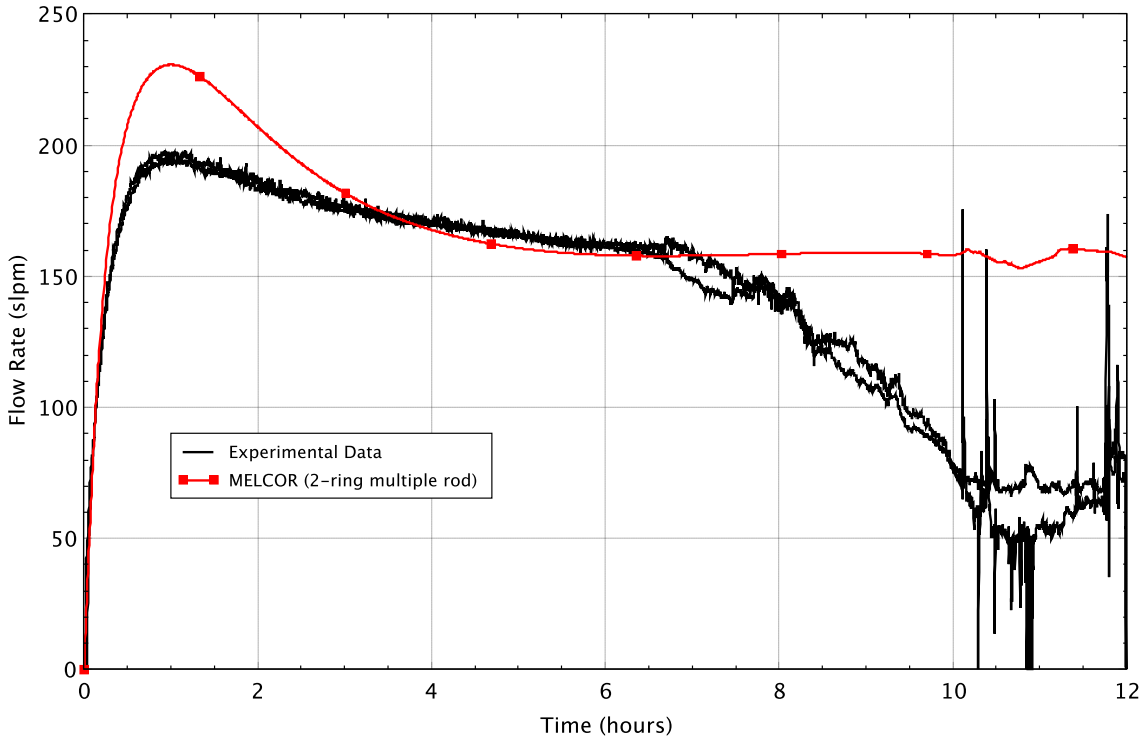

Figure 5.36 Central assembly volumetric flow rate for the 15 kW ignition test

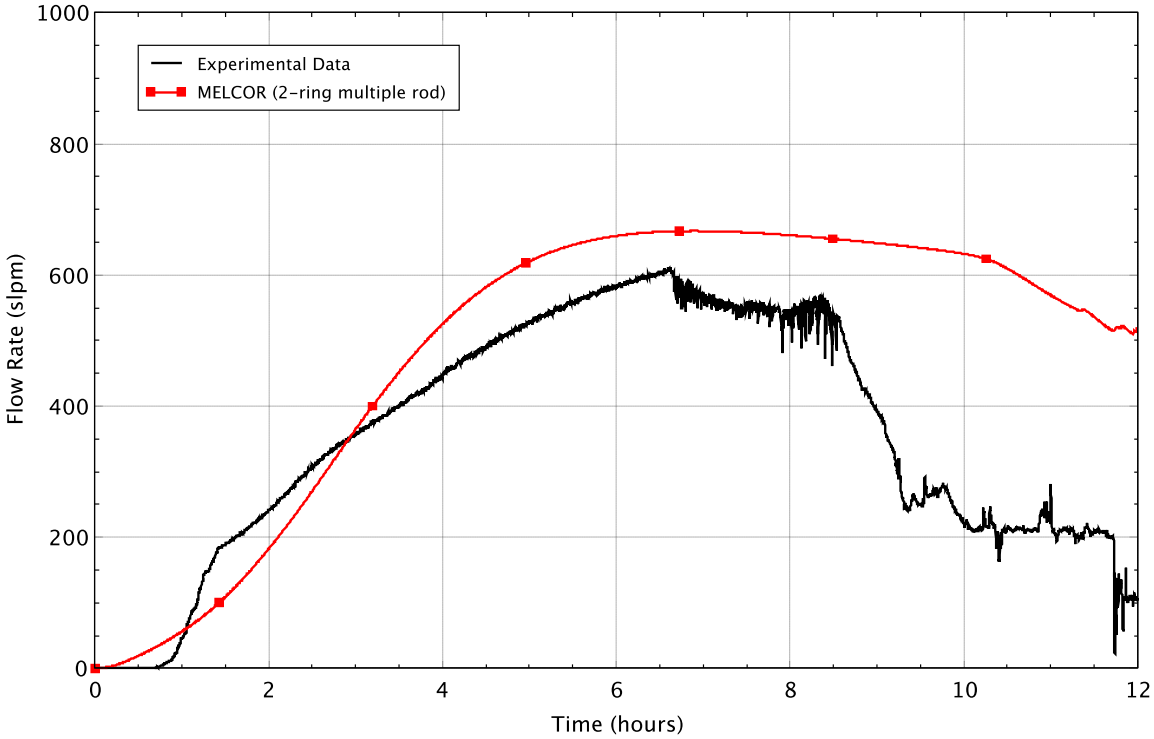

Figure 5.37 Peripheral assembly volumetric flow rate for the 15 kW ignition test

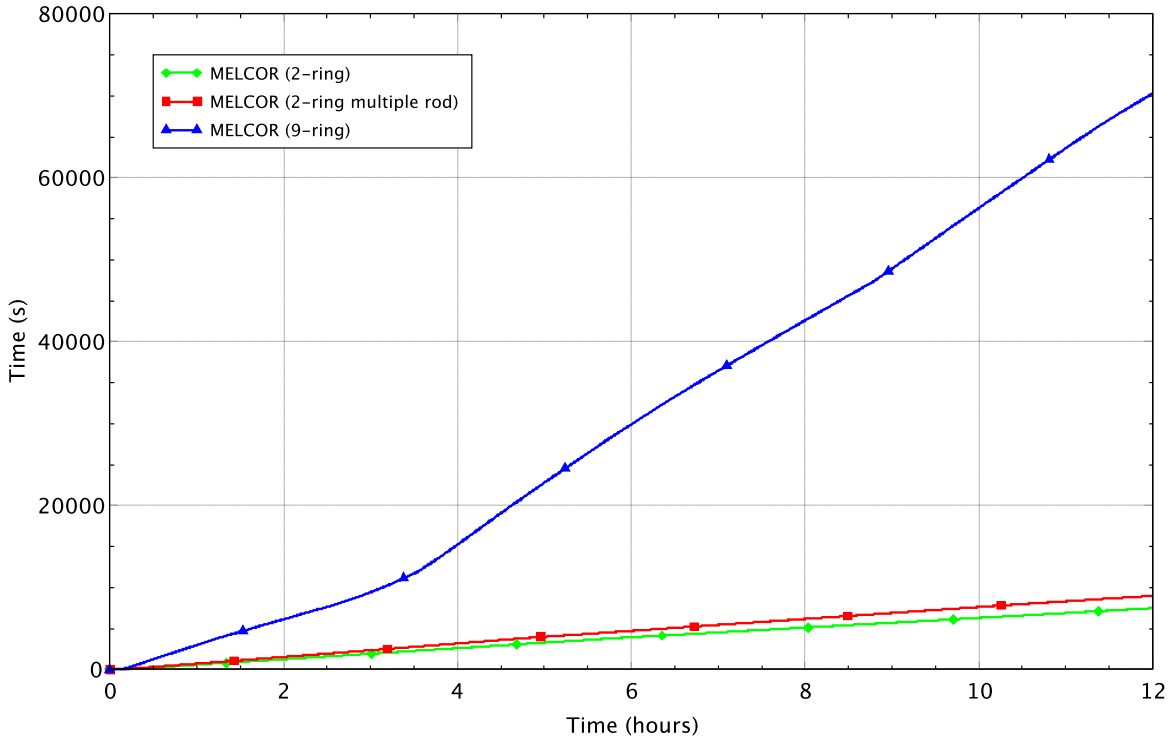

Figure 5.38 CPU times for the MELCOR simulations of the 15 kW ignition test

5.6 MELCOR Sensitivities

Two sensitivity studies were performed for simulation of the Phase II tests. These sensitivity cases were intended to investigate the effects on key figures-of-merit of the following phenomenological or modeling issues: 1) hydraulic flow loss coefficients S_{LAM} and Σk and 2) transition from pre- to post-breakaway oxidation kinetics.

5.6.1 Hydraulic Loss Coefficients

The hydraulic loss coefficients, namely the frictional loss coefficient (S_{LAM}) and the inertial loss coefficient (Σk) values were determined experimentally as described in NUREG/CR-7144 (Ref. 14). To determine these values, flow was forced through a fuel assembly at a given rate, and the pressure drop through the assembly was measured. From this data, equations for the loss coefficients were determined (Equations 5.3 and 5.4) where a1 and a2 are determined from curve fits to the ΔP data versus velocity data, D_h is the hydraulic diameter, L is the length over which the ΔP is measured, μ is the viscosity and ρ is the density.

$$S_{LAM} = 2 \cdot a_1 \cdot \left(\frac{D_h^2}{L \cdot \mu} \right) \quad 5.3$$

$$\Sigma k = \frac{2 \cdot a_2}{\rho} \quad 5.4$$

For the base runs, these loss coefficients are then input into the MELCOR model as constants over the entire length of the fuel assembly. However, as parameter S_{LAM} is a function of viscosity and Σk is a function of density, both of these parameters will change significantly during the transient. As temperature increases, S_{LAM} decreases and Σk increases. These two changes together represent a situation with competing effects. As temperature increases, the value of S_{LAM} decreases which leads to an increase in flow, while Σk increases leading to a decrease in flow. However, the magnitude of the changes are not equal and are not necessarily linear with respect to temperature. Given that these values are input as constants, it is not expected that the MELCOR computed flow will match the experimental data over the entire transient.

Sensitivity runs were performed with the 2-ring model where control functions were used to compute S_{LAM} and Σk at every flow path in the assemblies. Note that the starting point model used for these sensitivities is not the final 2-ring model presented above, rather it is an earlier version.

As seen in Figures 5.45 through 5.56 the results of these sensitivities show that the flow rate is in much better agreement with the test data when using variable loss coefficients in both the lower power non-ignition tests as well as the 15 kW ignition test. While sensitivities were performed for all power levels used in the experiments, the figures only show results for the 1 kW and 8 kW pre-ignition tests and the 15 kW ignition test. For each of the three power levels, the figures show flow in the central and peripheral assemblies as well as the peak cladding temperature in both central and peripheral assemblies. With the exception of the 1 kW pre-ignition test, the temperature response did not noticeably change given the change in flow rate. This is due to the fact that the experiments are dominated by radiation heat transfer which is not dependent on flow. At very low powers, convective heat transfer is important, and induced flow rates will make a difference in the results.

Computing the loss coefficients at each flow path takes eight control functions. To compute all the loss coefficients in just the center assembly of the 2-ring model requires 120 control functions. If this method were used for the 9-ring model, it would require over one thousand control functions, leading to an overly complicated and difficult to maintain model.

The resulting flow through the peripheral region did not show the same improvement as the center assembly with the use of variable loss coefficients. One possible reason for this is that the loss coefficients were based on tests with forced flow where the flow was somewhat uniform across the unheated assembly. In the case of the experiments, the heatup of the assembly is asymmetrical and flow would initially start only on the side that is being heated by the center assembly. The loss coefficients for this situation would be different than a case where flow was uniform across the assembly. If convective heat transfer is expected to be a significant factor, as would be the case in lower powered events, then a more thorough attempt at matching the experimental flow should be investigated.

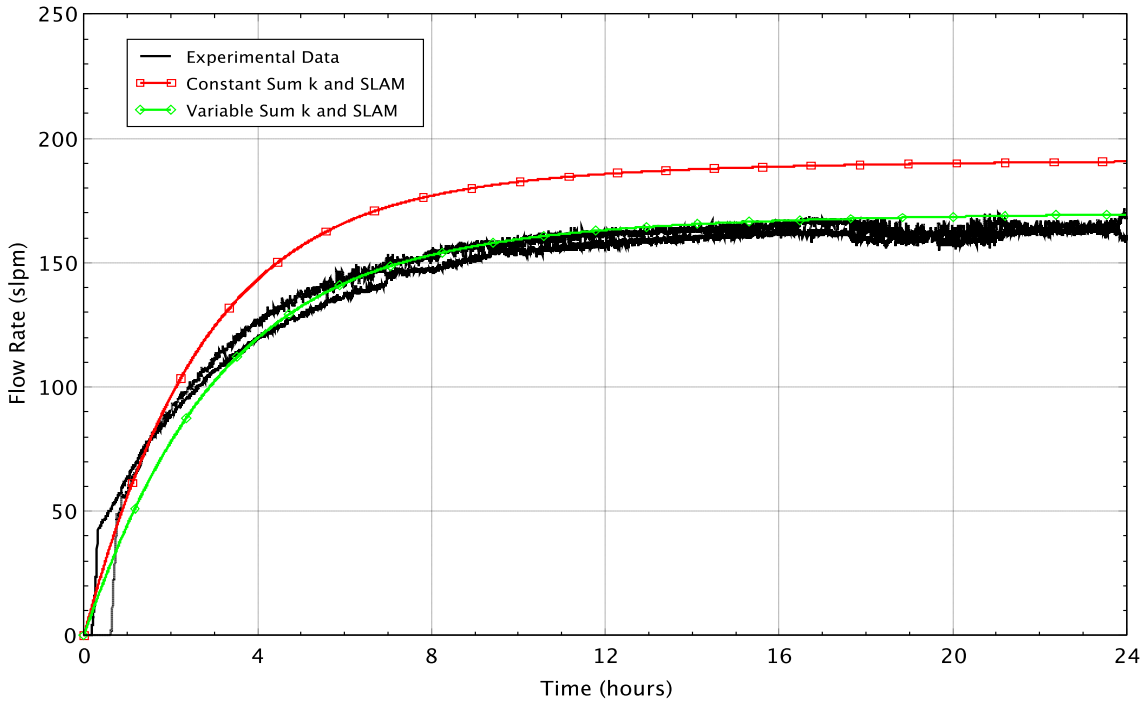

Figure 5.39 Flow rate in central assembly for 1 kW pre-ignition test using the 2-ring model

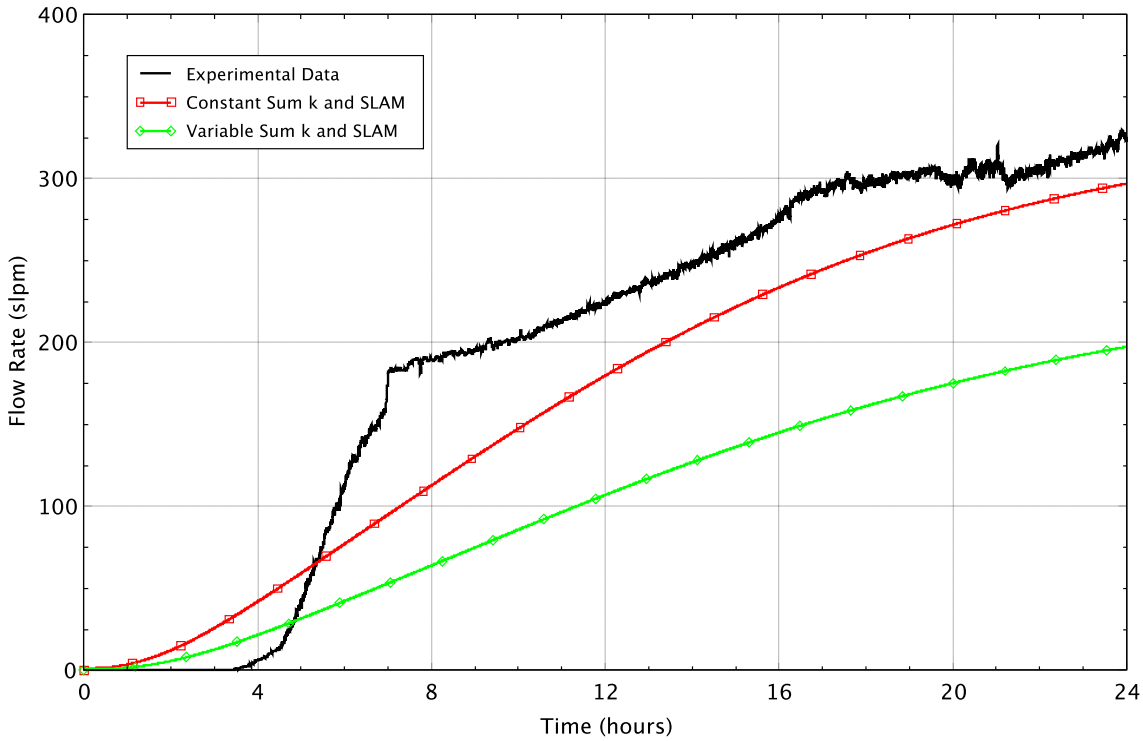

Figure 5.40 Flow rate in peripheral assemblies for 1 kW pre-ignition test using the 2-ring model

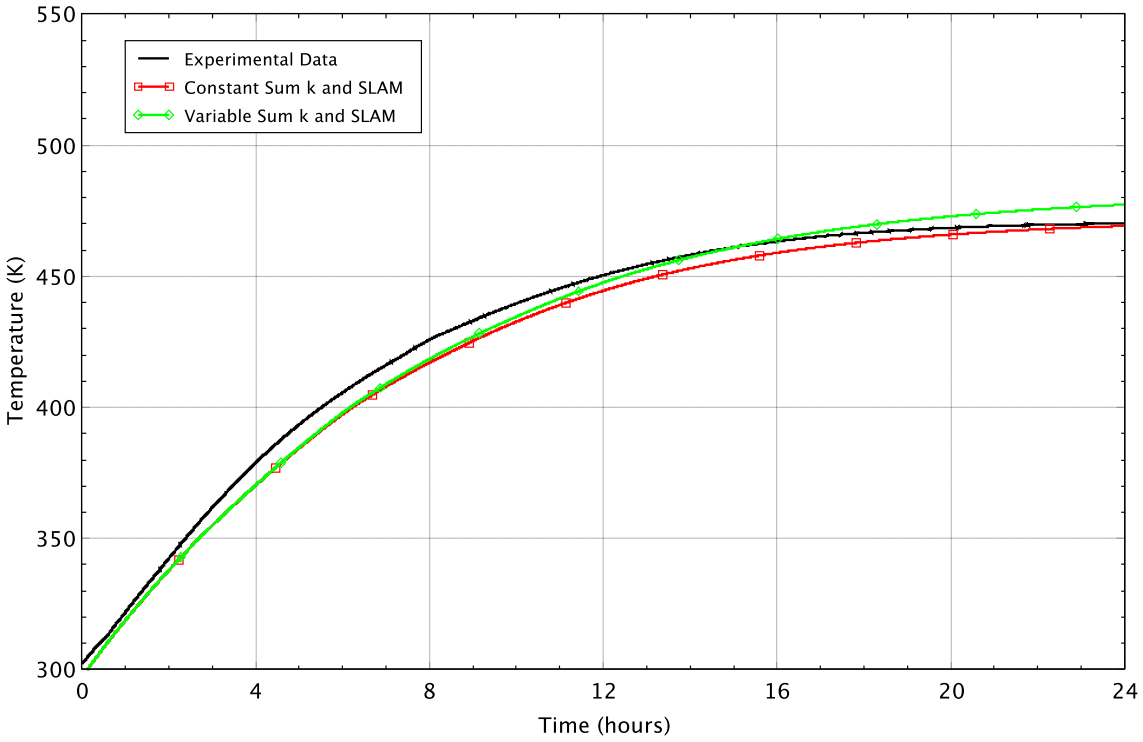

Figure 5.41 PCT in center assembly for 1 kW pre-ignition test using the 2-ring model

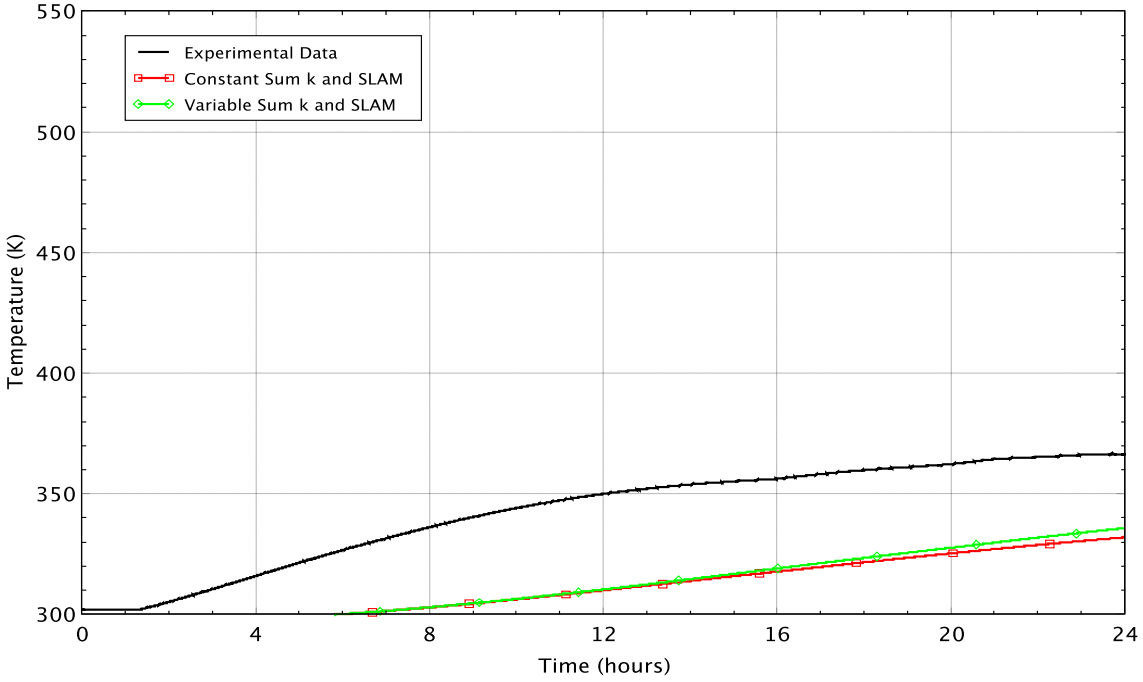

Figure 5.42 PCT in peripheral assemblies for 1 kW pre-ignition test using the 2-ring model

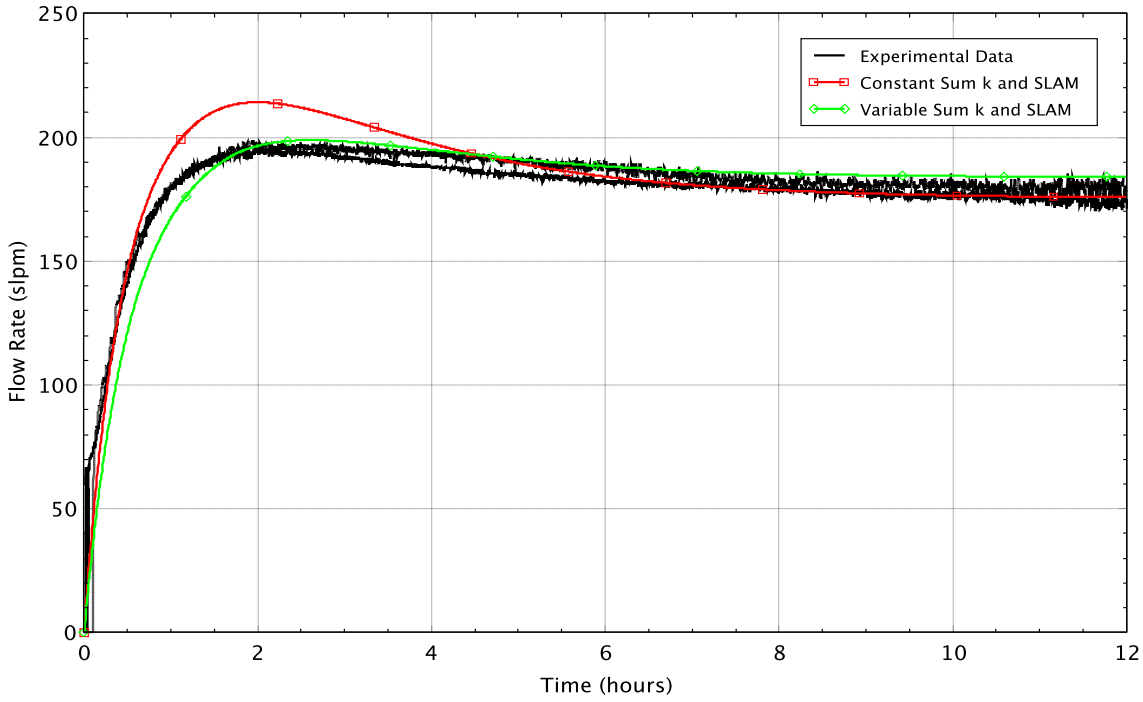

Figure 5.43 Flow rate in central assembly for 8 kW pre-ignition test using the 2-ring model

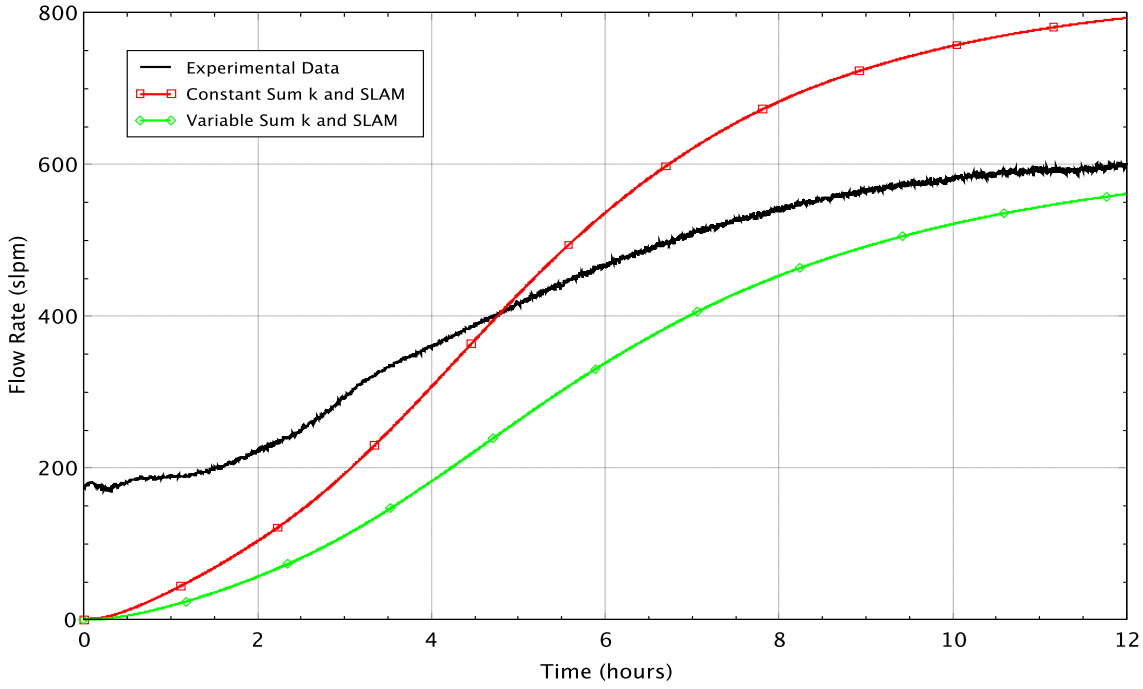

Figure 5.44 Flow rate in peripheral assemblies for 8 kW pre-ignition test using the 2-ring model

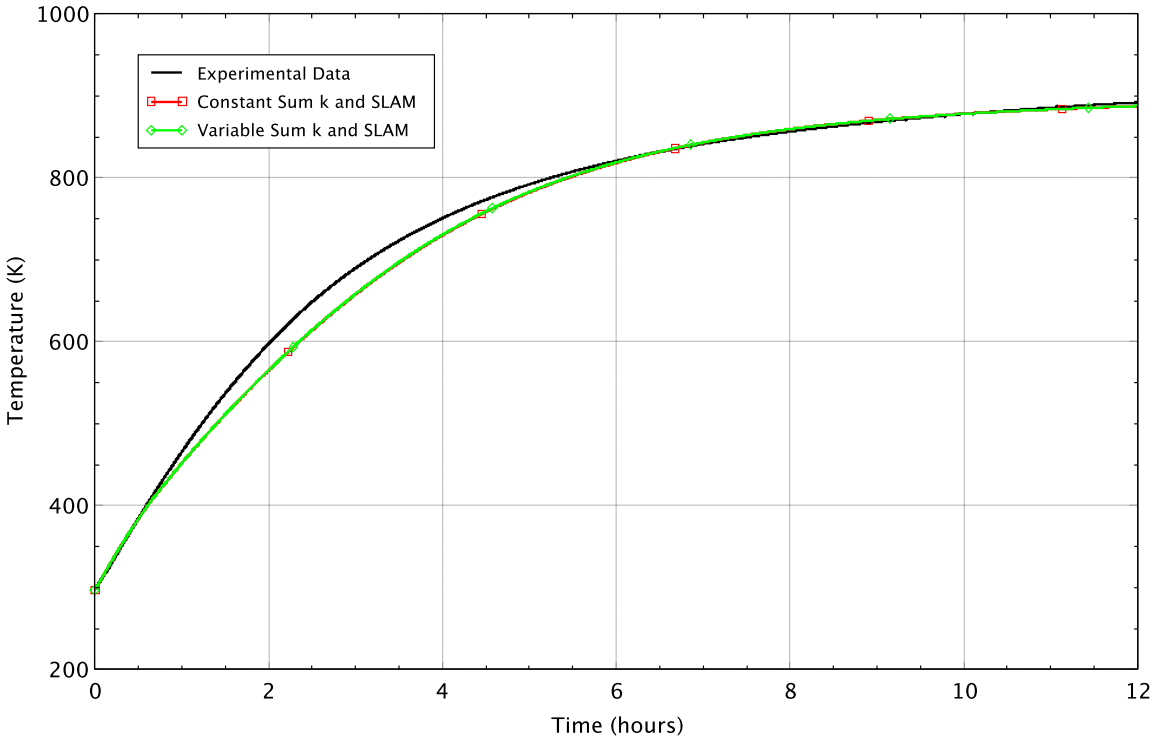

Figure 5.45 PCT in center assembly for 8 kW pre-ignition test using the 2-ring model

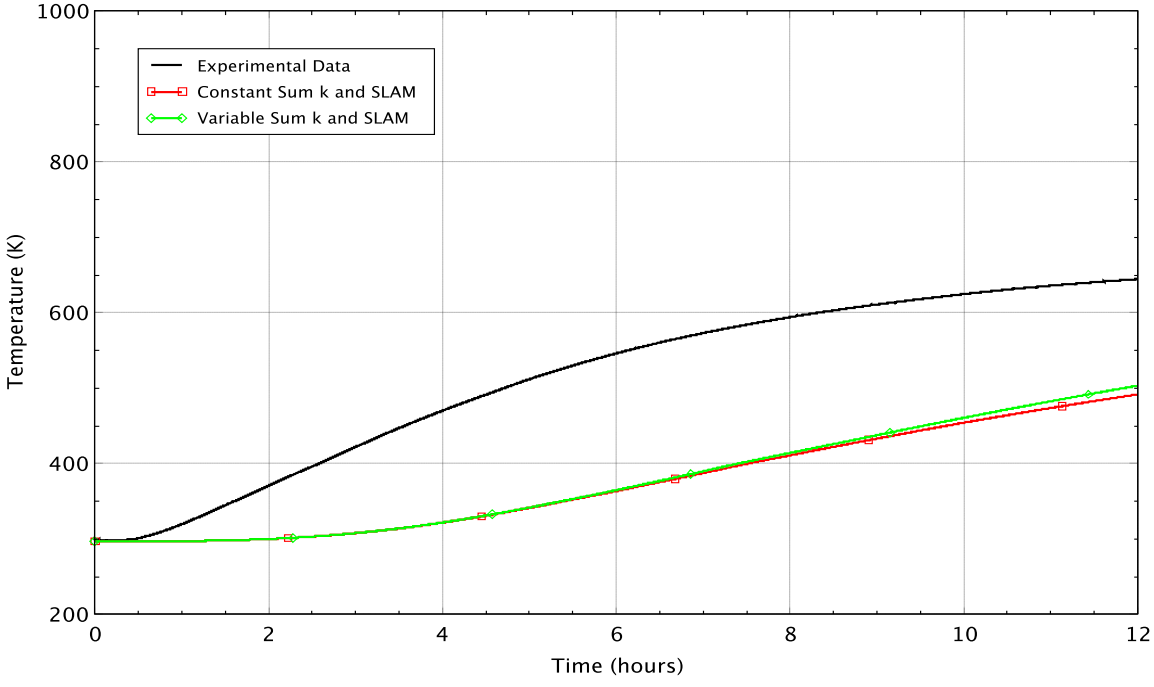

Figure 5.46 PCT in peripheral assemblies for 8 kW pre-ignition test using the 2-ring model

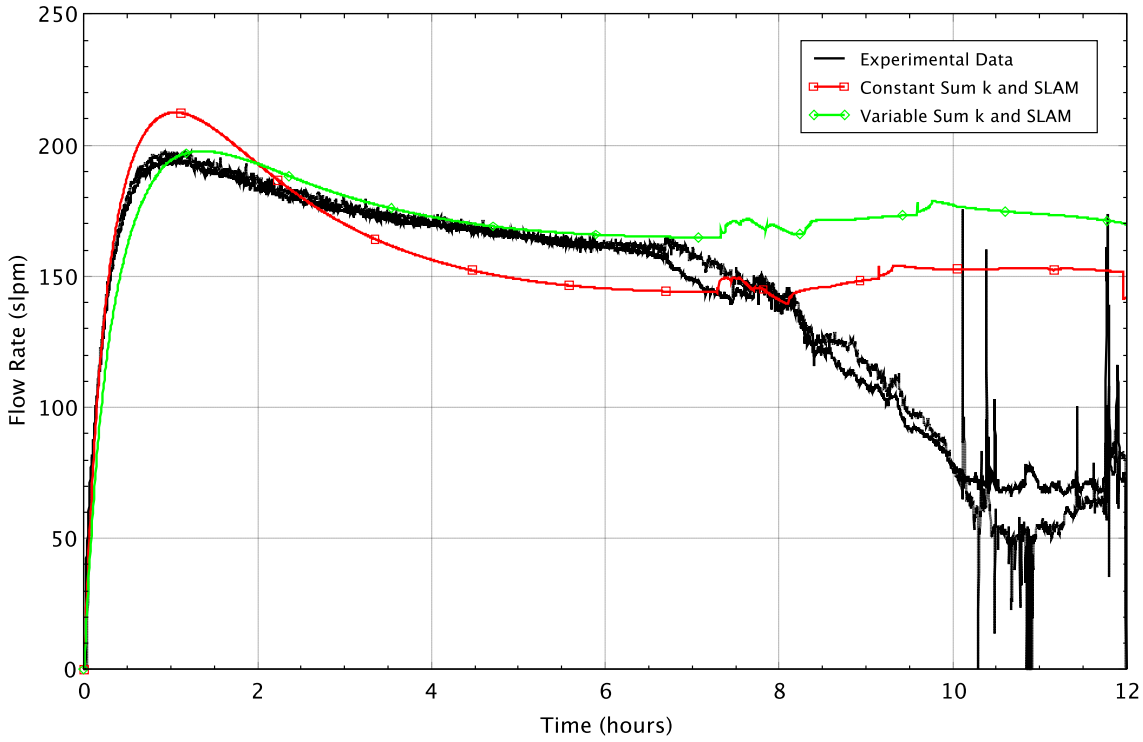

Figure 5.47 Flow rate in central assembly for 15 kW ignition test using the 2-ring model

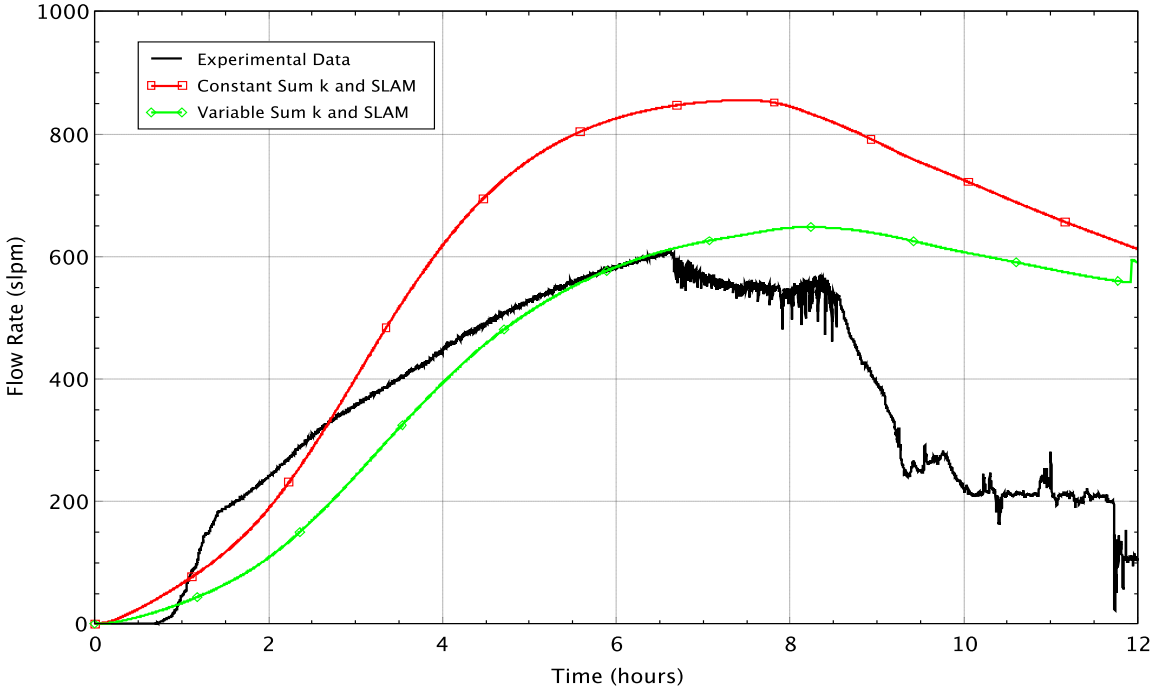

Figure 5.48 Flow rate in peripheral assemblies for 15 kW ignition test using the 2-ring model

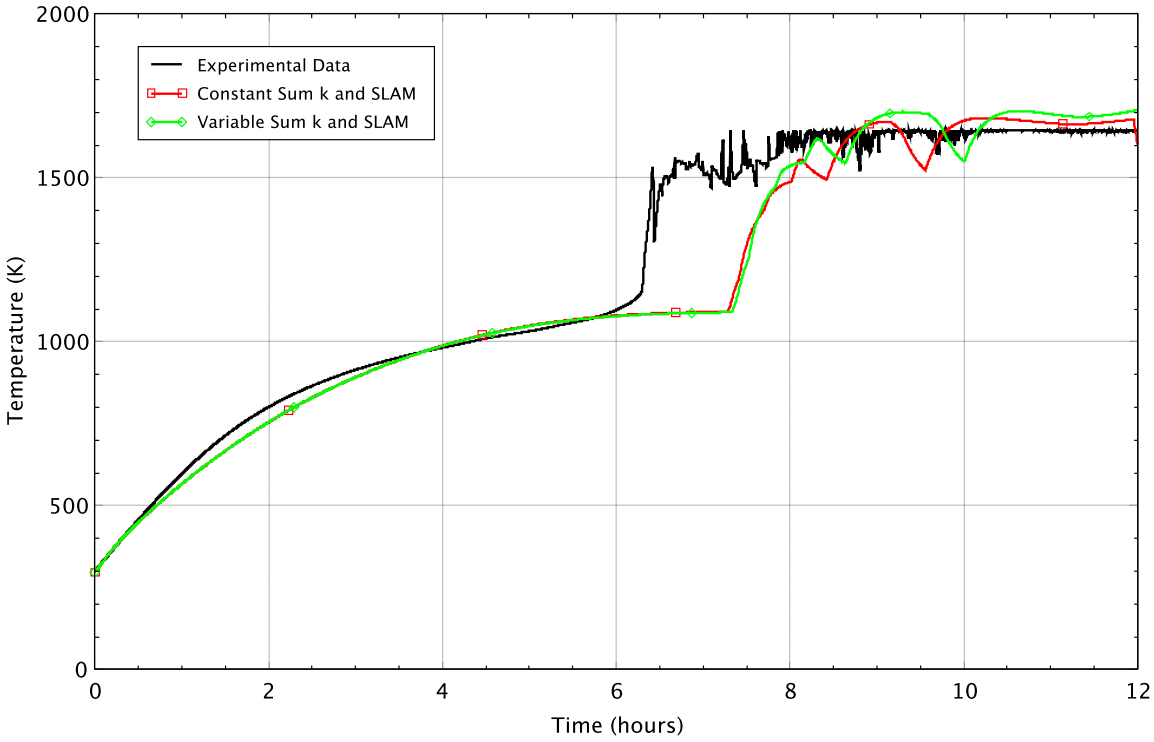

Figure 5.49 PCT in center assembly for 15 kW ignition test using the 2-ring model

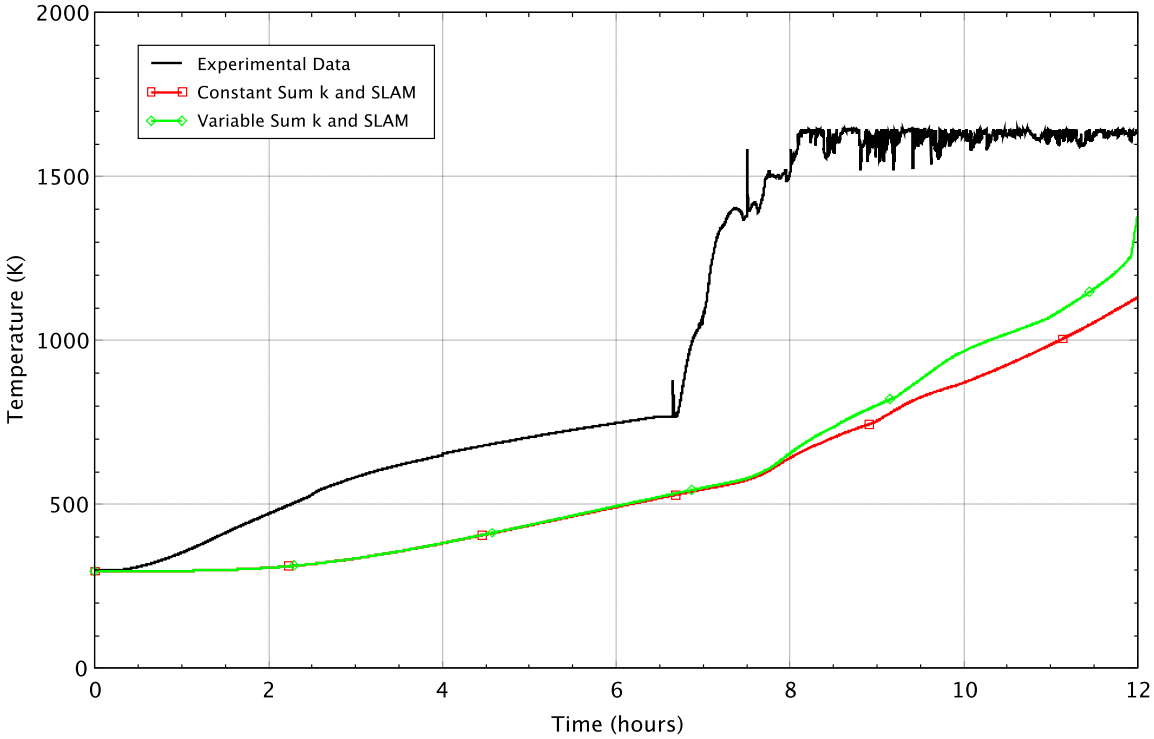

Figure 5.50 PCT in peripheral assemblies for 15 kW ignition test using the 2-ring model

5.6.2 Transition from pre- to post-breakaway oxidation kinetics

As discussed in Section 5.2.3, the coefficients in Equation 5.2 for the breakaway lifetime as a function of temperature were obtained by log-linear regression on experimental data obtained in tests performed at ANL and were subject to some uncertainty due to measurement error and to scatter in the data (See Figure 5.6). In order to understand the experimental results and assess the effect of the uncertainty, two sensitivity calculations were performed. The first is the use of a different oxidation model and the second is through the use of both low and high temperature pre-breakaway oxidation kinetics.

For the first sensitivity, an independent oxidation kinetics model was used. This model, which was recently added to the MELCOR code, was developed at the Paul Scherrer Institute and is referred to as the PSI oxidation kinetics model in this report. The PSI oxidation kinetics model was based on multiple separate and integral effects tests and is described in detail in Reference 15. While this model uses pre-breakaway parabolic kinetics similar to the default MELCOR model, it also includes the use of oxide thickness, linear kinetics, accelerated linear kinetics and a transition phase.

In the previous BWR spent fuel pool analysis (Ref. 18) it was discovered that better agreement to the test data could be made with use of both low and high temperature pre-breakaway oxidation kinetics correlations (see Section 8.4 of Reference 18). A sensitivity run was made where the high temperature oxidation rate was defined as 5.3 times that of the base (low temperature) oxidation rate. The factor of 5.3 is what was used in Reference 18. A transition from the low to high temperature oxidation rates was set to occur over the range 1,000 K [1,340°F] to 1,100 K [1,520°F]. This transition range is somewhat different than that used in the previous BWR analysis, as the values selected here were based on the PWR experimental data which showed a larger difference between PCT and average temperature than the BWR data. The transition region and new high temperature pre-breakaway kinetics are shown in Figure 5.51.

All sensitivities were made using the 2-ring multiple rod model. Figures 5.52 through 5.58 present results from four cases: 1) default oxidation kinetics using ANL data best fit coefficients, 2) default oxidation kinetics using ANL data lower uncertainty coefficients, 3) PSI oxidation model and 4) low and high temperature pre-breakaway oxidation kinetics.

Figures 5.52 and 5.53 present the peak cladding temperature in the center assembly at two different scales. As seen in these figures, the case using the ANL data best fit correlation approaches ~1,050 K [1,430°F] and reaches a quasi-steady condition where the total heat generated (core power and oxidation heat) is balanced by the convective and radiative heat losses. This results in a significant delay in ignition timing compared to the experiment. The system remains at this quasi-steady condition until the time-at-temperature is reached and breakaway occurs, which significantly increases the oxidation heat generated and leads to ignition. From Figure 5.6, it is seen that at 1,050 K [1,430°F] the time to breakaway is approximately 4 hours. In the case where the ANL data lower uncertainty curve is used, the time to breakaway (at the same temperature) is only 1 hour and demonstrates the large uncertainty in the breakaway data. When the lower uncertainty curve is used, the default oxidation kinetics model predicts ignition ~45 minutes before the experiment.

In addition to the difference in timing of breakaway (based on the best fit and lower uncertainty correlations) it appears that there is too little oxidation heat generated in the default oxidation model. In order to see the effect of additional oxidation heat, a high-temperature oxidation correlation was used (as described above). When using the low and high temperature oxidation correlations, the PCT does not reach a quasi-steady condition and increases at a rate slightly larger than the test data and shows ignition time is in excellent agreement with the experiment. The PSI model shows good agreement with the test data and predicts ignition about 30 minutes earlier than the experiment.

Figure 5.54 shows the peak cladding temperature in the peripheral region. Overall, these results are consistent with the center assembly and show delays from 30 to 60 minutes between center assembly ignition and peripheral assembly ignition. The PSI model adds more oxidation heat than the other models which results in a shorter time (30 minutes) between center and peripheral ignition. Table 5.4 shows ignition times for the sensitivity cases.

Figure 5.55 shows the total oxidation heat generation rate in the core. This figure shows that once breakaway occurs, significantly more oxidation heat is generated, leading to ignition. Figure 5.56 shows the change in center assembly peak cladding temperature over time (DT/dt). This figure shows that all the MELCOR cases show good agreement with the test data up through ~4.5 hours. At this time, all MELCOR cases and the experimental data show a PCT around 1,025 K [1,385°F]. In the case with the default oxidation kinetics and use of ANL best fit correlation, the DT/dt drops to zero while the data shows DT/dt levelling off around 50 K/hr [90°F/hr] and then increasing. In the case where the ANL lower uncertainty correlation is used, a sharp increase is seen just after 5 hours when breakaway occurs. The PSI model shows a more gradual increase after 5 hours and begins increasing faster than the data. The low and high temperature pre-breakaway oxidation kinetics case shows a much more gradual increase similar to the test data, however, it occurs earlier than the test data.

Figures 5.57 and 5.58 show the ignition propagation in the center and peripheral assemblies respectively. As seen in these figures the case with the low and high temperature pre-breakaway oxidation kinetics shows excellent agreement with the experiment. The default kinetics with ANL lower uncertainty correlation and the PSI model show similar results where ignition occurs earlier than the experiment. The case with default oxidation kinetics and the ANL best fit correlation show ignition is delayed over the experiment. In all cases, the rate of ignition propagation downward is in excellent agreement with the test data.

Overall, oxidation kinetics plays a significant role in this experiment. The default correlation in MELCOR tends to under predict the oxidation heat generated around 1,050 K [1,430°F] which results in a delay in breakaway. A sensitivity case with the ANL lower uncertainty correlation shows that the experimental data falls within the uncertainty range of the ANL data. The results indicate that there is reasonable uncertainty in the breakaway lifetime correlation that can yield a range of ignition times for this test spanning at least several hours. The use of low and high temperature pre-breakaway oxidation kinetics correlations resulted in excellent agreement to the experimental test data. The use of the PSI oxidation model resulted in good agreement with the test data showing ignition about 30 minutes early. Overall, the oxidation kinetics and the breakaway lifetime correlation are very important determinants of the predicted test results.

Table 5.4 Ignition times for the 15 kW ignition test

Description	Time of ignition*	
	Center	Peripheral
Experiment	6.31 hours	7.08 hours
2-ring multiple rod, ANL data best fit correlation	10.1 hours	10.9 hours
2-ring multiple rod, ANL data lower uncertainty correlation	5.62 hours	6.67 hours
2-ring multiple rod, PSI oxidation model	5.83 hours	6.38 hours
2-ring multiple rod, low and high temperature pre-breakaway oxidation kinetics	6.28 hours	7.27 hours

* Ignition defined when temperature exceeds 1,200 K [1,700°F].

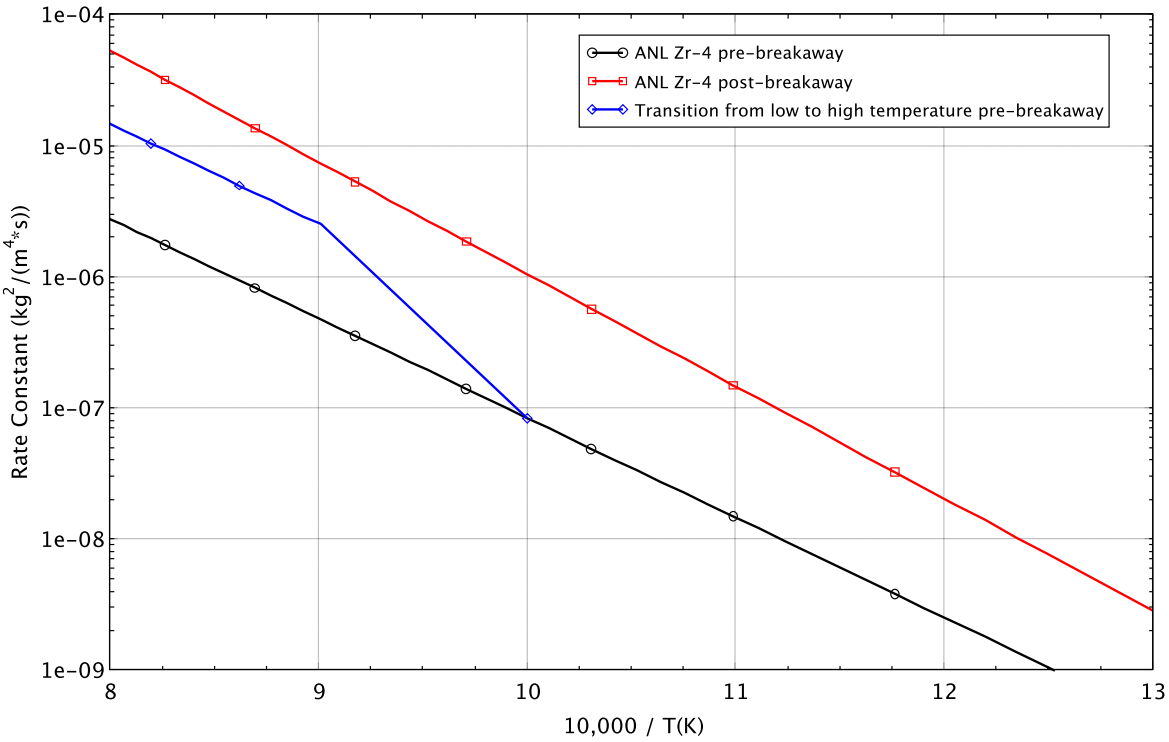

Figure 5.51 Modification of the default MELCOR oxidation kinetics model

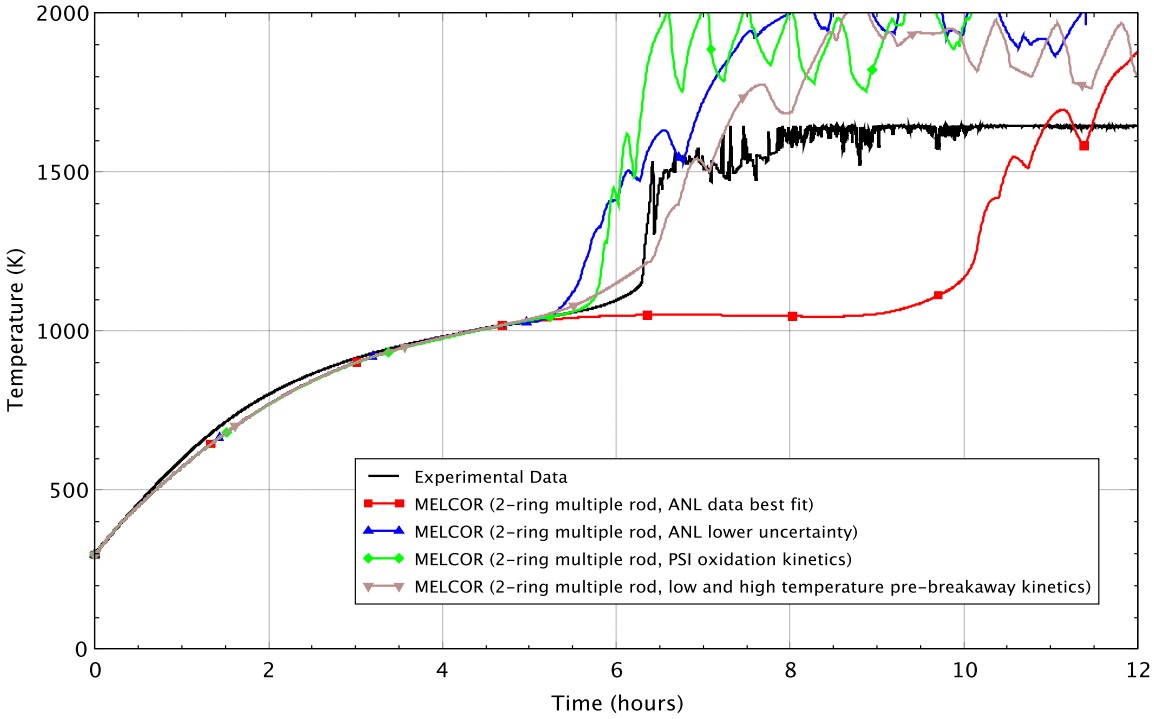

Figure 5.52 Peak cladding temperature in the center assembly for the 15 kW ignition test

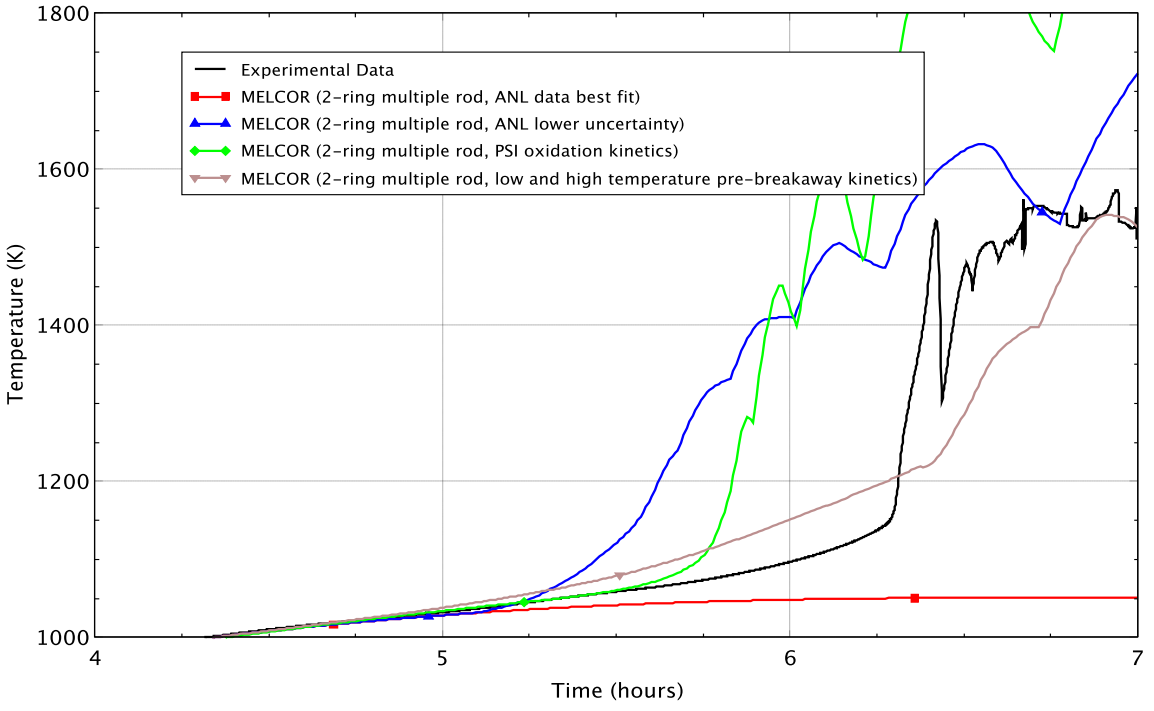

Figure 5.53 Peak cladding temperature in the center assembly for the 15 kW ignition test

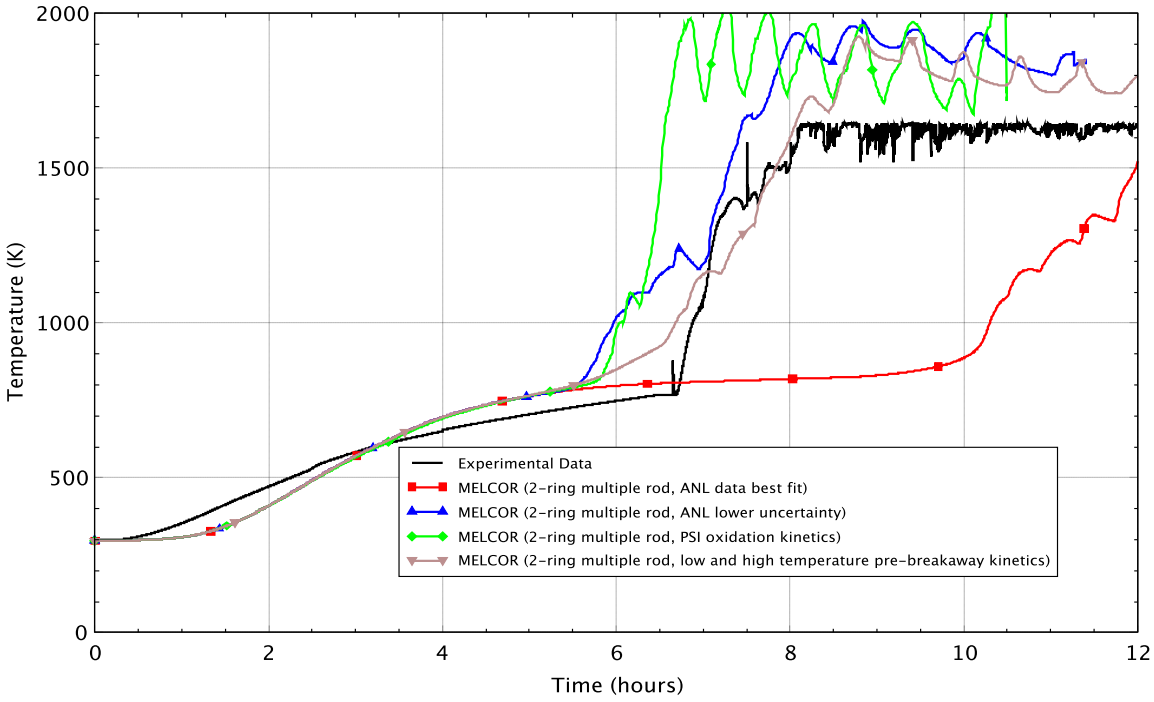

Figure 5.54 Peak cladding temperature in the peripheral assemblies for the 15 kW ignition test

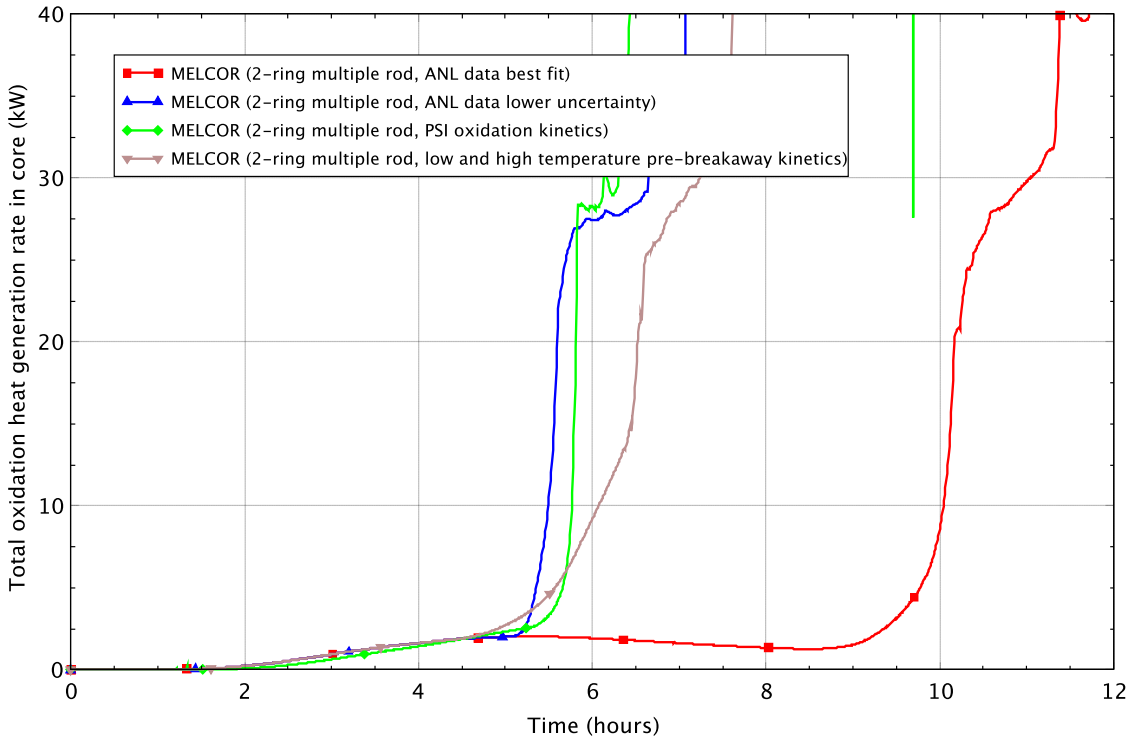

Figure 5.55 Total oxidation heat generation rate in core for the 15 kW ignition test

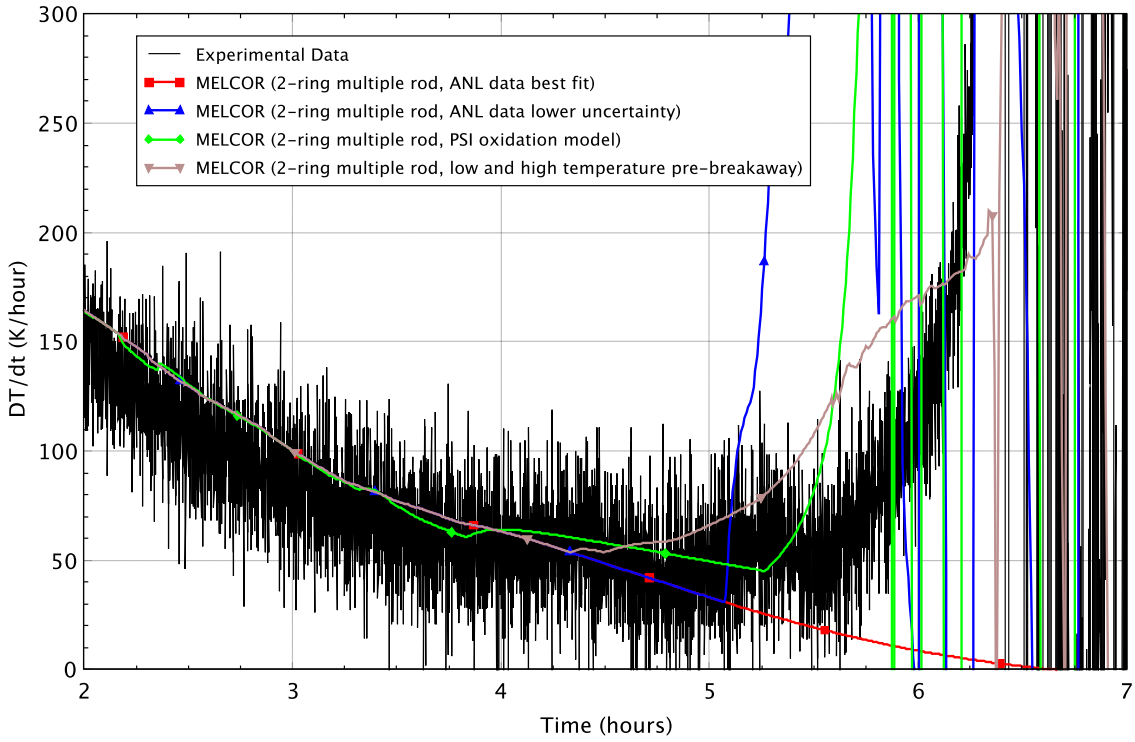

Figure 5.56 Center assembly peak cladding temperature DT/dt for the 15 kW ignition test

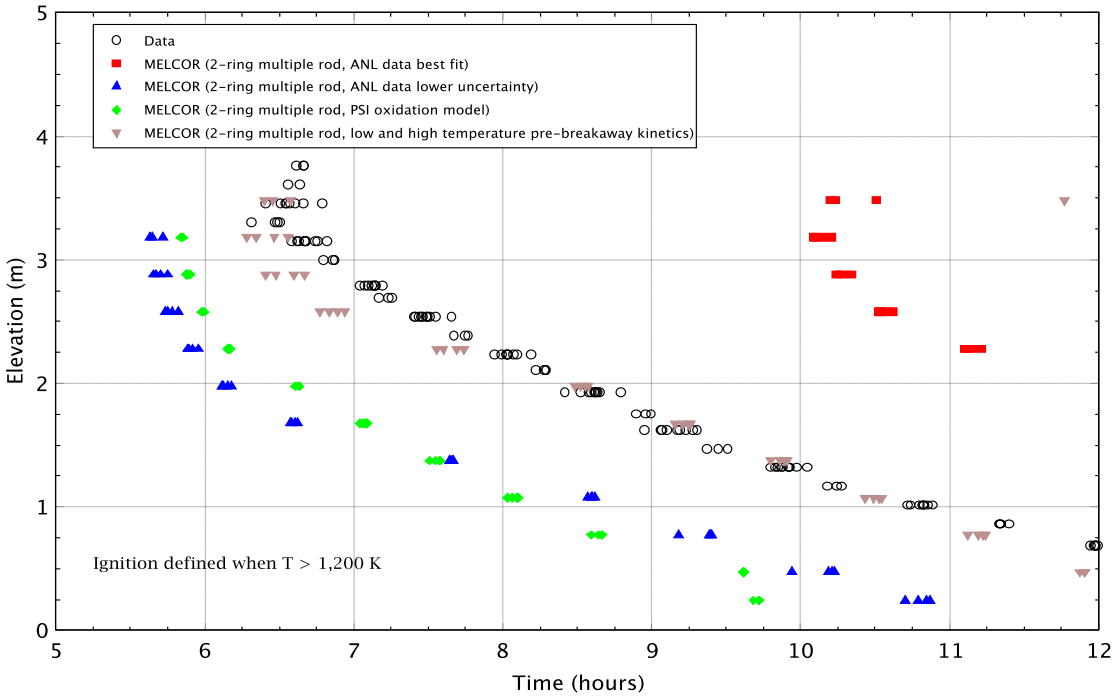

Figure 5.57 Central assembly ignition propagation for the 15 kW ignition test

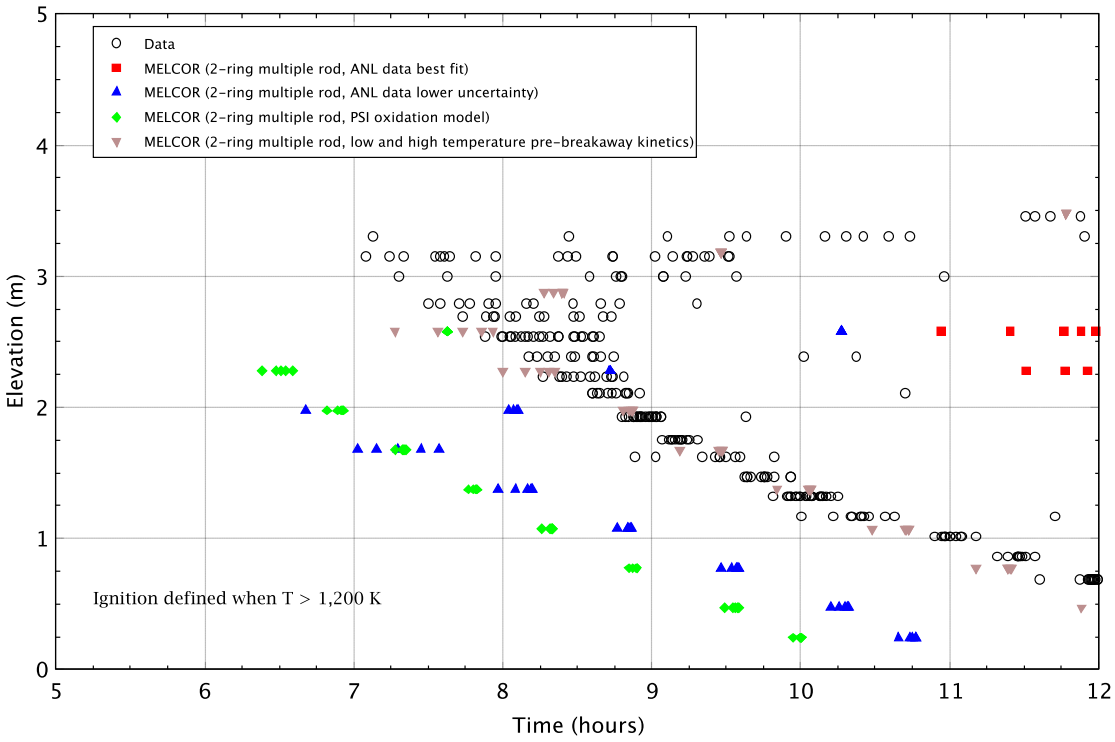

Figure 5.58 Peripheral assemblies ignition propagation for the 15 kW ignition test

6 SUMMARY

6.1 Phase II Test Results

Nine pre-ignition test were conducted with powers ranging from 1 kW to 15 kW which represented assemblies from as old as 96 months to as young as 3 months after offload (assuming 45 GWd/MTHM burnup). The pre-ignition tests were conducted for 12 hours or until the peak cladding temperature of 900 K [1,160°F] was reached in the center assembly. Tests conducted at powers greater than 8 kW were terminated before 12 hours. Tests at 1 kW and 4 kW were conducted for 24 hours in attempts at achieving steady state. As a measure of repeatability, the 4 kW power was tested twice, once for 12 hours and again for 24 hours.

The second stage of the OECD/NEA Spent Fuel Pool Project successfully concluded with the ignition of the Phase II test assembly on June 6, 2012. The total applied power to the center assembly was 15 kW, which represented an assembly with a 45 GWd burnup approximately 3 months after offload. The center assembly was surrounded on four sides by unpowered, peripheral assemblies. This configuration represented a “cold neighbor” configuration in a spent fuel pool. All five fuel assemblies were completely consumed as a result of the Zircaloy cladding fire. In addition, all of the pressurized fuel elements in the two pressurized, peripheral fuel bundles ballooned as a result of exposure to temperatures experienced during the ignition test.

Ignition of the Zircaloy was first observed in the center fuel assembly at the z = 3.302 m [130 in] level and at an elapsed test time of 6.31 hours based on a thermal criterion of 1,200 K [1,700°F]. The fire initially burned both upward and downward from this level but failed to reach the uppermost portion of the center assembly before becoming oxygen starved. The ignition front primarily swept down the fuel assemblies toward the most abundant source of oxygen at the assembly inlet. The burn progressed at an average rate of 0.457 m/hr [18 in/hr]. The cladding fire also propagated transversely into the peripheral assemblies starting at t = 7.08 h and at the z = 3.150 m [124 in] level. The ignition had progressed across the entire cross section of all of the peripheral assemblies by t = 8.74 hr. Examination of the individual peripheral assemblies revealed a degree of asymmetry in the propagation into the peripheral assemblies by up to 0.27 hours. This asymmetry is not ascribed to the ballooning events in the pressurized assemblies but is rather most likely due to the limitations of construction and the chaotic nature of the Zircaloy fire.

The ballooning events in the two assemblies occurred within approximately 3 minutes of each other at a given location despite the North and South assemblies being filled to different pressures, 6.2 MPa [900 psi] and 5.2 MPa [750 psi] respectively. Ballooning did not likely occur at a single axial level but rather between z = 2.692 and 3.302 m [106 and 130 in] based on PCT data at the time each rod ballooned. The thermal-hydraulic behavior of assemblies with ballooned rods did not appear to be discernible from the unpressurized assemblies.

A residual gas mass spectrometer was used to monitor the concentrations of the gas constituents exiting the center assembly over a 130 hour period. The gas constituents monitored were nitrogen, oxygen, argon, water, carbon dioxide, and helium. Since argon and helium are inert noble gases and do not react with zirconium, the concentration of these gases relative to the reactive gas species provides a measure of the removal and release of the reactive gases. The analysis shows two distinct stages of oxidation over the course of the test. The primary oxidation stage was very energetic and continued for 11 hours after ignition. During this stage all the oxygen entering the assembly was consumed by oxidation of zirconium

and a substantial portion of the nitrogen was consumed by production of the nitride from much (if not most) of the remaining unoxidized zirconium. During the 88 hour long second oxidation stage, all of the oxygen entering the assembly was consumed by the oxidation of zirconium nitride as indicated by the release of nitrogen gas. The additional release of energy from the wholesale production of zirconium nitride coupled with the significant reduction in convective energy removal during the primary oxidation stage are important phenomena to consider when assessing the propensity of an ignited assembly to propagate ignition to adjacent assemblies.

Finally, Table 6.1 lists a summary of events during the SFP Project Phase II ignition test. This list is not exhaustive but is intended to highlight the most significant events as judged by the authors.

Table 6.1 Summary events during the SFP Phase II ignition test

Local Time (MDT)	Elapsed Test Time (h)	Event
6/6/12 0:00	-0.02	Data file started
6/6/12 0:01	0.00	Test start, >95% of 15 kW
6/6/12 6:19	6.31	Max center temperature = 1,200 K [1,700°F], ignition at *z* = 3.302 m (C_J-9_130)
6/6/12 6:32	6.54	[O_2] in center assembly measured by RGA dropped below 10%
6/6/12 6:41	6.67	First pressurized rod ballooned
6/6/12 6:41	6.68	Heater rod power lost
6/6/12 6:41	6.82	Transverse propagation across center complete at *z* = 3.150 m (C_A-1_124)
6/6/12 7:05	7.08	Max peripheral temperature = 1,200 K [1,700°F], ignition at *z* = 3.150 m (N_J-3_124)
6/6/12 7:35	7.50	CYBL vessel exhaust fan activated
6/6/12 7:42	7.70	Nitrogen consumption by zirconium nitride (ZrN) formation began
6/6/12 8:13	8.22	[O_2] in South assembly dropped below 10%
6/6/12 8:32	8.53	[O_2] in East assembly dropped below 10%
6/6/12 8:33	8.54	Last pressurized rod ballooned
6/6/12 8:36	8.60	[O_2] in West assembly dropped below 10%
6/6/12 8:45	8.74	Transverse propagation across peripherals complete at *z* = 2.388 m (N_J-1_94)
6/6/12 8:46	8.77	[O_2] in North assembly drops below 10%

Table 6.1 Summary events during the SFP Phase II ignition test (Cont'd)

Local Time (MDT)	Elapsed Test Time (h)	Event
6/6/12 12:18	12.29	Axial propagation in center to z = 0.559 m (C_J-9_22)
6/6/12 12:54	12.91	Data acquisition failure
6/6/12 17:24	17.40	Net nitrogen consumption ends, nitrogen release by ZrN oxidation dominates
6/8/12 22:43	70.70	[O_2] measured by RGA rises above 10%, O_2 consumption and N_2 release ending
6/10/12 4:01	100.00	All oxidation complete

6.2 MELCOR Results

Three MELCOR models were developed to simulate the OECD/NEA SFP Phase II experiments. These models included a 9-ring model, a 2-ring model and a 2-ring model with multiple rods/ring. The ignition test is characterized by the conditions of ignition in a central fuel assembly and the propagation of the burn to peripheral unheated assemblies. However, the 2-ring model used with the current release version of MELCOR is unable to capture this phenomenon accurately because it cannot account for the large temperature gradient across the fuel assemblies that was observed in the experiments and necessary to predict radiant heat transfer and local ignition conditions. Code modifications were made to MELCOR Version 2.1.5287 which increase the number of fuel rod components available in a single ring and allow the user to simulate the test with much greater fidelity. MELCOR was successfully validated and this analysis shows that MELCOR is capable of predicting the conditions of the OECD/NEA SFP experiment with either a 9-ring or the 2-ring multiple rod model. The 2-ring multiple rod model (which was the focus of this analysis) shows good agreement to important parameters such as PCT, ignition time and ignition propagation when compared to the experimental test data when uncertainties in the oxidation kinetics are considered. When using the default oxidation kinetics model, better agreement to the experimental test data was found when using the lower uncertainty curve for breakaway timing over the best fit curve.

The new 2-ring multiple rod model has also been compared to the 9-ring model and comparisons show that while not identical, the new modeling is able to predict a similar response. The detailed 9-ring model did show slightly better agreement to the test data in terms of ignition timing in the center assembly than the 2-ring multiple rod model when using the code defaults for oxidation kinetics. As a result of the new code modifications that allow multiple rods/ring, code performance is improved and the 2-ring multiple rod input model is greatly simplified over the 9-ring model. It should be noted that the code modifications described are a work in progress and the models are currently strictly valid up until material begins to relocate. Further model development and refinement is necessary before these changes become part of a release version of MELCOR.

Two sensitivity studies were performed for simulation of the Phase II tests to investigate the effects on key figures-of-merit. The sensitivities on hydraulic loss coefficients showed that the MELCOR computed flow rate can better match the experimental data when variable loss coefficients are used, rather than constant values. These sensitivities also showed that the flow

rate had little difference on fuel rod temperatures in all but the lowest powered case (1 kW pre-ignition test). For situations where radiation heat transfer is the dominate heat transfer mode, the use of constant hydraulic loss coefficients is acceptable. For situations where convective heat transfer is dominate, variable hydraulic loss coefficients are recommended.

The sensitivities on pre- to post-breakaway oxidation kinetics showed that the results are highly sensitive to both oxidation kinetics and the transition to breakaway. Results from the sensitivities show that the predicted time of ignition can vary up to several hours based on the selection of individual models and selected modelling parameters. When using the default oxidation kinetics and default lifetime model (best fit curve in Figure 5.6), ignition times were delayed up to several hours, however, when using the lower uncertainty curve with the lifetime model, ignition times occurred about 45 minutes prior to that of the experiment. The PSI oxidation model was found to be more conservative than the default MELCOR model leading to ignition occurring 30 minutes prior to the experiment. Excellent agreement in ignition timing was obtained when using both low and high temperature pre-breakaway oxidation kinetics where the high temperature rate correlation was increased by a factor of 5.3 over the low temperature correlation as was done in the previous BWR study.

7 REFERENCES

1. NUREG/CR-7215, “Spent Fuel Project Phase I: Pre-Ignition and Ignition Testing of a Single Commercial 17×17 Pressurized Water Reactor Spent Fuel Assembly under Complete Loss of Coolant Accident Conditions,” U.S. Nuclear Regulatory Commission, Washington, DC, March 2016.

2. B.J. Ade and I.C. Gauld, 2011, “Decay Heat Calculations for PWR and BWR Assemblies Fueled with Uranium and Plutonium Mixed Oxide Fuel Using SCALE,” ORNL/TM-2011/290.

3. International Atomic Energy Agency, 2007, “Current Trends in Nuclear Fuel for Power Reactors,” 51st IAEA General Conference.

4. Y.S. Touloukian, and E.H. Buyco, *Thermophysical Properties of Matter. Vol 5: Specific Heat of Nonmetallic Solids*, IFI/Plenum, New York – Washington, 1970, pp. 142-144, Table 42, Curve 10.

5. G.A. Berna, C.E. Beyer, K.L. Davis, and D.D. Lanning, “FRAPCON-3: A Computer Code for the Calculation of Steady-State, Thermal-Mechanical Behavior of Oxide Fuel Rods for High Burnup”, NUREG/CR-6534 Vol. 2, PNNL-11513 v.2, 1997, pp. 2.19-2.21.

6. Y.S. Touloukian, R.W. Powell, C.Y. Ho, and P.G. Klemens, *Thermophysical Properties of Matter. Vol 2: Thermal Conductivity Nonmetallic Solids*, IFI/Plenum, New York – Washington, 1970, pp. 159-165, Table 27, Curves 62 to 70.

7. G. Zigh, and A. Velázquez-Lozada, “Experiments on Ignition of Zirconium-Alloy in a Prototypical Pressurized-Water Reactor Single Fuel Assembly in a Spent Fuel Pool During a Complete Draindown” *J. Nuclear Engineering*, Submitted for Publication (2013)

8. M. Steinbrück, “Prototypical experiments relating to air oxidation of Zirconium-4 at high temperatures,” *J. Nucl. Mater*. 392, 531-544 (2009).

9. M. Steinbrück, and M. Jung, “High-temperature reaction of α-Zr(O) with nitrogen,” Proceedings of ICAPP 2011, Nice, France, May 2-5, 2011, Paper 11395.

10. L. Krusin-Elbaum, and M. Wittmer, “Oxidation kinetics of ZrN thin films,” *Thin Solid Films, 107* (1983) 111-117.

11. NUREG/CR-6119, “MELCOR Computer Code Manuals, Vol. 1: Primer and Users’ Guide, Version 1.8.6,” U.S. Nuclear Regulatory Commission, Washington, DC, September 2001.

12. F.P. Incropera, and P. DeWitt, Fundamentals of Heat and Mass Transfer, John Wiley & Sons (1998).

13. NUREG/CR-6846, “Air Oxidation Kinetics for Zr-Based Alloys,” U.S. Nuclear Regulatory Commission, Washington, DC, July 2004.

14. NUREG/CR-7144, “Laminar Hydraulic Analysis of a Commercial Pressurized Water Reactor Fuel Assembly,” U.S. Nuclear Regulatory Commission, Washington, DC, January 2013.

15. Jonathan Birchley and Leticia Fernandez-Moguel, "Simulation of air oxidation during a reactor accident sequence: Part 1 – Phenomenology and model development," Annals of Nuclear Energy 40 (2012), pp. 163–170.

16. ANSYS FLUENT User Guide Version 14.5, ANSYS, Inc., Canonsburg, PA, 2012.

17. ANSYS FLUENT Theory Guide Version 14.5, ANSYS, Inc., Canonsburg, PA, 2012.

18. NUREG/CR-7143, “Characterization of Thermal-Hydraulic and Ignition Phenomena in Prototypic, Full-Length Boiling Water Reactor Spent Fuel Pool Assemblies After a Postulated Complete Loss-of-Coolant Accident,” U.S. Nuclear Regulatory Commission, Washington, DC, March 2013.

19. S.G. Durbin, and E.R. Lindgren, “Characterization of Hydraulic and Ignition Phenomena of Pressurized Water Reactor Fuel Assemblies: Phase II Test Plan”, SANDIA report SAND2012-1447, March 2012.

APPENDIX A – EXHAUST GAS ANALYSIS DETAILS

A.1 Introduction

The sampling and analysis of the gas stream exiting the center assembly was performed with an in-house built sample conditioning system coupled to a mass spectrometer (Pfieffer Model GSD 300T). With the Pfeiffer GSD 300T RGA, gases were ionized by a tungsten filament. These ions were filtered by the quadrapole mass spectrometer and then detected and amplified by the secondary electron multiplier (SEM). The SEM produced an electric current for each unique ion species, which was converted into gas concentrations and gas concentration ratios.

The gases of interest and the ion masses monitored were helium (4.0), water (18.0), nitrogen (28.0 and 14.0), oxygen (32.0 and 16.0), argon (40.0) and carbon dioxide (44.0). The analysis of these eight ions was recorded every 10 seconds.

A.2 Instrument Calibration

The responses for all the ions analyzed drifted due to temperature changes, filament age, instrument usage since refurbishment, and changes in baseline offset. In order to quantify instrument drift and signal deterioration, ambient air was sampled every two hours. During this two-hour sample gas period, measurements (cycles) were made about every 10 seconds for a total of 688 cycles. After two hours, a baseline offset calibration was performed and a three-way valve was activated to change the input gas to ambient air, which was sampled for about three minutes or a total of 18 cycles.

A.2.1 Baseline Drift Correction

The baseline offset calibration feature was used to reset the baseline value for signal noise to a standard current value, which was determined by averaging the signal in a region of the mass spectrum that typically has no current signal from the sample. Sample currents for all the different gas species were measured relative to this low baseline value. The offset calibration was performed every two hours, just before the analysis of ambient air. For the calibration, the collection tubing, fixtures, and fittings were purged with ambient air for two minutes. After the purge, the offset calibration was performed followed by the ambient air measurement. Figure A.1 shows the raw current for each ion analyzed as a function of time. The baseline offset calibration resulted in significant discontinuity of the currents before and after calibration for the minor components, helium and carbon dioxide. The discontinuity reflects the amount of baseline drift that occurred over the 2-hour sample analysis period. The direction and magnitude of the discontinuity changed over a 24 hour diurnal cycle suggesting the cause is due to small temperature changes in the gas sample ambient temperature. The baseline drift was corrected by assuming that the current for a given species should be the same before and after each calibration cycle. The required offset was added proportionally to each data point based on the time since the last calibration. The actual correction also included a 30 point moving average smoothing. The adjustment assumed a linear drift in baseline correction between calibration points. The effect of applying this treatment to the data was to smooth ridges caused by recalibration of the instrument and to set responses relative to the level of baseline noise. Figure A.2 shows the raw ion currents after the baseline offset correction and smoothing. The correction is applied to all species for all times except between about 5.3 hours and 11.2 hours when only helium is corrected. Over this period the uncorrected raw data for all species except helium are used so that the step changes in concentration due to rapid gas reaction with zirconium, argon release during rod ballooning and air infiltration into the gas sample are preserved unaltered.

A.2.2 Sensitivity Drift Correction

Figure A.2 also shows that a downward drift in overall sensitivity is evident for all ions analyzed. The gas sample consisted of ambient air near the beginning of the test (time zero) and at the end of the test (time 130 hours). The difference between the initial and final current for each ion is a measure of sensitivity drift over the test period. After 130 hours of analysis, the total drift for argon was about a factor of four.

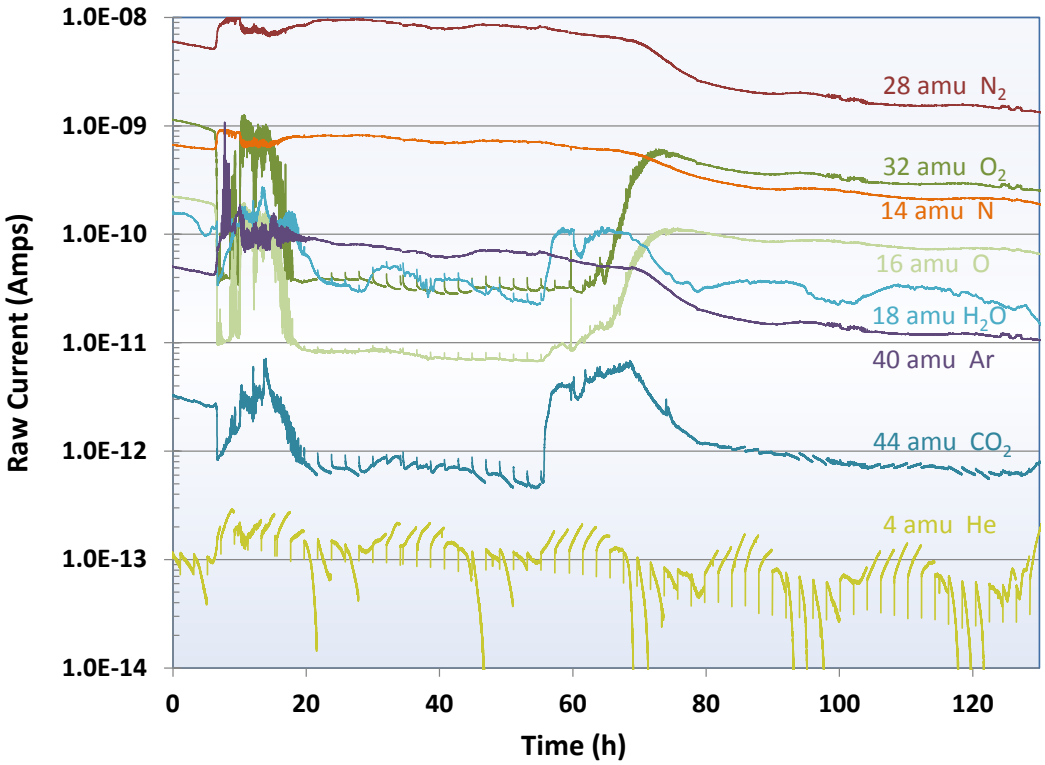

Figure A.1 Raw currents for all ions monitored.

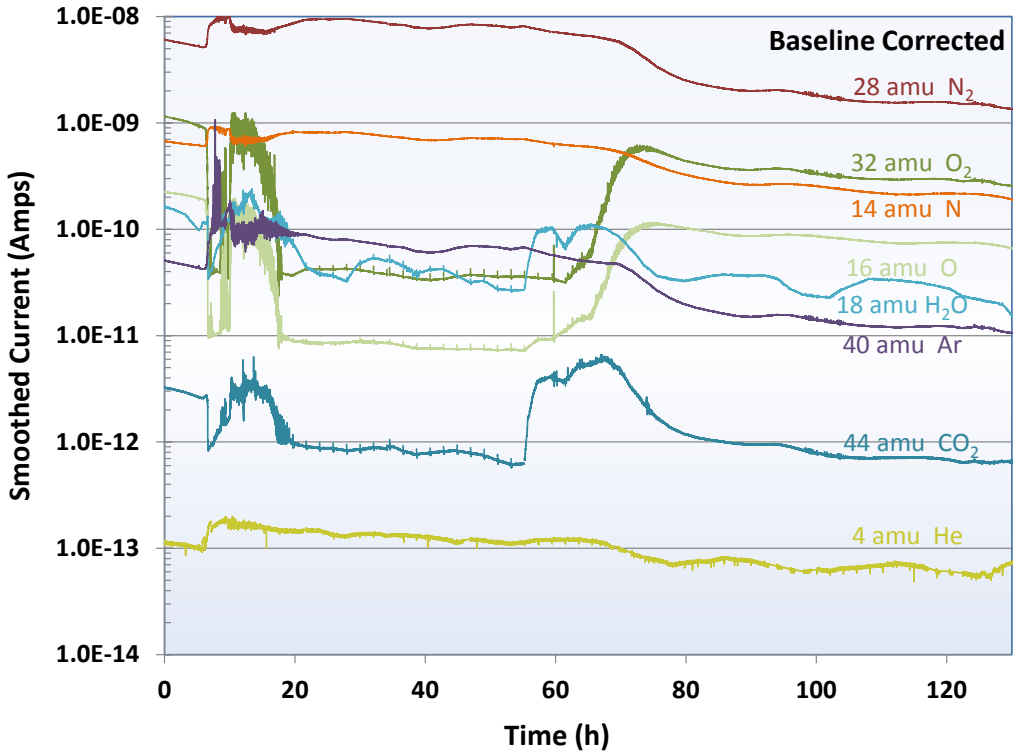

Figure A.2 Baseline corrected currents for all ions.

The baseline corrected currents were used to determine the responses for all the major components of air including, helium, water, nitrogen, oxygen, argon and carbon dioxide. The two ions measured for nitrogen and oxygen were summed to yield a single current for these two gas species. The current value of each air component was divided by the sum of all currents on a dry basis (water is excluded) to determine the response ratio for each gas.

The response ratios determined from the analysis of ambient air every two hours served as a running calibration for determining the molar or volumetric fraction of each gas species in the sample gas. The accepted concentration of a given species in ambient air (see e.g. http://en.wikipedia.org/wiki/Atmosphere_of_Earth) was divided by the corresponding response ratio derived from the analysis of ambient air to generate a calibration factor. The concentration of a given species was determined by multiplying the response ratio generated by the analysis of the unknown sample gas by the corresponding calibration factor generated by the analysis of ambient air.

Each calibration period yielded slightly different correction values for equivalent gases. The difference between one value and the next was attributed partly to instrument drift and ambient temperature changes. A single two-hour sample analysis period was adjoined by two calibration periods. The two sets of correction factors were applied to the response ratios for a set of 688 sample gas measurements. The multiplier used to make the correction was calculated by linearly weighting the two sets of correction factors relative to the placement of the measurement with the calibration interval.

A.2.3 Calibration Correction for Low Oxygen

Over the entire test period, the oxygen content of the gas mixture exiting the top of the assemblies varied between normal ambient air and very low oxygen levels. The RGA response for nitrogen and argon (the primary gas species besides oxygen) were different when oxygen was part of the mixture versus the response when oxygen was mostly absent. The use of air as a calibration gas was appropriate when the oxygen concentration was above 11 percent; however, using an air calibration when the oxygen levels were below 11 percent resulted in a nitrogen concentration error of greater than 2 percent. Calibration factor correction relationships were derived for nitrogen and argon when oxygen was mostly absent in the sample gas. Five calibration gases described in Table A.1 were employed to derive these calibration curves.

Table A.1 Calibration gases for the RGA

Calibration gas	Ar	Balance N_2	N_2/Ar	Normalized N_2/Ar
1	0.71%	99.29%	139.8	1.67
2	0.89%	99.11%	111.4	1.33
3	1.18%	98.82%	83.7	1.00
4	1.76%	98.24%	55.8	0.67
5	3.54%	96.46%	27.2	0.33

The five certified calibration gases were sampled the day before the ignition test began and the day after sampling was terminated. The response ratios for the calibration gases were evaluated against the correction factors for nitrogen and argon derived from using ambient air as a calibration gas. This was done to determine the apparent measured concentration of nitrogen and argon in low-oxygen conditions from using ambient air as a standard. The measured concentrations of nitrogen and argon from the pre- and post- test calibrations were averaged. The resulting correlations between the average measured concentration and the certified concentration are shown in Figures A.3 and A.4. It was important to establish this relationship because ambient air was used as a standard for calibration of gases in the sample stream during periods when there was very little oxygen present.

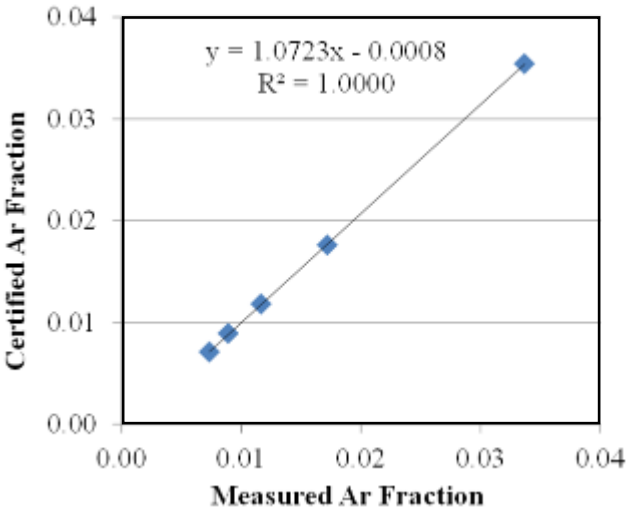

Figure A.3 Calibration correlation for argon.

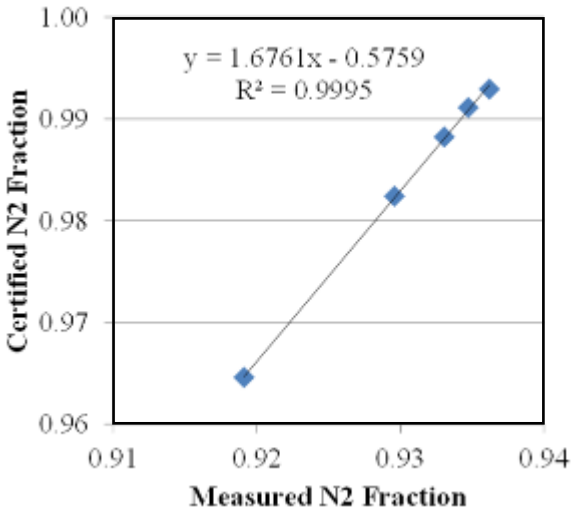

Figure A.4 Calibration correlation for nitrogen.

The correction correlations were used to correct the measured nitrogen and argon concentrations when the oxygen concentration in the sample stream was less than 11 percent. Figure A.5 shows the sample gas composition as a function of time over the entire 130 hour test period.

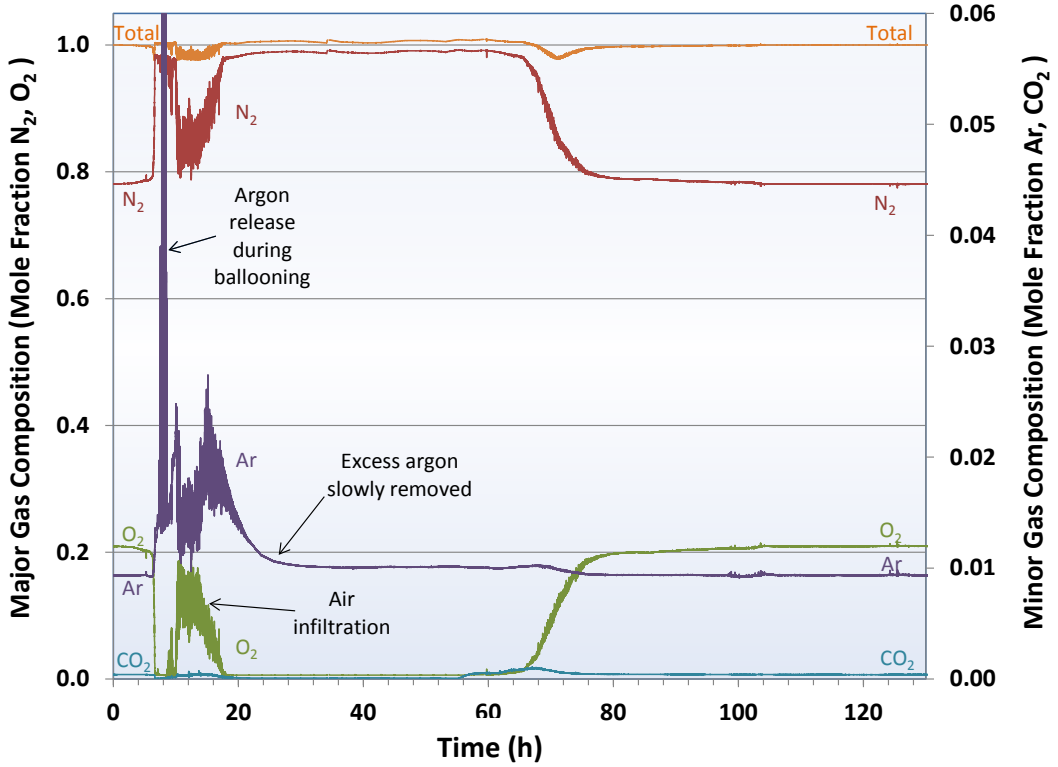

Figure A.5 Mole fraction concentration of major and minor constituents of sample gas.

Also shown on Figure A.5 is the total of all mole fractions, which should be unity. Any deviation from unity is a measure of the total error in the analytical scheme. From time zero until ignition

at 6.3 hours and again from about hour 80 to the end of sampling, oxygen concentrations were at ambient levels and the total was unity. From about 20 to 70 hours the oxygen concentration was near zero and the calibration gas correction was applied. The total was about 1.007 or 0.7 percent above unity. From about 10 hours until about 16 hours and again from about 69 to 75 hours the oxygen concentration was unstable or in transition and the total was low by up to 2.5 percent. After ignition occurred in the center assembly at 6.3 hours, the pressurized rods in the North and South peripheral assemblies ruptured. A series of ruptures occurred from about 7 hours until 8.3 hours. Since the pressurized rods were filled with argon, each rupture caused a spike in the argon concentration. At about 7.5 hours the CYBL vessel extraction fan was energized, which began purging the vessel with fresh air. The excess argon was slowly removed and argon concentration did not return to ambient levels until about 30 hours.

A.3 Data Analysis: Argon and Helium Ratios

Since argon is inert and does not react with zirconium, the concentration of argon relative to other reactive gas species was used as a measure of their removal and subsequent release. Figure A.6 shows the argon ratios for nitrogen, oxygen and, carbon dioxide normalized by the ratios found in ambient air. A normalized argon ratio of unity signifies no change from ambient air. Normalized argon ratios that are less than unity signify removal of a gas species. Normalized argon ratios greater than unity signify the release of a gas species. However, due to the argon release during pressurized rod ballooning and the subsequent slow removal of this excess argon the argon concentration between 6.5 and 30 hours is elevated above ambient. The increased argon concentration artificially reduces the argon ratios. In anticipation of this problem, helium was also measured. No certified calibration gas were available for developing a correction correlation for low oxygen conditions so the helium concentration was adjusted using the correlation developed for argon. The helium concentration in air is very low and near the detection limit of the instrument resulting in a noisy signal. Nonetheless meaningful data was obtained that is not influenced by the argon released during rod ballooning. Also shown in Figure A.6 is the reduced N_2/He ratio.

The O_2/Ar plot closely mirrors the oxygen concentration plot in the previous figure. At 6.3 hours when ignition occurs, the O_2/Ar ratio drops sharply to near zero where it remains until just after 60 hours. Air infiltration into the gas sample between 10 and 18 hours is evident. Between 60 and 80 hours, the O_2/Ar ratio raises to near ambient conditions. The return to ambient levels is complete at 105 hours signifying the end of all oxidation reactions.

The N_2/Ar, N_2/He and CO_2/Ar plots reveal two distinct oxidation stages and are discussed in the subsections below.

A.3.1 Stage 1 Oxidation

During the initial or primary oxidation stage and immediately following ignition at 6.3 hours, the ratios drop below unity indicating consumption of the gases. The Stage 1 reactions all involve the oxidation of zirconium metal. During this period the oxygen is consumed by the direct oxidation of zirconium metal:

$$Zr + O_2 \rightarrow ZrO_2 \qquad \text{A.1}$$

The N_2 ratios drop below unity signifying that nitrogen gas entering the center assembly is partly consumed by the zirconium nitride formation reaction:

$$Zr + \tfrac{1}{2}\, N_2 \rightarrow ZrN \qquad \text{A.2}$$

The carbon dioxide argon ratio also drops, suggesting that CO_2 is consumed by this zirconium carbide formation reaction:

$$2Zr + CO_2 \rightarrow ZrC + ZrO_2 \qquad A.3$$

Note that during the primary oxidation stage, the oxidation reaction consumed a gaseous reactant and produce solid products with no gaseous products. With most of the oxygen and much of the nitrogen consumed, much of the ambient air drawn into the assembly was removed and only part exited the top. The large drop in the flow of gas exiting the assembly may explain why ambient air infiltrated the gas sampled from the top of the assembly during this period.

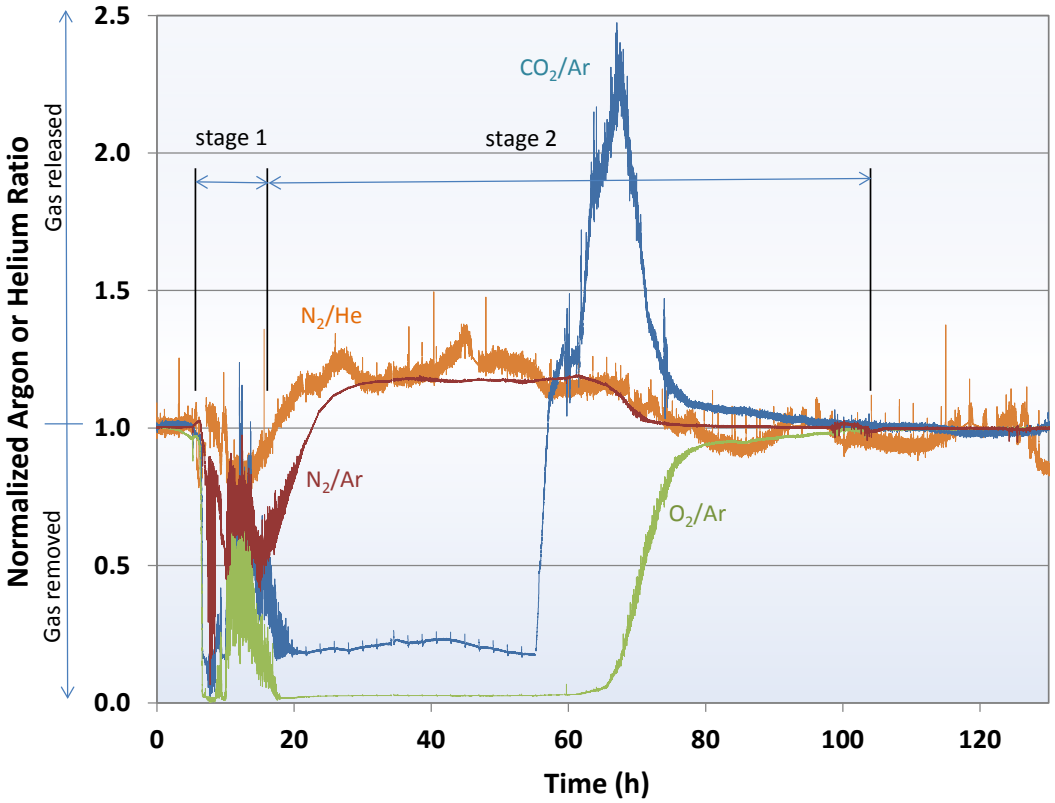

Figure A.6 Normalized argon ratios for nitrogen, oxygen and carbon dioxide.

A.3.1 Stage 2 Oxidation

The Stage 2 reaction primarily involved the oxidation of ZrN. The Stage 2 oxidation period begins at about 17 hours when the N_2/He ratio rises above unity signifying the transition from nitrogen removal to nitrogen release by reaction:

$$ZrN + O_2 \rightarrow ZrO_2 + \tfrac{1}{2} N_2 \qquad A.4$$

Note that the transition from Stage 1 to Stage 2 occurs five hours earlier than indicated by the nitrogen to argon ratio due to the excess argon released by the rod ballooning.

Carbon dioxide is consumed by the oxidation of ZrN to form zirconium oxide and zirconium carbide and release nitrogen gas:

$$ZrN + ½CO_2 \rightarrow ½ZrO_2 + ½ZrC + ½N_2 \quad \text{A.5}$$

At about 57 hours the CO_2/Ar ratio rises above unity signifying the release of carbon dioxide gas by the following reaction:

$$ZrC + 2O_2 \rightarrow ZrO_2 + CO_2 \quad \text{A.6}$$

The Stage 2 oxidation period was almost complete just after 80 hours, but was not completely over until about 105 hours.

During the secondary oxidation period gaseous products from the reaction were formed. Enough nitrogen gas was generated to offset half the oxygen removal. Since 90 percent of the gas drawn into the bottom of the assembly exited the top, there is little impetus for air infiltration into the gas sample as was seen during the primary oxidation period.

A.3.3 Implications

There are important implications of the staged oxidation progression that should be considered when modeling the post-ignition behavior of the burning assembly. The addition of significant energy from the partial oxidation of most of the zirconium by nitrogen coupled with the substantial reduction of convective energy exiting the assembly likely leads to a greater temperature increase during the primary oxidation period than can be predicted by oxidation with oxygen alone. The elevated temperatures significantly increase the propensity for the burn to propagate to adjacent assemblies. The oxidation of zirconium by nitrogen and subsequent oxidation of zirconium nitride need to be included in any models that assess burn propagation to adjacent assemblies.

A.4 Summary

A residual gas mass spectrometer (RGA) was used to monitor the concentrations of the gas constituents exiting the center assembly over a 130 hour period. The gas sample stream was conditioned by filtering particulates and the sample pressure was held constant by an electronic back pressure controller. Ambient air was automatically sampled at two hour intervals to correct instrument drift, which drifted by a factor of four. Calibration gases containing argon and nitrogen were used to correct the argon and nitrogen concentrations for the periods when oxygen was absent from the gas sample. The calibration correction reduced the mass balance error from about 3 percent to less than 1 percent.

The ratio of nitrogen to argon and helium was used to monitor the reaction of nitrogen with zirconium. The analysis clearly shows two distinct stages of oxidation over the course of the test as summarized in Table A.2. The primary oxidation stage was very energetic and continued for 11 hours after ignition. During this stage all the oxygen entering the assembly was consumed by oxidation of zirconium and a substantial portion of the nitrogen was consumed by production of the nitride from much (if not most) of the remaining unoxidized zirconium. The nitride reaction releases about a third of the energy of complete oxidation. All reactions consumed gaseous reactants so the flow exiting the assembly was substantially reduced. The added energy release from wholesale production of the nitride coupled with the significant reduction in convective energy removal are important phenomena to consider when assessing the propensity of an ignited assembly to propagate ignition to adjacent assemblies.

During the second oxidation stage, all of the oxygen entering the assembly was consumed by the oxidation of zirconium nitride as indicated by the release of nitrogen gas. This stage continued for 88 hours. The lower energy release of zirconium nitride oxidation (two thirds of complete zirconium oxidation) coupled with increased convective energy removal resulted in a less energetic burn during the second stage.

Table A.2 Summary of reaction regimes.

Start Time (hr)	End Time (hr)	Duration (hr)	Description
0	6.3	6.3	Pre-ignition ambient conditions.
6.3	17	10.7	Primary oxidation stage. Initial reaction of zirconium metal, oxidation, nitride production, carbide production. Complete oxidation by oxygen and partial oxidation by nitrogen and carbon dioxide. No gaseous products of reaction formed resulting in substantial reduction of outlet gas flow. The low outflow allows air to mix with sample gas. Down flow of air to the reaction may be possible. The addition of significant energy from the partial oxidation of most of the zirconium inventory coupled with the substantial reduction of energy convection out of the assembly leads to much greater temperature increase than can be predicted by oxidation by oxygen alone.
17	105	88	Secondary oxidation stage. Subsequent complete oxidation of partially oxidized zirconium, primarily ZrN, resulting in the release of nitrogen and carbon dioxide gases.
105	130	25	Return to ambient conditions.

NRC FORM 335
(12-2010)
NRCMD 3.7

U.S. NUCLEAR REGULATORY COMMISSION

BIBLIOGRAPHIC DATA SHEET

(See instructions on the reverse)

1. REPORT NUMBER
(Assigned by NRC, Add Vol., Supp., Rev., and Addendum Numbers, if any.)
NUREG/CR-7216

2. TITLE AND SUBTITLE
Spent Fuel Pool Project Phase II: Pre-Ignition and Ignition Testing of a 1x4 Commercial 17×17 Pressurized Water Reactor Spent Fuel Assemblies under Complete Loss of Coolant Accident Conditions

3. DATE REPORT PUBLISHED
MONTH: April
YEAR: 2016

4. FIN OR GRANT NUMBER

5. AUTHOR(S)
S.G. Durbin, E.R. Lindgren, and L. Humphries (Sandia National Laboratories)

Z. Yuan, M. Zavisca and M. Khatib-Rahbar (Energy Research, Inc.)

R. Beaton (U.S. Nuclear Regulatory Commission)

6. TYPE OF REPORT
Technical

7. PERIOD COVERED (Inclusive Dates)
July 2009 to June 2014

8. PERFORMING ORGANIZATION - NAME AND ADDRESS (If NRC, provide Division, Office or Region, U. S. Nuclear Regulatory Commission, and mailing address; if contractor, provide name and mailing address.)
Sandia National Laboratories, Albuquerque, NM 87185
Energy Research, Inc., Rockville, MD 20847-2034
U.S. Nuclear Regulatory Commission, Washington, DC 20555-0001

9. SPONSORING ORGANIZATION - NAME AND ADDRESS (If NRC, type "Same as above", if contractor, provide NRC Division, Office or Region, U. S. Nuclear Regulatory Commission, and mailing address.)
Division of Systems Analysis
Office of Nuclear Regulatory Research
U.S. Nuclear Regulatory Commission
Washington, DC 20555-0001

10. SUPPLEMENTARY NOTES

11. ABSTRACT (200 words or less)
The US Nuclear Regulatory Commission (NRC), in collaboration with the Organisation for Economic Co-operation and Development (OECD), and 12 international partners, conducted an experimental program to obtain experimental data for the characterization of hydraulic and ignition phenomena of prototypic light water reactor fuel assemblies in a spent fuel pool under complete loss of coolant accidents for validation of the MELCOR severe accident computer code. MELCOR is a fully integrated, engineering-level computer code whose primary purpose is to model the progression of postulated accidents in light water reactors as well as non-reactor systems (e.g., spent fuel pool and dry cask). The experimental program was conducted in two phases at Sandia National Laboratories. The first phase focused on axial heating and zirconium fire propagation in a single 17×17 PWR fuel assembly. The second phase consisted of pre-ignition and ignition tests of five prototypic PWR full-length 17×17 fuel assemblies to simulate a complete loss-of-coolant-accident in a spent fuel pool. The assemblies were placed in a 1×4 configuration where the center fuel assembly was electrically heated and the four surrounding assemblies were unheated. Two of the unheated assemblies contained pressurized rods to study ballooning effects.

12. KEY WORDS/DESCRIPTORS (List words or phrases that will assist researchers in locating the report.)
Spent Fuel Pool Project, Spent Fuel Pool, Spent Fuel Pool Loss of Coolant Accident, Pre-Ignition, Ignition, Spent Fuel Pool Pre-Ignition, Spent Fuel Pool Ignition

13. AVAILABILITY STATEMENT
unlimited

14 SECURITY CLASSIFICATION
(This Page)
unclassified
(This Report)
unclassified

15. NUMBER OF PAGES

16. PRICE

Federal Recycling Program

UNITED STATES
NUCLEAR REGULATORY COMMISSION
WASHINGTON, DC 20555-0001

OFFICIAL BUSINESS

NUREG/CR-7216

Spent Fuel Pool Project Phase II: Pre-Ignition and Ignition Testing of a 1x4 Commercial 17x17 Pressurized Water Reactor Spent Fuel Assemblies under Complete Loss of Coolant Accident Conditions

April 2016